New Laser Amplifier Materials at 1053 nm

Cesare Meroni

Normandie Université

THÈSE

Pour obtenir le diplôme de doctorat

Spécialité PHYSIQUE

Préparée au sein de l'Université de Caen Normandie

New Laser Amplifier Materials at 1053nm

Présentée et soutenue par
CESARE MERONI

Thèse soutenue le 27/09/2022 devant le jury composé de		
M. WILFRIED BLANC	Directeur de recherche, Université côte d'Azur	Rapporteur du jury
M. SEBASTIEN MONTANT	Directeur de recherche, CEA FAR	Membre du jury
M. BRUNO VIANA	Directeur de recherche au CNRS, UNIVERSITE PARIS 6 PIERRE ET MARIE CURIE	Président du jury
M. ALAIN BRAUD	Professeur des universités, Université de Caen Normandie	Directeur de thèse
M. PATRICE CAMY	Professeur des universités, Université de Caen Normandie	Co-directeur de thèse

Thèse dirigée par ALAIN BRAUD (Centre de recherche sur les ions, les matériaux et la photonique (Caen)) et PATRICE CAMY (Centre de recherche sur les ions, les matériaux et la photonique (Caen))

UNIVERSITÉ CAEN NORMANDIE

ED 591 PSIME

CIMAP

UNIVERSITÉ DE CAEN NORMANDIE

DOCTORAL THESIS

New Laser Amplifier Materials at 1.05 μm

Author:
Cesare MERONI

Supervisor:
Alain BRAUD
Patrice CAMY

A thesis submitted in fulfillment of the requirements for the degree of Doctor of Philosophy

in the

Centre de recherche sur les Ions, les Materiaux et la Photonique
U.F.R. des Sciences

27 September 2022

UNIVERSITÉ DE CAEN NORMANDIE

Abstract

Ecole Doctorale Physique, Sciences de L'Ingénieur, Matériux, Énergie
U.F.R. des Sciences

Doctor of Philosophy

New Laser Amplifier Materials at 1.05 μm

by Cesare MERONI

In this work, the co-doping of $CaF_2 : Nd^{3+}$ with different optically inactive buffer ions is investigated as a promising material for high energy laser applications. The main goal is to identify new neodymium doped compounds as potential substitutes for the Nd-doped phosphate glasses currently employed in the Laser Mégajoule (LMJ). A detailed optical spectroscopy investigation describes the effect of the different buffer ions on the neodymium spectroscopic properties. The buffer ions can be separated in two groups: buffer ions with a larger size than Nd lead to a single dominant Nd emitting site, while the smaller ions clearly exhibit two different types of Nd sites, that are evidenced in absorption and emission spectroscopy as well as and in the fluorescence dynamics. A multiple buffer ion co-doping, employing buffers from both groups in the same compound enable the engineering of the spectral bands. Four interesting compositions exhibiting a broad and flat profile around 1.05 μm have been identified and represent promising laser crystals for the LMJ applications. The amplification properties of the different laser crystals have been investigated using a dedicated pump-probe setup with two tunable laser sources. The results confirm the broad band amplification features of the most promising crystals. The CW laser operation and tunability of these materials show remarkable results with laser slope efficiencies close to the theoretical limit and very low laser thresholds. The ytterbium co-doping of $CaF_2 : 0.5\%Nd$ is also investigated using Yb ions both as active ions and buffer ions and shows interesting features for broadband oscillators around 1 μm. Finally, a preliminary study on molecular adherence with CaF_2 is realized with a pure CaF_2 bonded with a $CaF_2 : Nd, Lu$, exploiting the pure CaF_2 as a heat sink for optimal thermal management.

Acknowledgements

I would like to thank Alain Braud, for supervising and supporting me in those years during my PhD and for everything I learned in science and pedagogy. My scientific background and experience are sensibly enriched during these years. Also, I would like to thank him for the welcoming at my arrival and the help during the first months, to get through the difficulties of a foreigner (non-french speaker) in France. I would like to thank also Patrice Camy, as co-supervisor, for the interest in my work and the scientific discussions during my PhD.

I would like to thank also Cedric Maunier, Denis Penninckx and Sébastien Montant, without whom this experience would not have been possible. In particular to Sébastien, for the time spent in the explanation of the Laser Mégajoule, and consequently the help in the redaction of the introduction of this thesis.

I want to thank Jean-Louis Doualan and Florent Starecki for all the help and the scientific discussions concerning the laboratory work, and for everything I have learned from them. Every experimental requires engineers and technicians, and for this I have to thank Abdel Benayad for the crystal growth, Vivien Menard for the crystal preparation and Philippe Leprince of the mechanical workshop.

Afterwards, I want to thank all other the members of the OML equipe, Pavel, Gurvan, Simone, Sylvan, Hervè, Mathieu, the administration staff and the other members of CIMAP.

A special thank to the current and former PhD students of CIMAP, with whom I shared those years. I wish best of luck to Paramesh, Kirill, Liza for the continuation of their thesis. Kilian, Aline, Farah and Lauren, with the addition of Luz, Florent, Olivier, Julie and Raphaël: with all of you I had the pleasure to spend a great time outside of the lab, with nights out and crazy travels; not only I want to thank you all for the support and the help that I received, but also let you know how much I am grateful for all we shared, I will never forget that.

I had the luck to also meet a lot of great people during my experience in Caen, inside and outside the campus, that I would like to cite. To Seb, Dennis, Roisin, Luisa, Chiara and Marco; to the musicians of the Mazel Combo (with Leo and Savitri being also part of the campus life); to Jérôme and Titì, for all the memories we have collected with you in your bar; to everyone else that I forgot to cite explicitly; to Sara, for all the support that I have received from you; thank you all for everything.

I want to thank my family for the support that I received from them during my first experience abroad.

A thank also to my old friends in Italy, every time I go back it's so nice to have you there, including the ones among you that live abroad. I would like to mention Marco, Silvia, Valentino and Damiano, but I am of course referring to everyone else too.

The last one, from the bottom of my heart, a special thank to Angela, for always been there for me, supported me and visited me in France so many times.

Caen, September 27th, 2022

Contents

Abstract 3

Acknowledgements 5

List of Figures 9

List of Tables 17

Résumé 19

1 Introduction 39
- 1.1 High Energy Density and Ultra High Intensity Lasers 39
- 1.2 The Laser MégaJoule and PETAL 41
  - 1.2.1 FM-to-AM conversion 44
  - 1.2.2 Beam Smoothing 45
  - 1.2.3 Crossed Beam Energy Transfer 46
- 1.3 New Materials for LMJ 47
- 1.4 Chapters Overview 51

2 Optical Spectroscopy of $CaF_2 : Nd^{3+}$ Co-doped with Buffer Ions 53
- 2.1 Introduction 53
  - 2.1.1 Principles of Rare Earth Spectroscopy 53
  - 2.1.2 Nd-Doped Fluorites Spectroscopy 54
  - 2.1.3 The Choice of the Buffer Ions 56
- 2.2 Principles and Techniques 58
  - 2.2.1 Bridgman-Stockbarger Crystal Growth and Sample Preparation 58
  - 2.2.2 Absorption 60
  - 2.2.3 Luminescence and Excitation Spectroscopy 60
  - 2.2.4 Energy Level Lifetime 63
- 2.3 Judd-Ofelt Theory 64
  - 2.3.1 General Aspects 64
  - 2.3.2 Application of the J-O Theory 66
  - 2.3.3 J-O applied to the Neodymium Ion 67
- 2.4 Co-doping with One Buffer: $CaF_2 : Nd^{3+}, Bu^{3+}$ 68
  - 2.4.1 $Gd^{3+}, La^{3+}, Ce^{3+}, Y^{3+}, Lu^{3+}, Sc^{3+}$ Co-Doping 68
  - 2.4.2 Judd-Ofelt Calculations and Radiative Lifetime 81
- 2.5 Co-doping with Two Buffers: $CaF_2 : Nd^{3+}, Bu_1^{3+}, Bu_2^{3+}$ 84
  - 2.5.1 Gadolinium-Yttrium Hybrid Co-Doping 84
  - 2.5.2 Other Combinations: $La - Y, Gd - Lu, Ce - Y$ Co-Doping 89

2.6 Co-doping with Three Buffers: $CaF_2 : Nd^{3+}, Bu_1^{3+}, Bu_2^{3+}, Bu_3^{3+}$ 91
2.7 Neodymium and Ytterbium Co-Doping 95
2.7.1 Exciting Neodymium Ions 97
2.7.2 $Yb^{3+} \rightarrow Nd^{3+}$ Back-Transfer 101
2.7.3 $Nd^{3+} \rightarrow Yb^{3+}$ Energy Transfer Modeling 103
ETE Determination Using Integrated Luminescence Intensity 104
ETE Determination using Nd decays 108
2.8 Conclusions 113

3 Amplification Properties **115**
3.1 Introduction 115
3.2 Amplification Criterion 115
3.3 Gain Modelling 116
3.3.1 Rate Equations: Four-Level System 118
3.3.2 Propagation in the Amplifying Medium 120
3.3.3 Ground State Depletion and Gain Saturation 123
3.4 Experimental Amplification Measurements 125
3.5 Amplification Results 126
3.6 Conclusions 136

4 Continuous-Wave Laser Operation **137**
4.1 Introduction 137
4.2 Laser Crystal Preparation 138
4.2.1 Laser Crystal Orientation 139
4.3 CW Laser Operation 143
4.3.1 Laser Tunability Investigation 149
4.4 Round-Trip Losses Determination 154
4.4.1 Caird Analysis 154
4.4.2 Findlay-Clay Analysis 155
4.4.3 Results and Comparison Between the Models 156
4.5 Perspectives: Molecular Adherence 159
4.5.1 State of the Art 159
4.5.2 A First Molecular Adherence Try: $CaF_2||CaF_2 : Nd, Lu$ 160
4.6 Conclusions 170

Conclusions **173**

References **179**

List of Figures

1 Schéma de Principe de la fusion par confinement inertiel. . . . 21
2 Schéma de la chaîne d'amplification, illustrant la configuration du faisceau laser LMJ. Des verres phosphatés dopés au Nd^{3+} sont utilisés dans la cavité régénératrice, l'amplificateur frontal et les amplificateurs laser #1 et #2 [15]. 22
3 Schéma simplifié du laser «front-end» du LMJ avec les verres Nd:phosphate et avec $CaF_2 : Nd, ...$ 22
4 Intégration de l'intensité d'émission de $^4F_{3/2} \rightarrow ^4 I_{11/2}$ en fonction de la concentration de Lu^{3+} [40] 25
5 Conductivité thermique en fonction de la concentration de Lu en $CaF_2 : Nd, Lu$ [15]. 25
6 (a) Spectre de luminescence de $CaF_2 : 0.5\%Nd^{3+}, 5\%Bu^{3+}$, avec $Bu = (Gd, La, Ce, Y, Lu, Sc)$ avec une longueur d'onde d'excitation de 797 nm. (b) Spectres d'excitation avec une longueur d'onde de détection de 1054 nm. 28
7 Luminescence (a) et excitation (b) de $CaF_2 : Nd, Gd, Y$ pour différentes concentrations de gadolinium et d'yttrium, en gardant 5% comme concentration totale des tampons. 30
8 Spectre amplifié d'un faisceau sonde de 16 nm FWHM centré sur un faisceau d'entrée de 1053 nm avec un gain $G = 20.72$ pour différents milieux de gain, comparé au verre de référence LGG70 actuellement utilisé dans le LMJ. 32
9 Spectre d'amplification en fonction de λ_{probe} pour différents échantillons, avec la même puissance de pompe absorbée $P_{abs} = 400$ mW. $lambda_{pump} = 797$ nm, $P_{probe} = 1$ mW, $\omega(radius) = 50\ \mu$m. 33
10 Puissance de sortie du laser en fonction de la puissance de pompage absorbée pour les quatre coupleurs de sortie $T = 0,8\%, 1,7\%, 4,5\%, 8\%$, d'un $CaF_2 : 0,5\%Nd, 2,5\%Gd, 2,5\%Y$, avec une longueur d'onde de pompage de $\lambda_{pump} = 796$ nm . . 34
11 Courbes d'accord et reconstruction d'un $CaF_2 : 0.5\%Nd$ co-dopé avec $2.5\%Gd, 2.5\%Y$ (a), $4\%Gd, 1\%Y$ (b), $3\%Gd, 1.4\%Ce, 0.6\%Y$ (c) and $3.8\%Gd, 0.55\%La, 0.65\%Y$ (d). 37
12 Faisceau laser Titanium Sapphire à 797 nm, 2 W focalisé qui se propage à travers l'échantillon. Il est possible de voir que l'upconversion verte du Nd a lieu uniquement dans la partie non dopée. 38

13 Test laser utilisant une cavité plano-concave de $CaF_2||CaF_2 : 0.5\%Nd, 5\%Lu$ ($\triangle$) comparée à $CaF_2 : 0.5\%Nd, 5\%Lu$ ($\square$) avec le même diamètre $\phi = 14$ mm et une épaisseur de 5 mm, pour deux transmissions de coupleur de sortie de 8% (vert et noir) et 0.8% (bleu et rouge). 38

1.1 Connection of the high-energy density regime to physical and astrophysical systems [20]. 40
1.2 Targets used in ICF experiments, in direct and indirect drive configuration[21]. 41
1.3 Evolution of ultra-high intensity (UHI) lasers [3]. 42
1.4 Aerial view of the LMJ facility. 43
1.5 Scheme of the working principle. 43
1.6 Amplifying chain schematic, illustrating the LMJ laser beam setup. Nd^{3+}-doped phosphate glasses are employed in the regenerative cavity, the front-end amplifier, and the laser amplifiers #1 and #2 [15]. 44
1.7 Simplified scheme of the front-end of the LMJ with the Nd:phosphate glasses and with the $CaF_2 : Nd, ...$ 48
1.8 $^4F_{3/2} \rightarrow ^4 I_{11/2}$ integrate emission intensity versus Lu^{3+} concentration [40] 50
1.9 Thermal conductivity in function of Lu concentration in $CaF_2 : Nd, Lu$ [15]. 50

2.1 Fluorite lattice structures with different site symmetries for low Nd^{3+} doping [42]. 55
2.2 Illustration of the quenching of the $^4F_{3/2} \rightarrow {}^4I_{9/2}$ transition due to energy transfer between two Nd^{3+} ions 56
2.3 Bridgmann crystal growth setup: tapered-end configuration (a) and the growth from a seed (b). 59
2.4 Dieke's chart with the energy levels of neodymium highlighted in red [72]. 61
2.5 Spectrum of the 20 W tunsgten lamp corrected with the tungsten emissivity, compared with the Planck's law. 63
2.6 Ionic radius of the buffer ions chosen to perform the optical spectroscopy study on $CaF_2 : Nd, Bu$. 69
2.7 Absorption coefficient of $CaF_2 : 0.5\%Nd^{3+}, 5\%Bu^{3+}$, with Bu = (Gd,La,Ce,Y,Lu,Sc) 70
2.8 (a) Luminescence spectra of $CaF_2 : 0.5\%Nd^{3+}, 5\%Bu^{3+}$, with $Bu = (Gd, La, Ce, Y, Lu, Sc)$ with excitation wavelength 797 nm. (b) Excitation spectra with detection wavelength of 1054 nm. 71
2.9 Luminescence spectra of $CaF_2 : Nd, Gd$ (a) and $CaF_2 : Nd, Y$ (b), excited at 791 nm (blue) and 797 nm (red) 72
2.10 Excitation spectra of $CaF_2 : Nd, Gd$ (a) and $CaF_2 : Nd, Y$ (b), excited at 1049 nm (black) and 1054 nm (red) 73
2.11 Comparison lineshape absorption (red) and lineshape excitation spectra (black) for $CaF_2 : Nd, Gd$ (a) and $CaF_2 : Nd, Y$ (b) 75

2.12 (a) Experimental absorption coefficient of $CaF_2 : Nd, Y$ (black) compared with a reconstruction of it (red) obtained from a linear combination of the lineshape of the excitation spectra recorded at 1049 nm and 1054 nm. (b) Absorption coefficient of the N_1 and N_2 sites separately. 77
2.13 Luminescence spectra of $CaF_2 : Nd, Y$ tuning the excitation wavelength from 791 nm to 797nm with a 1 nm step. 78
2.14 Lifetime of $CaF_2 : Nd, Gd$ (a) and $CaF_2 : Nd, Y$ (b), of N_1 (black), $\lambda_{exc} = 791$ nm-$\lambda_{det} = 1049$ nm, and N_2 (red), $\lambda_{exc} = 797$ nm-$\lambda_{det} = 1054$ nm. 79
2.15 Fluorescence lifetimes of $CaF_2 : Nd, Bu$ for $Bu = (Gd, La, Ce, Y, Lu, Sc)$ of N_1, $\lambda_{exc} = 791$ nm-$\lambda_{det} = 1049$ nm, and N_2, $\lambda_{exc} = 797$ nm-$\lambda_{det} = 1054$ nm in function of the ionic radius. 80
2.16 Time Resolved Luminescence (a) and Excitation (b), for N_1 (black) with time window $[900 - 1500\ \mu s]$, and N_2(red) with time window $[10 - 60\ \mu s]$. 82
2.17 Absorption coefficient of $CaF_2 : Nd, Gd, Y$ for different gadolinium and yttrium concentration, keeping 5% as total buffers concentration. 85
2.18 Luminescence (a) and excitation (b) of $CaF_2 : Nd, Gd, Y$ for different gadolinium and yttrium concentration, keeping 5% as total buffers concentration. 86
2.19 $^4F_{3/2}$ energy level lifetime concentration trend of $CaF_2 : Nd, Gd, Y$ for different gadolinium and yttrium concentration, keeping 5% as total buffers concentration. . . . 87
2.20 Reconstruction via linear combination of the luminescence of $CaF_2 : 0.5\%Nd, 2.5\%Gd, 2.5\%Y$ (black), compared with the experimental spectrum (red), and the 5%Gd (green) and 5%Y (blue). Excitation wavelength at 797 nm 88
2.21 Luminescence of $CaF_2 : 0.5\%Nd, 2.5\%Gd, 2.5\%Y$ tuning the excitation wavelength from 795.4 nm to 797.0 nm with 0.2 nm step. highlighted in blue the flattest profile, corresponding to 796.2 nm. 88
2.22 Reconstruction via linear combination of the luminescence with excitation wavelength at 797 nm of $CaF_2 : 0.5\%Nd, 2.5\%Gd, 2.5\%Lu$ (a), $CaF_2 : 0.5\%Nd, 2.5\%Ce, 2.5\%Y$ (b), $CaF_2 : 0.5\%Nd, 2.5\%La, 2.5\%Y$ (c). 90
2.23 Reconstructed spectrum (black) compared to the experimental spectrum (red) of the luminescence of CaF_2 :$0.5\%Nd, 3.8\%Gd, 0.65\%Y, 0.55\%La$ 92
2.24 (a) Simulated spectrum (black) compared to the experimental spectrum (red) of the luminescence of CaF_2 :$0.5\%Nd, 1.9\%Gd, 1.6\%Sc, 1.5\%Y$. (B), the successful reconstruction excluding scandium from the linear combination. 93

2.25 Simulated spectrum (blue) compared to the experimental spectrum (red) of the luminescence of CaF_2 :0.5%Nd, 3%Gd, 1.4%Ce, 0.6%Y. The flat region is between 1049 nm and 1054 nm. 94
2.26 Scheme of the Nd $\rightarrow$ Yb energy transfer. 96
2.27 Absorption coefficient of the $CaF_2 : Nd, Yb, Gd$ crystals for different Yb and Gd concentration, keeping 0.5at.%Nd and 5at.% as total co-doping concentration. As a reference comparison are also reported the $CaF_2 : 5\%Yb$, 0.5%Nd and $CaF_2 : 0.5\%Nd, 5\%Lu$. 96
2.28 Luminescence of $CaF_2 : Nd, Yb, Gd$ crystals with excitation wavelength of 791 nm (a) and 797 nm (b). 98
2.29 Energy level lifetime for the $CaF_2 : 0.5\%Nd, 0.7\%Yb, 4.3\%Gd$ exciting at 791 nm and detecting at 1049 nm, corresponding to the $^4F_{3/2} \rightarrow {}^4I_{11/2}$ transition of the neodymium ion. 99
2.30 Energy level lifetime for the $CaF_2 : Nd, Yb, Gd$ exciting at 791 nm and detecting at 863 nm, corresponding to the $^4F_{3/2} \rightarrow {}^4I_{9/2}$ transition of the neodymium ion, for various ytterbium and gadolinium concentrations. 100
2.31 Energy level lifetime for the $CaF_2 : 0.5\%Nd, 0.2\%Yb, 4.8\%Gd$ exciting at 791 nm and detecting at 978 nm. 101
2.32 Luminescence of $CaF_2 : Nd, Yb, Gd$ crystals in the $925 - 1100$ nm region, with excitation wavelength of 922 nm (a), and in the $840 - 925$ nm region, with excitation wavelength of 978 nm (b) 102
2.33 Luminescence of $CaF_2 : 0.5\%Nd, 5\%Gd$, $CaF_2 : Nd, Yb, Gd$ and calculated difference in blue for every ytterbium concentration. Normalization is performed on the 863 nm peak of neodymium, where no luminescence of ytterbium is involved. 107
2.34 Luminescence spectrum of $CaF_2 : 5\%Yb$ compared with $CaF_2 : 0.5\%Nd, 3\%Yb, 2\%Gd$. 108
2.35 Energy transfer rate α_{ET} in function of the acceptor concentration N_{Yb}, deriving the energy transfer parameter K_{ET} from a linear fit. 109
2.36 Luminescence of $CaF_2 : Nd, Yb, Gd$ excited at 791 nm and 922 nm for every gadolinium concentration. Normalization is performed on the 863 nm peak of neodymium, where no luminescence of ytterbium is involved. 111
2.37 Energy transfer efficiency ETE in function of the acceptor concentration N_{Yb}, calculated from the luminescence integrals analysis and the lifetime analysis. 112

3.1 Amplified spectrum of a 16 nm FWHM probe beam centered at 1053 nm input beam with a gain $G = 20.72$ for different gain media, compared with the reference LGG70 glass currently used in the LMJ. 117

3.2 Amplified spectrum of a 16 nm input beam at 1053 nm employing the 3%Gd, 1.4%Ce, 0.6%Y as amplifying medium, for different values of gain. 117
3.3 Four-level system diagram of Nd^{3+} for laser operation at 1.05 μm pumped at 800 nm 118
3.4 Gain coefficient per centimeter calculated in small signal conditions for a 5 mm thick $CaF_2 : 0.5\%Nd^{3+}, 5\%Lu^{3+}$ crystal: $P_{p,0} = 0.5$W, $P_{L,0} = 1$mW, $\omega_{p,0} = \omega_{L,0} = 50\mu$m, $\lambda_p = 797$nm, $\lambda_L = 1053$nm. 122
3.5 (a) Amplification factor as a function of the pump power, for different probe powers. (b) Amplification factor as a function of the probe power, for different pump power values. Waists values: $\omega_p = \omega_L = 50$ μm. 124
3.6 Experimental setup for the gain measurement. 126
3.7 Typical experimental amplification signal with the double-modulation pump-probe setup. 127
3.8 Ratio between the absorption coefficient and the unpumped absorption coefficient (a), and ratio between the gain coefficient and the small gain coefficient (b), propagated in a 5 mm thick $CaF_2 : 0.5\%Nd^{3+}, 5\%Lu^{3+}$ crystal: $P_{p,0} = 0.5$W, $P_{L,0} = 1$mW, $\omega_{p,0} = \omega_{L,0} = 50\mu$m, $\lambda_p = 797$nm, $\lambda_L = 1053$nm. 129
3.9 Amplification P_{out}/P_{in} for the N_1 and N_2 center for $CaF_2 : Nd, Bu$ (Bu = Gd, La, Ce, Y, Lu, Sc) crystal. For N_1 (blue), $\lambda_p = 791$ nm, $\lambda_L = 1049$ nm; for N_2 (red), $\lambda_{pump} = 797$ nm, $\lambda_{probe} = 1054$ nm. For all experiments and calculations, the absorbed pump power is kept at 400 mW, $P_{probe} = 1$ mW, $\omega(radius) = 50$ μm. 130
3.10 Excitation spectrum and amplification spectrum varying λ_{pump} for $CaF_2 : 0.5\%Nd, 5\%Gd$ (a) and $CaF_2 : 0.5\%Nd, 5\%Lu$ (b) with $P_{pump} = 920$ mW, $\lambda_{probe} = 1053$ nm, $P_{probe} = 1$ mW, $\omega(radius) = 50$ μm. 132
3.11 Emission cross section and amplification spectrum as a function of λ_{probe} for $CaF_2 : 0.5\%Nd, 5\%La$ (a) and $CaF_2 : 0.5\%Nd, 5\%Y$ (b) with $P_{abs} = 400$ mW, $\lambda_{pump} = 797$ nm, $P_{probe} = 1$ mW, $\omega(radius) = 50$ μm. 134
3.12 Amplification spectrum as a function of λ_{probe} for different buffers, with the same absorbed pump power $P_{abs} = 400$ mW. $\lambda_{pump} = 797$ nm, $P_{probe} = 1$ mW, $\omega(radius) = 50$ μm. 135
3.13 Amplification spectrum as a function of λ_{probe} for different samples, with the same absorbed pump power $P_{abs} = 400$ mW. $\lambda_{pump} = 797$ nm, $P_{probe} = 1$ mW, $\omega(radius) = 50$ μm. 135

4.1 Plano-Concave Cavity Setup with the Lyot filter. 138
4.2 X-ray image with the Von Laue method of a non-oriented $CaF_2 : 0.5\%Nd, 3.8\%Gd, 0.65\%Y, 0.55\%La$ (left) and the same crystal oriented $[1, 1, 1]$ (right). 140

4.3 Depolarization effect in a non-oriented and $[1,1,1]$ oriented $CaF_2 : 0.5\%Nd, 3.8\%Gd, 0.65\%Y, 0.55\%La$ crystal, with pump wavelength of $\lambda_{pump} = 797$ nm and output coupling $T = 0.8\%$. The graph is displayed in polar coordinates. 140
4.4 Slope efficiency of a non-oriented $CaF_2 : 0.5\%Nd, 3.8\%Gd, 0.65\%Y, 0.55\%La$ (a) and the same crystal oriented $[1,1,1]$ (b), with pump wavelength of $\lambda_{pump} = 797$ nm. 141
4.5 Birefringence effect in a non-oriented $CaF_2 : 0.5\%Nd, 3.8\%Gd, 0.65\%Y, 0.55\%La$ crystal, with pump wavelength of $\lambda_{pump} = 797$ nm and pump power $P_{pump} = 3$ W. 143
4.6 Laser output power versus absorbed pump power for the four output couplers $T = 0.8\%, 1.7\%, 4.5\%, 8\%$, of a $CaF_2 : 0.5\%Nd, 2.5\%Gd, 2.5\%Y$, with pump wavelength of $\lambda_{pump} = 796$ nm. 144
4.7 Laser output power versus absorbed pump power for the four output couplers $T = 0.8\%, 1.7\%, 4.5\%, 8\%$, of a $CaF_2 : 0.5\%Nd, 4\%Gd, 1\%Y$ (a) and $CaF_2 : 0.5\%Nd, 3\%Gd, 1.4\%Ce, 0.6\%Y$ (b), with pump wavelength of $\lambda_{pump} = 797$ nm. 145
4.8 Image of the laser beam obtained with the $CaF_2 : 0.5\%Nd, 2.5\%Gd, 2.5\%Y$, with a lasing wavelength $\lambda_L = 1065$ nm. 147
4.9 Fit of the laser beam divergence according to eq. (4.7) in order to derive the waist value and the M^2 for the laser beam generated by the $CaF_2 : 0.5\%Nd, 2.5\%Gd, 2.5\%Y$, with a lasing wavelength $\lambda_L = 1065$ nm for both the x direction (a) and the y direction (b). 148
4.10 Laser output power versus absorbed pump power of a $CaF_2 : 0.5\%Nd, 2.5\%Gd, 2.5\%Y$, with output coupler $T = 8\%$, for different pump wavelengths. 149
4.11 Tuning curves and reconstruction of a $CaF_2 : 0.5\%Nd$ co-doped with $2.5\%Gd, 2.5\%Y$ (a), $4\%Gd, 1\%Y$ (b), $3\%Gd, 1.4\%Ce, 0.6\%Y$ (c) and $3.8\%Gd, 0.55\%La, 0.65\%Y$ (d). 152
4.12 Tuning curve of a $CaF_2 : 0.5\%Nd, 2.5\%Gd, 2.5\%Y$, with output coupler $T = 8\%$, for different pump wavelengths. 154
4.13 Passive losses calculation for the $CaF_2 : 0.5\%Nd, 2.5\%Gd, 2.5\%Y$, performed both with the Findlay-Clay analysis (a) and the Caird analysis (b). 157
4.14 Passive losses calculated with the Findlay-Clay (red) and the Caird (blue) method for different laser crystals. 158
4.15 Comparison between laser polished surface and sub-nanometric polished surface, for $CaF_2 : 0.5\%Nd, 5\%Lu$ 162
4.16 Left, the two crystals separately, with diameter $\phi = 14$ mm, and a 5 mm thickness for the doped sample and 4 mm for the pure CaF_2. Right the two crystals in contact. 163

4.17 Left, a picture of the optical contact, showing the part of the crystal where the optical contact has been successfully achieved and the part where it is not. Right, a picture showing the stable bonding between the two crystals. 163
4.18 Sensofar picture before thermal treatment, bright field (left) and qualitative roughness. Molecular adherence is present on roughly 30% of the sample. 164
4.19 Sensofar picture after the first thermal treatment, bright field and roughness. Molecular adherence is present for roughly 40% of the sample. The roughness measurement is purely qualitative, due to the lack of resolution of the Sensofar microscope. 164
4.20 Bright field Sensofar picture after the second thermal treatment. The difference in contrast between the two parts of the interface is much lower. The red box identifies the reference for Figure 4.22. 165
4.21 Sensofar picture after the third thermal treatment, bright field. There is no difference in contrast between the former adherent and non-adherent parts. The red box identifies the reference for Figure 4.22. 166
4.22 Comparison result after the second thermal treatment (left) and the third (right). The parts of the samples correspond at the zone of the sample identified with the red box in Figure 4.20 and 4.21 respectively. 166
4.23 Titanium Sapphire laser beam at 797 nm, 2 W focalized that propagates through the sample. It is possible to see that only in the undoped part the Nd up-conversion is taking place. . . 167
4.24 Temporal heat propagation due to laser excitation at 797 nm, 2 W focalized. 168
4.25 Laser test using a plano-concave cavity of $CaF_2||CaF_2 : 0.5\%Nd, 5\%Lu$ ($\triangle$) compared with $CaF_2 : 0.5\%Nd, 5\%Lu$ ($\square$) with the same diameter $\phi = 14$ mm and a of thickness 5 mm, for two output coupler transmission of 8% (green and black) and 0.8% (blue and red). 169
4.26 SEM image of the bonded sample. Upper the doped CaF_2, down the pure one. The bright points are simply residuals of the carbonation process. 170

List of Tables

2.1 Fluorescence lifetimes of $CaF_2 : Nd, Bu$ for Bu $=$ (Gd, La, Ce, Y, Lu, Sc) of N_1, $\lambda_{exc} = 791$ nm-$\lambda_{det} = 1049$ nm, and N_2, $\lambda_{exc} = 797$ nm-$\lambda_{det} = 1054$ nm. 80

2.2 Judd-Ofelt parameters and branching ratios of $^4F_{3/2}$ for $CaF_2 : 0.5\%Nd, 5\%Bu$. 81

2.3 $^4F_{3/2}$ radiative lifetime estimated with the J-O theory. 83

2.4 Peak emission wavelengths for the six $CaF_2 : 0.5\%Nd, 5\%Bu$. 84

2.5 Reconstruction coefficients used in the linear combination eq. 2.28, for simulating the experimental spectra of $CaF_2 : 0.5\%Nd, 2.5\%Bu_1, 2.5\%Bu_2$ 91

2.6 Flatness and center wavelength of the four promising combinations. 94

2.7 Energy level lifetime for the $CaF_2 : Nd, Yb, Gd$ exciting at 791 nm and detecting at 1049 nm, corresponding to the $^4F_{3/2} \rightarrow {}^4I_{11/2}$ transition, for various ytterbium and gadolinium concentrations. 100

2.8 ETE for different Yb and Gd concentrations, estimated using the integrated luminescence intensity. 105

3.1 Parameters used in the amplification model for each $CaF_2 : 0.5\%Nd, 5\%Bu$ for both N_1 and N_2 site. For all of them, $P_L = 1$ mW, $\omega_p = \omega_L = 50$ μm, $L_z = 5$ mm, $N_T = 1.225 \cdot 10^{26}$ m^{-3}, $\beta = 0.5$. The pump power is set in order that $P_{abs} = 400$ mW. 130

4.1 Laser slope efficiency and threshold power for the various laser crystals, with output coupler $T = 8\%$. 143

4.2 Measured slope efficiencies and theoretical slope efficiencies for each output coupler. 146

4.3 Values of the ratio B/A for the fit in eq. (4.12) for the four studied crystals. 153

4.4 Fit parameters and losses for the Caird and Findlay-Clay (F-C) models. 158

4.5 Some remarkable examples of successfully achieved molecular adherence, to which it is worth adding the work of R. Gaumè [146]. 161

Résumé

Motivations et problématiques

Les lasers à haute densité d'énergie (HED) et à ultra-haute intensité (UHI) suscitent l'intérêt de la communauté scientifique depuis des décennies en raison de leurs vastes applications potentielles. La possibilité de fournir une densité d'énergie élevée, avec une précision spatiale et temporelle optimale, les rend idéaux pour diverses applications académiques et pratiques. Par exemple, les lasers très intenses peuvent être utilisés pour extraire efficacement de la matière des protons énergétiques, qui peuvent être accélérés pour des applications biomédicales [1], ou pour créer dans un laboratoire des conditions extrêmes de pression et de température afin d'étudier le comportement de différents matériaux, pour des applications fondamentales et/ou industrielles [2]. De plus, ces types de lasers rendent possible l'étude de la physique subatomique en exploitant le champ électromagnétique intense qui peut être créé.

Un intérêt majeur est également consacré à la physique des plasmas et à la physique des hautes densités d'énergie [3]. L'un des principaux défis concerne la réalisation et le contrôle de la fusion par confinement inertiel (ICF). Le concept de la FCI est basé sur une réaction en chaîne de fusion par compression libérant une grande quantité d'énergie, qui peut être appliquée dans le domaine de la défense, donc dans le développement d'armes de dissuasion nucléaire, et dans le domaine de la production d'énergie, en poursuivant le rêve d'une énergie durable sans carbone en fournissant une alternative à la recherche sur la fusion magnétique [4]. Un autre champ d'étude futur possible et fascinant consiste à recréer et à étudier dans un environnement contrôlé les conditions de température et de densité du cœur des étoiles et des planètes, ouvrant ainsi la voie à ce que l'on appelle "l'astrophysique de laboratoire" [5, 6].

Suite à l'intérêt croissant pour les lasers HED et UHI, tout un domaine de recherche sur l'architecture des amplificateurs, les matériaux lasers, les sources et leurs designs, s'est ouvert, dans le but de dépasser les verrous technologiques qui affectent le développement de telles installations. Pour atteindre une densité d'énergie très élevée, l'idée, actuellement mise en œuvre dans plusieurs installations comme le laser National Ignition Facility (NIF) aux États-Unis [7] et le Laser Mégajoule en France [8], est d'utiliser plusieurs lignes de faisceaux laser convergeant vers le même point, dans ce qu'on appelle la chambre cible. Ces deux installations ont un vaste programme consacré aux expériences de FCI, pour lesquelles deux "schémas"

principaux sont en fait possibles: le schéma de fusion direct et le schéma de fusion indirect. Dans le schéma de fusion direct, la cible est une bille de quelques millimètres de diamètre, contenant un mélange d'environ 10 milligrammes de deutérium (D) ^{2}H et de tritium (T) ^{3}H. Les faisceaux laser vont comprimer et chauffer le combustible pour atteindre les conditions nécessaires à la fusion nucléaire [9]. Dans le schéma indirect, la cible est un petit cylindre de métal lourd, souvent de l'or ou du plomb, appelé "hohlraum", qui contient le mélange D-T. Le hohlraum est rempli d'eau et de gaz. Le hohlraum est rempli d'un gaz pour éviter toute déformation pendant le pompage, en contrebalançant l'expansion et l'effondrement des parois. Le cylindre de l'hohlraum absorbe le rayonnement laser et émet de l'énergie sous forme de rayons X mous, qui vont exciter le mélange D-T [10].

Un problème majeur rencontré dans la réalisation des chaînes laser HED et UHI est lié aux effets non linéaires provoqués par les très fortes puissances crêtes des lasers, qui peuvent à terme endommager ou casser les composants optiques aux différentes étapes de la chaîne laser. Pour remédier à ce problème, la technique qui a permis le développement des lasers UHI, (prix Nobel de physique en 2018), est l'amplification à dérive de fréquence (CPA) [11]. En bref, l'idée est d'étirer dans le temps l'impulsion optique, ce qui réduit considérablement sa puissance crête, et d'amplifier cette impulsion étirée avant sa recompression. De cette manière, un faisceau beaucoup plus puissant peut être généré en évitant d'endommager le système d'amplification. La mise en œuvre de cette technique a permis d'augmenter l'intensité du laser focalisé de plusieurs ordres de grandeur.

Le Laser Mégajoule est une installation installée au Barp, au sein du Centre d'études scientifiques et techniques d'Aquitaine (CESTA). La construction a commencé en 2002 et l'installation a été déclaré opérationnelle en 2014. En 2019 a été réalisée la première expérience réussie de génération de protons via le processus de fusion D-T. Le bâtiment mesure 300 m de long, 150 m de large et 35 m de haut. L'objectif principal est d'obtenir 1.8 MJ de lumière laser UV, impactant la cible de quelques millimètres, comme montré sur la Figure 1. L'installation, encore en construction, accueillera à terme quatre baies laser de 125 m de long pour un total de 192 de lignes de faisceaux laser collimatés arrivant simultanément dans la chambre de réaction contenant la cible de combustible nucléaire. L'une des baies laser abrite le laser PETawatt Aquitaine (PETAL), une chaîne conçue pour délivrer des impulsions de 500 fs à 1 ps de long avec une énergie par impulsion de 351 nm (largeur complète à mi-hauteur (FWHM) $=$ 3.5 nm), obtenue à partir de l'amplification et du triplement de fréquence d'un faisceau laser de 1053 nm avec une FWHM de 16 nm. En dehors des expériences dédiées qui peuvent être réalisées avec l'installation PETAL, l'objectif principal de cette chaîne laser est d'être couplée avec les impulsions laser nanoseconde du LMJ pour réaliser une ICF efficace par allumage par choc [8, 12].

Dans l'installation LMJ, la cible de combustible nucléaire est excitée à l'aide du schéma indirect, dans lequel l'émission de rayons X est générée

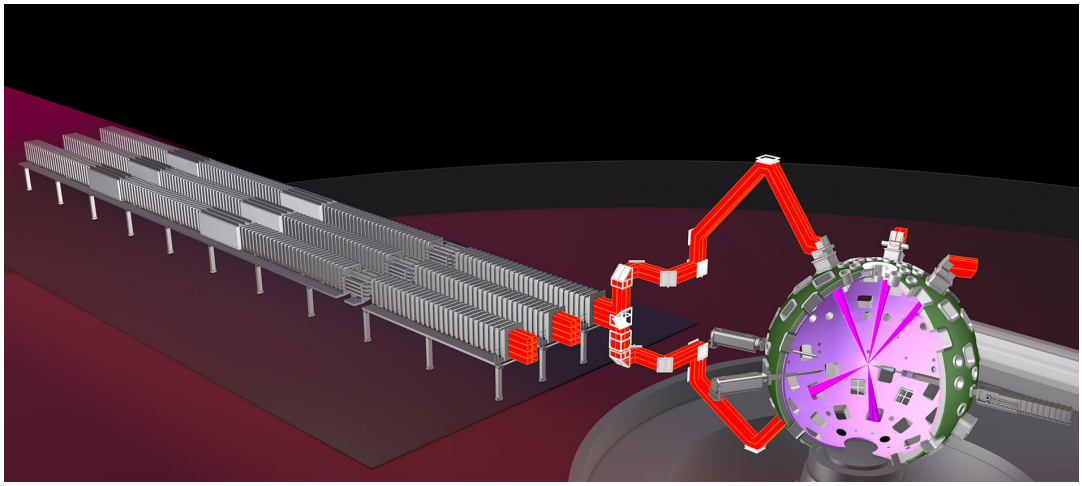

FIGURE 1: Schéma de Principe de la fusion par confinement inertiel.

par des faisceaux laser à 351 nm, qui sont à leur tour obtenus par conversion d'énergie de faisceaux à 1053 nm. Ces faisceaux laser à 1053 nm sont obtenus via la transition bien connue $^4F_{3/2} \rightarrow {}^4I_{11/2}$ du néodyme trivalent, pompé à 800 nm. Des verres phosphates dopés au néodyme, tels que le LGG70 produit par Schott et le LHG-8 produit par Hoya, également utilisés dans l'installation NIF, sont utilisés dans les composants du laser «front-end» et les étages d'amplification principaux, ce qui permet au dispositif de délivrer potentiellement des impulsions UV de 1.8 MJ entre 0.3 ns et 25 ns.

Ces verres phosphate ont été choisis en premier lieu pour plusieurs raisons: la possibilité de fabriquer facilement et efficacement des verres de grande taille à l'échelle industrielle, offrant une grande homogénéité optique, essentielle pour éviter les aberrations, un faible nombre d'inclusions et d'imperfections qui pourraient causer des dommages optiques [13]. De plus, ces verres possèdent une très faible énergie de phonon, de larges fenêtres de transparence dans le domaine du proche infrarouge ainsi que des bandes d'émission très larges, ce qui les rend utilisables dans le monde entier pour des applications de lasers ultra-courts. Néanmoins, le principal avantage des verres de Nd-phosphate en tant qu'amplificateurs réside dans leur fluence de saturation (4.5 J/cm^2 [14]), soit environ 5 fois leur seuil de dommage induit par laser (LIDT) (25 J/cm^2), ce qui représente un bon compromis entre le dépôt d'énergie élevée et l'efficacité d'extraction.

Cependant, leur principal inconvénient est leur faible conductivité thermique, qui est le facteur limitant actuel de toute la chaîne laser, en termes de fréquence de répétition et de temps de fonctionnement, ce qui a suscité un intérêt majeur pour le développement de nouveaux amplificateurs à base de cristaux.

Dans le cas particulier de ce travail, les efforts se sont concentrés sur le laser «front-end» du LMJ.

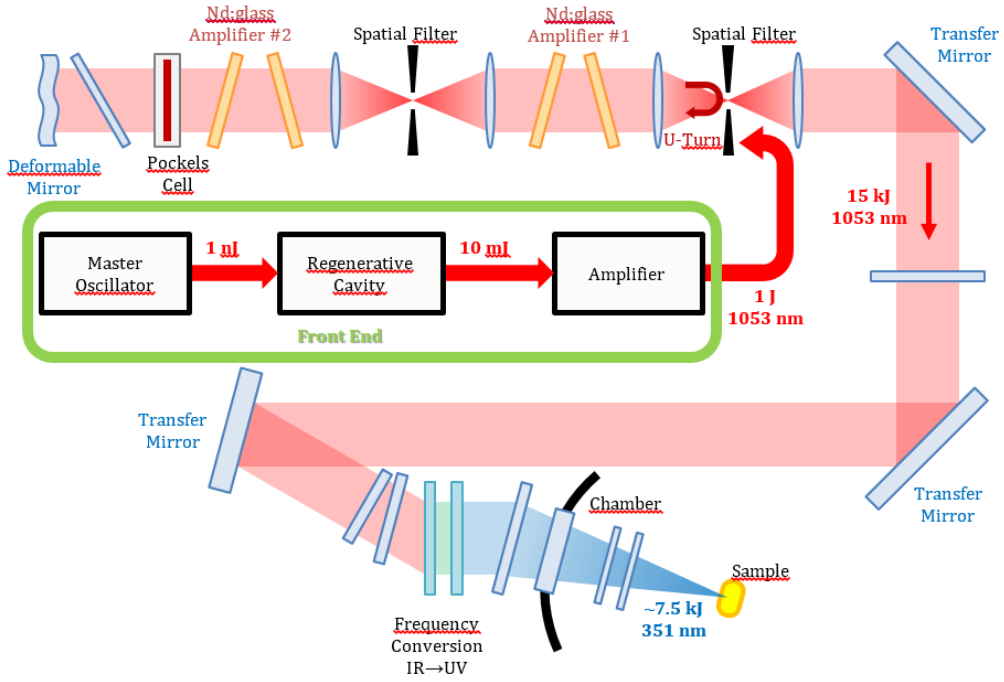

FIGURE 2: Schéma de la chaîne d'amplification, illustrant la configuration du faisceau laser LMJ. Des verres phosphatés dopés au Nd^{3+} sont utilisés dans la cavité régénératrice, l'amplificateur frontal et les amplificateurs laser #1 et #2 [15].

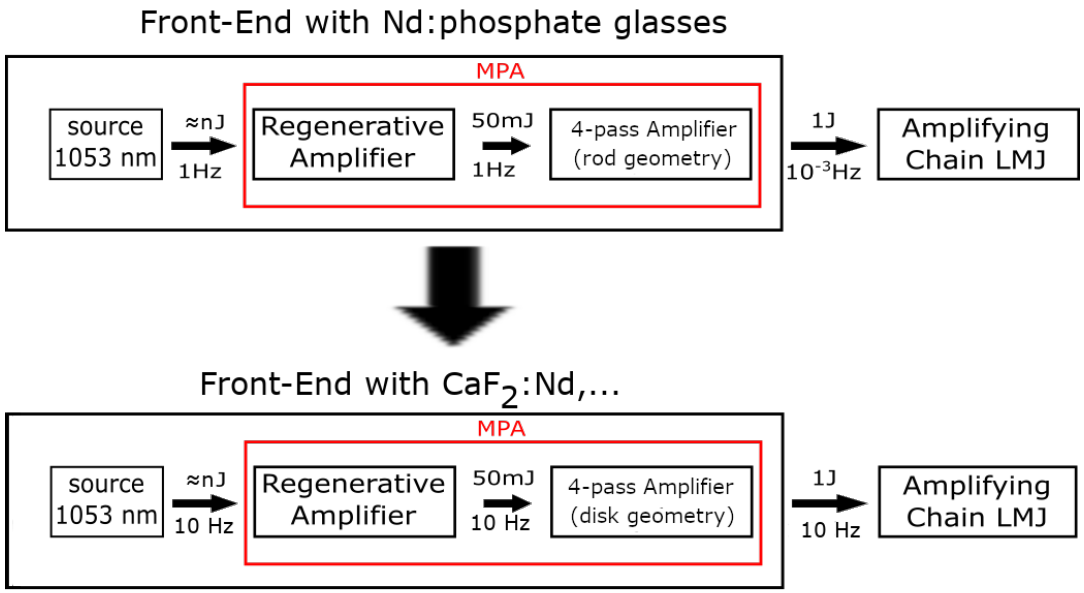

FIGURE 3: Schéma simplifié du laser «front-end» du LMJ avec les verres Nd:phosphate et avec CaF_2 : Nd, ...

Cette partie particulière de l'installation est la section du LMJ responsable de la génération et de l'amplification initiale des faisceaux laser, qui seront ensuite amplifiés dans le reste de la chaîne (voir Figure 2). La Figure 3 présente un schéma simplifié du laser «front-end», qui commence par une source fibrée, générant le faisceau initial à 1053 nm et un module de préamplification (MPA), représentant le premier étage de l'amplification. La sortie de la source fibrée délivre des impulsions de 1 nJ avec un taux de répétition de 1 Hz. Ce faisceau laser est injecté dans l'amplificateur régénératif, qui augmente l'énergie de l'impulsion à 50 mJ. La sortie de l'amplificateur régénératif est ensuite injectée dans un amplificateur à 4 passages, avec une énergie de sortie de 1J et une fréquence de répétition de 10^{-3} Hz. Ce taux de répétition est évidemment très faible et il est prévu d'augmenter son taux de répétition dans un avenir proche.

L'objectif principal de ce travail de thèse est donc d'étudier de nouveaux matériaux cristallins qui pourraient remplacer les verres phosphatés dopés au Nd actuellement utilisés dans le front-end. La conductivité thermique beaucoup plus élevée des matériaux cristallins permettra d'augmenter le taux de répétition du laser « front –end », de 10^{-3} Hz à 10 Hz. Ce changement de matériaux actifs sera complété par un changement de géométrie dans l'amplificateur à 4 passages.

Les paramètres de conception de l'amplificateur sont très délicats, afin d'éviter les effets qui limiteront ultérieurement les performances globales de l'installation. Le paramètre le plus évident est la longueur d'onde du laser à 1053 nm, qui est la longueur d'onde centrale du faisceau source fibré. Une distorsion spectrale du profil spectral de l'impulsion peut générer une conversion FM vers AM. Afin de limiter cet effet, le spectre de l'amplificateur doit être aussi plat que possible autour de cette longueur d'onde centrale. De plus, une large bande spectrale d'amplification est nécessaire pour générer des impulsions à large bande avec un temps de cohérence court, une exigence pour obtenir un lissage du faisceau efficace le long de la chaîne d'amplification.

Pour satisfaire à toutes ces exigences, le critère qui a été retenu pour le laser «front-end», est une bande passante spectrale de l'amplificateur centrée à 1053 nm avec un profil plat de 3 nm. Ce critère semble presque impossible à atteindre pour les cristaux conventionnels dopés au Nd, qui présentent généralement un pic d'émission très étroit, avec une largeur à mi-hauteur (FWHM) à 1.05 μm autour ou même en dessous de 1 nm.

Dans ce contexte, le laboratoire CIMAP et le CEA-CESTA ont entamé une collaboration pour explorer le potentiel des cristaux de fluorure comme nouveaux matériaux amplificateurs. Contrairement à la plupart des cristaux laser, $CaF_2 : Nd$ présente de larges bandes d'absorption et d'émission qui sont comparables à ce que l'on trouve dans les verres phosphates. Cependant, les fluorites dopées au Nd n'ont pas été considérées

pendant longtemps comme des matériaux laser prometteurs, en raison de l'agrégation des ions Nd même à un très faible niveau de dopage Nd. Cette agrégation provoque un transfert d'énergie par relaxation croisée entre les ions néodyme qui supprime l'émission à 1μm. La collaboration entre le CIMAP et le CEA-CESTA a débuté par l'étude du codopage du CaF_2 : Nd avec du lutécium comme ion tampon pour éviter la formation de clusters de Nd [15].

Cette première étude a permis d'obtenir plusieurs résultats intéressants qui ont servi de point de départ à de futurs travaux, tels que celui présenté ici. Un résultat intéressant obtenu par spectroscopie optique est représenté sur la Figure 4. L'émission du Nd augmente considérablement lorsque la concentration en ions tampon (lutécium) augmente. En particulier, la figure 4 montre que 8at.% de co-dopant est suffisant pour casser tous les clusters de Nd optiquement non actifs. Les propriétés thermo-mécaniques de CaF_2 : Nd ont également été étudiées à l'aide de techniques thermo-optiques, telles que la spectrométrie par lentille thermique et l'interférométrie Jamin-Lebedev. Il est bien connu que les propriétés thermo-mécaniques ont tendance à se dégrader avec l'augmentation du niveau de dopage. L'étude a montré, comme prévu, que la concentration en codopant a un impact significatif sur la conductivité thermique comme le montre la figure 5 avec la dépendance de la conductivité thermique avec la concentration en ions tampon (Lu). Ainsi, un équilibre entre la disparition des clusters de Nd et la préservation de bonnes propriétés thermomécaniques doit être trouvé. Le compromis optimal est trouvé en utilisant un niveau de codopage de 5at.% qui est la référence pour la concentration en ions tampon dans l'ensemble de ce travail.

Les propriétés thermo-optiques et thermo-mécaniques du CaF_2 : Nd, Lu ont également été étudiées en détail au CEA-CESTA, par exemple avec les travaux de D. Stoffel [16]. Dans ce travail, Stoffel et al. [17] ont effectué une étude détaillée de la chaleur déposée dans le cristal laser lors du processus de pompage, et de l'impact conséquent sur les contraintes mécaniques générées par le gradient thermique et la biréfringence induite.

En comparant le CaF_2 : Nd avec les verres phosphate dopés au Nd, du point de vue de la spectroscopie optique, le CaF_2 s'est avéré être un candidat solide pour remplacer les verres phosphate, après une étude approfondie de diverses matrices à base de fluorite, à savoir le SrF_2, le BrF_2 et les compositions hybrides de fluorite.

En outre, le compromis entre la fluence de saturation et la fluence LIDT, est à peu près le même que pour les verres phosphate puisque pour le CaF_2 : 0.5%Nd, 5%Lu $F_{sat} = 5.9\mathrm{J/cm^2}$ avec $F_{LIDT} = 23\mathrm{J/cm^2}$.

De plus, le potentiel du cristal de CaF_2 : 0, 5%Nd, 5%Lu en tant que cristal laser prometteur a également été prouvé, avec une expérience préliminaire de verrouillage de mode, permettant d'obtenir des impulsions fs, ainsi qu'un

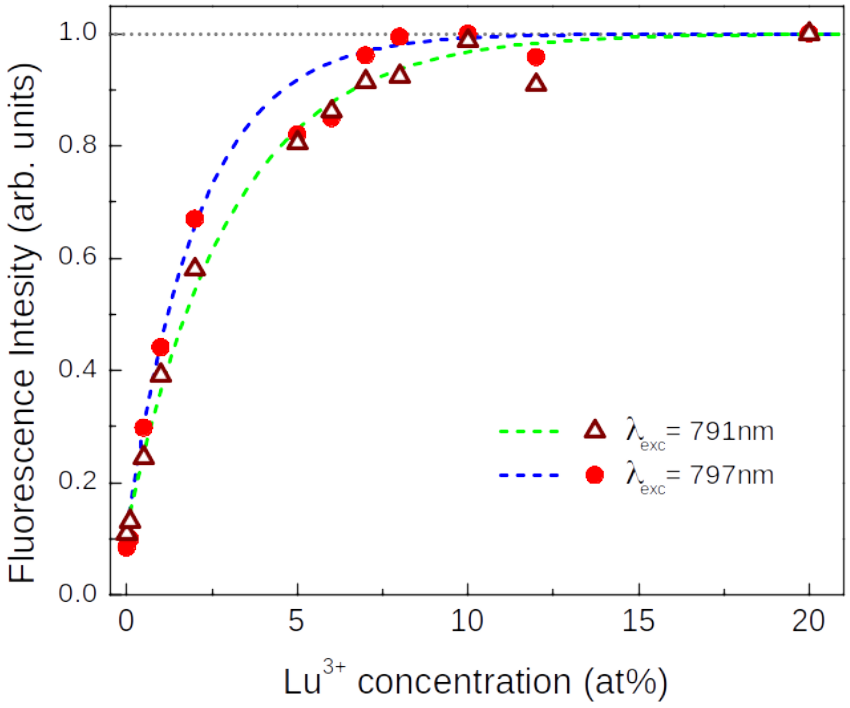

FIGURE 4: Intégration de l'intensité d'émission de $^4F_{3/2} \rightarrow ^4I_{11/2}$ en fonction de la concentration de Lu^{3+} [40]

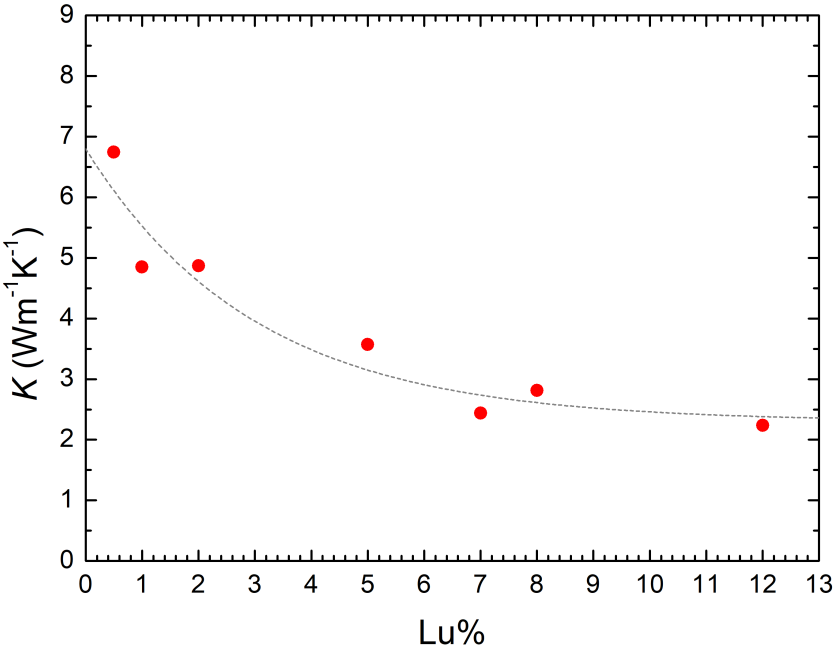

FIGURE 5: Conductivité thermique en fonction de la concentration de Lu en CaF_2 : Nd, Lu [15].

effet laser avec une efficacité de 44% à 1062 nm.

Bien que $CaF_2 : 0.5\%Nd, 5\%Lu$, ait donné des résultats laser très intéressants, il n'offre pas les bandes d'émission plates et larges qui sont requises pour les applications LMJ. Ce travail de thèse est donc consacré à l'étude du codopage de $CaF_2 : Nd$ en utilisant différents ions tampons et en les combinant avec deux ou trois ions tampons dans la même composition. Les ions tampons de différentes tailles peuvent modifier le champ cristallin local et donc les propriétés optiques du cristal. Ce travail vise donc à mieux comprendre comment la nature de l'ion tampon et sa concentration affecteront la conception de l'amplificateur.

Contenu de la thèse

Dans le contexte décrit dans les sections précédentes, ce document présente les méthodes, les techniques et les résultats obtenus pour le développement et la caractérisation de nouveaux matériaux amplificateurs de laser à 1.05 μm.

Le chapitre 1 est l'introduction de la thèse, expliquant le contexte général du projet et l'intérêt de développer ce matériau en tant qu'amplificateur.

Le chapitre 2 est consacré à la spectroscopie optique des CaF_2 dopés au néodyme, en commençant par un état de l'art et un résumé des principales questions. Ensuite, le codopage par ions tampons (Bu) est introduit et étudié, avec la fabrication de $CaF_2 : Nd, Bu$, en utilisant différents ions tampons et en étudiant les différentes influences qu'ils ont sur la spectroscopie du néodyme. Des compositions plus complexes sont ensuite introduites, sur la base des résultats obtenus dans l'étude du codopage avec un seul ion tampon, en utilisant d'abord deux ion tampons différents, puis trois, montrant le potentiel de ces cristaux en termes d'ingénierie des propriétés spectroscopiques. La dernière partie du chapitre est consacrée à l'approche du codopage Nd, Yb, où les ions Yb agissent non seulement comme des ions tampons, mais aussi comme des ions actifs impliquant des transferts d'énergie entre les ions Nd et Yb.

Le chapitre 3 est consacré aux propriétés d'amplification des cristaux étudiés dans le chapitre 2, en se concentrant sur les plus prometteurs pour les applications LMJ. Une première section est consacrée à un critère de milieu amplificateur spécifique aux applications LMJ et à la nécessité d'un milieu amplificateur à large bande. La section suivante est consacrée aux simulations de gain et d'amplification, tandis que la section 3.6 présente une étude expérimentale des propriétés d'amplification des différents cristaux présentés dans le chapitre 2. Le montage pompe-sonde utilisé pour ces expériences est présenté ainsi que les résultats expérimentaux et une comparaison avec le modèle développé.

Le chapitre 4 se concentre sur les expériences laser réalisées avec les cristaux laser caractérisés dans le chapitre [gain] en utilisant une cavité plano-concave. Cette étude englobe les propriétés laser, l'accordabilité spectrale et une analyse détaillée des pertes aller-retour. La dernière section de ce chapitre est consacrée à une étude préliminaire de l'adhérence moléculaire entre un $CaF_2 : Nd, Bu$ dopé et un CaF_2 pur, afin d'exploiter le cristal pur comme dissipateur thermique dans les applications laser, en profitant de la haute conductivité thermique du CaF_2 pur. Contrairement au collage optique ordinaire, l'adhérence moléculaire ne nécessite pas d'adhésif spécifique pour coller les deux composants ensemble. Ainsi, elle présente de très faibles pertes à l'interface entre les deux cristaux. Ce chapitre commence par un état de l'art général et la technique de fabrication développée pour le CaF_2 , ainsi que quelques caractérisations préliminaires de l'échantillon final.

Le dernier chapitre résume les résultats, en traçant les conclusions finales, en soulignant et en discutant les perspectives d'investigations futures.

Spectroscopie optique du $CaF_2 : Nd$

Les résultats de l'étude de la spectroscopie optique détaillée de $CaF_2 : Nd, Bu$, où Bu est un ion tampon, ont révélé que le codopage est efficace pour éliminer les clusters $Nd - Nd$.

Le codopage avec un seul ion tampon, tel que le gadolinium, le lanthane, le cérium, le lutécium, l'yttrium et le scandium, montre clairement comment le choix de l'ion tampon peut modifier les propriétés spectroscopiques de $CaF_2 : Nd$, en divisant principalement les ions tampons en deux groupes différents. Les ions tampons de plus grande taille que l'ion Nd^{3+}, le gadolinium, le lanthane et le cérium, conduisent à un seul site d'émission dominant Nd, tandis que les ions plus petits, l'yttrium, le lutécium et le scandium, présentent deux types différents de sites Nd (Figure 6). Les deux sites Nd ont des caractéristiques d'absorption et d'émission et des durées de vie caractéristiques, ce qui permet non seulement de les distinguer dans le domaine spectral en choisissant des longueurs d'onde d'absorption et d'émission spécifiques, mais aussi dans le temps, en choisissant des fenêtres de temps spécifiques à l'aide de la spectroscopie résolue en temps pour isoler la signature de chaque site. Le premier site, appelé N_1, et commun aux deux groupes de cristaux, présente un pic d'absorption caractéristique autour de 791 nm et un pic d'émission autour de 1049 nm, avec une durée de vie plus longue autour de $450 - 500$ μs, tandis que le second site, appelé N_2, est caractérisé par un pic d'absorption autour de 797 nm, un pic d'émission autour de 1054 nm et une durée de vie plus courte, autour de $300 - 400$ μs. Ces deux centres différents sont associés à des centres quasi-rhombiques pour N_1 et des centres quasi-tétragonaux pour N_2 [18].

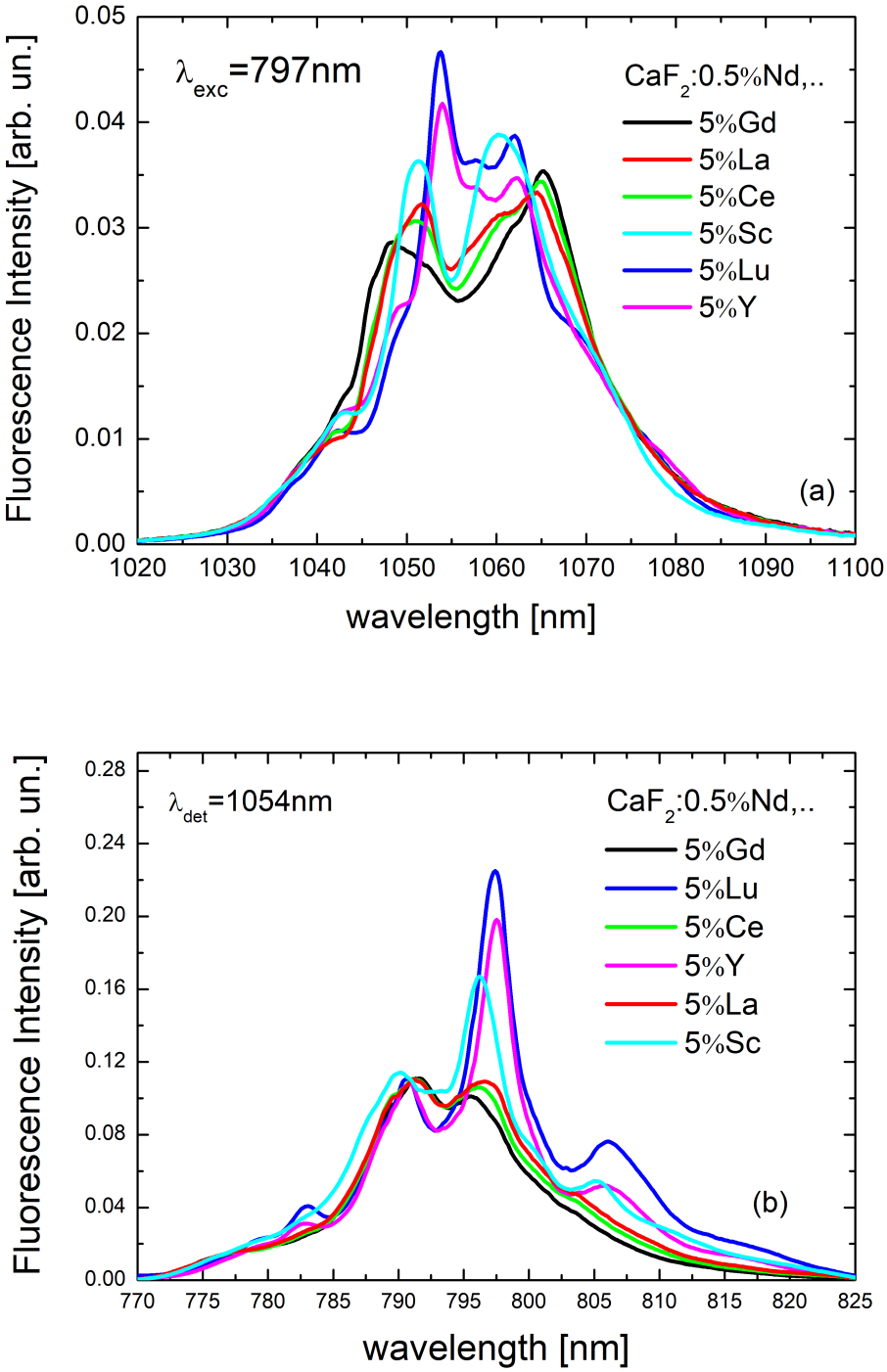

FIGURE 6: (a) Spectre de luminescence de $CaF_2 : 0.5\%Nd^{3+}, 5\%Bu^{3+}$, avec Bu = (Gd, La, Ce, Y, Lu, Sc) avec une longueur d'onde d'excitation de 797 nm. (b) Spectres d'excitation avec une longueur d'onde de détection de 1054 nm.

Ensuite, une approche de codopage hybride, employant un ion tampon de grande taile et un tampon de plus petite taille, $CaF_2 : Nd, Bu_1, Bu_2$ a été étudiée avec des résultats intéressants. En fonction de la concentration des deux ions tampons, il est possible d'obtenir des comportements spectroscopiques intermédiaires, entre les deux cristaux co-dopés simples $CaF_2 : Nd, Bu_1$ et $CaF_2 : Nd, Bu_2$, ce qui permet de personnaliser les propriétés spectroscopiques en choisissant soigneusement la nature et la concentration en ions tampons. La concentration totale en ions tampons a été maintenue à 5% pour garantir l'absence de clusters $Nd - Nd$ sans dégrader davantage les propriétés thermomécaniques. De plus, la possibilité d'effectuer des simulations des propriétés spectroscopiques avant la croissance a été étudiée avec succès, en combinant les spectres du seul $CaF_2 : Nd, Bu_1$ et du $CaF_2 : Nd, Bu_2$ par combinaison linéaire, et en obtenant exactement le spectre expérimental du $CaF_2 : Nd, Bu_1, Bu_2$. Ceci permet une ingénierie spectrale de $CaF_2 : Nd, Bu_1, Bu_2$, en ajustant la nature et la concentration des ions tampons en fonction de l'application souhaitée (Figure 7). De plus, dans le cas d'un pompage monochromatique de cristaux avec un petit ion tampon tel que Y, la longueur d'onde de pompage s'avère critique à un niveau sub-nanométrique dans la plage 795-797 nm pour obtenir la forme spectrale souhaitée, puisque dans cette région spectrale, le coefficient d'absorption des sites N_2 augmente de façon spectaculaire. Nous avons également étudié la possibilité de modifier davantage les propriétés spectroscopiques du Nd en employant un troisième ion tampon tout en conservant la même concentration totale en ions tampon de 5at.%. La linéarité de cette approche à triple ions tampons a été corroborée, à l'exception du scandium. En effet, alors que le scandium seul casse les clusters Nd-Nd, nous montrons que dans une structure à triple co-dopage, le scandium ne participe pas à la formation des clusters de Nd. La raison en est son très petit rayon ionique (88 pm comparé à 104 pm pour l'yttrium par exemple).

Quelques compositions ont été identifiées, conduisant à un profil d'émission plutôt plat autour de 1053 nm, comme souhaité pour les applications LMJ, telles que $\mathbf{CaF_2 : 0.5\%Nd, 3\%Gd, 1.4\%Ce, 0.6\%Y}$ avec une bande d'émission plate de 5 nm lorsqu'il est excité à 797.0 nm, ou $\mathbf{CaF_2 : 0.5\%Nd, 2.5\%Gd, 2.5\%Y}$ excité à 796.2 nm. Le cristal $\mathbf{CaF_2 : 0.5\%Nd, 4\%Gd, 1\%Y}$ excité à 797.0nm représente également une alternative valable, avec un profil plutôt plat de 5 nm, similaire au cristal $3\%Gd, 1.4\%Ce, 0.6\%Y$. Enfin, le cristal $\mathbf{CaF_2 : 0.5\%Nd, 3.8\%Gd, 0.65\%Y, 0.55\%La}$ donne également un profil d'émission plat sur 4.4 nm ce qui est légèrement plus petit que pour les trois autres compositions.

Enfin, les cristaux de $CaF_2 : Nd, Yb, Gd$ sont étudiés avec la particularité d'utiliser les ions Yb à la fois comme ions actifs et comme ions tampons. Ce codopage est intéressant en raison de sa très large bande d'émission lors du pompage des ions néodyme, ainsi que de la possibilité de profiter de la grande section efficace d'absorption du néodyme pour peupler l'état

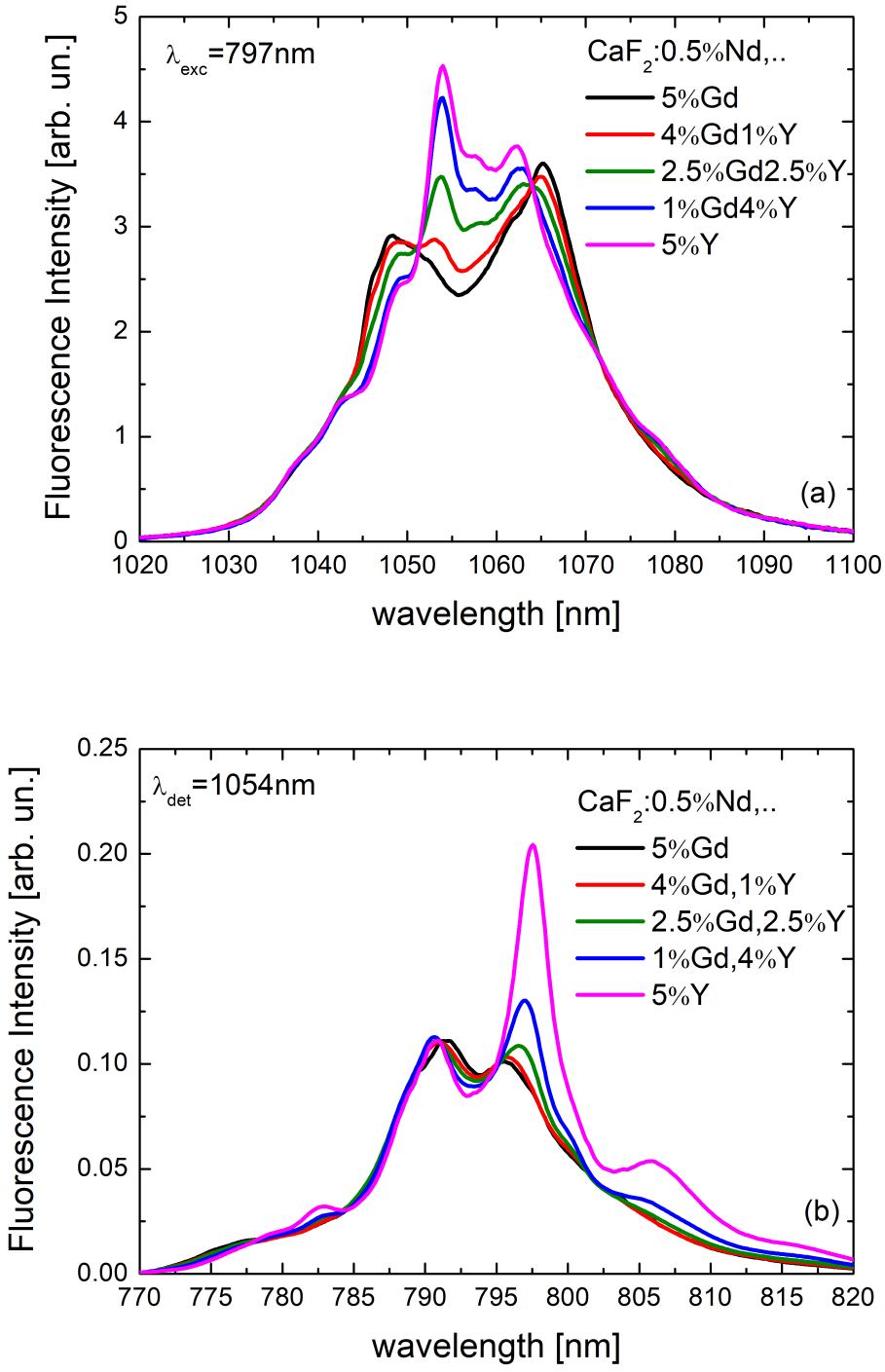

FIGURE 7: Luminescence (a) et excitation (b) de $CaF_2 : Nd, Gd, Y$ pour différentes concentrations de gadolinium et d'yttrium, en gardant 5% comme concentration totale des tampons.

$^2F_{7/2}$ de l'ytterbium par transfert d'énergie depuis le Nd. L'efficacité du transfert d'énergie (ETE) du Nd au Yb est estimée à l'aide de deux approches différentes basées sur des mesures d'intensité et des durées de vie qui donnent des résultats très similaires. Une ETE maximale de 80% est obtenue dans le cristal $CaF_2 : 0,5\%Nd, 3\%Yb, 2\%Gd$.

Propriétés d'amplification

Les propriétés d'amplification laser des $CaF_2 : Nd$ codopés par des ions tampons ont également été étudiées.

Tout d'abord, la collaboration avec le CESTA a permis de définir un critère d'amplification qui vise un spectre sonde amplifié de 3 nm de FWHM après un facteur d'amplification de 10^9. Ce critère a été testé avec les cristaux les plus prometteurs identifiés dans l'étude spectroscopique du chapitre 2, à savoir le $CaF_2 : 0.5\%Nd$ codopé avec $2.5\%Gd, 2.5\%Y$, // $4\%Gd, 1\%Y$, // $3.8\%Gd, 0.65\%Y, 0.55\%La$ et $3\%Gd, 1.4\%Ce, 0.6\%Y$ qui ont donné les bandes de fluorescence les plus larges. La largeur à mi hauteur (FWHM) de 3 nm du spectre de la sonde amplifiée (typique du verre Nd:LGG70 actuellement utilisé dans le LMJ) est dépassé pour tous les cristaux étudiés, atteignant environ $5 - 6$ nm (Figure 8), tandis que le centrage à 1053.0 nm est plus problématique. Alors que tous les cristaux ont leur signal amplifié maximal à 1053 nm, la largeur de bande chute brusquement sur la partie grande longueur d'onde du spectre.

Le facteur d'amplification du laser P_{out}/P_{in} avec $CaF_2 : Nd$ codopé avec des ions tampons a été étudié à l'aide d'une configuration pompe-sonde à double modulation. Un facteur d'amplification de 35% est mesuré dans le cristal $CaF_2 : 0,5\%Nd, 5\%Lu$ à 1054 nm pour 400 mW de puissance de pompe absorbée, tandis que les autres cristaux dopés par des ions tampons conduisent à un gain laser de 20% pour la même puissance de pompage absorbée. Ces résultats sont comparés à un modèle dédié basé sur une approche avec des équations de population qui comprend également la propagation des faisceaux de sonde et de pompe dans le milieu amplificateur. Ce modèle prend également en compte les effets de saturation, tels que le dépeuplement de l'état fondamental et la saturation du gain. La comparaison entre l'amplification calculée et mesurée montre un bon accord pour les cristaux co-dopés avec de grands ions tampons (Gd, La, Ce) qui présentent un centre actif dominant Nd^{3+}. Le cas des petits ions tampons est plus compliqué car un calcul d'amplification exact nécessiterait deux ensembles de paramètres spectroscopiques pour N_1 et N_2 ainsi que la détermination de la concentration de chaque centre dans le cristal. Cette limitation souligne encore plus la pertinence d'une mesure expérimentale directe du gain du laser comme celle présentée dans ce travail.

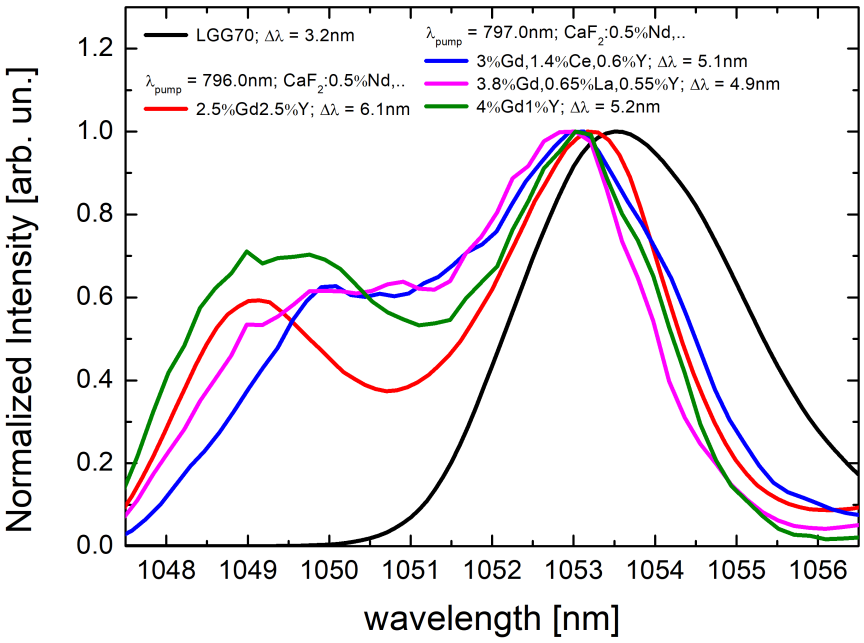

FIGURE 8: Spectre amplifié d'un faisceau sonde de 16 nm FWHM centré sur un faisceau d'entrée de 1053 nm avec un gain $G = 20.72$ pour différents milieux de gain, comparé au verre de référence LGG70 actuellement utilisé dans le LMJ.

L'accordabilité des faisceaux de pompe et de sonde a été exploitée pour effectuer des mesures de gain à différentes longueurs d'onde de pompe et de sonde (Figure 9). Les mesures d'amplification réalisées sur les cristaux les plus prometteurs pour les applications LMJ, à savoir les cristaux 2.5%Gd, 2.5%Y, 4%Gd, 1%Y, 3.8%Gd, 0.65%Y, 0.55%La et 3%Gd, 1.4%Ce, 0.6%Y co-dopés, montrent une amplification de 20% pour 400 mW de puissance de pompe absorbée et 1 mW de puissance de sonde. Plus intéressant encore, le spectre d'amplification en fonction de la longueur d'onde de la sonde présente un profil plat dans la plage spectrale de $1048 - 1055$ nm.

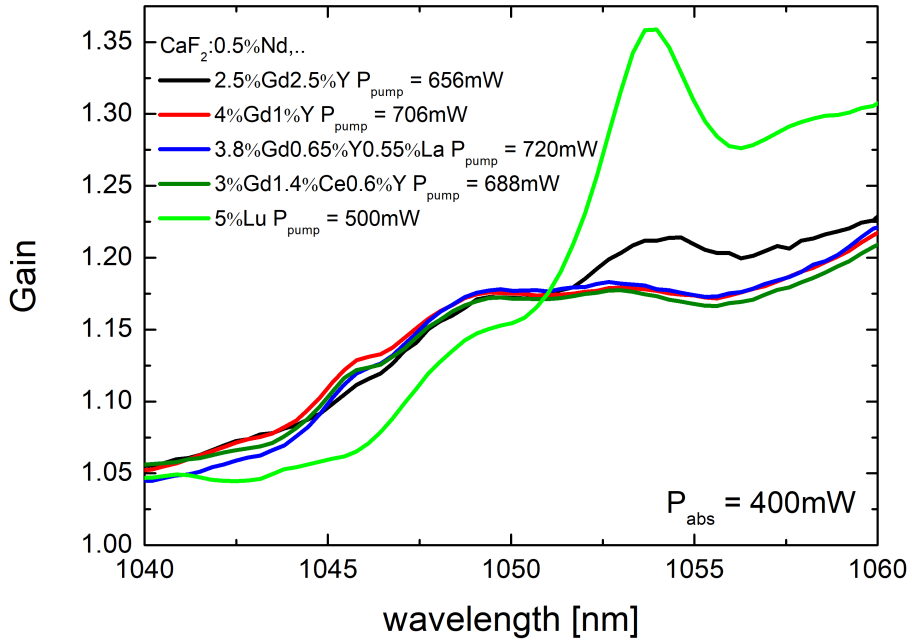

FIGURE 9: Spectre d'amplification en fonction de λ_{probe} pour différents échantillons, avec la même puissance de pompe absorbée $P_{abs} = 400$ mW. $lambda_{pump} = 797$ nm, $P_{probe} = 1$ mW, $\omega(radius) = 50$ μm.

Effets Laser

La dernière partie du travail porte sur le fonctionnement laser. Tout d'abord, le rôle de la préparation et de l'orientation du cristal est discuté, en se concentrant sur l'importance d'orienter le cristal le long de la direction $(1, 1, 1)$ pour éviter les effets de dépolarisation. Différents cristaux laser ont été étudiés en utilisant la même cavité plano-concave. Pour la plupart des cristaux, l'efficacité du laser est de l'ordre de 40% en fonction de la puissance de pompage absorbée, tandis que la puissance de seuil laser reste très faible,

de l'ordre de quelques dizaines de mW. Une attention particulière a été consacrée aux performances du laser utilisant le $CaF_2 : 0.5\%Nd, 2.5\%Gd, 2.5\%Y$. Parmi les différents résultats, on peut souligner qu'une efficacité de 44% en fonction de la puissance de pompage absorbée a été obtenue lors du pompage à 796 nm avec une transmission du coupleur de sortie de 8% (Figure 10). La puissance de pompage au seuil laser était de 60 mW avec une longueur d'onde d'émission de 1065.0 nm.

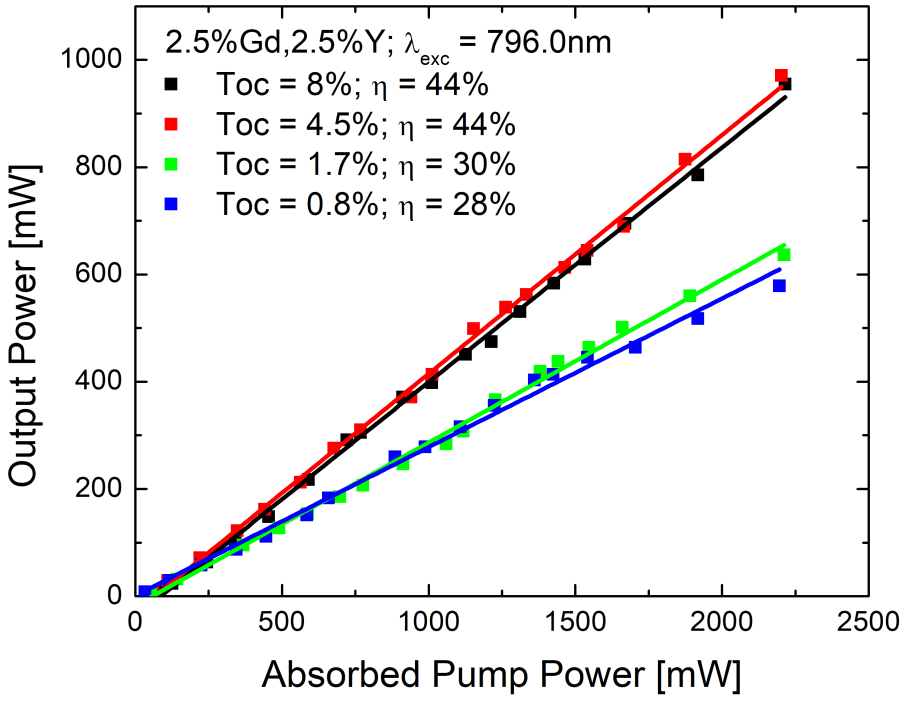

FIGURE 10: Puissance de sortie du laser en fonction de la puissance de pompage absorbée pour les quatre coupleurs de sortie $T = 0,8\%, 1,7\%, 4,5\%, 8\%$, d'un $CaF_2 : 0,5\%Nd, 2,5\%Gd, 2,5\%Y$, avec une longueur d'onde de pompage de $\lambda_{pump} = 796$ nm

Les faibles puissances de seuil laser enregistrées pour tous les cristaux laser démontrent la bonne qualité optique des cristaux laser et la très bonne efficacité quantique du niveau émetteur $^4F_{3/2}$. Pour les différentes transmissions du coupleur de sortie, les efficacités laser enregistrées sont proches de l'efficacité théorique, ce qui indique que les effets parasites tels qu'un recouvrement spatial imparfait entre les faisceaux laser et de pompe n'ont pas lieu dans nos expériences. De plus, les caractéristiques du faisceau laser sont étudiées, ce qui conduit à un $M^2 = 1.1$ et une divergence $\theta = 20$ mrad. Cette très bonne qualité du faisceau laser de sortie montre que les effets thermiques ont un effet limité sur les performances du cristal laser dans la

plage de la pompe absorbée qui est typiquement inférieure à 1.5 W.

L'accordabilité des cristaux laser sélectionnés a été étudiée à l'aide d'un filtre biréfringent inséré dans la cavité laser et a montré une forte cohérence avec les caractéristiques de spectroscopie optique présentées au chapitre 2. Une accordabilité dans la gamme spectrale de $1048 - 1070$ nm avec une région plate de 6 nm entre 1049 et 1055 nm est obtenue. Un calcul de la forme de la courbe d'accord laser à l'aide du spectre de la section efficace d'émission est présenté et montre un bon accord avec la courbe d'accord expérimentale de plusieurs cristaux tels que $CaF_2 : 0.5\%Nd, 3\%Gd, 1.4\%Ce, 0.6\%Y$ et $CaF_2 : 0.5\%Nd, 4\%Gd, 1\%Y$ (Figure 11).

Les pertes aller-retour dues au cristal laser sont évaluées à l'aide de deux méthodes différentes, à savoir l'analyse de Findlay-Clay et de Caird. Les deux modèles donnent des valeurs similaires qui sont inférieures à 2% pour tous les cristaux étudiés, illustrant une fois de plus la bonne qualité optique des cristaux laser. Ironiquement, un inconvénient de cette bonne qualité est le faible seuil laser correspondant. Ces faibles valeurs de seuil sont accompagnées d'une incertitude assez importante lors de l'utilisation d'un coupleur de sortie à faible transmission (dans notre étude, $T = 0.8\%$), ce qui limite l'utilisation de l'analyse de Findlay-Clay pour les coupleurs de sortie à faible transmission.

Enfin, une étude préliminaire sur l'adhérence moléculaire a été réalisée. Une procédure spécifique a été identifiée pour fabriquer un cristal de $CaF_2||CaF_2 : Nd, Lu$ lié, (cf Figure 12). Les exigences relatives à la qualité de la surface et à la procédure de traitement thermique pour obtenir le résultat souhaité sont présentées. L'enregistrement de la propagation de la chaleur de la partie dopée vers la partie non dopée de l'échantillon collé illustre l'avantage d'avoir un CaF_2 pur comme dissipateur thermique. Un cristal de $CaF_2 : Nd, Lu$ ayant le même diamètre de 14 mm et la même épaisseur de 5 mm montre des performances laser plus faibles avec une puissance laser intra-cavité élevée, tandis que le dissipateur thermique qu'est le CaF_2 non dopé permet de meilleures performances laser de l'échantillon collé en raison d'une réduction des effets thermiques (Figure 13), ouvrant la voie à des perspectives intéressantes. Par exemple, de nouvelles géométries de cristaux laser peuvent être envisagées avec un cristal non dopé de part et d'autre du matériau dopé ou la concaténation de différents cristaux avec différents codopages, afin d'obtenir des caractéristiques spectroscopiques et laser hybrides, de manière similaire à ce qui a été obtenu par Mukhin et al. avec $Yb : YAG||Yb : GGG$ [19].

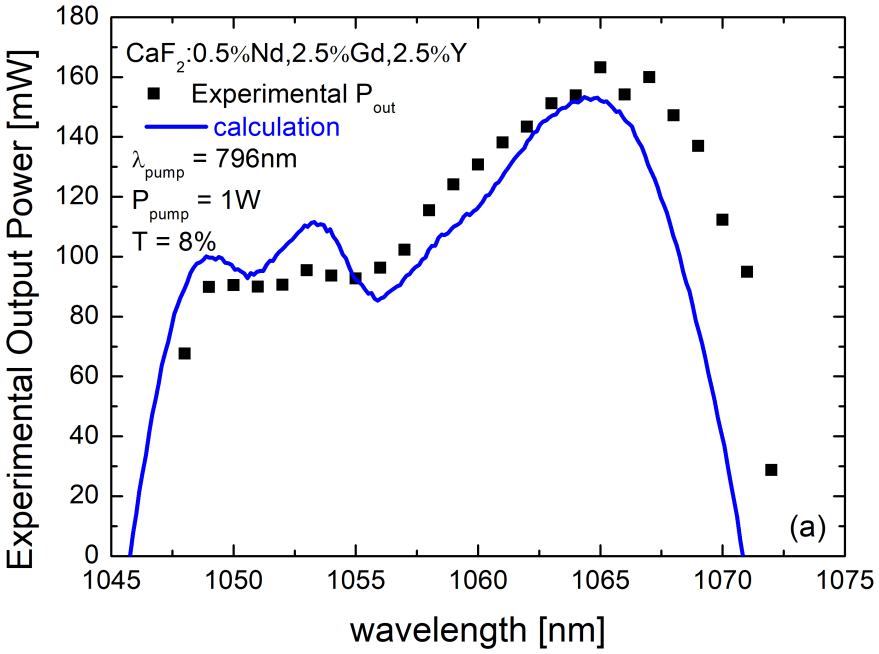
CaF2:0.5%Nd,2.5%Gd,2.5%Y
Experimental Pout
calculation
λpump = 796nm
Ppump = 1W
T = 8%
(a)
Experimental Output Power [mW]
wavelength [nm]
0
20
40
60
80
100
120
140
160
180
1045
1050
1055
1060
1065
1070
1075

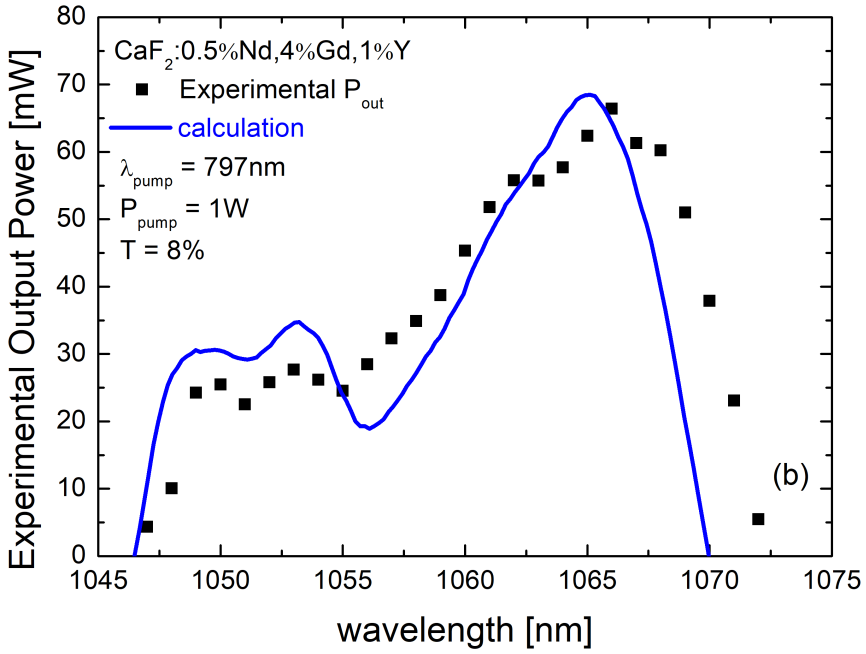
CaF2:0.5%Nd,4%Gd,1%Y
Experimental Pout
calculation
λpump = 797nm
Ppump = 1W
T = 8%
(b)
Experimental Output Power [mW]
wavelength [nm]
0
10
20
30
40
50
60
70
80
1045
1050
1055
1060
1065
1070
1075

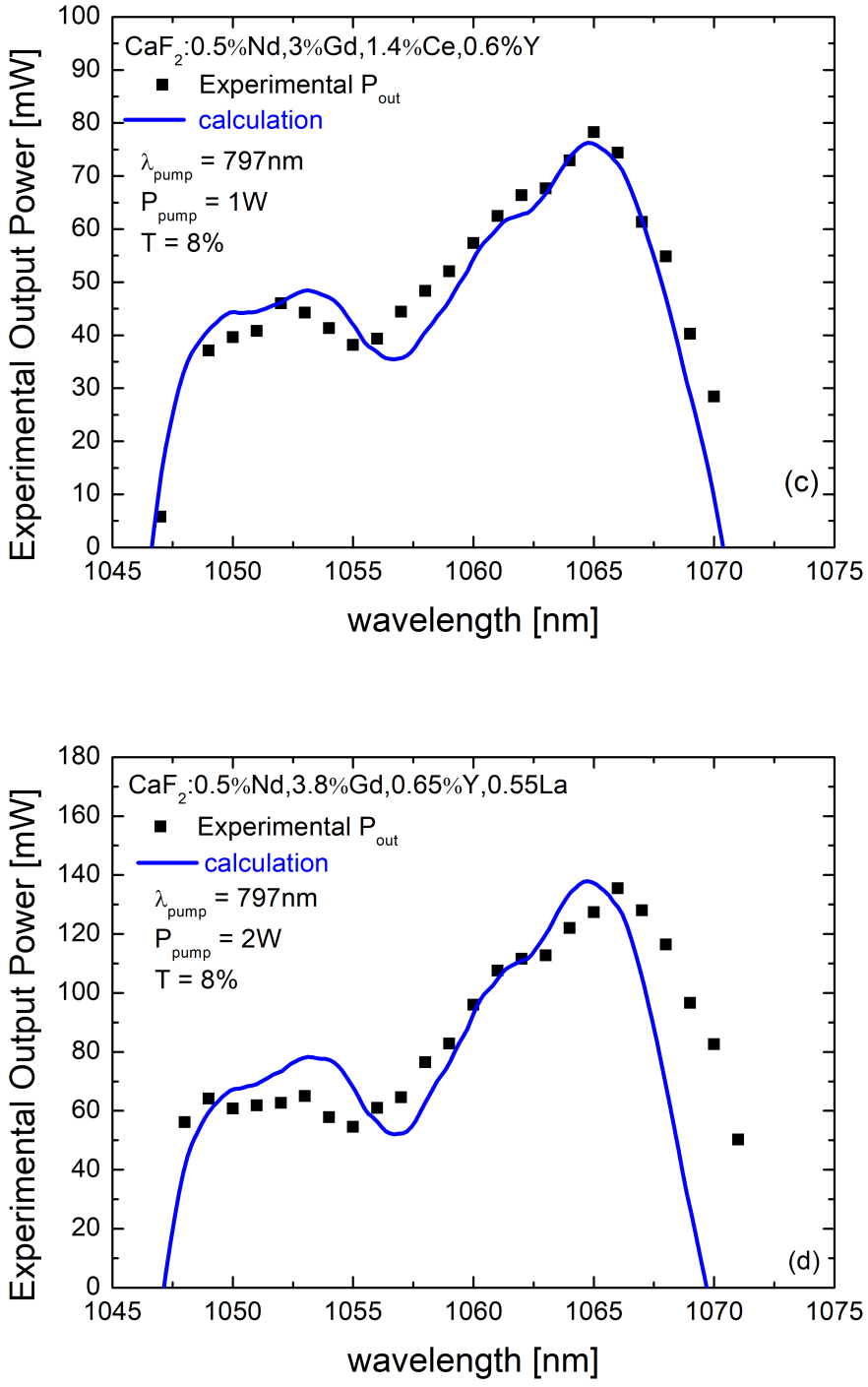

FIGURE 11: Courbes d'accord et reconstruction d'un CaF_2 : 0.5%Nd co-dopé avec 2.5%Gd, 2.5%Y (a), 4%Gd, 1%Y (b), 3%Gd, 1.4%Ce, 0.6%Y (c) and 3.8%Gd, 0.55%La, 0.65%Y (d).

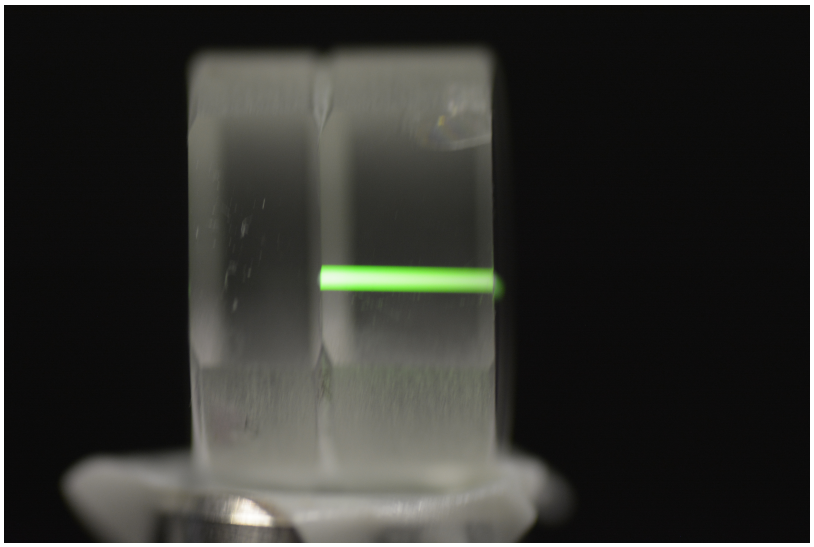

FIGURE 12: Faisceau laser Titanium Sapphire à 797 nm, 2 W focalisé qui se propage à travers l'échantillon. Il est possible de voir que l'upconversion verte du Nd a lieu uniquement dans la partie non dopée.

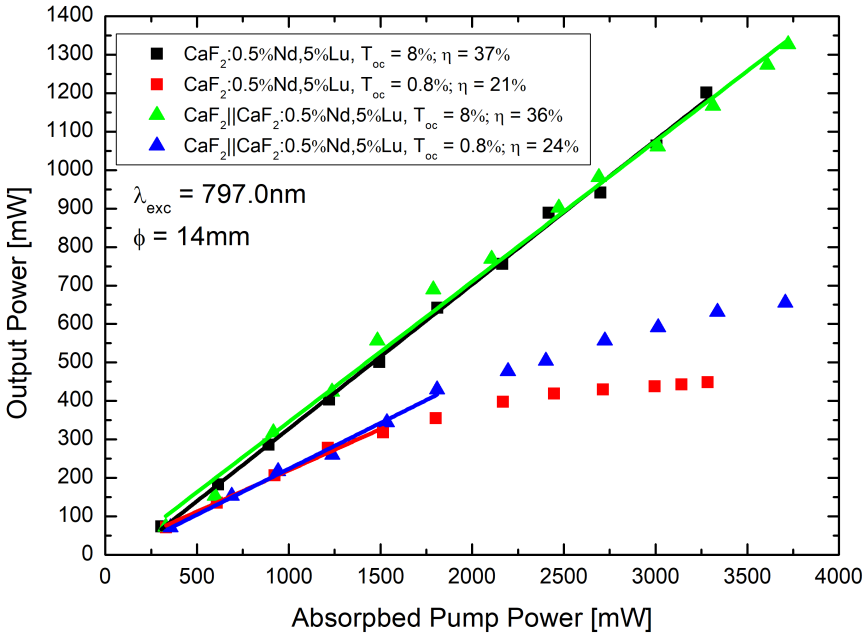

FIGURE 13: Test laser utilisant une cavité plano-concave de $CaF_2||CaF_2 : 0.5\%Nd, 5\%Lu$ (△) comparée à $CaF_2 : 0.5\%Nd, 5\%Lu$ (□) avec le même diamètre $\phi = 14$ mm et une épaisseur de 5 mm, pour deux transmissions de coupleur de sortie de 8% (vert et noir) et 0.8% (bleu et rouge).

Chapter 1

Introduction

This thesis is dedicated to the design and the characterization of new laser amplifiers materials at 1 μm for applications in high-energy laser chains. This work takes place within a long-term collaboration between the OML team in CIMAP and the CEA-CESTA, to investigate crystalline materials as potential substitutes of the Nd-doped phosphate glasses currently employed in the Laser Mégajoule (LMJ) and PETAL high energy laser facilities located in Bordeaux. Despite their performance in generating high-energy pulses, Nd-doped phosphate glasses as amplifier media, have a main limitation related to their low thermal conductivity and therefore long heat dissipation time, that translates into a limitation of the repetition rate and operating time.

1.1 High Energy Density and Ultra High Intensity Lasers

High Energy Density (HED) and Ultra High Intensity (UHI) Lasers have been a matter of interest for the scientific community for decades due to their vast potential applications (Figure 1.1). The possibility to provide high energy density, with an optimal spatial and temporal accuracy makes them ideal for various academic and practical applications. For example, very intense lasers can be used to extract efficiently energetic protons from matter, which can be accelerated for bio-medical applications [1], or to create in a laboratory extreme conditions of pressure and temperature to study the behavior of different materials, for fundamental and/or industrial applications[2]. Moreover these types of lasers makes possible the study of subatomic physics exploiting the intense electro-magnetic field that can be created.

A major interest is also dedicated to plasma physics and high energy density physics [3]. One of the primary challenges concerns the realization and the control of inertial confinement fusion (ICF). ICF concept is based on a compression fusion chain reaction releasing large amount of energy, that can be applied in the defense domain, therefore in the development of nuclear deterrents, and in the energy production field, following the dream of a carbon-free and sustainable energy and providing an alternative to the magnetic fusion research [4]. Another intriguing possible future field of study is to recreate and study in a controlled environment the temperature and density conditions of the core of star and planets, opening the so-called

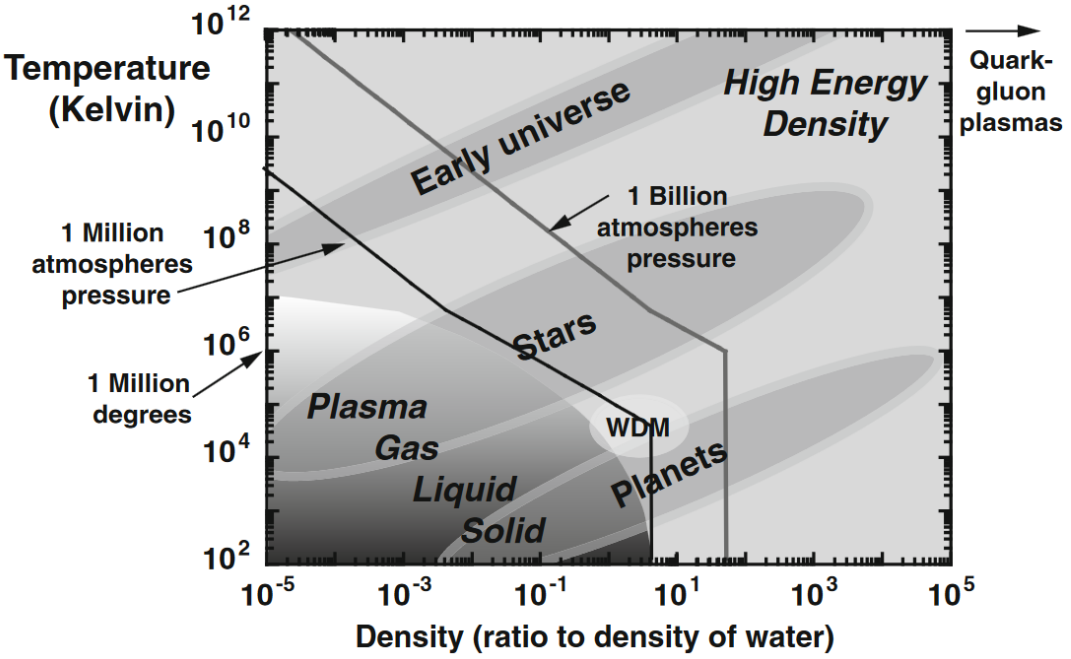

FIGURE 1.1: Connection of the high-energy density regime to physical and astrophysical systems [20].

"laboratory astrophysics" [5, 6].

Following the increasing interest in HED and UHI lasers, a whole domain of research on amplifier architecture, materials, sources and geometries design, opened, with the goal of exceeding the technological limits and problems that affect the development of such facilities. To achieve very high energy density, the idea, currently implemented in several facilities like the National Ignition Facility (NIF) laser in the USA [7] and the Laser Mégajoule in France [8], is to employ multiple laser beamlines converging in the same spot, in the so-called target chamber. Both facilities have a vast program dedicated to ICF experiments, for which two main "schemes" are actually possible: the direct drive fusion scheme and the indirect drive fusion scheme, both of them displayed in Figure 1.2. In the direct drive scheme, the target is a spherical pellet with a diameter of few millimeters, containing a mixture of about 10 milligrams of deuterium (D) ^{2}H and tritium (T) ^{3}H. The laser beams will compress and heat the fuel reaching the conditions for nuclear fusion [9]. In the indirect drive scheme, the target is a a small cylinder of heavy metal, often gold or lead, known as a "hohlraum" that contains the D-T mixture. The hohlraum is filled with a gas to avoid deformation during the pumping, counterbalancing the expansion and collapse of the walls. The hohlraum cylinder absorbs the laser radiation and emits the energy in form of soft x-rays, that will hit the D-T mixture [10].

A problem encountered in the realization of HED and UHI laser chains is related to the non-linear effects caused by the laser very high peak powers, that can eventually damage or break optical components at different stages

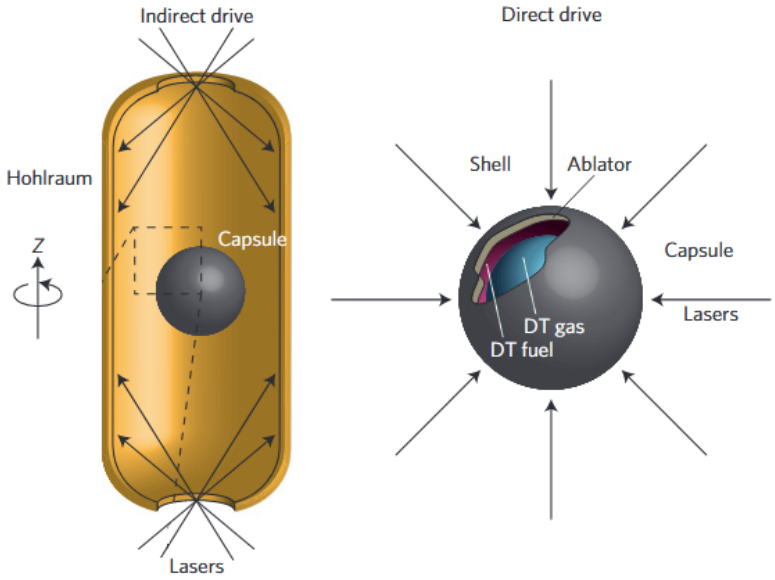

FIGURE 1.2: Targets used in ICF experiments, in direct and indirect drive configuration[21].

of the laser chain. To overcome this problem, the technique that enabled the development of UHI lasers, (Nobel prize award in physics in 2018), is the chirped pulse amplification (CPA) [11]. In short, the idea is to stretch in time the optical pulse, thus reducing significantly the peak power, and to amplify this streched pulse before its recompression. In this way, a much more powerful beam can be generated avoiding damages to the amplification system. The implementation of this technique permitted an increase of the laser focused intensity by several orders of magnitude, as displayed in Figure 1.3.

1.2 The Laser MégaJoule and PETAL

The Laser Mégajoule is a facility installed in Le Barp, in the Centre d'etudes scientifiques et techniques d'Acquitaine (CESTA). The construction began in 2002 and it was declared operational in 2014, and in 2019 was realized the first successful experiment of proton generation via D-T fusion process. The building is 300 m long, 150 m large and 35 m high, and the aerial view is displayed in Figure 1.4. The main objective is to obtain 1.8 MJ of UV laser light, impacting the few millimeters size target, as simplified in Figure 1.5. The facility, still in construction, will host four 125 m long laser bays for a total of 192 collimated laser beam-lines coinciding within the reaction chamber containing the nuclear fuel target. One of the laser bays hosts the PETawatt Aquitaine Laser (PETAL), a chain designed to deliver 500 fs to 10 ps long pulses with a kJ energy per pulse at 351 nm (full width half maximum (FWHM) = 3.5 nm), obtained from the amplification and frequency tripling of a 1053 nm laser beam with a 16 nm FWHM. Apart from the dedicated experiments that can be performed with the PETAL facility, the main purpose

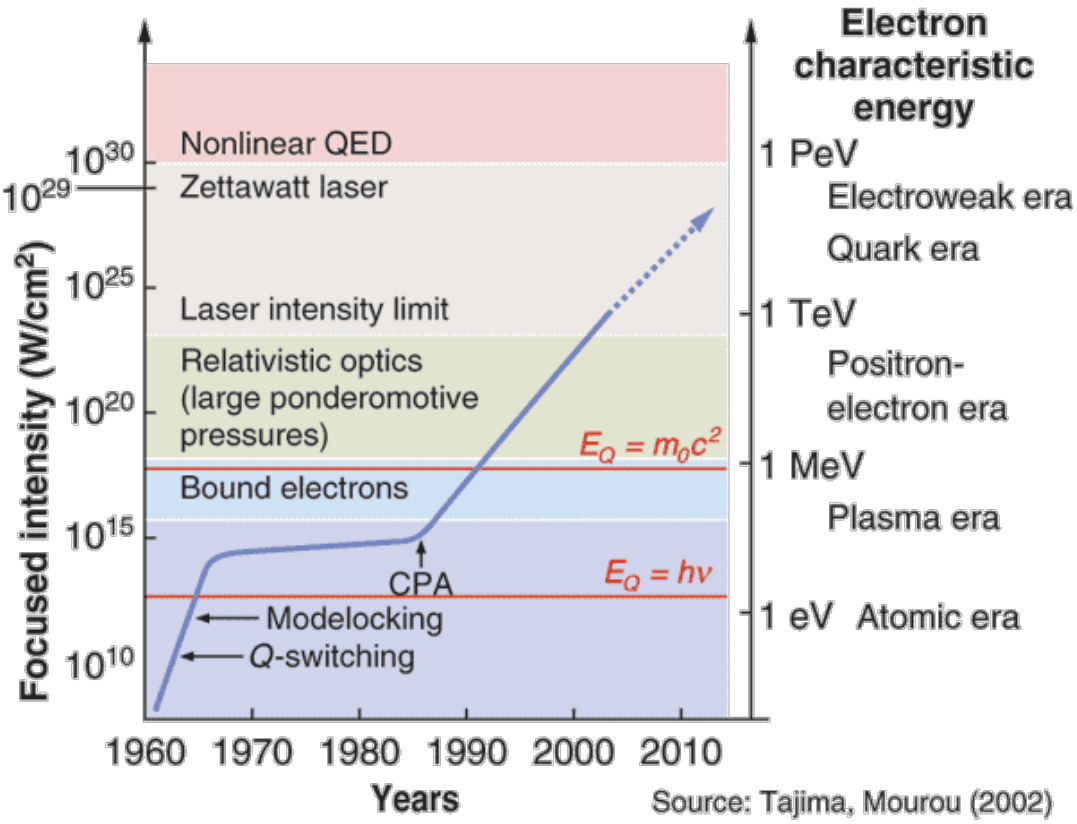

FIGURE 1.3: Evolution of ultra-high intensity (UHI) lasers [3].

of this laser chain is to be coupled with the ns-long laser pulses from the LMJ to achieve an efficient ICF via shock ignition [8, 12].

Within the LMJ facility the nuclear fuel target is excited using the indirect drive scheme, in which the x-ray emission is generated from laser beams at 351 nm, that in turn are obtained by energy conversion of beams at 1053 nm, as displayed in Figure 1.6. Those 1053 nm laser beams are obtained via the well-known $^4F_{3/2} \rightarrow {}^4I_{11/2}$ transition of trivalent neodymium, pumped at 800 nm. Neodymium-doped phosphate glasses, such as the LGG70 produced by Schott and the LHG-8 produced by Hoya, used also in the NIF facility, are used in both the front-end components and the main amplifier stages, allowing the setup to potentially deliver UV pulses with 1.8 MJ between 0.3 ns and 25 ns (Figure 1.6).

These phosphate glasses have been chosen in the first place for several reasons: the possibility to grow easily and efficiently large size glasses on an industrial scale, providing high optical homogeneity, essential to avoid aberrations, low number of inclusions and imperfections that could cause optical damages [13]. Additionally, these glasses possess very low phonon energy, wide transparency windows in the NIR range as well as very broad emission bands, that made them used worldwide for ultrashort lasers applications. Nevertheless, the principal advantage of Nd-phospate glasses as amplifiers resides in their saturation fluence (4.5 J/cm^2 [14]), that is roughly 5 times their laser induced damage threshold fluence (LIDT) (25 J/cm^2),

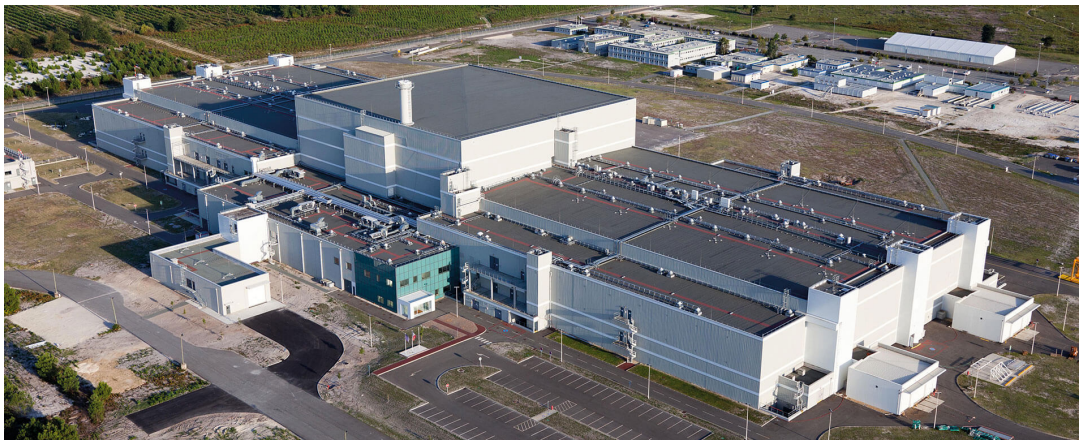

FIGURE 1.4: Aerial view of the LMJ facility.

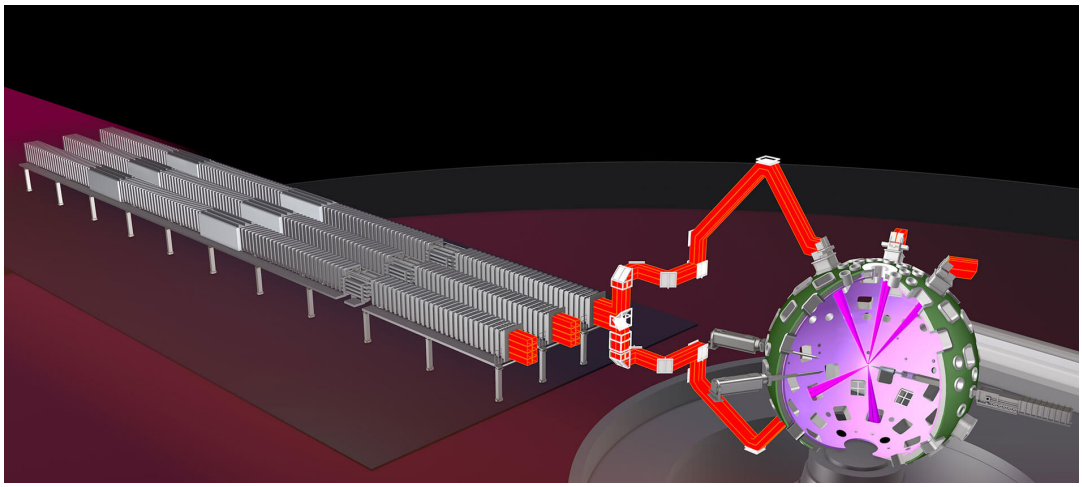

FIGURE 1.5: Scheme of the working principle.

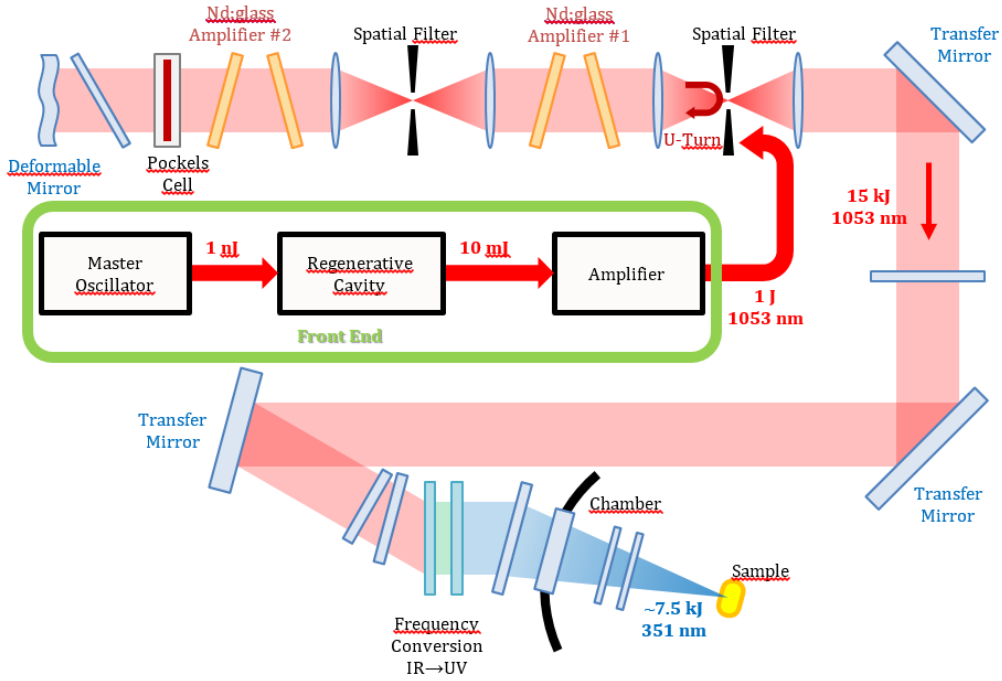

FIGURE 1.6: Amplifying chain schematic, illustrating the LMJ laser beam setup. Nd^{3+}-doped phosphate glasses are employed in the regenerative cavity, the front-end amplifier, and the laser amplifiers #1 and #2 [15].

representing a good compromise between high energy deposition and extraction efficiency.

However, as already stated, their main drawback is represented by their low thermal conductivity, that is the current limiting factor for the whole laser chain, in terms of repetition rate and operating time, which triggered the interest to develop new crystalline based amplifiers.

In order to correctly comprehend the material design requirements, it is essential to understand the different effects and issues that occur when trying to perform an ICF experiment. The overall goal is to achieve an uniform pumping of the D-T mix and thus an efficient ICF reaction. Different effects have to be precisely control in order to provide an optimal interaction between the target and the laser beams, in both the direct and the indirect drives. Three main effects which will be described in the following section, have to be carefully mitigated: FM-AM conversion, beam smoothing and cross-beam energy transfer.

1.2.1 FM-to-AM conversion

One of the main feature which ensures the best coupling between the laser beams and the target is the control of the temporal shape of the laser pulses.

The main issue related to this temporal shape is the so-called FM-AM conversion.

For a smooth propagation of the laser beam along the amplification chain, the optical spectrum of the front end laser has to be broadened in order to avoid stimulated Brillouin scattering in large optics and to ensure an efficient beam smoothing at the focal spot. This broadening is achieved using a specific frequency modulation (FM) process. However, a vast class of effects, including gain narrowing, but also, for example, non uniform spectral transmission through the optics or group velocity dispersion and polarization dispersion will actually act as a spectral filtering of the laser spectrum. As a consequence, this deformation of the spectrum will be converted in temporal Modulation of the laser Amplitude (AM) [22, 23]. This overall process is thus called FM to AM conversion.

As FM-to-AM conversion occurs during the beam propagation, it can potentially happen with different magnitudes for each singular beam depending on their respective parameters, this effect is problematic for several reasons. A first problem is related to the degradation of the optical components along the laser chain, reason for which it is critical to perform FM in the first place [24].

Furthermore, the idea of ICF is based on the synchronization of all the laser beams on the target. Therefore a fluctuation of the laser intensity in time (AM), which can be different for each beam, is of course limiting the efficiency of the whole process [23]. Thus, the correct fusion of the target can be compromised, having certain parts of the target receiving more or less intensity varying in time, making difficult to foresee and correctly perform the compression and subsequent fusion of the D-T mix. Moreover, in case of indirect driving, an intensity modulation will cause perturbations on the final temporal shape of the generated x-ray beams within the hohlraum, making the heating and pressure on the target non-uniform and difficult to control. In particular, the interaction between the beams and the gas in the hohlraum, produces a local plasma, that "mediates" the laser-target interaction. The laser-plasma coupling is thus a very critical aspect, and any modulation of the laser intensity easily leads to plasma instabilities, that are not only very difficult to control, but also enhance non-linear effects like Brillouin and Raman retro-diffusion [25, 26].

Lastly, it has been demonstrated that the spectral bandwidth of the pulse has a critical impact on the FM-to-AM conversion, which will be more pronounced and difficult to control with a larger spectral pulse width [23, 24].

1.2.2 Beam Smoothing

Another important issue, principally linked to the uniform pumping of the target, is related to the cumulative effects that can occur along the beam propagation in terms of small phase aberrations introduced by each optical

element, both linear and non-linear. Those can produce random intensity non-uniformities at the output, that can become very difficult to control and handle. For this reason, the topic of optical smoothing, or beam smoothing has been vastly studied both at the LMJ and the NIF. The basic idea of the beam smoothing mechanism is to divide the beam in several beamlets with a coherence time t_c much shorter than the pulse duration t_p. The implementation of several optical delays, larger than the coherence time, upon different transverse sections of the beam create a spatial incoherence. The focusing of the resulting beamlets will create a complicated interference pattern that will vary over time, modulated by a smooth envelope due to the diffraction of each individual beamlet. For a time scale $t \gg t_c$ the interference pattern will average to zero, consequently leaving only the smooth diffraction pattern, that will be insensitive to non-uniformities [27, 28].

A first technique has been suggest by Kato et al. [29], in which the beam smoothing is obtained with a random phasing mask. Different mechanisms to achieve spatio/temporal incoherence have been proposed in the following years, achieving the required spatial incoherence using echelons [27], rotating random phasing plate (RPP) [30], smoothing by multi-mode fibers (SOF) [31] and smoothing by spectral dispersion (SSD) [32]. The latter is the most used currently, being the one that provide the best results in terms of spatial incoherence along the beam spot and temporal incoherence combined [33].

It is worth to mentioning that regardless of the mechanism involved, the smoothing will affect the FM-to-AM conversion. In fact, it is necessary to control precisely the trade-off between a large bandwidth pulse to improve the smoothing and a reduced pulse bandwidth to limit the FM-to-AM conversion. This aspect has been studied extensively by Penninckx et al. [34], in which they demonstrated how a moderate level of FM-to-AM conversion will have a low impact on the performance of the beam smoothing. Duluc et al. [24] also showed that, in the specific geometry of the LMJ, in which each beam is split in four sub-beams, a longitudinal SSD distributing the spectral broadening to the quadruplet sub-beams, will drastically reduce the FM-to-AM conversion.

1.2.3 Crossed Beam Energy Transfer

Crossed beam energy transfer (CBET) arises when multiple propagating laser beams intersect in an active medium. In the specific case of ICF facilities like the LMJ and the NIF, this effect takes place within the plasma [35–37], that is generated by the laser-target interaction in the case of the direct drive [9, 38], and by the interaction between the laser beams and the gas in the hohlraum in the case of the indirect drive [39].

The beam crossing induces a periodic density perturbation via the ponderomotive force of the overlapping fields acting on the electrons in the direction of the difference wavevector between the beams. When the

induced plasma response is resonant with the ponderomotive force, this leads to a net energy transfer between the single beams. Thus, a control of the laser-plasma coupling is critical, and will of course depend on the beam smoothing described earlier. In the specific case of indirect driving, CBET can distort the temporal and/or spatial symmetry of the generated x-ray drive [39].

A proposition to suppress CBET consists in shifting the beam wavelength. This type of solution is currently employed in the NIF facility with the so-called four-colors scheme, employing beams with four slightly different wavelengths. A slight shift of the wavelength, in a simplified description, changes the resonance frequency of the plasma for each wavelength, and thus impairing the energy transfer effect which is a resonant mechanism [39].

The work of Hüller et al. [33] shows how a spatio-temporal smoothing by SSD, will not affect significantly the CBET effect, unless a very large bandwidth, > 100 GHz, is introduced. A way to suppress the CBET effect is explored extensively in the work of Bates et al. , first with the use of broad laser pulse bandwidth. This has to done of course, without generating more FM-to-AM conversion.

As a conclusion, the beam smoothing and cross-beam energy transfer explained above call for a large pulse bandwidth while trying to limit the FM to AM conversion. This trade-off imposes spectral constraints on the amplifier active medium whose gain spectrum has to be both broad and flat enough.

1.3 New Materials for LMJ

The effects described above are critical, and impose design constraints to the amplifier development. In the particular case of this work, the efforts are concentrated on the front-end laser of the LMJ.

This particular part of the facility is the section of the LMJ responsible for the generation and the initial amplification of the laser beams, that will be further amplified in the rest of the chain (see Figure 1.6). A simplified scheme of the front-end is depicted in Figure 1.7, which starts with a fibered source, generating the initial beam at 1053 nm and a pre-amplifier module (MPA), representing the first bulk stage of the amplification. The output of the fibered source delivers nJ pulses with a 1 Hz repetition rate. This laser beam is injected in the regenerative amplifier, which increases the pulse energy to 50 mJ. The output of the regenerative amplifier is then injected in a 4-pass amplifier, with an output energy of 1 J and a repetition rate of 10^{-3} Hz. This repetition rate is obviously very low and the plan is to increase its repetition rate in the near future.

The main goal of this PhD work is thus to investigate new crystalline materials which could be substituted to the Nd-doped phosphate glasses

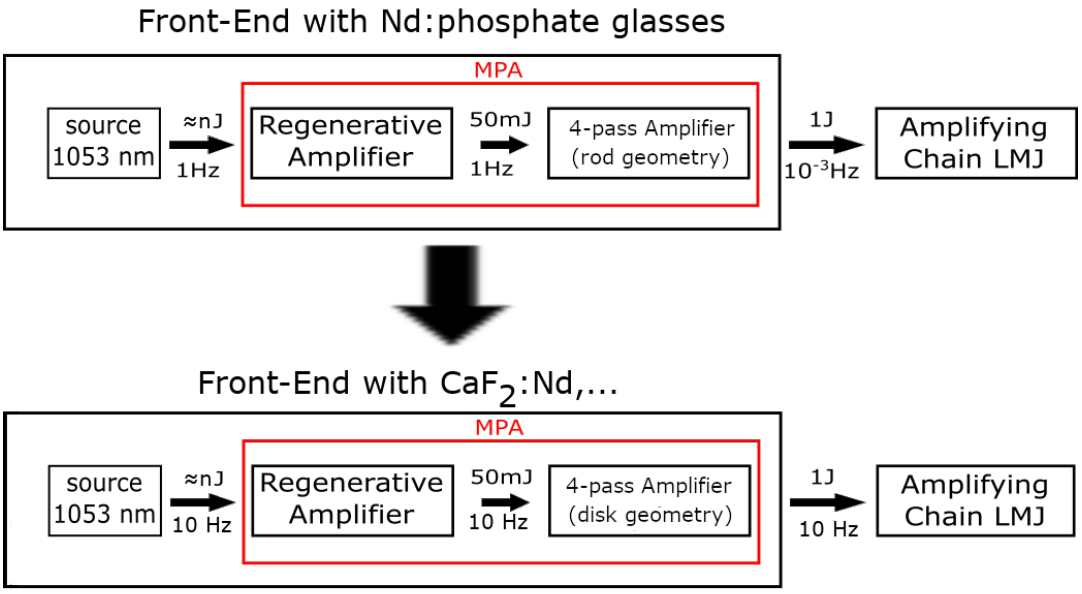

FIGURE 1.7: Simplified scheme of the front-end of the LMJ with the Nd:phosphate glasses and with the CaF_2 : Nd, ...

currently used in the front end. The much higher thermal conductivity of crystalline materials will allow to increase the repetition rate of the front end laser from 10^{-3} Hz to 10 Hz. This change of active materials will be complemented with a change of geometry in the 4-pass amplifier from rod shaped to disks amplifiers.

As we have seen in the previous sections, the design parameters of the amplifier are very delicate, in order to avoid effects that will later limit the overall facility performance. The most obvious parameter is represented by the laser wavelength peak at 1053 nm, which is the center wavelength of the fibered source beam. As mentioned earlier, a spectral distortion of the pulse spectral profile can generate FM-to-AM conversion. In order to limit this effect the amplifier spectrum has to be as flat as possible around that center wavelength. Moreover, a broad amplifier band is necessary to generate broadband pulses with short coherence time, a requirement to achieve an efficient beam smoothing along the amplification chain.

To satisfy all these requirements the criterion which has been retained for the front end is an amplifier spectral bandwidth centered at 1053 nm with a flat profile of 3 nm. This criterion seems almost impossible to reach for conventional Nd doped crystals which usually have a very narrow emission peak, with a FWHM at 1.05 μm around or even below 1 nm.

Within this context, the CIMAP laboratory and the CEA-CESTA started a collaboration to explore the potential of fluoride crystals as potential new amplifier materials. Unlike most laser crystals CaF_2 : Nd exhibits broad absorption and emission bands which are comparable to what is found in

phosphate glasses. However, as explained extensively in the section 2.1.2, Nd-doped fluorites were not considered for a long time as laser or amplifier materials, because of Nd clustering even at very low Nd doping level. This clustering provokes an energy transfer by cross-relaxation between neodymium ions that quenches the transition at 1 μm. The collaboration between the CIMAP and the CEA-CESTA started by the investigation of the co-doping of $CaF_2 : Nd$ with lutetium as a buffer ion to avoid the formation of quenched Nd clusters [15].

Several interesting results were obtained with this first investigation that acted as starting points for future works, such as the one presented here. An interesting result obtained with the optical spectroscopy investigation is depicted in Figure 1.8. The Nd emission increases drastically as the buffer concentration (Lutetium) increases. In particular, Figure 1.8 shows that 8at.% of co-dopant concentration is enough to break all the optically non-active Nd clusters. The thermo-mechanical properties of $CaF_2 : Nd$ were also investigated using thermo-optics techniques, like thermal lens spectrometry and Jamin-Lebedev interferometry. It is well known that thermo-mechanical properties tend to be degraded with the increase of the doping level. The investigation showed, as expected, that the codopant concentration has a significant impact on the thermal conductivity as displayed in Figure 1.9 with the dependence of the thermal conductivity with the buffer concentration (Lu). Thus a balance between the Nd cluster breaking and preserving good thermo-mechanical properties has to be found. The optimal compromise is found by using a co-doping level of 5at.% which will be the reference for the codoping concentration in this entire work.

The thermo-optic and thermo-mechanical properties of $CaF_2 : Nd, Lu$ have been also studied deeply in CEA-CESTA, for example with the work of Stoffel [16]. In this work, Stoffel et al. [17] performed a detailed investigation of the heat deposited in the laser crystal with the pumping process, and the consequent impact on the mechanical constraints generated by the thermal gradient and the subsequent induced birefringence.

When comparing $CaF_2 : Nd$ with Nd doped phosphate glasses, from the optical spectroscopy point of view, CaF_2 turned out to be a solid candidate to substitute the phosphate glasses, after an extensive investigation of various fluorite based matrices, namely SrF_2, BrF_2 and hybrid fluorite compositions.

Additionally, the compromise between the saturation fluence and the LIDT fluence, introduced in section 1.2 is about the same as for the phosphate glasses since for $CaF_2 : 0.5\%Nd, 5\%Lu$ $F_{sat} = 5.9 J/cm^2$ with $F_{LIDT} = 23\ J/cm^2$.

Moreover, the potential of $CaF_2 : 0.5\%Nd, 5\%Lu$ as a promising laser crystal has been also proven, with a preliminary mode-locked experiment, obtaining fs-long pulses, as well as CW-laser action with a slope efficiency of

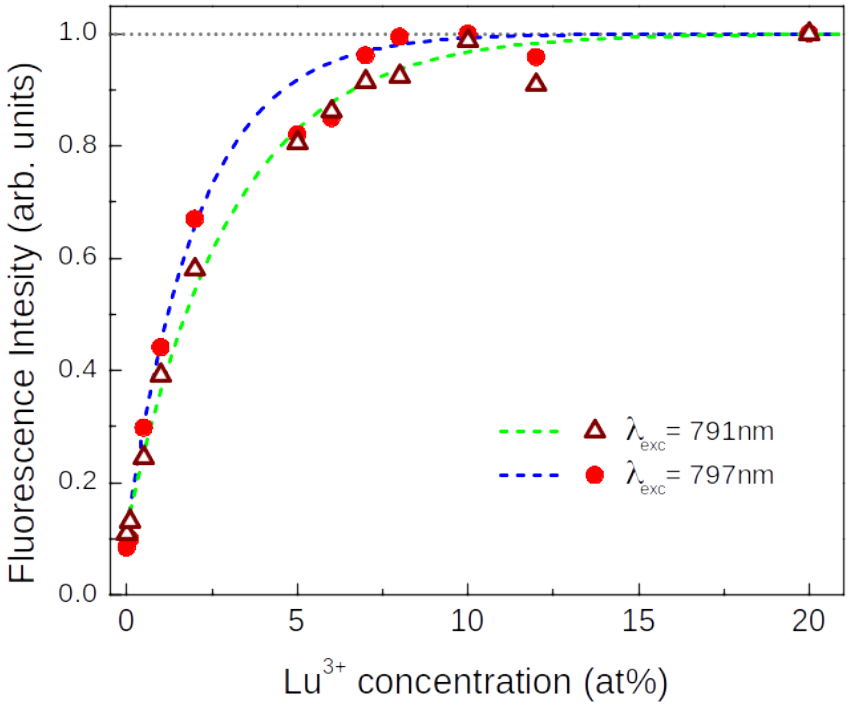

FIGURE 1.8: $^4F_{3/2} \rightarrow ^4 I_{11/2}$ integrate emission intensity versus Lu^{3+} concentration [40]

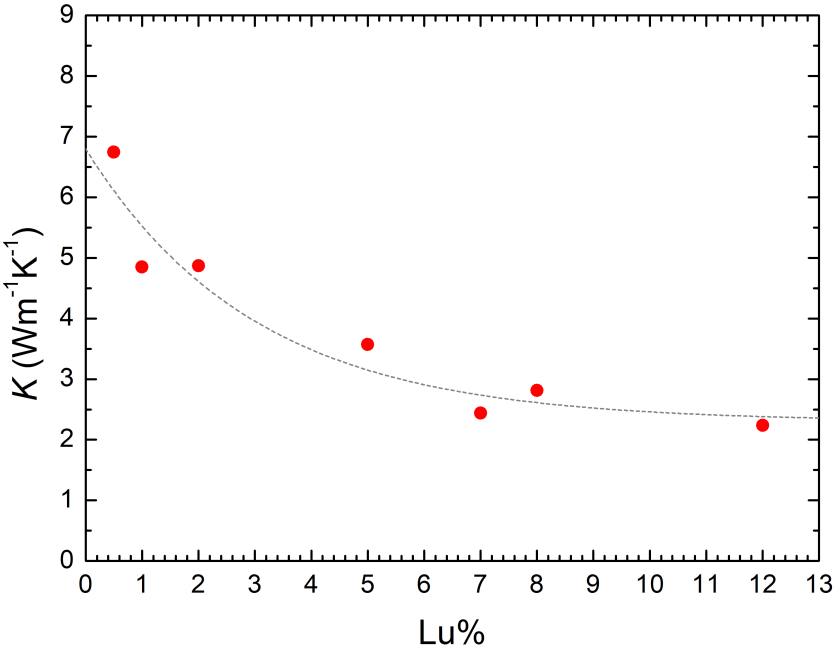

FIGURE 1.9: Thermal conductivity in function of Lu concentration in CaF_2 : Nd, Lu [15].

44% at 1062 nm.

While $CaF_2 : 0.5\%Nd, 5\%Lu$, gave very interesting laser results, it does not offer the flat and broad emission bands which are required for the LMJ applications. This PhD work is therefore dedicated to the investigation of the codoping of $CaF_2 : Nd$ using various buffer ions and combining them with two or three buffer ions within the same composition. As will be explained extensively in the next chapters, buffer ions of different size can modify the local crystal field and thus the crystal optical properties. Thus this work aims to better understand how the nature of the buffer ion and its concentration will affect the design of the amplifier.

1.4 Chapters Overview

In the context described in the previous sections, this document presents the methods, techniques and results obtained for the development and characterization of new laser amplifier materials at 1.05 μm.

Chapter 2 is dedicated to the optical spectroscopy of neodymium-doped CaF_2, starting from a state of the art and a summary of the main issues. Afterwards, the buffer (Bu) ion co-doping is introduced and investigated, with the fabrication of $CaF_2 : Nd, Bu$, using different buffer ions and studying the different influences that they have on neodymium spectroscopy. More complicated compositions are then introduced, based on the results obtained in the single buffer co-doping investigation, first employing two different buffers and then three, showing the potential of those crystals in terms of spectroscopic properties engineering. The last part of the chapter is dedicated to the Nd, Yb co-doping approach, where Yb ions act not only as buffer ions, but also as active ions implying energy transfers between the Nd and Yb ions.

Chapter 3 is dedicated to the amplification properties of the crystals studied in chapter 2, focusing on the most promising for the LMJ applications. A first section is dedicated to an amplifier medium criterion specific for the LMJ applications and the need for a broadband amplifier medium. The following section is dedicated to gain and amplification simulations, while section 3.6 presents an experimental investigation of the amplification properties of the various crystals presented in Chapter 2. The pump-probe setup used for these experiments is presented along with the experimental results and a comparison with the developed model.

Chapter 4 focuses on laser experiments performed with the laser crystals characterized in Chapter 3 using a plano-concave cavity. This study encompasses CW laser action properties, spectral tunability and a detailed analysis of the round trip losses. The last section of this chapter is dedicated to a preliminary study of molecular adherence between a doped $CaF_2 : Nd, Bu$ and a pure CaF_2, in order to exploit the pure crystal as a heat sink in laser

applications, taking advantage of the pure CaF_2 high termal conductivity. Unlike regular optical bonding, molecular adherence does not require a specific adhesive to glue the two components together. Thus, it presents very low losses at the interface between the two crystals. This section starts with a general state of the art and the fabrication technique developed for CaF_2, as well as some preliminary characterizations of the final sample.

The last chapter will summarize the results, tracing the final conclusions, highlighting and discussing the perspectives for further investigation.

Chapter 2

Optical Spectroscopy of $CaF_2 : Nd^{3+}$ Co-doped with Buffer Ions

2.1 Introduction

In order to understand the peculiarities of co-doping Nd-doped CaF_2 with buffer ions, an extensive optical spectroscopy investigation has been performed. The key spectroscopic parameters investigated are the absorption and emission cross sections, the emission spectral shapes, and the fluorescence and radiative lifetimes of the different active Nd sites in the various co-doping samples. Specifically, this part of the study is at first focused on the spectroscopy of the Nd centers when the buffer co-doping is realized with a big ion, namely gadolinium, cerium and lanthanum, compared to the co-doping with a smaller ion, yttrium, lutetium and scandium, with a focus on how the nature of the buffer is influencing the spectroscopic properties. In a further step of this first part, the possibility of mixing the various buffers is explored, with the idea of achieving an engineering of the spectroscopic properties changing the buffer relative concentrations, firstly with two different co-dopants and after with three.

The last part of this chapter is dedicated to the possibility of Nd^{3+}-Yb^{3+} doping of CaF_2, with the goal to study the non-radiative energy transfer process between Nd and Yb and evaluate the potential application of this crystal to optical amplifiers and laser applications.

2.1.1 Principles of Rare Earth Spectroscopy

Rare-earth (RE) elements have unique features in terms of optical spectroscopy, depending both on the doping ion and the host matrix structure. Their interesting optical features are due to the weak interaction of the free ion with the surrounding crystal field. Their peculiarities reside in their electronic configuration, $[Xe]4f^n$ and in the shielding of the $4f$ electron shell from its crystalline environment by the outer $5s$ and $5p$ shells. As a consequence, the RE energy levels positions depend firstly on the ion itself, but the precise intensity and spectral width of the emission and absorption bands depend

on the interaction between the 4f electron orbitals and the local crystal field: in fact, the static electric field due to the surrounding ligands creates a splitting of the free ion energy levels due to the Stark effect, leading to the Stark sublevels. [41].

2.1.2 Nd-Doped Fluorites Spectroscopy

RE ions embedded in crystalline hosts occupy incorporation sites with a well defined site symmetry. As a consequence, the spectral bands are characterized by very narrow line-widths contrary to glasses or other disordered structures, where the different local site geometries lead to broader and flatter bands. However, some exceptions can be found among crystalline hosts, like the case of fluorite structures, where spectral bandwidths are comparable to what is observed in doped glasses.

In RE^{3+} doped fluorite type crystals XF_2, the RE^{3+} ions substitute the X^{2+} cations in the lattice, leading to the formation of local site geometries with interstitial F^- ions to ensure the charge compensation. This, in turns leads to the formation of RE^{3+} clusters [42–44].

Since the mid '60s, the scientific community has been interested in understanding the exact nature and mechanism of RE^{3+} aggregation, and the possibility to develop laser materials with such systems [45]. Among the possible fluorite type crystals, CaF_2 is an appealing candidate because it is possible to grow large single crystals with very high optical quality by the Czochralski method. Moreover, this crystal possesses a very high thermal conductivity (9 $Wm^{-1}K^{-1}$ when undoped) as compared to the well-known laser crystal YAG (14 $Wm^{-1}K^{-1}$). When doped with Nd^{3+} ions, it exhibits very broad absorption and emission bands . However, $CaF_2 : Nd^{3+}$ is known to experience clustering even at low dopant concentration, below 0.1at.% [42, 46]. In fact, inserting trivalent lanthanide ions in CaF_2, gives rise to the formation of different optical centers, depending on the lattice position of the doping ion and the corresponding local symmetries created by the additional interstitial F^- ions. The different Nd^{3+} centers can be discriminated by studying the absorption and emission spectra (shape, peaks and relative intensities depending on the excitation wavelength) along with the Nd^{3+} energy level lifetimes associated with each incorporation site. The various studies on RE^{3+} doped CaF_2 show that before RE^{3+} clustering occurs, large dopant ions tend to form sites with a C_{4v} symmetry while smaller tend to form C_{3v} sites ([42, 44, 47]). In the case of Nd^{3+}, at low Nd^{3+} concentration several centers have been discriminated in the work of Payne (Figure 2.1):

- a first one labeled as uncompensated, where Nd^{3+} substitute for Ca^{2+} ion and the charge compensation does not occur locally, the Nd^{3+} ion occupies an O_h symmetry site
- nearest-neighbor (nn) compensation, where the F_i^- is located in the nearest neighbour cell, giving rise to a C_{4v} symmetry

- next-nearest-neighbour (nnn) compensation: F_i^- is located in the next-nearest-neighbour cell, giving rise to a C_{3v} symmetry

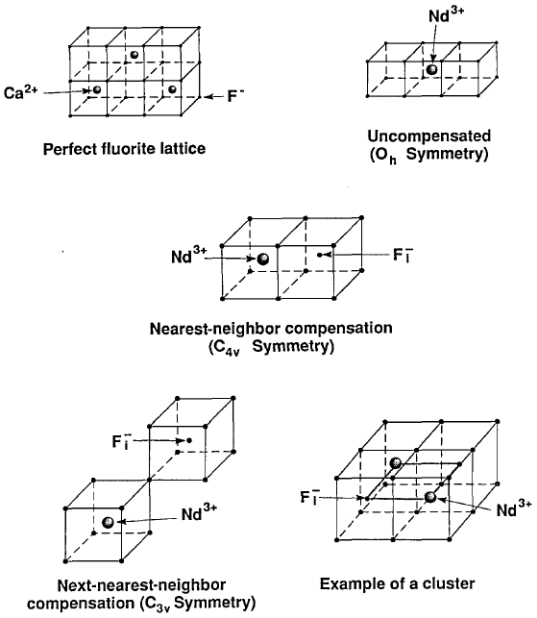

FIGURE 2.1: Fluorite lattice structures with different site symmetries for low Nd^{3+} doping [42].

For Nd^{3+} concentration higher than 0.05%, Nd^{3+} ions start to form clusters, leading to more complicated structures. CaF_2 is known to be the matrix host in which the RE^{3+} clustering effect is the strongest between all fluorite type crystals. Within clusters, Nd^{3+} ions sit very close to each other, being no more isolated. In this situation, strong dipole-dipole interaction can take place, leading to non-radiative energy transfer processes. The energy transfer between the $^4F_{3/2}$ and the $^4I_{9/2}$ levels leads to the quenching of the transition at 1 μm ($^4F_{3/2} \rightarrow {}^4I_{11/2}$) as displayed in Figure 2.2

The Nd^{3+} local site geometries within clusters are different from what is observed at lower Nd^{3+} concentration. The three main types of cluster geometries are the following [48–51]:

- tetragonal C_{4v} symmetry centre (often labeled in literature as L centre), again with the F_i^- ion in the nearest available interstitial position; it disappears at high Nd^{3+} concentrations
- rhombic C_s symmetry centre (often labeled as M centre), where a pair of Nd^{3+} ions is associated with two interstitials F_i^-
- rhombic C_s symmetry centre (often labeled as N centre), where four Nd^{3+} ions are associated with four interstitials F_i^-.

The RE clustering effect cannot be avoided, but in order to avoid the luminescence quenching, a solution has been proposed, consisting in the addition of a second type of dopant acting as a buffer, that has to be optically inactive, avoiding energy transfer. This co-doping creates clusters with Nd^{3+} and

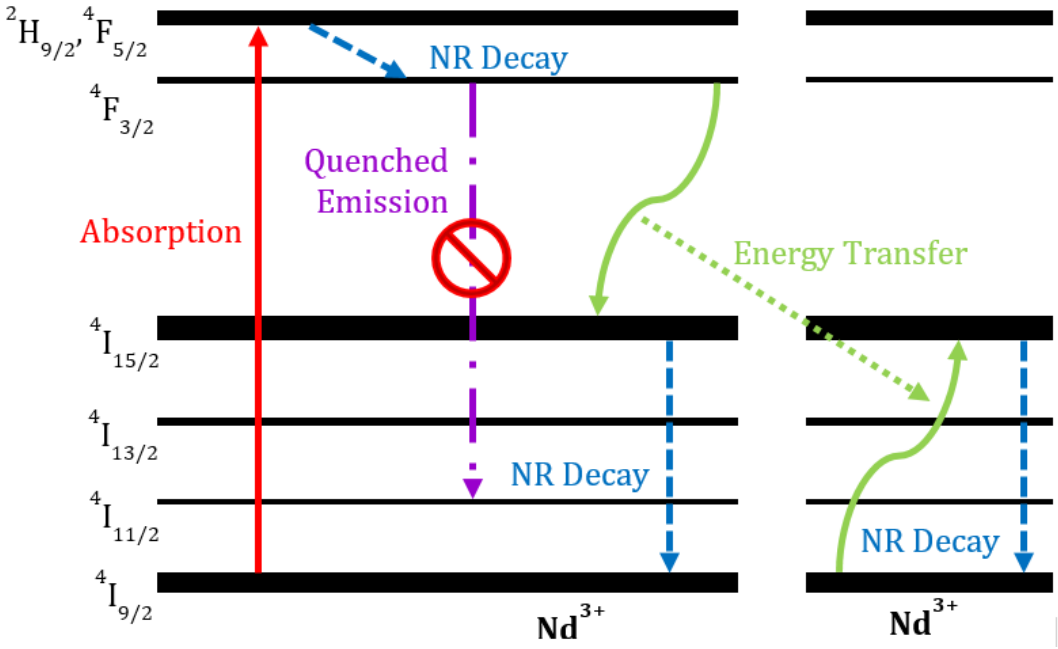

FIGURE 2.2: Illustration of the quenching of the $^4F_{3/2} \rightarrow {}^4I_{9/2}$ transition due to energy transfer between two Nd^{3+} ions

.

buffer (Bu) ions avoiding the formation of quenched Nd^{3+} clusters. In other words it represents a simple way of isolating Nd^{3+} ions from each other.

2.1.3 The Choice of the Buffer Ions

Several ions can be considered as buffer ion candidates. However, three main criteria have to be fulfilled by the buffer ion. First of all, the buffer co-dopant has to be optically inactive meaning it must exhibit no energy level within the visible or infrared range.

As a second requirement, the valence has to be trivalent. Finally, in order to properly incorporate the buffer ions within the clusters and isolate the single Nd^{3+} ions, the buffer ionic radius has to be as close as possible to the one of Nd^{3+}.

This solution has been proposed for the first time by Bagdasarov [52], choosing Y^{3+} as a buffer exploring different co-dopant concentrations keeping the same Nd^{3+} concentration. It was clearly demonstrated that the presence of yttrium impurities causes a redistribution of the absorption lines intensities, slightly modifying the cluster site symmetries compared to pure Nd^{3+} clusters. The new sites are thus quasi-tetragonal or quasi-rhombic and are often labeled in literature as M', N' and L' centers. Moreover, the Nd $^4F_{3/2}$ radiative lifetime decreases, and the Nd emission intensity increases. This last feature is due to the breaking of quenched $Nd - Nd$ clusters, leading to an increase of the number of emitting Nd^{3+} ions when increasing

the Y^{3+} concentration. As a consequence, $CaF_2 : Nd, Y$ has been successfully tested as laser material in several occasions [53–59].

Another successfully employed co-dopant is lutetium which has been studied in the CIMAP laboratory by Normani et al. as mentioned earlier in section 1.3. One important outcome of this work has been the identification of the optimum doping and co-doping levels, as 0.5at.%, for Nd^{3+} and 5% for Lu^{3+}. As mentioned previously, the co-doping concentration degrades the thermo-mechanical properties of the crystal as displayed in Figure 1.9, and thus a balance between the Nd cluster breaking and preserving good thermo-mechanical properties has to be found. The detailed study of the optical properties of $CaF_2 : Nd, Lu$ evidenced the presence of two main types of Nd-Lu clusters associated with the quasi-rhombic M' and quasi-tetragonal L' centers which will further referred to as N_1 and N_2. These two types of clusters can be discriminated in wavelength and time:

- the N_1 quasi –rhombic has an absorption peak at 791 nm, a luminescence peak at 1049 nm and a longer lifetime around 500 μs
- the N_2 quasi tetragonal has an absorption peak at 797 nm, a luminescence peak at 1054 nm and a shorter lifetime around 300 to 400 μs

Moreover, the concentration study of these clusters in $CaF_2 : Nd, Lu$ suggests that N_1 and N_2 clusters efficiently replace the Nd clusters and become the only two optically active clusters once the concentration of Lu^{3+} ions reaches 5%at. Moreover, the number of N_2 sites appears to be negligible at low Lu^{3+} concentration and the dominant cluster is the N_1 M' center which is gradually replaced by the N_2 center as the Lu^{3+} concentration increases.

A third candidate is lanthanum [60], that has been studied recently as a potential co-dopant in $CaF_2 : Nd,$.. Results show interesting CW laser operation in $CaF_2 : Nd, La$ [61, 62]. The other two buffer ions present in literature to our knowledge are Gd^{3+} [63, 64] and Sc^{3+} [65], with more focus on the laser performance than on the spectroscopic investigation.

The spectroscopic results in all these co-doped Nd doped CaF_2 crystals show that the exact position of the absorption and luminescence peaks and bandwidths along with the energy level lifetime seem to change with the type of buffer ions. This can be explained first by considering the different size of the buffer ions: the co-dopant will slightly change the Nd surrounding crystal field and thus the Stark sublevels, leading to changes in the optical spectroscopy features. However a deep and detailed spectroscopic analysis with multiple buffer ions cannot be found in the literature. So we develop in this work a specific study keeping the same neodymium doping level and changing the nature of the buffer ion and exploring the different spectroscopic parameters. This is crucial to engineer and optimize specific laser materials for the desired amplifier or laser application. In the following sections, after an introduction on the experimental methods and techniques, the optical spectroscopy investigation of $CaF_2 : Nd, Bu,$

will be presented considering at first six different buffer (Bu) ions, chosen to satisfy the criteria described at the beginning of this subsection, namely gadolinium, lanthanum, cerium, yttrium, lutetium and scandium.

Afterwards, an approach of hybrid co-doping will be presented, with the idea of a fine optimization and tuning of the spectroscopic properties, employing first two different co-dopants, $CaF_2 : Nd, Bu_1, Bu_2$, and then three different co-dopants $CaF_2 : Nd, Bu_1, Bu_2, Bu_3$, always keeping constant the total co-doping level at 5at.%. Lastly, an hybrid doping solution with $Nd - Yb$ in $CaF_2 : Nd, Yb, Gd$ is also examined, with a preliminary study on the energy transfer between the Nd^{3+} and Yb^{3+} ions, following a previous work performed in CIMAP by Petit et al. [66].

2.2 Principles and Techniques

In the design and optimization of a laser amplifier it is crucial to have a clear comprehension of the spectroscopic properties and the potential pumping mechanism. In the particular case of Nd^{3+} , the laser operation at 1 μm, ($^4F_{3/2} \rightarrow {}^4I_{11/2}$ transition) is a four-level system. This transition takes place with the pump wavelength matching the absorption transition $^4I_{9/2} \rightarrow {}^4F_{5/2}$, $^4H_{9/2}$ around 800 nm followed by the non-radiative relaxation of the $^4F_{5/2}$ and $^4H_{9/2}$ to the $^4F_{3/2}$ level.
In this section, after a presentation of the crystal growth and sample preparation, the absorption, luminescence and energy level lifetime techniques and setups, employed in the investigation, are presented.

2.2.1 Bridgman-Stockbarger Crystal Growth and Sample Preparation

The crystal growth has been realized with the Bridgman-Stockbarger technique. This procedure includes two similar processes employed in the realization of the crystal boules and the solidification of polycrystalline samples via melting and crystallization, the Bridgman [67] and Stockbarger [68] methods. Both techniques share the same basic principle of growth from a melt, heating the material over its fusion temperature and afterwards slowly cooling it down, achieving the solidification that leads to an atomic rearrangement into a crystalline structure. The presence of a single-crystal grain at the solid-liquid interface ensures the growth in a form of a single crystal boule [69]. The difference between the Bridgman and the Stockbarger techniques resides in the technical details of the furnace. In fact, while the Bridgman oven applies a temperature gradient along the axis, leading to a vertical or horizontal growth with a crucible , the Stockbarger uses a two-zone furnace at different set temperatures, in order to have a control of the interface position.

The Bridgman vertical crucible chosen for the setup consists in a cylindrical tube with a tapered lower end. The melting temperature T_m of calcium fluoride is between 1360°C and 1480°C. The ampoule containing the material is lowered in the cylinder, making the crystallization taking place first within the lower part. The lower section of the ampoule being tapered, creates a restricted space. This allows for the single nucleation event, necessary to generate a single-crystal grain, to take place. From the first grain lattice, the "seed", the growth condition is defined at the phase-transition interface, and so is the entire crystal lattice orientation. An alternative to achieve single-crystal growth consists in starting from a previously grown single-crystal seed, which is inserted in an appropriate holder in the lower section, providing the initial grain. Both alternatives are depicted in Figure 2.3.

In the specific case of this study, the crystals were grown using the Bridgman method into cylindrical barrels several centimeters long and 6mm in diameter. After the growth, the crystals dedicated to the optical spectroscopy investigation are cut with a wire saw to have a thickness of 5mm, and polished with a manual standard polishing machine. This procedure permits to achieve shining surfaces with a roughness around 20 to 50 nm.

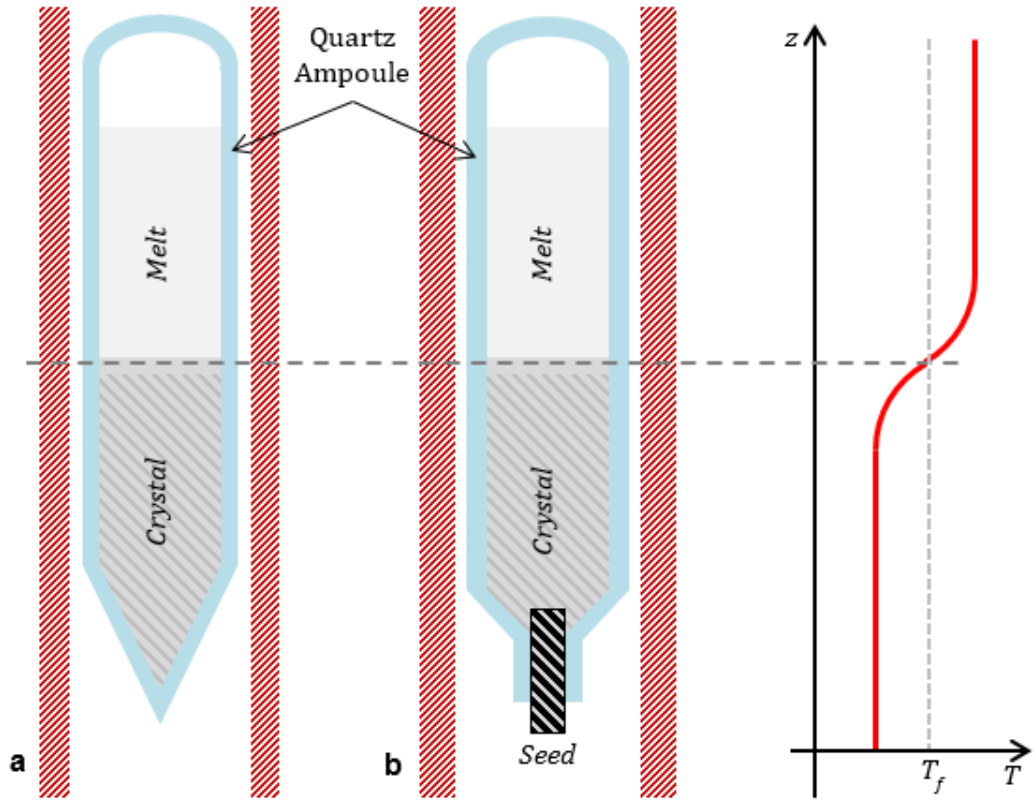

FIGURE 2.3: Bridgmann crystal growth setup: tapered-end configuration (a) and the growth from a seed (b).

2.2.2 Absorption

The absorption measurement is performed comparing the intensity of two different monochromatic beams, one passing through the sample and the other acting as a non- absorbed reference while tuning the wavelength with a monochromator in order to cover the spectral range of interest. In the specific case of this study, this measurement is performed with a commercial Perkin-Elmer Lambda 1050 spectrophotometer, with a 0.2 nm spectral resolution. This specific procedure permits to estimate the crystal absorbance, from which it is possible to calculate the absorption cross section, and derive the optimum pump wavelength. From the absorption spectra calibrated in cross sections, it is possible to estimate the radiative lifetimes and transition branching ratios of the different energy levels using the Judd-Ofelt analysis, which will be presented in the next section.
The absorption coefficient α of a material of thickness l can be modeled with the well known Lamber-Beer law [70, 71], which gives the transmitted intensity I_{tr} as a function of the incident intensity I_0:

$$I_{tr} = I_0 \exp(-\alpha l) \tag{2.1}$$

The absorption coefficient α, in absence of non-linear effects and ground state depletion, is defined as a function of the active ion concentration N and the absorption cross section σ_{abs} as

$$\alpha(\lambda) = N \cdot \sigma_{abs}(\lambda) \tag{2.2}$$

2.2.3 Luminescence and Excitation Spectroscopy

The principle of luminescence spectroscopy is based on the excitation of the sample by light at an absorption wavelength and the collection of the intensity of the spontaneous emission as a function of the wavelength. This permits not only to study the optimum emission wavelength under a specific pumping as well as the width and shape of the emission bands, but the luminescence spectrum is crucial to calculate the stimulated emission cross sections via the Füchtbauer-Landenburg equation, reported in eq. 2.3 that links the stimulated emission cross sections to the spontaneous emission intensity [73–75]:

$$\sigma_{em} = \frac{\beta\lambda^5}{8\pi c n^2 \tau_{rad}} \frac{I(\lambda)}{\int \lambda I(\lambda) \mathrm{d}\lambda} \tag{2.3}$$

where c is the speed of light in vacuum, n is the host refractive index, τ_{rad} is the radiative lifetime, β is the transition branching ratio, λ is the photon wavelength corresponding to the energy hc/λ, $I(\lambda)$ is the emission intensity.

Another experimental technique based on the luminescence is excitation spectroscopy. As in the case of the luminescence spectroscopy the sample is pumped with a monochromatic source, but the emission intensity is

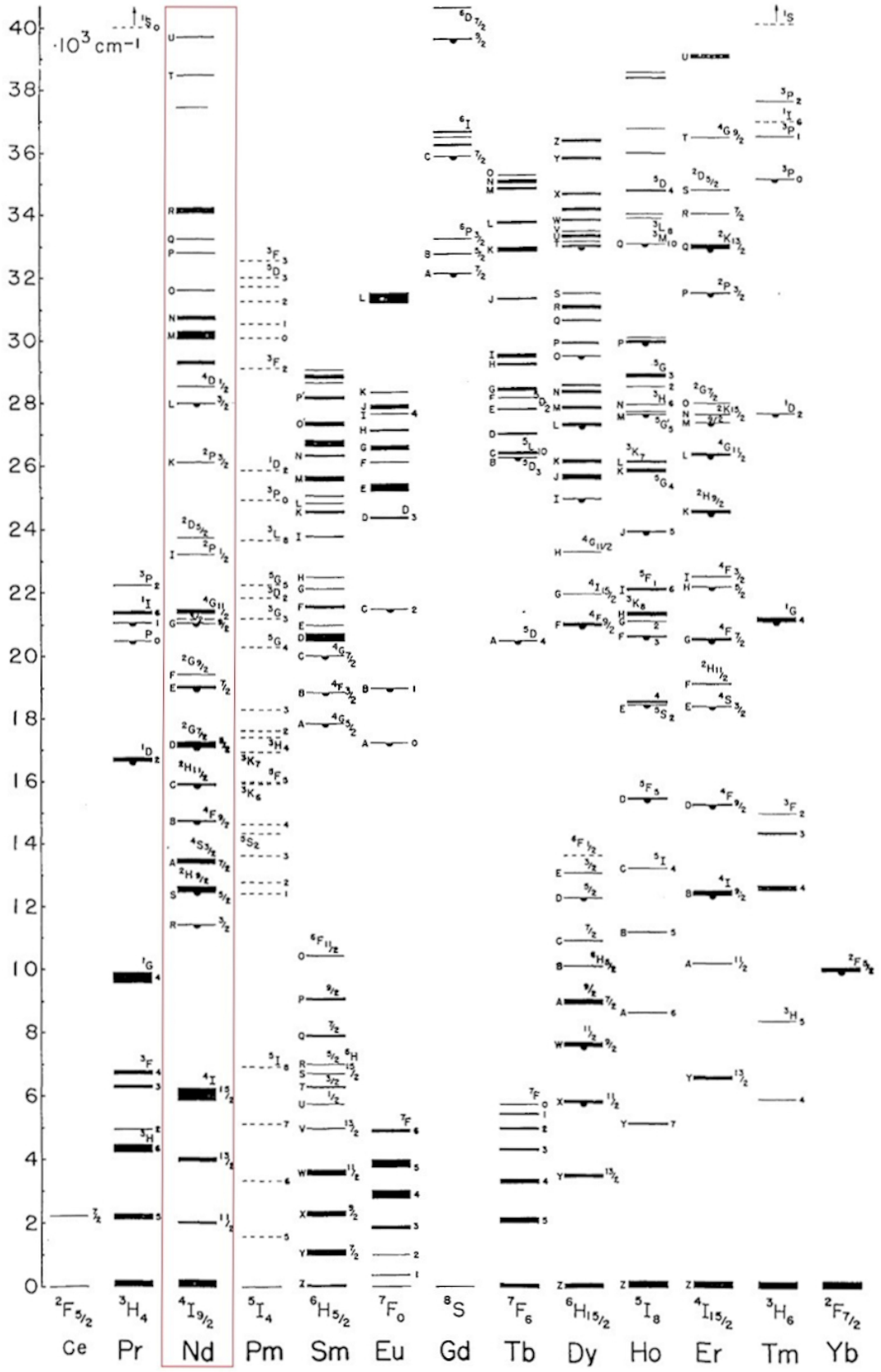

FIGURE 2.4: Dieke's chart with the energy levels of neodymium highlighted in red [72].

collected for a fixed emission wavelength, tuning the pump wavelength. The comparison between the excitation spectrum and the absorption spectrum, allows to study the emission efficiency as a function of the absorption wavelength. In absence of ground state depletion or strong upconversion processes the excitation spectrum will have the same shape as the absorption spectrum provided than only one type of emitting site is present in the sample. However, if multiple sites coexist and have different emission efficiency, the bands and shapes of the excitation spectrum will display differences with the absorption spectrum.

In the specific case of this work, the luminescence and excitation spectroscopy measurements are performed exciting the samples with a coherent 890 tunable Ti:Sapphire laser, pumped with a Verdi V6 visible laser. The emitted light is collected with a HRS2 Jobin-Yvon monochromator with 0.2 nm spectral resolution, equipped with an Hamamatsu R5108 photomultiplier tube.

Concerning the luminescence measurements, it is necessary to consider the spectral response of the detector, the monochromator, the mirror, lenses and filters. The easiest way to take into account for all the elements of the setup is to measure directly the transmittivity $T(\lambda)$ of the setup. In fact, the real luminescence of the crystal is given by

$$I_{real}(\lambda) = I_{recorded}(\lambda)/T(\lambda) \tag{2.4}$$

where $I_{recorded}(\lambda)$ is the recorded luminescence. It is possible to measure the spectrum of a blackbody lamp $I_{lamp}(\lambda)$ and calculate $T(\lambda)$ from the very well known Planck's law

$$I_{BB}(\lambda) = \frac{2\pi hc}{\lambda^5}\frac{1}{\exp(hc/\lambda k_B T) - 1} \tag{2.5}$$

with h the Planck's constant, c the speed of light, k_B the Boltzmann's constant and T the temperature. Thus, the transmittivity $T(\lambda)$ can be obtained as

$$T(\lambda) = I_{lamp}(\lambda)/I_{BB}(\lambda) \tag{2.6}$$

In the specific case of this work, a 20 W tungsten lamp is used as a blackbody lamp which spectrum resembles the black body spectral shape , as displayed in Figure 2.5.

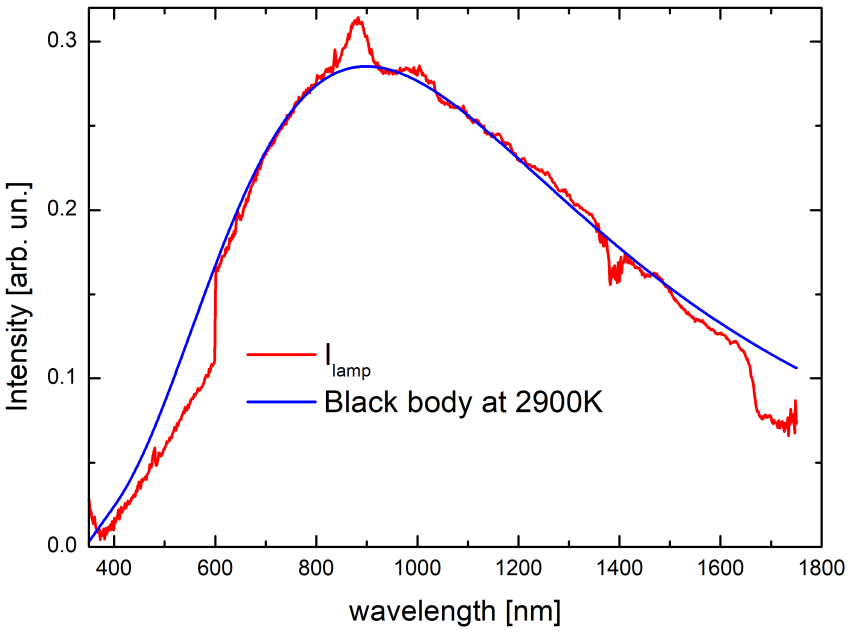

FIGURE 2.5: Spectrum of the 20 W tunsgten lamp corrected with the tungsten emissivity, compared with the Planck's law.

2.2.4 Energy Level Lifetime

The fluorescence lifetime of any given energy level can be measured exciting the sample at an absorption wavelength with a pulsed monochromatic source and collecting the emission intensity decay. In this work, fluorescence lifetimes are recorded with a 77200 Oriel monochromator combined with a Hamamatsu R5108 photomultiplier tube exciting the crystals with a Continuum Horizon optical parametric oscillator pumped by a Continuum Surelite frequency tripled Nd^{3+} : YAG pulsed laser at 355 nm.

This measurement is critical to obtain the excited level transition probability, which by definition is $1/\tau_f$ where τ_f is the fluorescence lifetime. In the simplest case, the intensity decay $I(t)$ is a single-exponential, so it can be fitted with the following equation

$$I(t) = I_0 \exp\Big(-\frac{t}{\tau_f}\Big) \tag{2.7}$$

where I_0 is the fluorescence intensity at $t = 0$. However, in some cases the lifetime does not follow a single exponential behavior. In this case, it is common to fit the signal with a double exponential function as follows:

$$I(t) = A \exp\Big(-t/\tau_1\Big) + B \exp\Big(-t/\tau_2\Big) \tag{2.8}$$

where A, B, τ_1 and τ_2 are the fitting parameters. It is however complicated to interpret the physical meaning of τ_1 and τ_2: the presence of a double exponential decay is not sufficient to prove the presence of two distinct active sites. In fact non-single-exponential decays may be due to direct energy transfer process [76].

A solution to this problem is to define the fluorescence lifetime as

$$\tau_f = \frac{1}{I_0} \int_0^\infty I(t) \mathrm{d}t \tag{2.9}$$

The estimation of the lifetimes, together with the knowledge of the absorption, luminescence and excitation spectroscopy, provides meaningful information to distinguish one emitting center from another.

The comparison between the fluorescence lifetime and the radiative lifetime enables to estimate the quantum efficiency of a given emitting level. Moreover the Füchtbauer-Ladenburg equation 2.3, shows that a precise knowledge of the radiative lifetime is necessary to derive the stimulated emission cross-section. The radiative lifetime for a given manifold is defined as [77]:

$$\tau_{rad} = \frac{1}{\sum_j A_{i,j}} \tag{2.10}$$

where $A_{i,j}$ are the radiative transition rates from a given energy level to all the underlying energy levels. An estimation of the radiative lifetime can be performed using the Judd-Ofelt analysis [78, 79].

2.3 Judd-Ofelt Theory

The Judd-Ofelt theory is a model describing the radiative rates of lanthanide and actinide transitions in solids and solutions and is formulated assuming the system as static via a mean-field approach, considering all ions as surrounded by an electrostatic field due to the host matrix crystal field. Ions are considered as free, and the electrostatic field is modeled as a first order perturbation to the free ion Hamiltonian.

2.3.1 General Aspects

According to the Laporte's selection rule [80], electrical dipole (ED) transitions are forbidden between wavefunctions having the same parity, for instance between states within the $4f$ shell. Nevertheless, rare earths exhibit sharp and intense spectral lines, indicating the contrary, since magnetic dipole (MD) transitions cannot explain all the observed transitions, and quadrupole transitions are too weak to explain the high intensities observed

[81]. The explanation lies in the fact that if the atom is placed in a non-centrosymmetric field, the odd part terms of the crystal field mixes the 4fn configuration with excited configuration such as 4fn-15d having an opposite parity, thus mitigating the Laporte's rule . More formally, considering initial and final mixed-parity states, $\langle\psi_a|$ and $|\psi_b\rangle$, and V being the operator that mixes the configurations, following the treatment developed by Walsh [82]:

$$\begin{cases} \langle\psi_a| = \langle\psi_a| + \sum_\beta \frac{\langle\phi_a|\hat{V}|\phi_\beta\rangle}{E_a - E_\beta} \langle\phi_\beta| \\ |\psi_b\rangle = |\psi_b\rangle + \sum_\beta \frac{\langle\phi_\beta|\hat{V}|\phi_b\rangle}{E_b - E_\beta} |\phi_\beta\rangle \end{cases} \tag{2.11}$$

where $\langle\phi_a|$ and $|\phi_b\rangle$ are the initial and final states of the 4 f configuration, while ϕ_β are states of the higher energy opposite parity configuration. It is then possible to evaluate the ED matrix element D for any transition as

$$D = \langle\phi_a|\,\hat{P}\,|\phi_b\rangle = \sum_\beta \left[\frac{\langle\phi_a|\,\hat{V}\,|\phi_\beta\rangle\,\langle\phi_\beta|\,\hat{P}\,|\phi_b\rangle}{E_a - E_\beta} + \frac{\langle\phi_a|\,\hat{P}\,|\phi_\beta\rangle\,\langle\phi_\beta|\,\hat{V}\,|\phi_b\rangle}{E_b - E_\beta} \right] \tag{2.12}$$

with $\hat{P}$ the electric dipole operator defined as

$$\hat{P} = -e \sum_i \hat{r}_i \tag{2.13}$$

and considering the ED transitions forbidden between states of the same parity, $\langle\phi_a|\,\hat{P}\,|\phi_b\rangle = 0$ and $\langle\phi_\beta|\,\hat{P}\,|\phi_\beta\rangle = 0$.

At this point, two main assumptions can be suggested to simplify the problem, that are moderately met for most rare earth ions:

- the energy of excited configurations above the $4f^{(n)}$ is taken as an average, meaning that all the states ϕ_β are completely degenerate in total angular momentum J
- the energy gap between the $4f$ energy levels and the excited configuration is constant ($E_a - E_\beta = E_b - E_\beta$)

These offer great simplifications, allowing to remove the denominators in eq. (2.12) from the sum and using the closure, $|\phi_\beta\rangle\,\langle\phi_\beta| = 1$, that expresses the fact that the states of the excited state configurations form a complete othonormal sets of wavefunctions. The details of the calculations can be found in the work of Walsh [82].

In the case of indistinguishable Stark levels, a major simplification can be performed, adding two more assumptions:

- all Stark levels within a manifold are equally populated
- the material is optically isotropic

The oscillator strength f is defined for ED transitions as

$$f = \frac{8\pi^2 m_e c}{h\bar{\lambda}e^2} n \left(\frac{n^2+2}{3n}\right)^2 \sum_{MM'} |\langle \alpha JM| \hat{P} |\alpha' J' M'\rangle|^2 \tag{2.14}$$

with m_e the electron mass, c the speed of light in vacuum, h the Planck's constant, e the elementary electric charge, n the material's refractive index and $\bar{\lambda}$ the mean wavelength of the transition. With the four assumptions detailed earlier, Judd and Ofelt gave an expression of the oscillator strength [82, 83]:

$$f = \frac{8\pi^2 m_e c}{3h\bar{\lambda}(J+1)} n \left(\frac{n^2+2}{3n}\right)^2 \sum_{\lambda=2,4,6} \Omega_\lambda |\langle \phi_a| U^{(\lambda)} |\phi_b\rangle|^2 \tag{2.15}$$

where J is the total angular quantum number of the initial manifold, and Ω_λ are the so-called Judd-Ofelt parameters. Eq. (2.15) represents the approximate solution of the J-O theory. In principle, is it possible to calculate the Ω_λ ab-initio, but it is a lot easier to treat them as phenomenological parameters, that can be determined from the fitting of experimental absorption measurements with the theoretical expression. The procedure to determine the three Ω_λ parameters and to derive from them the radiative parameters is described in the following section.

2.3.2 Application of the J-O Theory

In practice, the determination of the J-O parameters Ω_λ relies on the experimental measurement of absorption cross sections σ_{abs}, integrated in wavelength over the various transitions. In fact, the linestrength S_m of a transition m can be obtained from

$$S_m = \frac{3ch(2J+1)}{8\pi^3 e^2 \bar{\lambda}} n \left(\frac{3}{n^2+2}\right) \int_m \sigma_{abs} \mathrm{d}\lambda \tag{2.16}$$

where

$$\bar{\lambda} = \frac{\int \lambda \sigma_{abs}(\lambda) \mathrm{d}\lambda}{\int \sigma_{abs} \mathrm{d}\lambda} \tag{2.17}$$

and compared to the approximate solution of the J-O formalism, that states

$$S_j = \sum_{i=1}^{3} M_{ij} \Omega_{2i} \tag{2.18}$$

where M_{ij} are the matrix elements expressed explicitly in eq. (2.15). Note these matrix elements only depend on the rare earth ion and do not depend on the host, and it is possible to calculate them manually or find them in literature.
At this point, it is possible to estimate the J-O parameters via a least-squares

fitting method, comparing eq. (2.16) and (2.18). Defining the squared difference Σ^2 as

$$\Sigma^2 = \sum_{j=1}^{N} \left(S_j - \sum_{i=1}^{3} M_{ij}\Omega_{2i} \right)^2 \tag{2.19}$$

the minimizing condition is written for $\lambda = 2, 4, 6$ as

$$\frac{\partial \Sigma^2}{\partial \Omega_\lambda} = 0 \tag{2.20}$$

which leads to

$$\sum_{j=1}^{N} M_{ij} \left(S_j - \sum_{i=1}^{3} M_{ij}\Omega_{2i} \right) = 0 \tag{2.21}$$

Once the J-O parameters Ω_λ are determined, they can be used to calculate the transition probabilities (from the linestrength) as

$$A(J, J') = \frac{64\pi^4 e^2}{3h(2J'+1)\bar{\lambda}^3} \left[n \left(\frac{n^2+2}{3} \right)^2 S_{ED} + n^2 S_{MD} \right] \tag{2.22}$$

where S_{ED} and S_{MD} are the ED and MD linestrengths respectively. The MD transition only occurs provided that it satisfies the selection rule : $\Delta J = 0, \pm 1$.

With the knowledge of the transition probability it is possible to calculate the radiative lifetime τ_{rad} and branching ratios $\beta_{J',J}$.

$$\begin{cases} \frac{1}{\tau_{rad}} = \sum_J A(J', J) \\ \beta_{J',J} = \frac{A(J',J)}{\sum_J A(J',J)} \end{cases} \tag{2.23}$$

2.3.3 J-O applied to the Neodymium Ion

The Judd-Ofelt analysis requires the calculation of the matrix elements M_{ij} given by

$$M_{ij} = |\langle \phi_a | U^{(\lambda)} | \phi_b \rangle|^2 \tag{2.24}$$

as expressed explicitly in eq. (2.15). This calculation has been performed several times in the literature for Nd^{3+} ion and some examples are represented by the work of Carnall [84, 85] and Kaminksii [86]. Some of those matrix elements can be equal to zero or negligible. In the case of Nd^{3+}, Ω_2 is determined only by the transition $^4I_{9/2} \rightarrow {}^4G_{5/2} + {}^2G_{7/2}$ since the corresponding square matrix element M_{ij} is equal to 0.974 while the matrix elements for all the other transitions are less than 0.05 [84, 87]. Since Ω_2 is determined by only two absorption bands, it is statistically less reliable, bringing the uncertainty specifically on this parameter even to 50%, as evidenced on

Nd : YAG [88]. Fortunately, in the calculation of the $^4F_{3/2}$ radiative rate the parameter Ω_2 has no role, since the $U^{(2)}$ matrix elements M_{ij} for the transitions $^4F_{3/2} \rightarrow {}^4I_{J'}$ is equal to zero. Thus, the $^4F_{3/2}$ radiative rate estimate only depends on Ω_4 and Ω_6. The uncertainty on the calculation of the $^4F_{3/2}$ radiative lifetime can be considered as typical for any Judd-Ofelt analysis, that is a reliability of $10\% - 20\%$ and the $^4F_{3/2}$ radiative lifetime is expected to be roughly similar in any lattice within a factor of 2 [88].

2.4 Co-doping with One Buffer: $CaF_2 : Nd^{3+}, Bu^{3+}$

In this section the results of the co-doping of CaF_2 : 0.5%Nd with one buffer (Bu) ion will be presented. Firstly the investigation will be focused on gadolinium, lanthanum, cerium, yttrium, lutetium and scandium. Those buffers are the six buffers selected in the first place, Figure 2.6, according to the three criteria presented in Chapter 1:

- trivalent valence state
- size as close as possible to the Nd^{3+} ion
- optically non-active in the visible and infrared range

The six crystals grown are $CaF_2 : 0.5\%Nd^{3+}, 5\%Bu^{3+}$, with $Bu = (Gd, La, Ce, Y, Lu, Sc)$. The neodymium doping level is kept as constant at 0.5at.%, and the co-dopant level at 5at.%

2.4.1 $Gd^{3+}, La^{3+}, Ce^{3+}, Y^{3+}, Lu^{3+}, Sc^{3+}$ Co-Doping

The absorption spectra of $CaF_2 : 0.5\%Nd^{3+}, 5\%Bu^{3+}$, with $Bu = (Gd, La, Ce, Y, Lu, Sc)$ is reported in Figure 2.7 around 790 nm, corresponding to the $^4I_{9/2} \rightarrow {}^4F_{5/2}$ transition.

Figure 2.6 displays the ionic radius for the six trivalent buffer ions for a coordination number equal to 8 [89]. This coordination number of 8 is close to what has been found by EXAFS measurements where Ma et al. showed that the coordination number in CaF_2 co-doped with Nd^{3+} and Y^{3+} ions actually reaches 9 [53]. Figure 2.6 shows that three buffer ions (Y^{3+}, Lu^{3+} and Sc^{3+}) are clearly smaller than the Nd^{3+} ion (radius = 110 pm) while the other buffer ions are larger or of the same size as Nd^{3+} such as Gd^{3+}. It is clear from the absorption spectra (figure 2.7) that in samples with large buffer ions, namely 5%Gd, 5%La and 5%Ce, the most intense peak appears around 791 nm. In crystals doped with smaller ions, namely 5%Y, 5%Sc and 5%Lu, a more prominent peak appears around 797 nm. This suggests the division of the buffer co-dopants in two different groups and indicates a correlation between the ionic radius and the spectroscopic properties. The fluorescence spectra of the $^4F_{3/2} \rightarrow {}^4I_{11/2}$ transition for the different co-doped crystals,

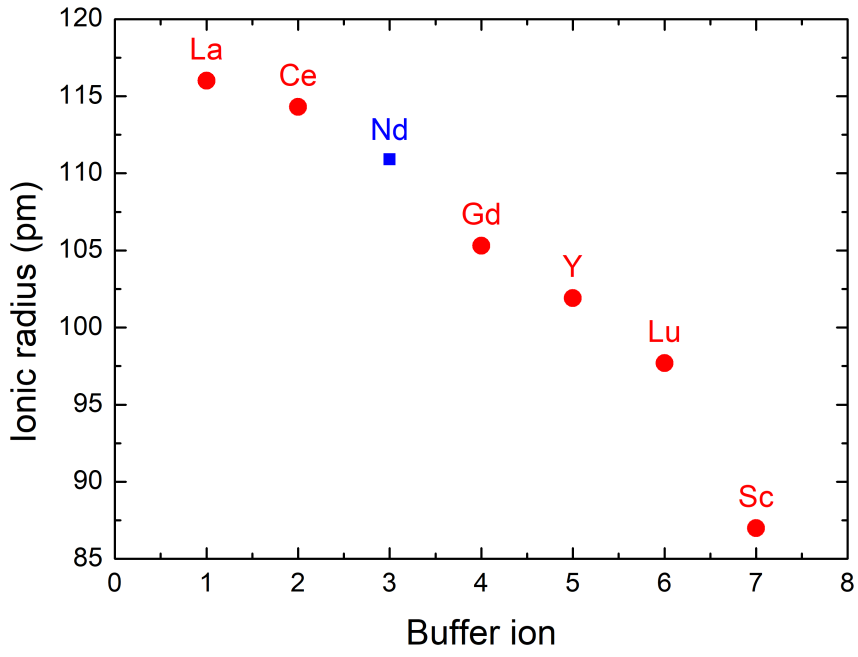

FIGURE 2.6: Ionic radius of the buffer ions chosen to perform the optical spectroscopy study on $CaF_2 : Nd, Bu$.

exciting at 797 nm ($^4I_{9/2} \rightarrow {}^4F_{5/2}$ transition) are shown in Figure 2.8 (a) and confirm the remarks made from the absorption spectra. In fact, the 5%Gd, 5%La and 5%Ce (large buffer ions) doped samples exhibit two main peaks around 1050 and 1065nm while for the 5%Y, and 5%Lu co-doping the main peak is around 1054 nm. As for the Sc co-doped crystal, it exhibits a peculiar emission spectrum with a main peak at 1060 nm.

The excitation spectra with a detection wavelength fixed at 1054 nm presented in Figure 2.8 (b) confirm the similarity between the 5%Y, 5%Sc and 5%Lu doped crystals with a similar main peak at 797 nm. This peak is not prominent in the three other co-doped crystals that clearly belong to the same group of large buffer ions.

As mentioned earlier, two types of active centers, quasi-rhombic labeled N_1 and quasi-tetragonal labeled N_2 have been identified in both Y^{3+} and Lu^{3+} co-doping [40]. In order to clarify this double site nature in all co-dopings, we recorded the emission spectra when exciting the samples at the two characteristic wavelengths identified in absorption and excitation spectra, namely 791 nm and 797 nm. As expected, the emission spectrum changes drastically in the small buffer ions group (Y^{3+}, Sc^{3+} and Lu^{3+}) as illustrated in Figure 2.9 (b) for the 5%Y co-doped sample . We observe for this sample a rise of a peak at 1054 nm characteristic of the N_2 centre when exciting at 797 nm and on the contrary a main peak at 1049 nm characteristic of the N_1 centre when exciting at 791 nm. In comparison the emission spectrum for the group of large buffer ions (5%Gd, 5%La and 5%Ce) exhibits

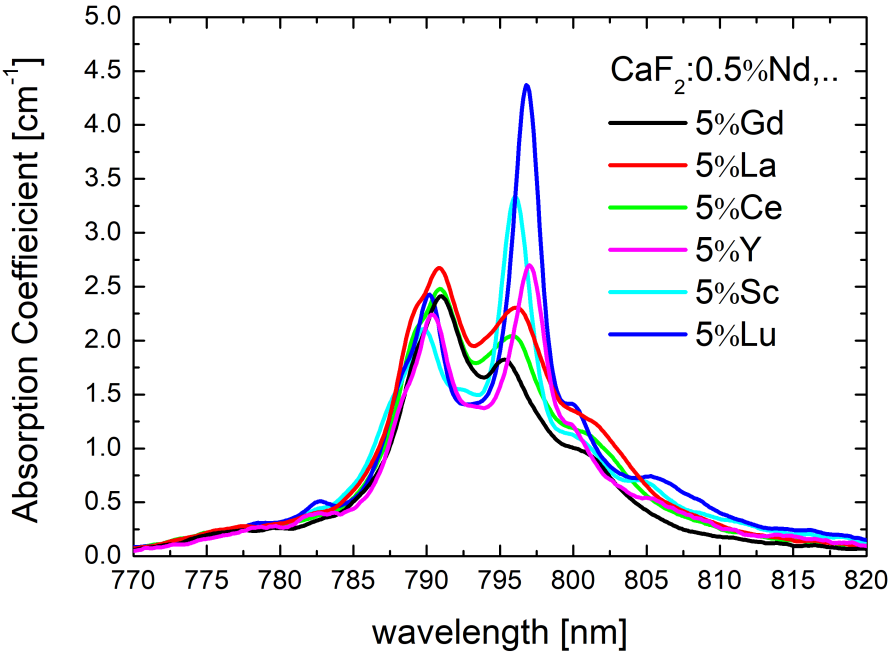

FIGURE 2.7: Absorption coefficient of $CaF_2 : 0.5\%Nd^{3+}, 5\%Bu^{3+}$, with Bu = (Gd,La,Ce,Y,Lu,Sc)

little change when changing the excitation wavelength as shown in Figure 2.9 (a) for the Gd^{3+} codoping.

As a result, the co-doped samples can be convincingly divided in two groups where small buffer ions clearly show the presence of the two Nd incorporation sites labeled N_1 and N_2 while larger buffer ions exhibit one predominant site.

The same behavior can be further confirmed by excitation spectroscopy, comparing the same two crystals for two detection wavelengths at 1049 nm and 1054 nm. As reported in Figure 2.10, the excitation spectrum recorded at 1054 nm is characterized by a peak at 797 nm in the Y co-doped crystal, proof again of the N_2 center. On the other hand, the spectra of the Gd co-doped crystal recorded at 1049 nm and 1054 nm are similar and are comparable in shape with the spectrum of the Y co-doped crystal detected at 1049 nm since they both exhibit a main peak at 791 nm. As mentioned earlier, this excitation peak at 791 nm is characteristic of the quasi-rhombic N_1 center.

To summarize the co-doping with a large buffer ion such as gadolinium, lanthanum and cerium, gives rise to a predominant quasi-rhombic N_1 site while the co-doping with a smaller buffer ion, such as yttrium, lutetium and scandium shows emission from two Nd sites: a similar quasi-rhombic N_1 site and a quasi-tetragonal N_2 site.

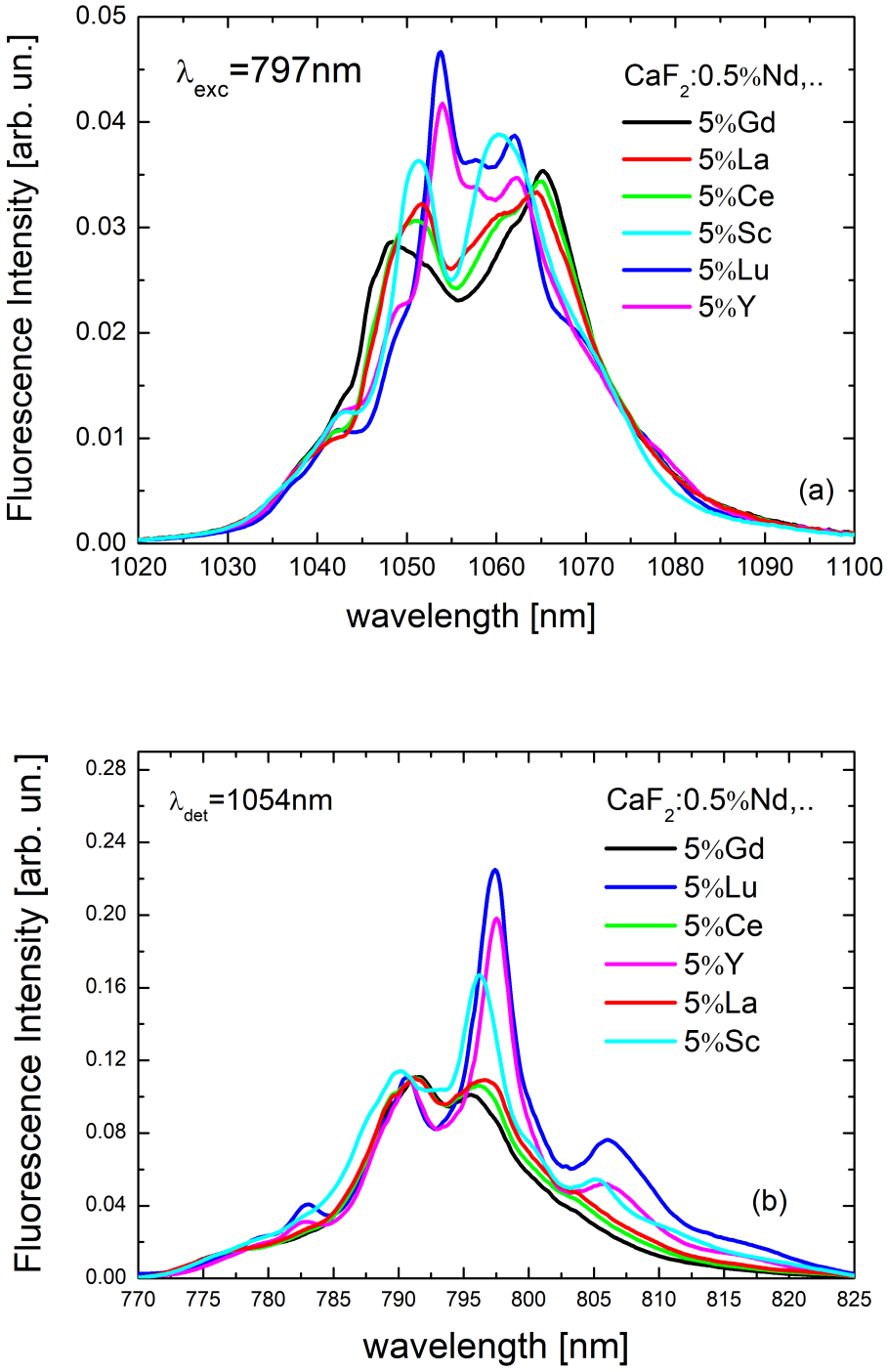

FIGURE 2.8: (a) Luminescence spectra of $CaF_2 : 0.5\%Nd^{3+}, 5\%Bu^{3+}$, with $Bu = (Gd, La, Ce, Y, Lu, Sc)$ with excitation wavelength 797 nm. (b) Excitation spectra with detection wavelength of 1054 nm.

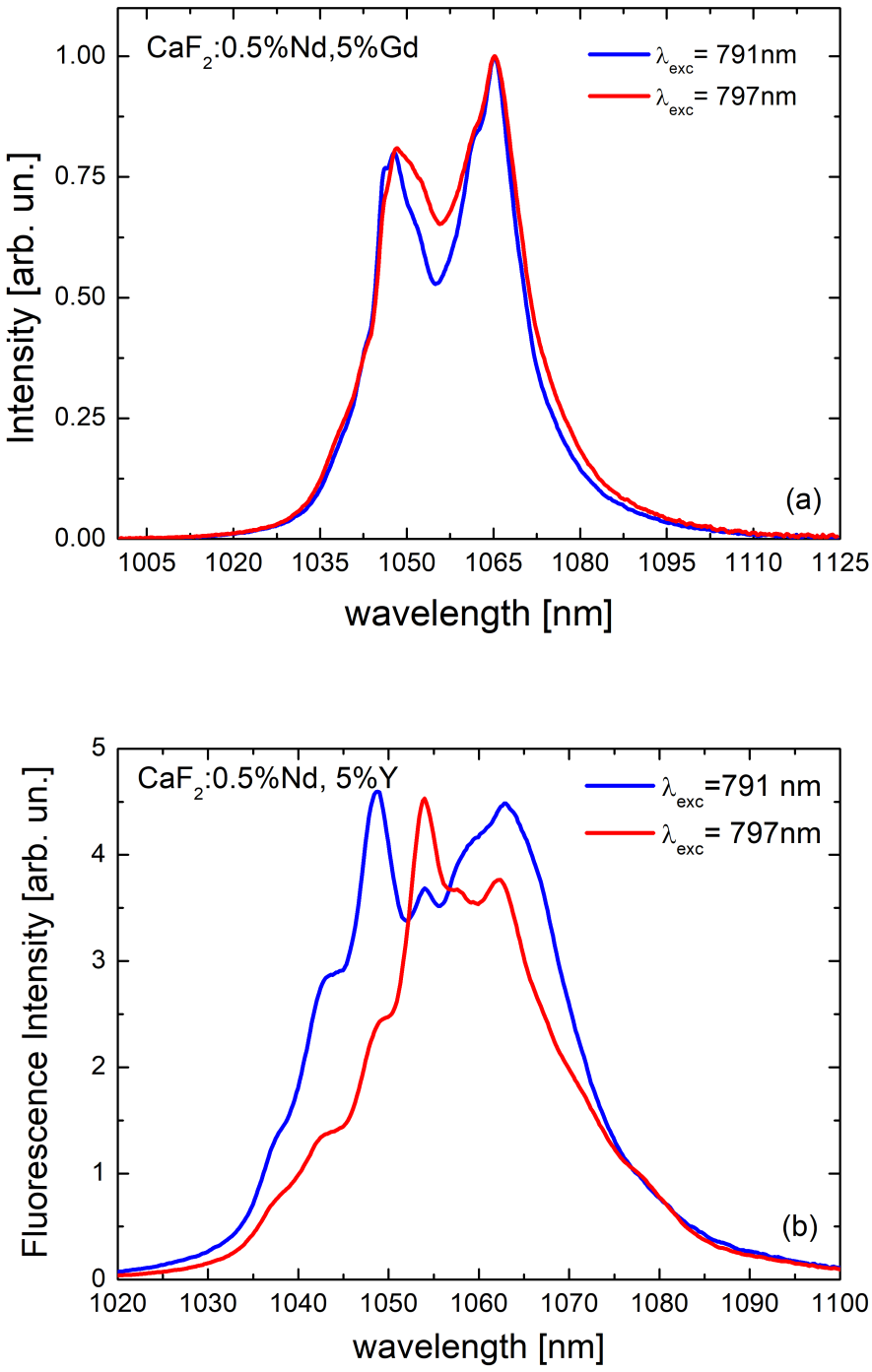

FIGURE 2.9: Luminescence spectra of $CaF_2 : Nd, Gd$ (a) and $CaF_2 : Nd, Y$ (b), excited at 791 nm (blue) and 797 nm (red)

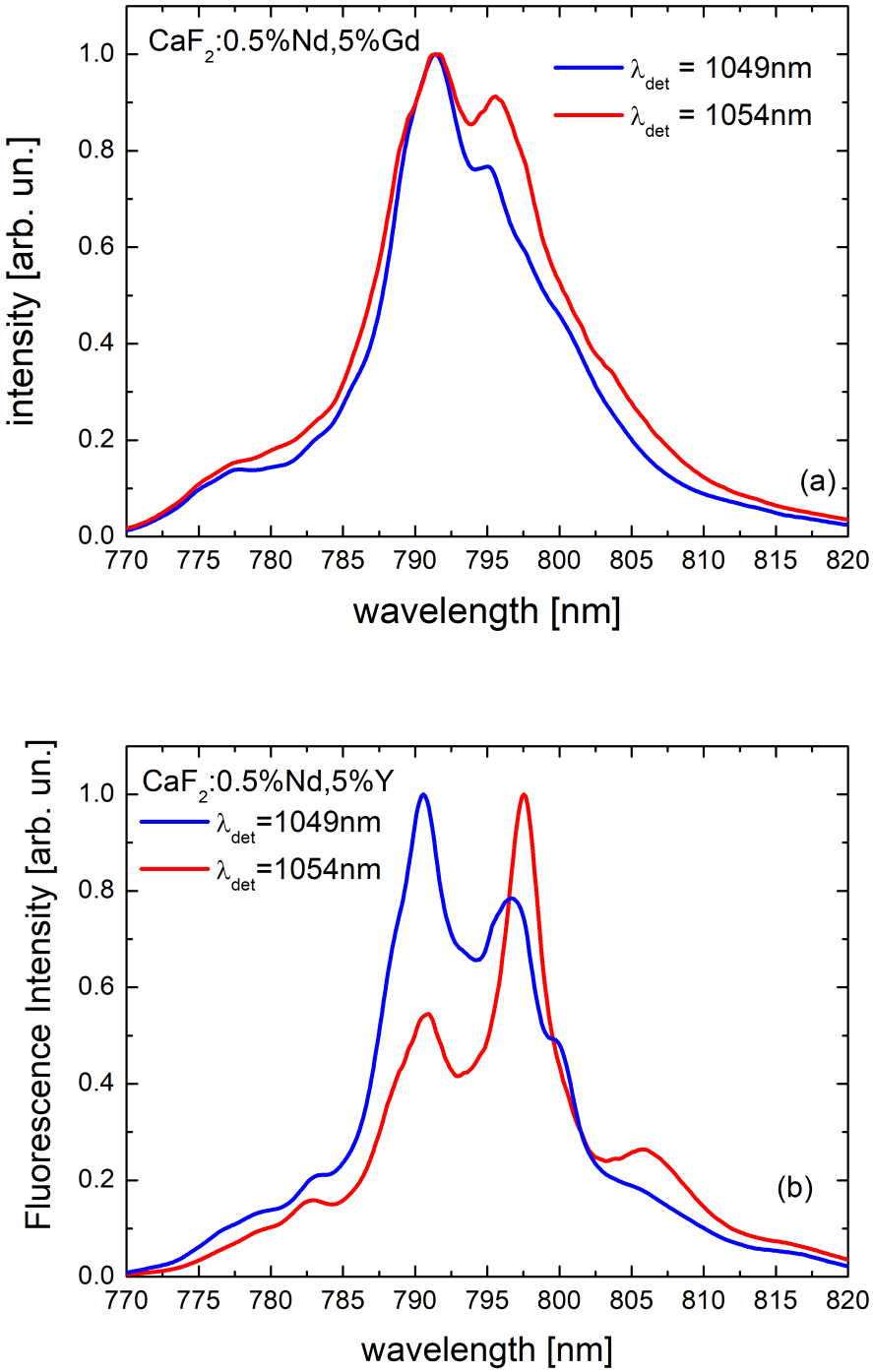

FIGURE 2.10: Excitation spectra of $CaF_2 : Nd, Gd$ (a) and $CaF_2 : Nd, Y$ (b), excited at 1049 nm (black) and 1054 nm (red)

The two sites N_1 and N_2 can be distinguished clearly using their characteristic couple of excitation-emission wavelengths, i.e. 791 nm − 1049 nm for N_1 and 797 nm − 1054 nm for N_2.

The correlation between the trivalent ion radius and the rare-earth (RE^{3+}) clusters in CaF_2 has been investigated theoretically by looking at the stability of different types of clusters [90]. The charge compensation of trivalent ions replacing Ca^{2+} divalent cation is ensured by interstitial F^- ions. The small ionic radius of the dopant allows extensive relaxation of the dopant ion within its incorporation site and therefore the creation of different types of clusters depending on the relative position of the dopant. On the opposite large buffer ions will tend to occupy a specific position and will create only one type of cluster. In the small buffer group Sc^{3+} occupies a peculiar place as it exhibits a quite different emission spectrum (Figure 2.8 (a)). The reason for this particular shape is most likely connected to its smaller radius of 89 pm, when compared to the other small buffers like Y^{3+} or Lu^{3+} that have larger ionic radius of 102 pm and 98 pm, respectively. When the buffer ionic radius becomes very small, it will induce not only a displacement of the buffer ion itself from its generally accepted position, but it will cause also a displacement of the corresponding F^- interstitial ions, which will come closer to the buffer ion within a distorted cluster [90]. This inward movement of the F^- interstitial ions will increase the Coulomb interaction between the trivalent buffer ion and the F^- interstitials increasing the cluster stability. This change in the cluster geometry will in turn change the corresponding local crystal field and thus the Stark sublevels energy and the fluorescence spectral shape.

As expected, the excitation spectra (Figure 2.10) and the absorption spectra (Figure 2.7) share a very similar shape. Nevertheless, one can observe differences in particular for the small buffer ions. As illustrated in Figure 2.11 (b) for the yttrium co-doping, the absorption spectrum shows a much more pronounced absorption peak at 791 nm in comparison with the excitation spectrum while the two spectra are similar for large buffer ions such as the gadolinium co-doping. This difference is associated with the fact that the excitation spectra are recorded at 1054 nm which is the characteristic emission peak for the N_2 site. Therefore, the excitation spectrum reflects primarily the N_2 site absorption spectrum lineshape, with a predominant excitation peak at 797 nm while the absorption spectrum (Figure 2.7) comprises absorption spectra of both N_1 and N_2 sites. For large buffer ions, the existence of just one dominant N_1 site explains the resemblance between absorption and excitation spectra (Figure 2.11 for Gd^{3+}).

To further investigate the N_1 and N_2 sites in crystals with small buffer ions such as $CaF_2 : 0.5\%Nd, 5\%Y$, we recorded the emission spectra around 1050 nm (Figure 2.13) by tuning the excitation wavelength between 791 nm and 797 nm with a 1 nm step. Here it is possible to observe that while between 791 nm and 795 nm the fluorescence spectral shape does not change

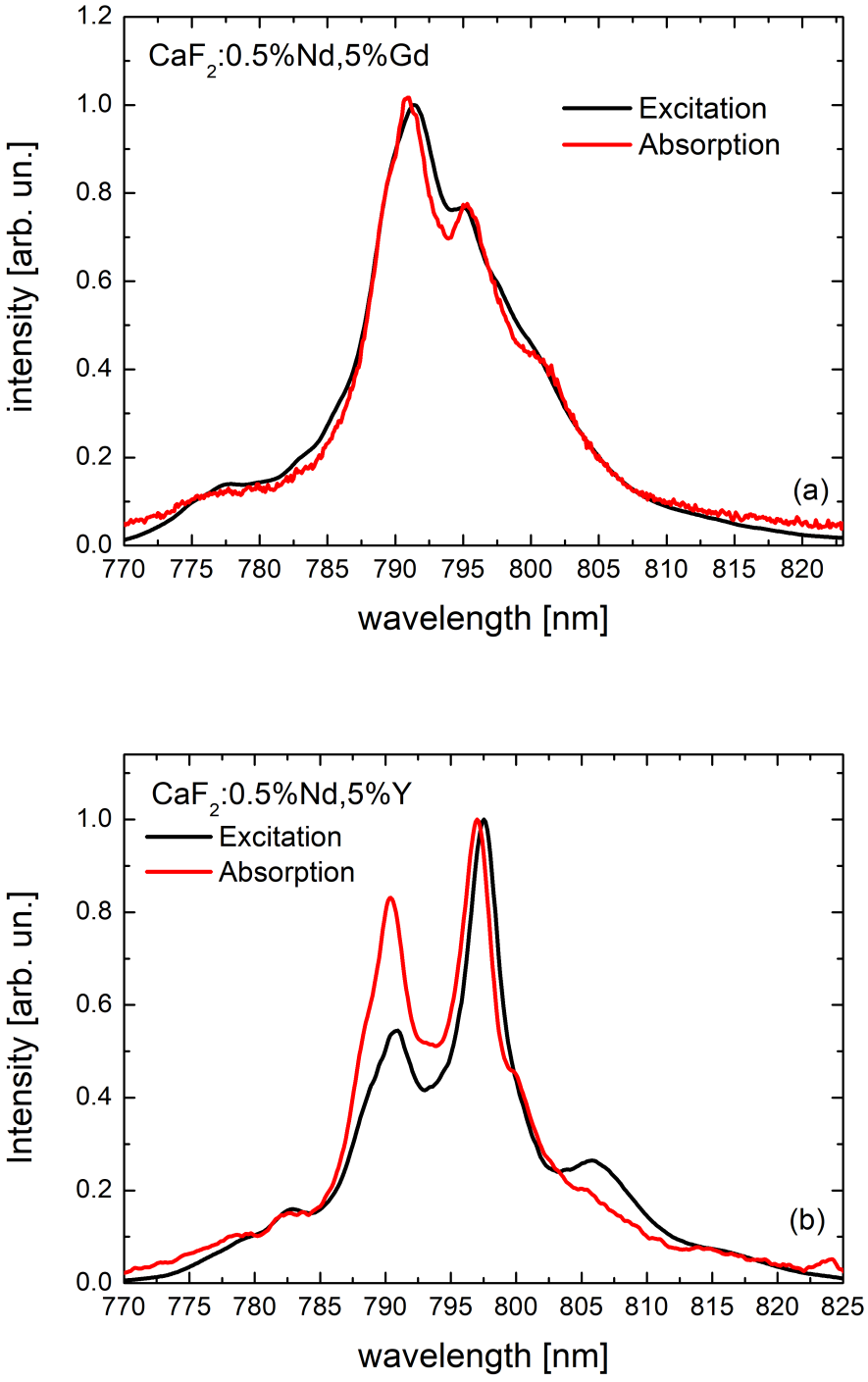

FIGURE 2.11: Comparison lineshape absorption (red) and lineshape excitation spectra (black) for $CaF_2 : Nd, Gd$ (a) and $CaF_2 : Nd, Y$ (b)

drastically, between 795 nm and 791 nm the spectral shape changes dramatically with the rise of the 1054 nm peak and the reduction of the 1049 nm line, illustrating the dominance of the N_2 emission over N_1.

The sudden change can be understood with the calculation of the absorption coefficient in $CaF_2 : Nd, Y$ for the two different sites. The excitation spectra in Figure 2.10 recorded at 1049 nm and 1054 nm are first considered as representing N_1 and N_2 absorption coefficient spectra respectively since these wavelengths are characteristic of each center. Then, the linear combination of these two excitation spectra is compared with the absorption coefficient spectrum of the $CaF_2 : Nd, Y$ crystal 2.7. As reported in Figure 2.12 (a), the linear combination of excitation spectra matches the absorption spectrum.

The coefficients found for this linear combination represent the respective integrated absorption coefficient of both centers following the expression:

$$\alpha(\lambda) = g_1(\lambda) \int \alpha(N_1, \lambda) d\lambda + g_2(\lambda) \int \alpha(N_2, \lambda) d\lambda \tag{2.25}$$

being $g_1(\lambda)$ and $g_2(\lambda)$ the normalized lineshape factors of the excitation spectra of N_1 and N_2 respectively, defined as

$$g_i(\lambda) = \frac{I_i(\lambda)}{\int I_i(\lambda) d\lambda} \tag{2.26}$$

for $i = 1, 2$.

The two terms in equation 2.25 represent the absorption coefficient of N_1 and N_2. Thus, it is possible to obtain the absorption coefficients of the two centers N_1 and N_2 separately. Those are displayed in Figure 2.12 (b), where it is possible to observe that in the 791 nm to 795 nm interval, the absorption coefficient is about the same for both centers meaning that the pump power is equally absorbed by the two centers. This explains in turns why the emission spectrum does not change much in this spectral range . However, in the 795 nm to 797 nm regime, the absorption coefficient of the N_2 site increases dramatically, reaching 1.8 cm^{-1}, while the absorption coefficient of the N_1 site is staying around 0.9 cm^{-1}. The drastic difference in the absorption coefficient of the N_2 site explains the rapid change in the lineshape of the luminescence which is dominated by the N_2 site at 797 nm (Figure 2.13).

The investigation of the $^4F_{3/2}$ energy level decay further supports the above conclusions. For this purpose, the $^4F_{3/2}$ fluorescence lifetime of all $CaF_2 : Nd, Bu$ was recorded exciting at 791 nm and detecting at 1049 nm, the excitation-emission wavelengths associated with N_1, and exciting at 797 nm and detecting at 1054 nm, the excitation-emission wavelengths associated with N_2. It is clear from Figure 2.14, where the decay curves of $CaF_2 : Nd, Gd$ and $CaF_2 : Nd, Y$ are reported, that while for the gadolinium co-doped sample the two lifetimes are very close to each other around 400 μs, for the yttrium co-doped crystal two very different lifetimes for the two centers are recorded: a longer one around 440 μs for the N_1 site, and

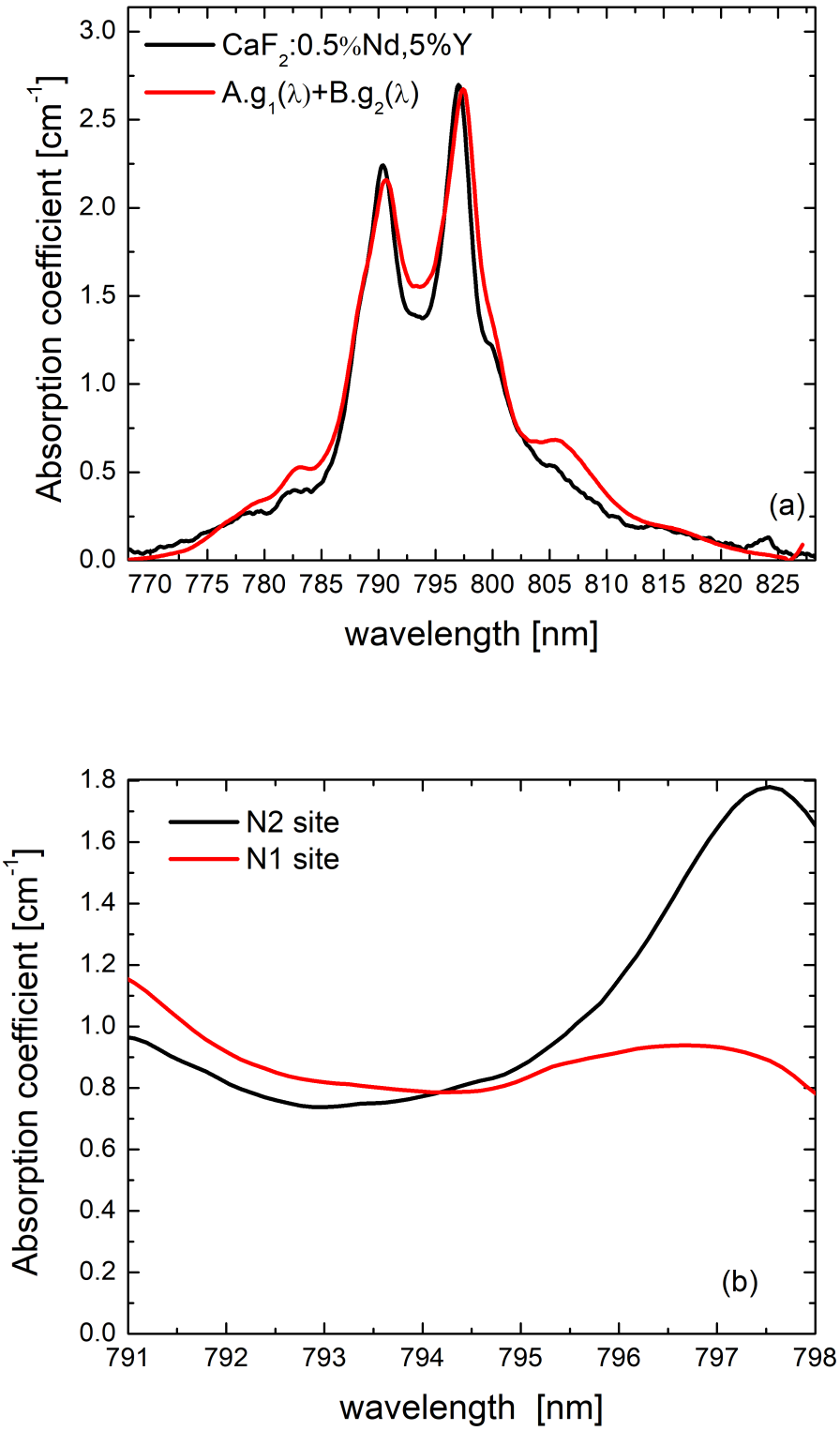

FIGURE 2.12: (a) Experimental absorption coefficient of $CaF_2 : Nd, Y$ (black) compared with a reconstruction of it (red) obtained from a linear combination of the lineshape of the excitation spectra recorded at 1049 nm and 1054 nm. (b) Absorption coefficient of the N_1 and N_2 sites separately.

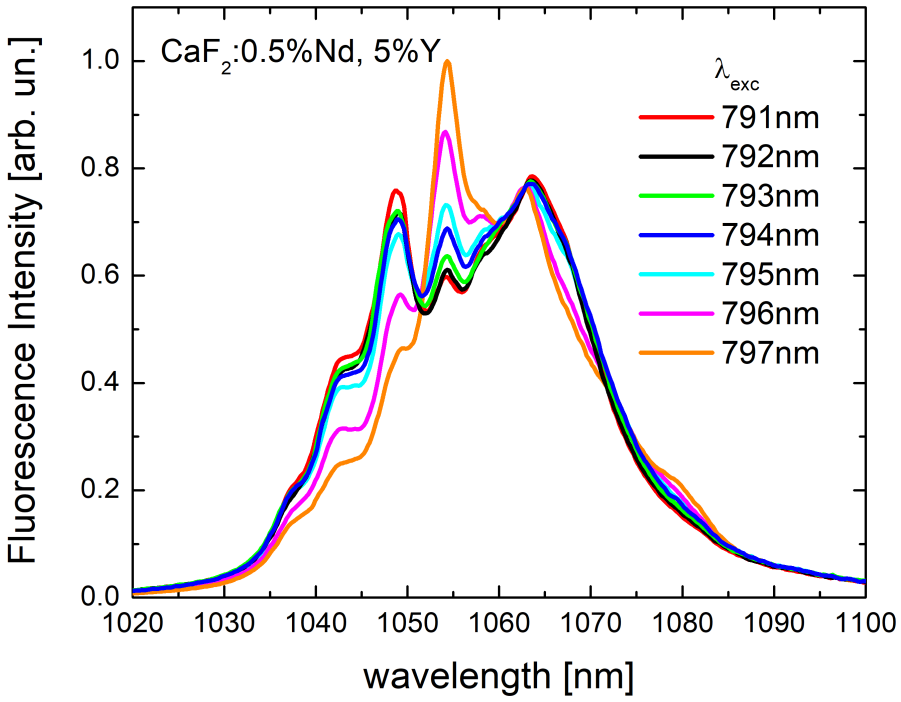

FIGURE 2.13: Luminescence spectra of $CaF_2 : Nd, Y$ tuning the excitation wavelength from 791 nm to 797nm with a 1 nm step.

a faster one around 352 μs for the N_2 site. This further corroborates the existence of two different sites N_1 and N_2 for small buffer ions and one dominant N_1 site for larger buffer ions.

It is worth mentioning that the decay curves are not single-exponential since different clusters are present in all samples but only one is dominant for the Gd, La and Ce co-dopings, while two main clusters coexist for the Y, Lu and Sc co-dopings.

Table 2.1 gives a summary of the fluorescence lifetime according to equation 2.9. Figure 2.15 shows the lifetime as a function of the buffer ionic radius. The minor change in lifetime in the Gd, La and Ce co-doping when exciting the N_1 and N_2 sites indicates that a small portion of N_2 sites is present. This is consistent with the minor changes observed in the emission spectrum (Figure 2.9) when changing the excitation wavelength and in the excitation spectrum (2.10) when changing the detection wavelength.

The major change in lifetime between the N_1 and N_2 centres for the Y, Lu and Sc co-doping makes it possible to further distinguish the two different centers by time-resolved spectroscopy.

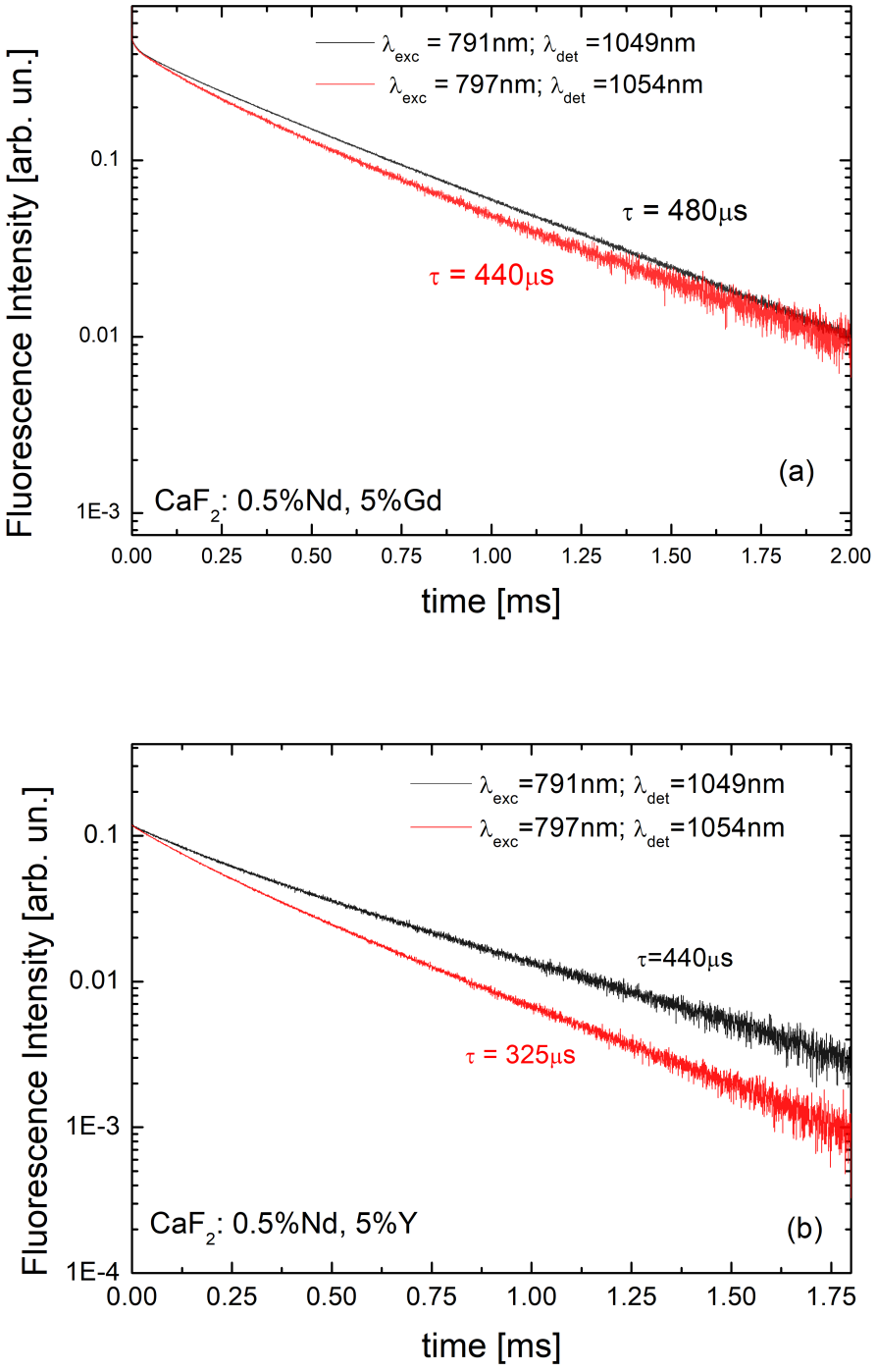

FIGURE 2.14: Lifetime of $CaF_2 : Nd, Gd$ (a) and $CaF_2 : Nd, Y$ (b), of N_1 (black), $\lambda_{exc} = 791$ nm-$\lambda_{det} = 1049$ nm, and N_2 (red), $\lambda_{exc} = 797$ nm-$\lambda_{det} = 1054$ nm.

$CaF_2 : 0.5\%Nd, ..$	τ_{N1}	τ_{N2}
5%Gd	490 μs	440 μs
5%La	450 μs	430 μs
5%Ce	410 μs	390 μs
5%Y	440 μs	325 μs
5%Lu	450 μs	300 μs
5%Sc	470 μs	340 μs

TABLE 2.1: Fluorescence lifetimes of $CaF_2 : Nd, Bu$ for $Bu = (Gd, La, Ce, Y, Lu, Sc)$ of N_1, $\lambda_{exc} = 791$ nm-$\lambda_{det} = 1049$ nm, and N_2, $\lambda_{exc} = 797$ nm-$\lambda_{det} = 1054$ nm.

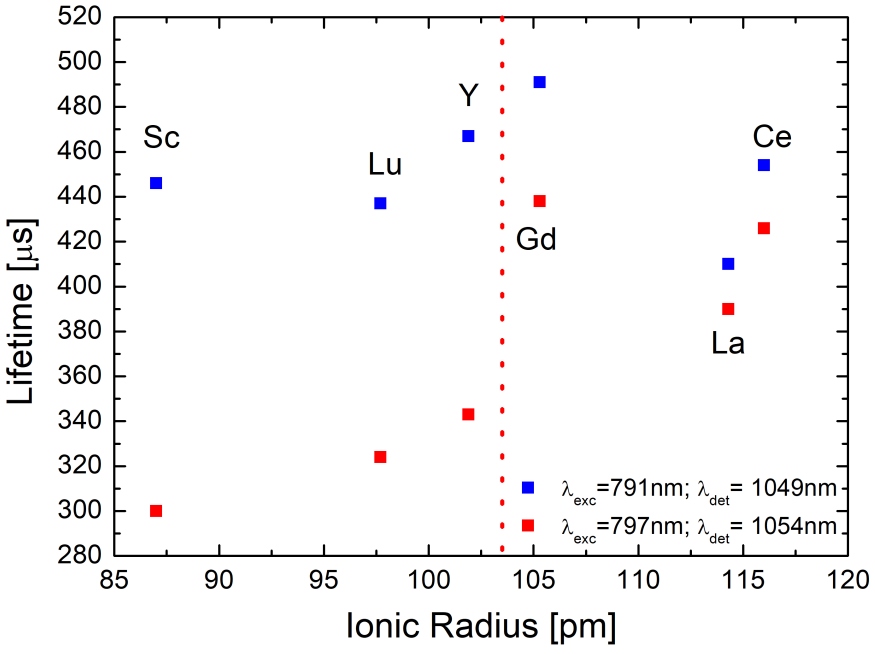

FIGURE 2.15: Fluorescence lifetimes of $CaF_2 : Nd, Bu$ for $Bu = (Gd, La, Ce, Y, Lu, Sc)$ of N_1, $\lambda_{exc} = 791$ nm-$\lambda_{det} = 1049$ nm, and N_2, $\lambda_{exc} = 797$ nm-$\lambda_{det} = 1054$ nm in function of the ionic radius.

Based on the lifetimes results of Table 2.15, the time windows chosen to record time-resolved emission and time-resolved excitation spectra are $[10 - 60\ \mu s]$, when the contribution of N_2 is dominant, and $[900 - 1500\ \mu s]$, when the contribution of N_1 is the only one remaining. Figure 2.16 shows the corresponding time-resolved emission spectra when exciting at 797 nm and time-resolved excitation spectra detected at 1054 nm.

2.4.2 Judd-Ofelt Calculations and Radiative Lifetime

As already stated, the radiative rates for all Nd transitions can be calculated with the Judd-Ofelt formalism, explained in section 2.3, using the absorption spectra of $CaF_2 : 0.5\%Nd, Bu$ in the $300 - 900$ nm wavelength range. The calculated Judd-Ofelt parameters and branching ratios are reported in Table 2.2 for all six crystals.

$CaF_2 : 0.5\%Nd, ..$	$\Omega_2[10^{-20}\ cm^2]$	$\Omega_4[10^{-20}\ cm^2]$	$\Omega_6[10^{-20}\ cm^2]$
5%Gd	0.13	3.14	4.11
5%La	0.55	3.39	5.24
5%Ce	0.03	3.80	4.41
5%Y	0.01	3.33	4.89
5%Lu	0.014	3.22	4.40
5%Sc	0.12	3.52	5.23

$CaF_2 : 0.5\%Nd, ..$	$\beta(^4F_{3/2} \rightarrow\ ^4I_{15/2})$	$\beta(^4F_{3/2} \rightarrow\ ^4I_{13/2})$
5%Gd	0.49	10.2
5%La	0.52	10.9
5%Ce	0.47	9.68
5%Y	0.51	10.6
5%Lu	0.50	10.4
5%Sc	0.52	10.7

$CaF_2 : 0.5\%Nd, ..$	$\beta(^4F_{3/2} \rightarrow\ ^4I_{11/2})$	$\beta(^4F_{3/2} \rightarrow\ ^4I_{9/2})$
5%Gd	50.5	38.8
5%La	52.1	36.6
5%Ce	49.3	40.5
5%Y	51.6	37.2
5%Lu	51.0	38.2
5%Sc	51.7	37.1

TABLE 2.2: Judd-Ofelt parameters and branching ratios of $^4F_{3/2}$ for $CaF_2 : 0.5\%Nd, 5\%Bu$.

From those parameters it is possible to calculate the radiative lifetimes as reported in Table 2.3.

For the large buffer ions with a single incorporation site, namely gadolinium, lanthanum and cerium, the JO analysis is straightforward. However, for small buffer ions the two coexisting sites pose a problem. As stated earlier, to derive a separate Judd-Ofelt analysis for each site implies the determination

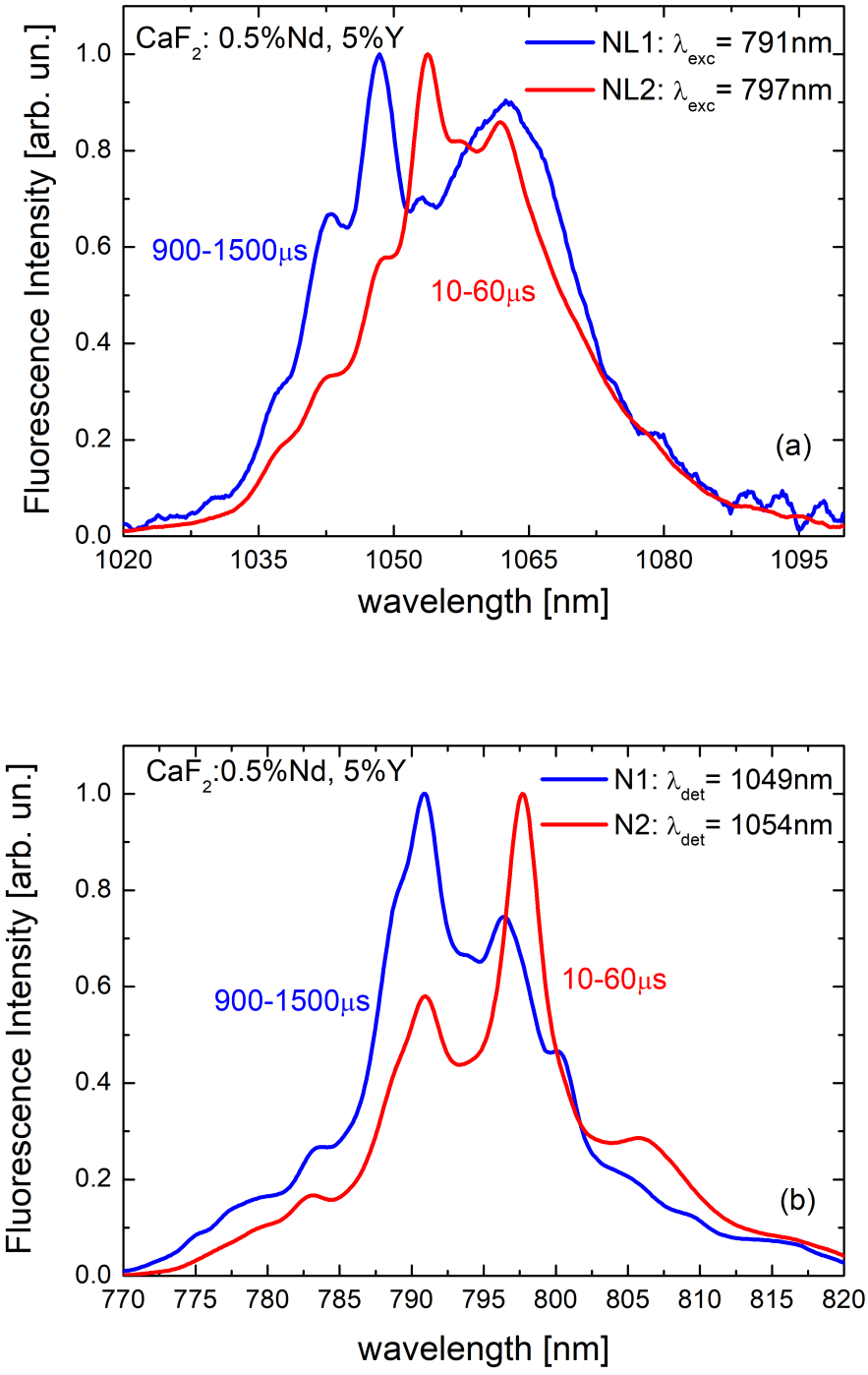

FIGURE 2.16: Time Resolved Luminescence (a) and Excitation (b), for N_1 (black) with time window $[900 - 1500\ \mu s]$, and N_2(red) with time window $[10 - 60\ \mu s]$.

of the specific absorption spectra of each site. This is complicated since it involves to separate the contribution of each site in the absorption spectra of all Nd transitions. Thus, the radiative lifetimes for small buffer ions (Y, Lu and Sc) in table 2.3 represent only an average radiative lifetime encompassing contributions from both N_1 and N_2 sites.

$CaF_2 : 0.5\%Nd, ..$	$\tau_{rad}[\mu s]$ from J-O
5%Gd	590 μs
5%La	495 μs
5%Ce	525 μs
5%Y	520 μs
5%Lu	560 μs
5%Sc	490 μs

TABLE 2.3: $^4F_{3/2}$ radiative lifetime estimated with the J-O theory.

To conclude this section on the spectroscopy of $CaF_2 : Nd, Bu$ crystals, it is important to recall that the first motivation for studying these crystals resides in their broad Nd^{3+} emission bandwidth. As mentioned earlier, in well-known crystals like $Nd : YAG$, $Nd : YLF$ and $Nd : YVO_4$, the fluorescence full width half maximum (FWHM) of the 1.05 μm transition is about $1 - 2$ nm , while in $CaF_2 : Nd, Bu$ the FWHM is much larger and comparable to glasses since it varies with the buffer ion between 18 nm for $CaF_2 : Nd, Lu$ and 30 nm for $CaF_2 : Nd, Gd$ as depicted in Figure 2.8. Moreover, as illustrated by the spectroscopy of the small buffer ions, a change of the FWHM can be achieved by choosing the buffer ion, but also by changing the excitation wavelength for crystals doped with small buffer ions. As discussed earlier, the emission spectrum changes drastically when exciting at 791 nm or at 797 nm as in $CaF_2 : Nd, Y$ (Figure 2.9). The excitation at 791 nm gives a characteristic N_1 broad spectrum with a FWHM around 30 nm while the excitation at 797 nm leads to a typical N_2 emission spectrum with a narrower linewidth around 20 nm.

Interestingly in the case of laser development, the choice of the buffer ion also has an impact on the laser emission wavelength. Since the Nd laser transition at 1050 nm is a four level scheme, the laser action will take place at the fluorescence maximum intensity. Table 2.4 shows the wavelength of the maximum intensity for the six codoped $CaF_2 : 0.5\%Nd, 5\%Bu$ when exciting at 797 nm (see Figure 2.8). Thus, the laser wavelength is expected to vary between 1053.7 nm for Lu^{3+} and 1065.3 nm for Gd^{3+} with various values within this range depending on the crystal.

$CaF_2 : 0.5\%Nd, ..$	$5\%Lu^{3+}$	$5\%Y^{3+}$	$5\%Sc^{3+}$	$5\%La^{3+}$	$5\%Ce^{3+}$	$5\%Gd^{3+}$
λ_{max} [nm]	1053.7	1054.0	1060.3	1064.5	1065	1065.3

TABLE 2.4: Peak emission wavelengths for the six $CaF_2 : 0.5\%Nd, 5\%Bu$

2.5 Co-doping with Two Buffers: $CaF_2 : Nd^{3+}, Bu_1^{3+}, Bu_2^{3+}$

Besides the study of crystals with one buffer ion, we investigated crystals containing two buffer ions, namely $CaF_2 : Nd, Bu_1, Bu_2$ and studied their spectroscopic properties as a function of the buffer concentration. The idea is to explore the possibility of mixing the different spectroscopic signatures coming from small and large buffer ions, with the aim of "engineering" the optical properties. The total co-doping concentration is kept at 5at.%, assuring an efficient breaking of the quenched $Nd - Nd$ clusters, and preserving the same thermo-mechanical properties as the singly co-doped crystals. The Nd concentration is kept at 0.5at.%.

Buffers are chosen in order to have crystals with one large buffer ion ($Bu_1 = Gd, La,$ or Ce) while the second buffer is a smaller ion such as Y or Lu. Firstly we present the specific case of $Gd - Y$, followed by other combinations, namely $Gd - Lu$, $Ce - Y$ and $La - Y$.

2.5.1 Gadolinium-Yttrium Hybrid Co-Doping

The idea of combining a large buffer ion, like Gd, behavior with a smaller buffer, like Y in the same co-doped crystal may have the advantage of combining the small buffer ion emission spectrum with a peak position at 1054 nm and a FWHM of 20 nm, with the larger emission bandwidth of the large buffer (FWHM around 30 nm) and a strong peak at 1049 nm. The aim is to improve the bandwidth of the pure N_2 emission spectrum while tuning the center wavelength.

We first investigated CaF_2, Nd, Gd, Y crystals and studied the effect of a gradual change in concentration from a 5%Gd to a 5%Y doped sample. The crystals grown for this purpose are 4%Gd1%Y, 2.5%Gd2.5%Y and 1%Gd4%Y, together with the 5%Gd and 5%Y doped crystals already considered in section 2.4.

In Figure 2.17 the absorption coefficient of the five crystals is depicted. It is possible to observe a buffer concentration trend, starting from the 5%Gd doped sample and gradually introducing yttrium and decreasing gadolinium, which clearly indicates the presence of the 791 nm, peak that remains unchanged with the gradual rise of a second peak at 797 nm, indicating the gradual increase of the presence of the N_2 sites.

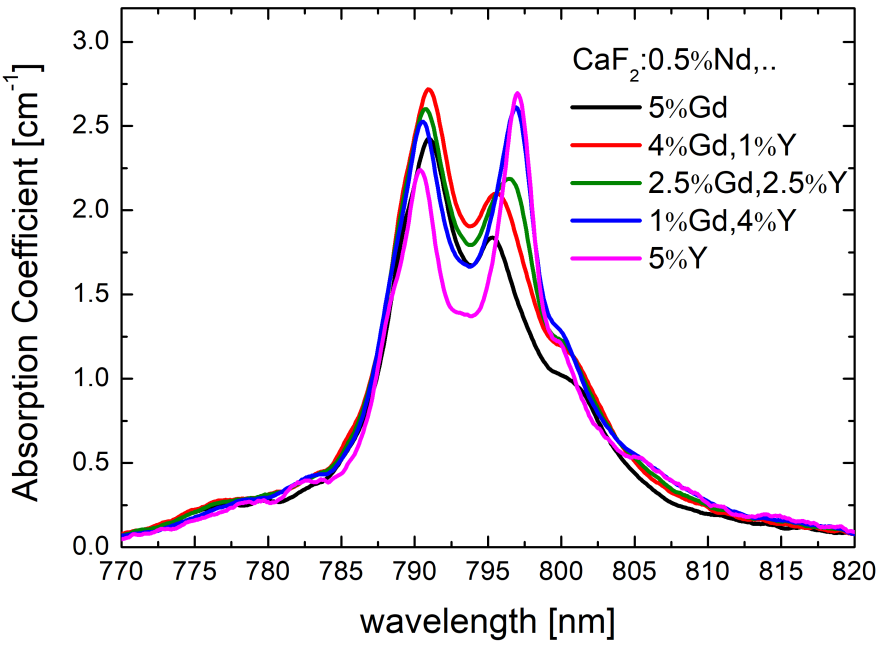

FIGURE 2.17: Absorption coefficient of $CaF_2 : Nd, Gd, Y$ for different gadolinium and yttrium concentration, keeping 5% as total buffers concentration.

Similarly to the investigation carried on single buffer ions in section 2.4, the luminescence spectra exciting at 797 nm and excitation spectra detected at 1054nm, characteristic of the N_2 site are reported in Figure 2.18. It is possible to observe, in both luminescence and excitation, the gradual change of the lineshape from the gadolinium-like behavior towards the yttrium-like, passing through several intermediate shapes. Concerning the luminescence spectrum there is a gradual decrease of the 1049 nm peak intensity with the rise of the 1054 nm peak, while for the excitation spectrum one can observe the emergence of the second peak at 797 nm.

The measurement of the $^4F_{3/2}$ energy level lifetime in these crystals exciting at 797 nm and detecting at 1054 nm, displayed in Figure 2.19, shows a clear lifetime shortening with the increase of yttrium concentration with a linear dependence with the buffer concentration.

The gradual change in the lineshape and the linear change in lifetime with the buffer concentration suggests that it could be possible to simulate the emission spectra of the double buffer co-doped samples using a linear combination of the emission spectra of Y^{3+} and Gd^{3+} single-buffer doped crystals. To corroborate this hypothesis, the normalized luminescence spectrum $I(\lambda)$ exciting at 797 nm of CaF_2 :0.5%Nd, 2.5%Gd, 2.5%Y has been simulated as

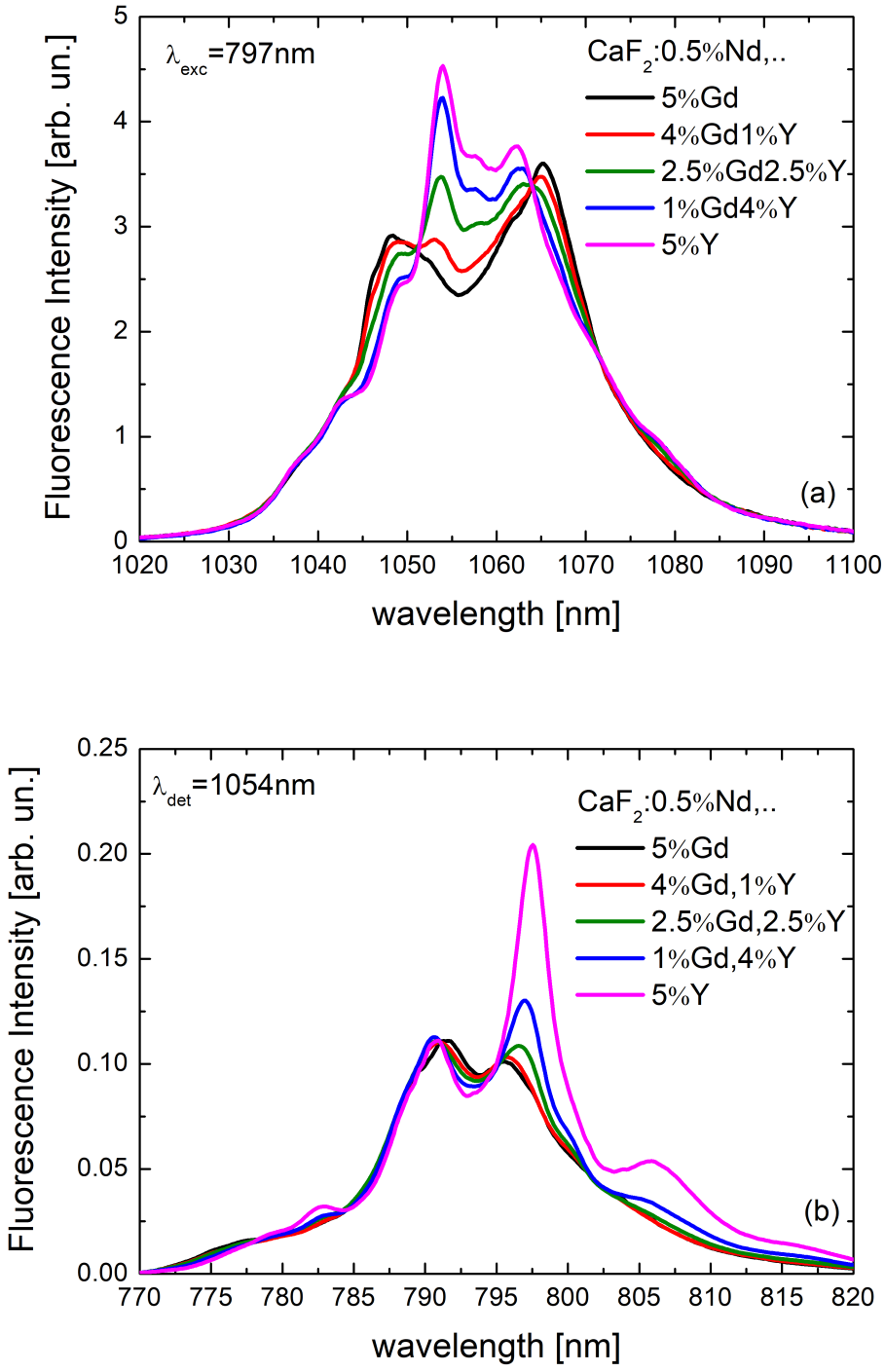

FIGURE 2.18: Luminescence (a) and excitation (b) of $CaF_2 : Nd, Gd, Y$ for different gadolinium and yttrium concentration, keeping 5% as total buffers concentration.

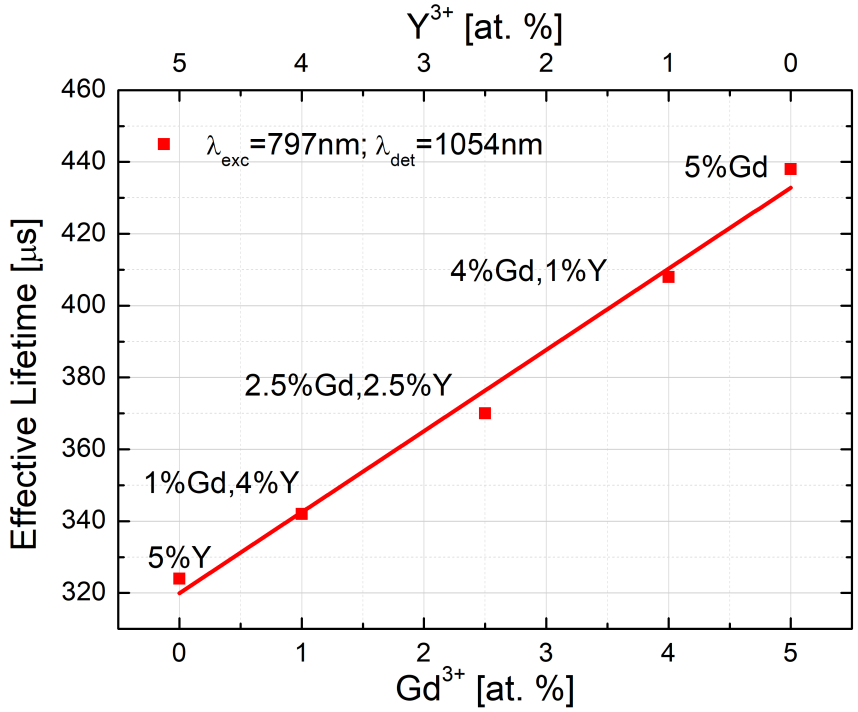

FIGURE 2.19: $^4F_{3/2}$ energy level lifetime concentration trend of $CaF_2 : Nd, Gd, Y$ for different gadolinium and yttrium concentration, keeping 5% as total buffers concentration.

$$I^{sim}_{2.5\%Gd,2.5\%Y} = 0.5 \times g^{exp}_{5\%Gd} + 0.5 \times g^{exp}_{5\%Y} \tag{2.27}$$

where $g(\lambda)$ is the normalized lineshape functions of each emission spectrum defined as in eq. (2.25).

The simulated lineshape $I^{sim}_{2.5\%Gd,2.5\%Y}$ is compared in Figure 2.20 to the experimental one. It is possible to observe that the two lineshapes are in very good agreement. The 0.5 coefficients used in Figure 2.20 mean that each luminescence spectrum from the single buffer doped crystal plays an equal role in the double buffer co-doped crystal emission spectrum which is consistent with the equal Gd and Y concentrations The same conclusion has been verified in a similar way for the other two combinations 4%Gd1%Y and 1%Gd4%Y, by adjusting the coefficients of the linear combinations following the respective concentration of the two buffers. This not only enables pre-growth simulations of future crystals, but it also shows that there is no need to speculate on the presence of other kind of Nd emitting centers due to the hybrid co-doping.

We also investigated the fine tuning of the excitation wavelength to achieve the flattest luminescence spectrum as possible. This has been done in the 795.4 nm to 797.0 nm range with a 0.2 nm step as shown in Figure 2.21, obtaining the flattest profile by exciting at 796.2 nm. This confirms the emission spectrum change following a small shift of the excitation

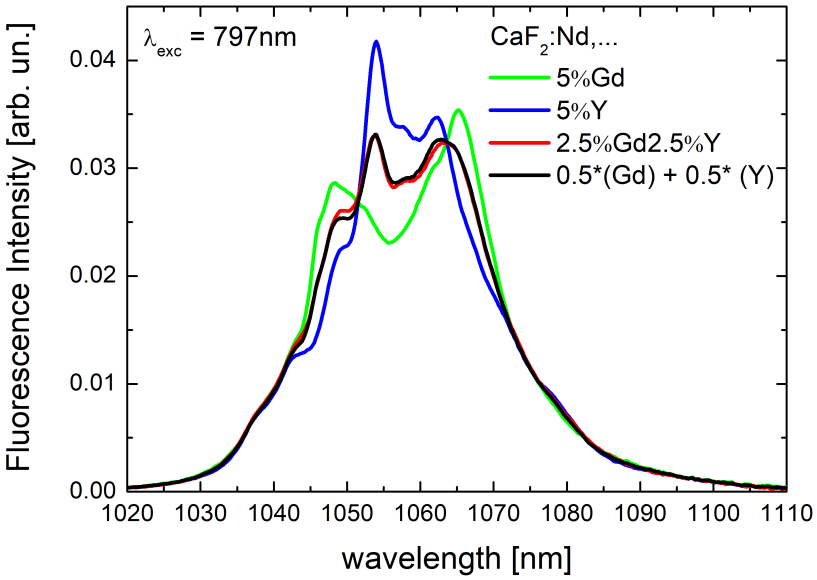

FIGURE 2.20: Reconstruction via linear combination of the luminescence of CaF_2 : 0.5%Nd, 2.5%Gd, 2.5%Y (black), compared with the experimental spectrum (red), and the 5%Gd (green) and 5%Y (blue). Excitation wavelength at 797 nm

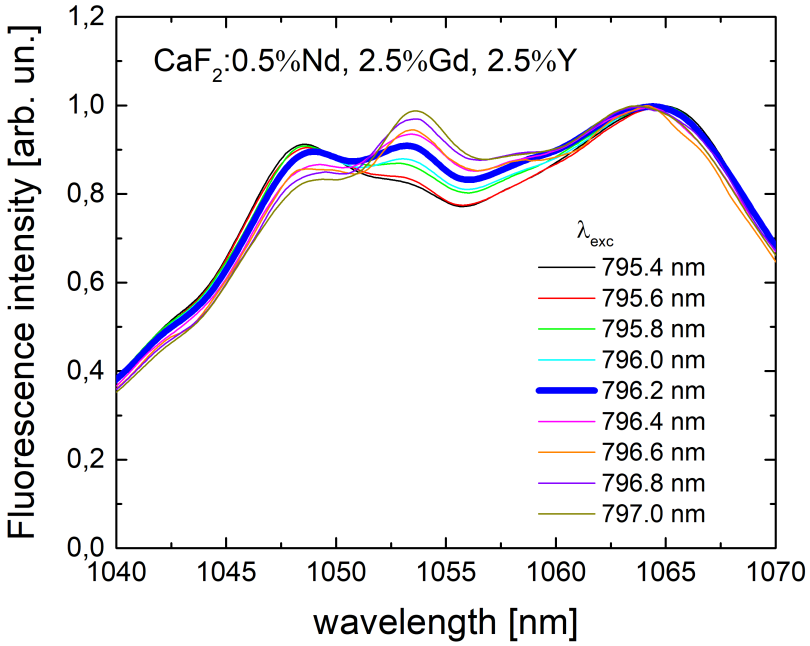

FIGURE 2.21: Luminescence of CaF_2 : 0.5%Nd, 2.5%Gd, 2.5%Y tuning the excitation wavelength from 795.4 nm to 797.0 nm with 0.2 nm step. highlighted in blue the flattest profile, corresponding to 796.2 nm.

wavelength, already observed in the Y co-doped sample (Fig. 2.13) due to the rise of the N_2 centre absorption coefficient in the 795 to 797 nm excitation range.

2.5.2 Other Combinations: $La - Y$, $Gd - Lu$, $Ce - Y$ Co-Doping

In order to validate the possibility to simulate the luminescence spectra, the same investigation was carried out for three other buffer combinations, growing the following crystals:

- $CaF_2 : 0.5\%Nd, 2.5\%Gd, 2.5\%Lu$
- $CaF_2 : 0.5\%Nd, 2.5\%La, 2.5\%Y$
- $CaF_2 : 0.5\%Nd, 2.5\%Ce, 2.5\%Y$

and trying to reconstruct the experimental spectra of $CaF_2 : 0.5\%Nd, 2.5\%Bu_1, 2.5\%Bu_2$ using a linear combination like for the $Gd - Y$ case:

$$I^{sim}_{2.5\%Bu,2.5\%Bu} = k_{Bu1} \times I^{exp}_{5\%Bu_1} + k_{Bu2} \times I^{exp}_{5\%Bu_2} \tag{2.28}$$

The simulated spectra are displayed in Figure 2.22, where the reconstructed spectra match nicely the experimental spectra.

The linear combination coefficients k_{Bu} used to reconstruct the experimental spectra are reported in Table 2.5. It is possible to see that in the $Gd - Lu$ case the coefficients are not $0.5 - 0.5$ as in the other cases, but we observe a stronger coefficient associated with the Lu doped crystal ($k_{Lu} = 0.6$)The reason for that stronger component lies in the fact that the luminescence intensity depends on the excited level population N^*, the branching ratio β of the studied transition (here $^4F_{3/2} \rightarrow {}^4I_{11/2}$) and the radiative lifetime τ_{rad}. Therefore, the k_{Bu} coefficient can be written as:

$$k_{Bu} \propto N^* \cdot \beta \cdot \tau_{rad}^{-1} \tag{2.29}$$

with N^* the $^4F_{3/2}$ emitting level population, defined in the steady–state regime as $N^* = \alpha_{abs} N \phi \tau_f$ with τ_f the fluorescence lifetime, ϕ the pump photon flux, N the total Nd concentration and α_{abs} the absorption coefficient leading to the relation:

$$k_{Bu} \propto \alpha_{abs} \cdot \tau_f \cdot \phi \cdot N \cdot \beta \cdot \tau_{rad}^{-1} \tag{2.30}$$

While these spectroscopic parameters may vary from one crystal to another, the main difference in the case of the Lu codoping resides in the absorption coefficient at 797 nm which is larger ($\alpha = 4.3$ cm^{-1}, Figure 2.7) than for the Gd codoping ($\alpha = 1.5$ cm^{-1}, Figure 2.7). This is therefore the main explanation why the k_{Bu} coefficient is larger for Lu in the $Gd - Lu$ linear combination.

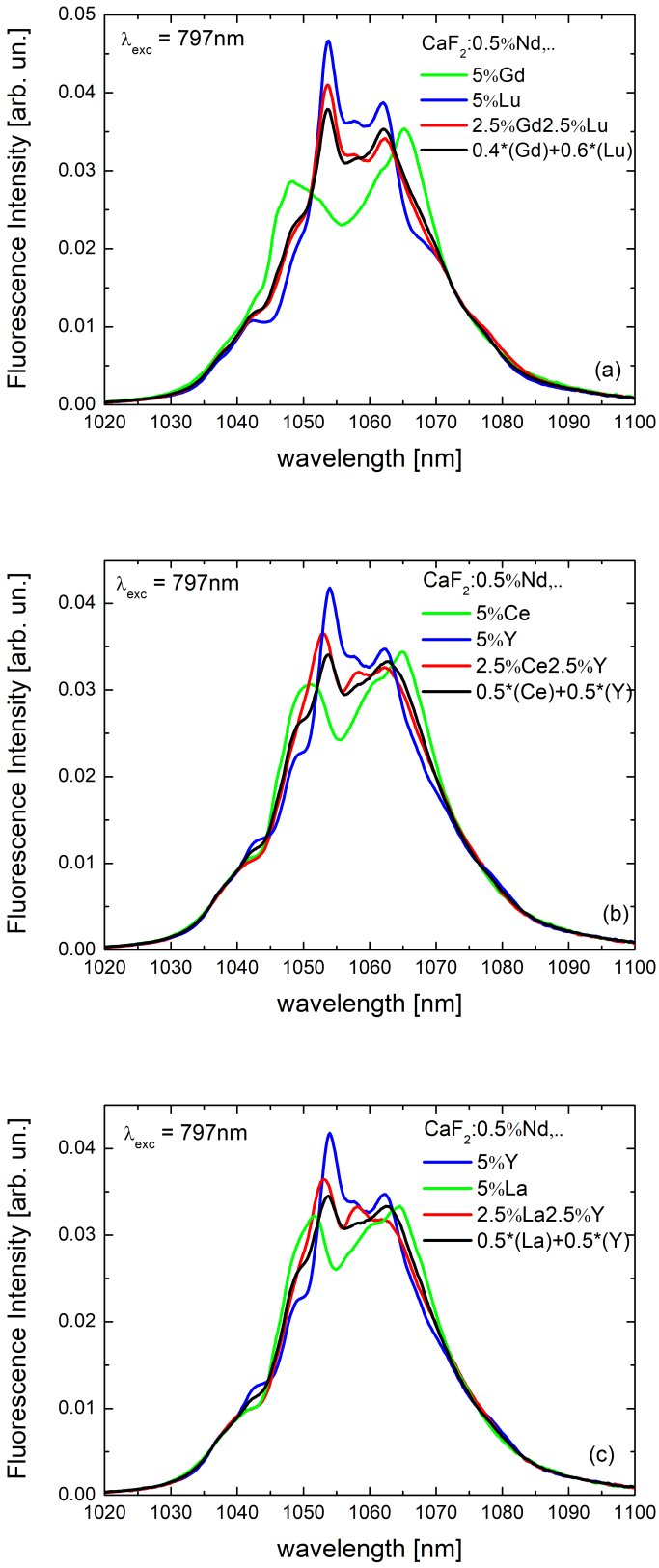

FIGURE 2.22: Reconstruction via linear combination of the luminescence with excitation wavelength at 797 nm of $CaF_2 : 0.5\%Nd, 2.5\%Gd, 2.5\%Lu$ (a), $CaF_2 : 0.5\%Nd, 2.5\%Ce, 2.5\%Y$ (b), $CaF_2 : 0.5\%Nd, 2.5\%La, 2.5\%Y$ (c).

$CaF_2 : 0.5\%Nd, ..$	k_{Bu1}	k_{Bu2}
5%Gd, 5%Y	0.5	0.5
5%Ce, 5%Y	0.5	0.5
5%La, 5%Y	0.5	0.5
5%Gd, 5%Lu	0.4	0.6

TABLE 2.5: Reconstruction coefficients used in the linear combination eq. 2.28, for simulating the experimental spectra of $CaF_2 : 0.5\%Nd, 2.5\%Bu_1, 2.5\%Bu_2$

2.6 Co-doping with Three Buffers: $CaF_2 : Nd^{3+}, Bu_1^{3+}, Bu_2^{3+}, Bu_3^{3+}$

With the aim of achieving the flattest emission profile possible around 1050 nm we studied compositions with three different buffer ions.

Using the linear combinations of the emission spectra with a single buffer ion (Y, Lu, Sc, La, Gd and Ce) (Figure 2.8 (a)), we investigated multiple combinations and finally chose to retain three compositions. These compositions exhibit a rather flat emission profile according to the simulation:

- 3.8%Gd, 0.65%Y, 0.55%La
- 1.9%Gd, 1.6%Sc, 1.5%Y
- 3%Gd, 1.4%Ce, 0.6%Y

These crystals were grown according to the desired compositions and their emission spectra were recorded exciting at 797 nm. The experimental emission spectrum of CaF_2 :0.5%Nd, 3.8%Gd, 0.65%Y, 0.55%La has been successfully compared with the linear combination, as seen in Figure 2.23. The linear combination used is as follows:

$$I^{sim}_{3.8\%Gd,0.65\%Y,0.55\%La} = 0.76 \times I^{exp}_{5\%Gd} + 0.13 \times I^{exp}_{5\%Y} + 0.11 \times I^{exp}_{5\%La} \quad (2.31)$$

Interestingly, the emission spectrum exciting at 797 nm exhibits a flat profile over 4.5 nm between 1048.5 nm and 1053.0 nm.

For $CaF_2 : 0.5\%Nd, 1.9\%Gd, 1.6\%Sc, 1.5\%Y$ the experimental luminescence spectrum exciting at 797nm gave an unexpected result, reported in Figure 2.24, since it does not match the simulated curve. The simulated spectrum gives a quite flat profile around 1050 nm while the real spectrum exhibits a peak at 1054 nm. The most likely explanation resides in the small size of scandium ion (ionic radius of 88 pm, compared to yttrium, 104 pm). While Sc is quite efficient at forming $Sc - Nd$ clusters when used as a single buffer ion, but when it is used in a multiple buffer crystal the majority of the clusters formed are $Nd - Gd$ or $Nd - Y$. This is further confirmed by a

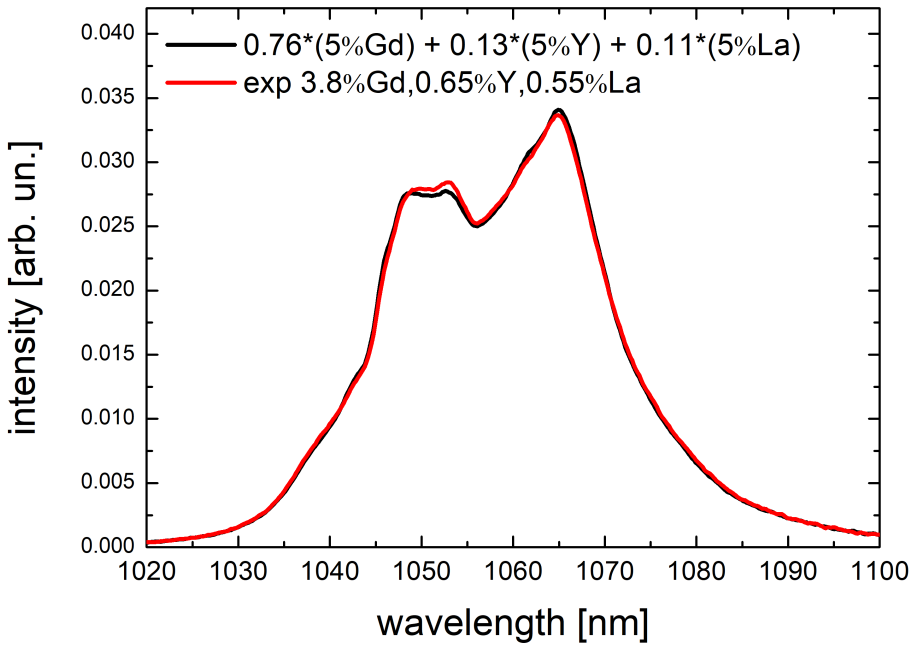

FIGURE 2.23: Reconstructed spectrum (black) compared to the experimental spectrum (red) of the luminescence of CaF_2 :0.5%Nd, 3.8%Gd, 0.65%Y, 0.55%La

linear combination of emission spectra excluding the scandium doped emission spectrum and retaining only the $Nd-Gd$ and $Nd-Y$ clusters emission spectra. As a result, the linear combination of these two spectra matches nicely the CaF_2 : 0.5%Nd, 1.9%Gd, 1.6%Sc, 1.5%Y emission spectrum.

A third crystal has been investigated, containing gadolinium, cerium and yttrium ions. The optimal composition with these three buffer ions according to the linear combination is CaF_2 :0.5%Nd, 3%Gd, 1.4%Ce, 0.6%Y. As can be seen in Figure 2.25, the simulated emission spectrum is in good agreement with the experimental luminescence lineshape exciting at 797 nm. One can observe a flat region between 1049 nm and 1054 nm, making this particular crystal very interesting for a wide band amplifier application.

As a summary, between the double and triple co-doping approach, four different interesting combinations have been identified in terms of flatness around 1050 nm:

- CaF_2 : 0.5%Nd, 2.5%Gd, 2.5%Y
- CaF_2 : 0.5%Nd, 4%Gd, 1%Y
- CaF_2 : 0.5%Nd, 3.8%Gd, 0.65%Y, 0.55%La
- CaF_2 : 0.5%Nd, 3%Gd, 1.4%Ce, 0.6%Y

All four crystals will be further investigated with the characterization of their amplification properties and laser action in the next chapters.

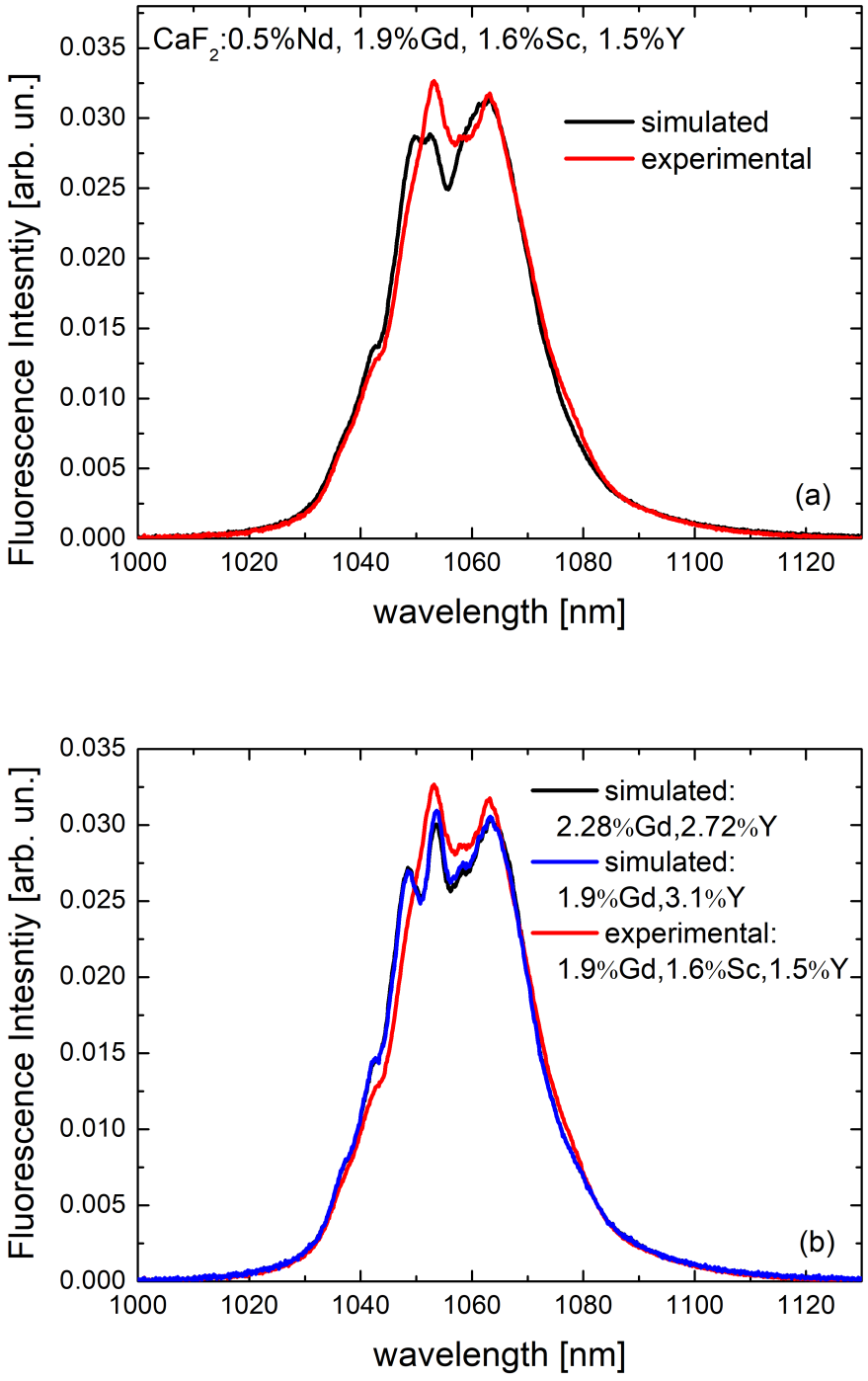

FIGURE 2.24: (a) Simulated spectrum (black) compared to the experimental spectrum (red) of the luminescence of CaF_2 :0.5%Nd, 1.9%Gd, 1.6%Sc, 1.5%Y. (B), the successful reconstruction excluding scandium from the linear combination.

As reported in Table 2.6, the 3%Gd, 1.4%Ce, 0.6%Y co-doping is particularly interesting for the LMJ applications, with a 5 nm of flatness in the $1049.0 - 1054.0$nm.

$CaF_2 : 0.5\%Nd, ..$	Excitation Wavelength	Center Wavelength
2.5%Gd, 2.5%Y	796.2nm	1051.0nm
4%Gd, 1%Y	797.0nm	1050.9nm
3.8%Gd, 0.65%Y, 0.55%La	797.0nm	1050.9nm
3%Gd, 1.4%Ce, 0.6%Y	797.0nm	1051.0nm

$CaF_2 : 0.5\%Nd, ..$	Flatness	Flatness Range
2.5%Gd, 2.5%Y	5.6nm	$1048.2 - 1053.8$ nm
4%Gd, 1%Y	4.9nm	$1048.5 - 1053.4$ nm
3.8%Gd, 0.65%Y, 0.55%La	4.4nm	$1048.7 - 1053.1$ nm
3%Gd, 1.4%Ce, 0.6%Y	5nm	$1049.0 - 1054.0$ nm

TABLE 2.6: Flatness and center wavelength of the four promising combinations.

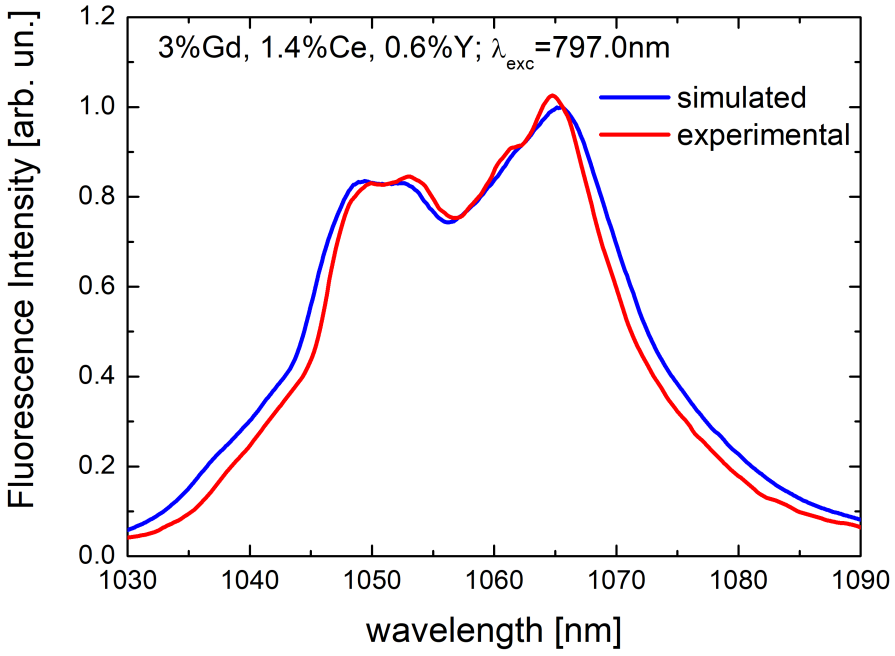

FIGURE 2.25: Simulated spectrum (blue) compared to the experimental spectrum (red) of the luminescence of CaF_2 :0.5%Nd, 3%Gd, 1.4%Ce, 0.6%Y. The flat region is between 1049 nm and 1054 nm.

2.7 Neodymium and Ytterbium Co-Doping

In this last section of the chapter, the possibility of using an active ion in CaF_2 : Nd is investigated. In contrast with all the previous approaches, that employed only buffer ions, this section is dedicated to the $Nd - Yb - Gd$ doping.

The laser performance of CaF_2 : Yb is very well known, due to the long energy level lifetime of its emitting level, around 2.4 ms [91], but its limit is represented by its low absorption cross section, that reduces the efficiency of the pumping process. In order to overcome this problem, a pumping scheme for the Yb^{3+} $^2F_{5/2}$ level via energy transfer from the Nd^{3+} $^4F_{3/2}$ level has been investigated both in glasses [92–94] and in crystals hosts [66, 91, 95–97]. As depicted in Figure 2.26, the idea is to pump neodymium ions at 800 nm on the $^4F_{5/2}$ level, which is followed by a non-radiative relaxation to the $^4F_{3/2}$, and a subsequent energy transfer to ytterbium ions for an emission at 1 μm.

In this work, the spectroscopy of CaF_2 : Nd, Yb, Gd crystals is investigated, with the idea of not only looking at the pumping of Yb ions through Nd ions , but also studying the emission spectral shape of this compound around 1 μm. Indeed, the Yb emission spectrum is located at shorter wavelengths than the $^4F_{3/2} \rightarrow {}^4I_{13/2}$ transition. As a consequence one can expect a very broad and possibly flat emission profile combining the emission spectra of both Yb and Nd ions.

Within this study, a particular attention was paid to the $Nd \rightarrow Yb$ energy transfer, estimating the energy transfer (ET) parameter and energy transfer efficiency (ETE).

In a similar way as the other crystals studied in this work, the Nd^{3+} concentration is kept constant at 0.5at.%. The two co-dopants, gadolinium and ytterbium act as buffer ions , keeping the total co-doping concentration at 5at.%, ensuring the absence of $Nd - Nd$ clusters. Yb^{3+} has a ionic radius of 98.5 pm which is close to the Lu^{3+} one (97.8 pm). Yb^{3+} can thus be considered as a small buffer ion alike Lu^{3+} or Y^{3+}. The concentration of ytterbium has been varied between 0.2at.% and 3at.%. For this study, six crystals have been grown following the same Bridgman-Stockbarger procedure described before:

- CaF_2 : 0.5%Nd, 0.2%Yb, 4.8%Gd
- CaF_2 : 0.5%Nd, 0.4%Yb, 4.6%Gd
- CaF_2 : 0.5%Nd, 0.7%Yb, 4.3%Gd
- CaF_2 : 0.5%Nd, 1%Yb, 4%Gd
- CaF_2 : 0.5%Nd, 2%Yb, 3%Gd

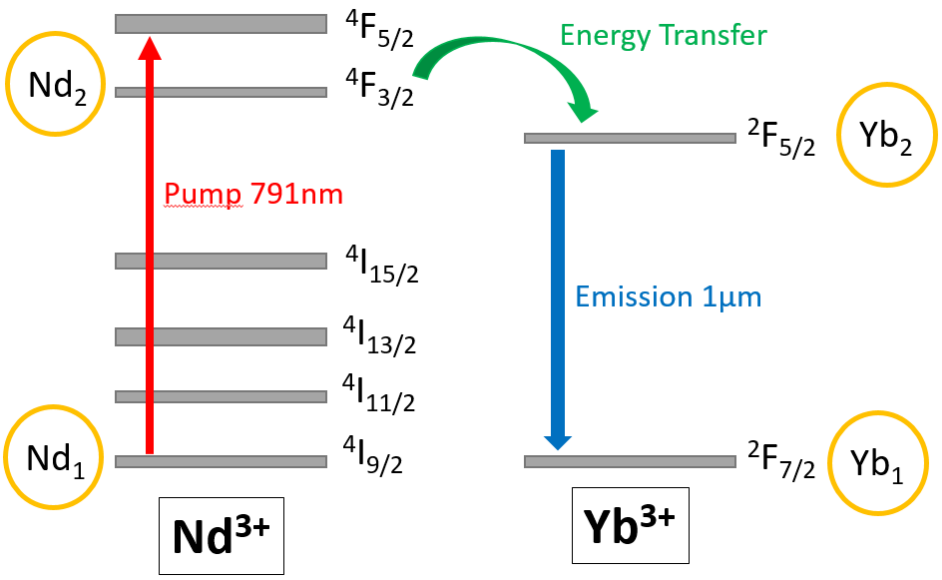

FIGURE 2.26: Scheme of the Nd → Yb energy transfer.

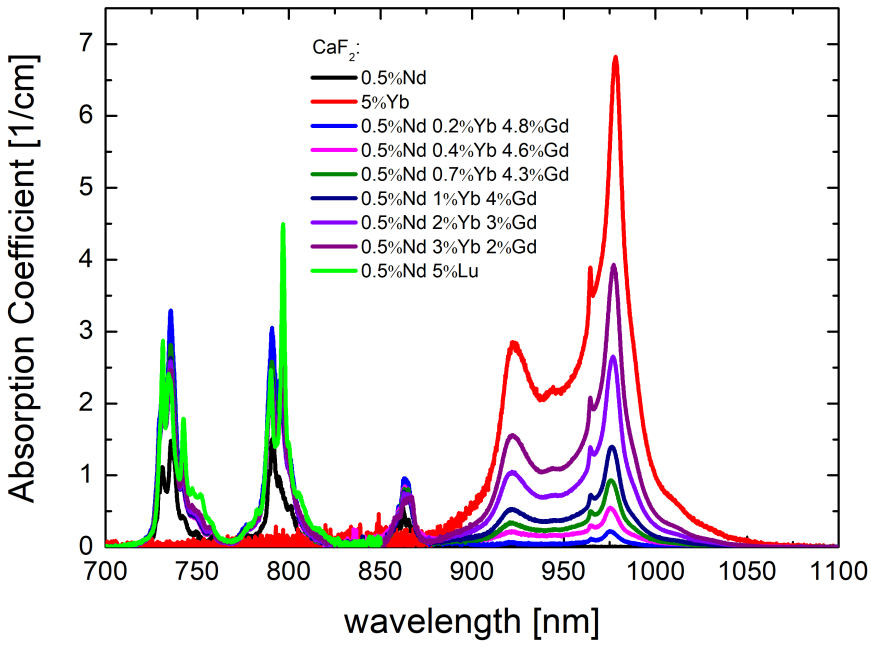

FIGURE 2.27: Absorption coefficient of the $CaF_2 : Nd, Yb, Gd$ crystals for different Yb and Gd concentration, keeping 0.5at.%Nd and 5at.% as total co-doping concentration. As a reference comparison are also reported the $CaF_2 : 5\%Yb$, 0.5%Nd and $CaF_2 : 0.5\%Nd, 5\%Lu$.

- $CaF_2 : 0.5\%Nd, 3\%Yb, 2\%Gd$

The absorption spectra of the various $CaF_2 : Nd, Yb, Gd$ samples are reported in Figure 2.27, in which one can observe the Nd absorption spectrum for the three main transitions around 730 nm, 800 nm and 860 nm along with the Yb absorption around 980 nm. As expected the Yb absorption coefficient increases as the Yb concentration becomes larger. It is clear that the Yb absorption peak at 980 nm equals the Nd absorption peak at 800 nm , once the Yb concentration reaches 3% while the Nd concentration is kept at 0.5% illustrating the much higher absorption cross section of neodymium.

In the following subsections, the luminescence and lifetime studies both exciting the neodymium and ytterbium ions are reported, together with the study of the energy transfer.

2.7.1 Exciting Neodymium Ions

In Figure 2.28 are reported the luminescence spectra of the $CaF_2 : Nd, Yb, Gd$ crystals when exciting at 791 nm and 797 nm, thus exciting neodymium ions. It is possible to observe the luminescence of Nd^{3+} alone in the $850 - 925$ nm region, with a peak at 863 nm, while in the $925 - 1100$ nm region it is superposed with the ytterbium luminescence spectrum. The typical emission spectrum of $CaF_2 : Nd, Gd$ can be observed around 1050 nm while the ytterbium emission lies at shorter wavelengths with a peak at 978 nm [95]. As expected, the increase of Yb concentration leads to an increase of Yb emission since the Nd to Yb energy transfer becomes more and more efficient as the concentration of Yb acceptor ions increases. This increase is accompanied by a decrease of Nd $^4F_{3/2}$ emissions around 1050 nm and 900 nm which further evidences the increase of the Nd to Yb energy transfer.

The comparison between the luminescence spectra when exciting at 791 nm and 797 nm reveal little differences indicating that a single type of site dominates the neodymium spectroscopy, even at high ytterbium concentration and low gadolinium concentration. Since Yb^{3+} has a similar ionic radius as Y^{3+} one could expect a double Nd site signature as in $CaF_2 : Nd, Y, Gd$. The explanation lies in the fact that the efficient energy transfer $Nd \rightarrow Yb$ within $Nd - Yb$ clusters quenches the Nd emission. The energy transfer is made particularly strong within these $Nd - Yb$ clusters since Nd and Yb ions are close to each other. So the Nd emitting N_2 site due to the Y codoping which was observed in the $Y - Gd$ codoping can no longer be observed in $Nd - Yb$ co-doping since it is replaced by an emission from Yb ions instead of Nd ions.

To further confirm this Nd to Yb energy transfer, we investigated the Nd and Yb emission dynamics. The $^4F_{3/2}$ lifetime was measured exciting at 791 nm and detecting at 1049 nm, ($^4F_{3/2} \rightarrow {}^4I_{11/2}$ transition), revealing a first non-exponential part of the decay in the first 2 ms which is typical of the Nd^{3+} ion, followed by a second single-exponential long decay,

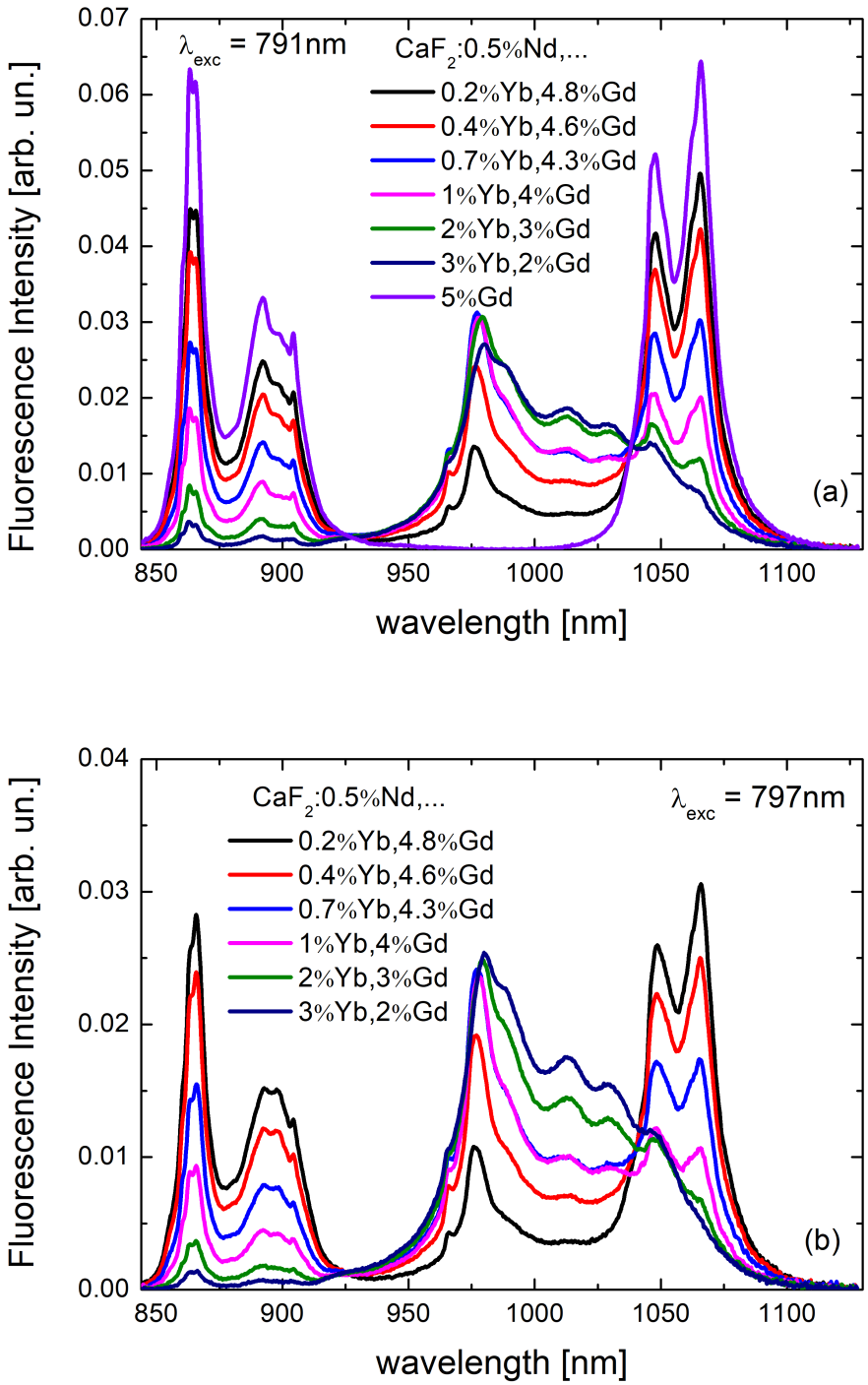

FIGURE 2.28: Luminescence of $CaF_2 : Nd, Yb, Gd$ crystals with excitation wavelength of 791 nm (a) and 797 nm (b).

after 2 ms as displayed for the $CaF_2 : 0.5\%Nd, 0.7\%Yb, 4.3\%Gd$ sample in Figure 2.29. No significant difference is observed between an excitation at 791 nm and at 797 nm further confirming the dominance of one type of Nd emitting center. Table 2.7 shows the lifetime values for the two parts of the decay for the different samples. The long part of the decay is as expected around 2.3 ms which is the typical lifetime value for Yb in CaF_2 [66]. However, the increase of the ytterbium concentration reveals a surprising lengthening of the early part of the decay attributed to Nd ions while the long part of the decay remains the same. One would expect a quenching of the $^4F_{3/2}$ level because of the energy transfer and thus a shortening of this early part of the decay. In fact the lengthening of the early part of the decay is misleading and cannot be attributed to only Nd ions since the contribution of Yb ions to the early part of the decay at 1049 nm increases as the Yb concentration increases. To have a clear estimate of the Nd lifetime evolution we recorded the $^4F_{3/2}$ decay at 863 nm ($^4F_{3/2} \rightarrow {}^4I_{11/2}$ transition) as displayed in Figure 2.30, where the detected decay corresponds only to Nd ions. As expected, the neodymium lifetime shows a clear drop with the increase of ytterbium concentration going from 400μs to 100μs.

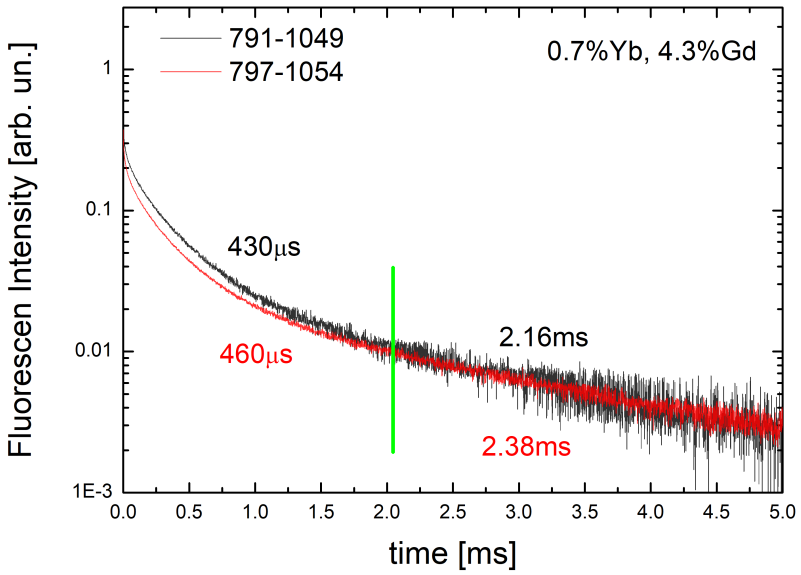

FIGURE 2.29: Energy level lifetime for the $CaF_2 : 0.5\%Nd, 0.7\%Yb, 4.3\%Gd$ exciting at 791 nm and detecting at 1049 nm, corresponding to the $^4F_{3/2} \rightarrow {}^4I_{11/2}$ transition of the neodymium ion.

One last evidence of the Nd to Yb energy transfer is given by the Yb decay recorded at 978 nm, thus on the ytterbium emission peak while exciting Nd^{3+} at 791 nm. The example of $CaF_2 : 0.5\%Nd, 0.2\%Yb, 4.8\%Gd$, is displayed in Figure 2.31 where even at very low ytterbium concentration the Nd $\rightarrow$ Yb energy transfer takes place. One can clearly see a fast rise up time

$CaF_2 : 0.5\%Nd, ..$	$\tau[0\ \mu s - 2ms]$	$\tau[2ms - 5ms]$
0.2%Yb, 4.8%Gd	440 μs	-
0.4%Yb, 4.6%Gd	435 μs	-
0.7%Yb, 4.3%Gd	430 μs	2.16 ms
1%Yb, 4%Gd	535 μs	2.29 ms
2%Yb, 3%Gd	950 μs	2.39 ms
3%Yb, 2%Gd	1.50 ms	2.45 ms

TABLE 2.7: Energy level lifetime for the $CaF_2 : Nd, Yb, Gd$ exciting at 791 nm and detecting at 1049 nm, corresponding to the $^4F_{3/2} \rightarrow {}^4I_{11/2}$ transition, for various ytterbium and gadolinium concentrations.

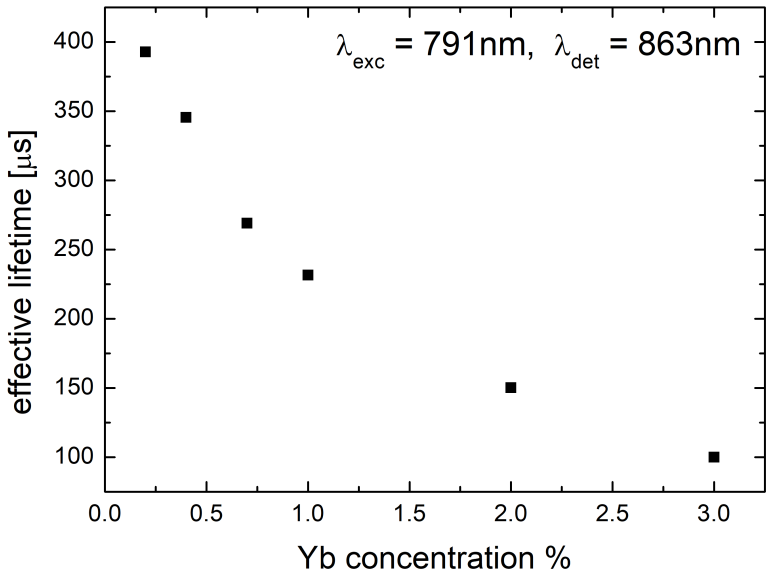

FIGURE 2.30: Energy level lifetime for the $CaF_2 : Nd, Yb, Gd$ exciting at 791 nm and detecting at 863 nm, corresponding to the $^4F_{3/2} \rightarrow {}^4I_{9/2}$ transition of the neodymium ion, for various ytterbium and gadolinium concentrations.

associated with the $^4F_{3/2}$ Nd lifetime accompanied by a 2.2 ms decay typical of Yb ions in CaF_2.

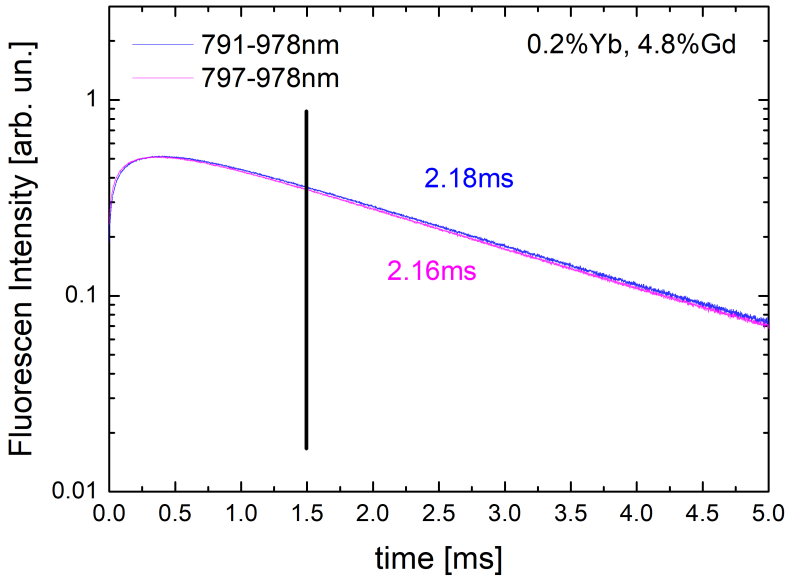

FIGURE 2.31: Energy level lifetime for the $CaF_2 : 0.5\%Nd, 0.2\%Yb, 4.8\%Gd$ exciting at 791 nm and detecting at 978 nm.

2.7.2 $Yb^{3+} \rightarrow Nd^{3+}$ Back-Transfer

After having qualitatively investigated the spectroscopy of $CaF_2 : Nd, Yb, Gd$ exciting neodymium ions, this particular subsection is dedicated to the excitation of ytterbium ions in order to assess whether or not a back-transfer from Yb to Nd takes place. The luminescence spectra of all $CaF_2 : Nd, Yb, Gd$, samples exciting Yb ions at 922 nm are depicted in Figure 2.32. One can notice an apparent broadening of the Yb emission spectrum as the Yb concentration increases. This broadening is misleading since it is actually the emission peak intensity at 980 nm which decreases because of a well-known reabsorption mechanism in Yb doped materials. Additionally, spectra in Figure 2.32 show no sign of Nd emission around 1050 nm. In a similar way, no Nd emission can be observed around 860 nm when exciting Yb ions (Fig 2.32, (b)) indicating the absence of energy back-transfer from Yb to Nd. This result is not surprising since the Yb $^2F_{5/2}$ level is located at lower energy than the Nd $^4F_{3/2}$ level. As a consequence the energy transfer from Yb to Nd must be assisted by phonons which energy has to be taken from the host matrix to compensate for the lack of donor (Yb) energy. This type of energy transfer is very unlikely in particular in a fluoride crystal such as CaF_2 which exhibits low phonon energy.

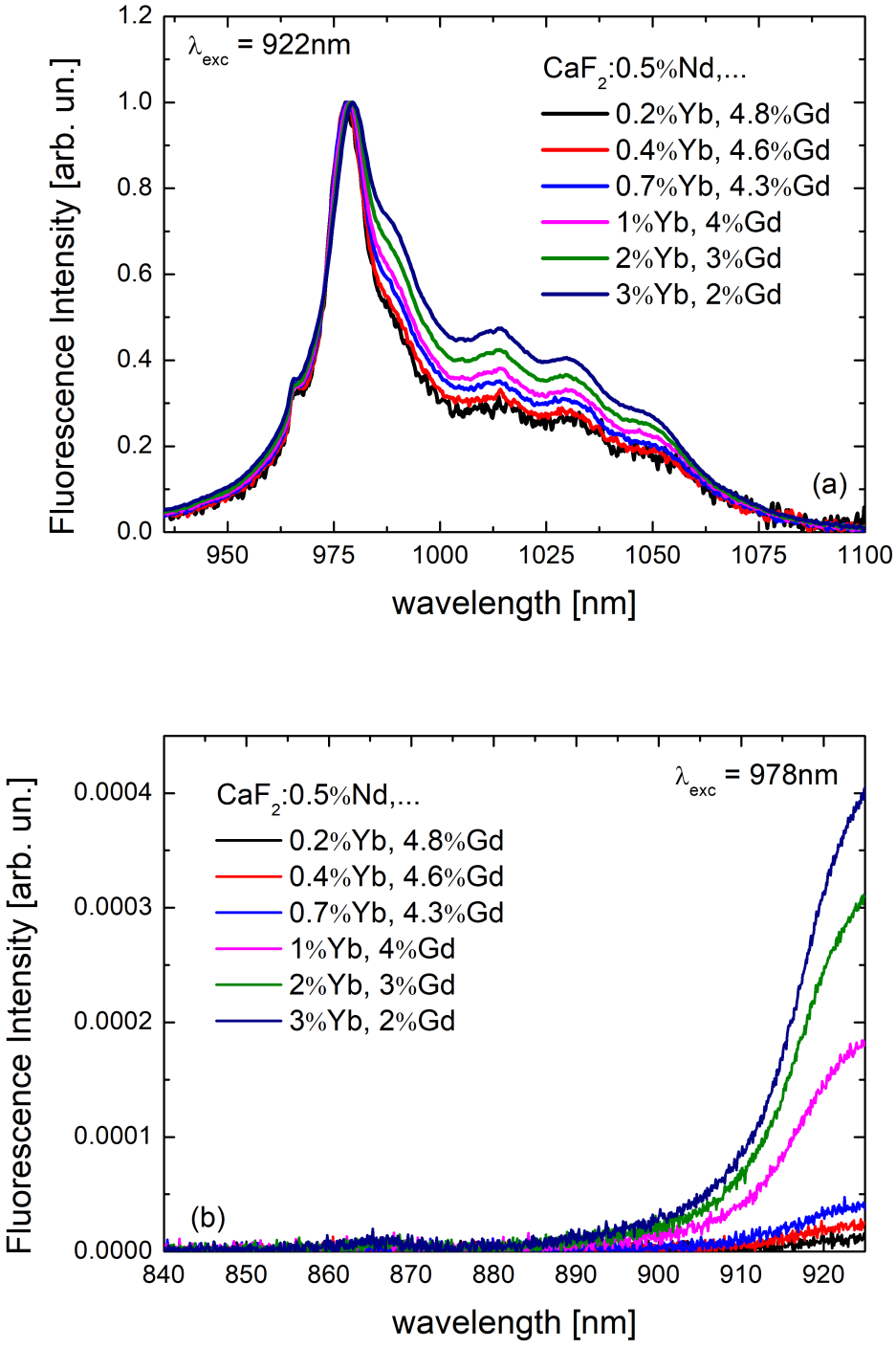

FIGURE 2.32: Luminescence of $CaF_2 : Nd, Yb, Gd$ crystals in the $925 - 1100$ nm region, with excitation wavelength of 922 nm (a), and in the $840 - 925$ nm region, with excitation wavelength of 978 nm (b)

A similar result is reported at room temperature in the literature in oxide crystals having a much larger maximum phonon energy [97]. Interestingly the work of Jaque et. al. [97] shows that the $Yb^{3+} \rightarrow Nd^{3+}$ back-transfer can be thermally activated, with an efficiency that increases spectacularly for $T \geq 400$K, arriving even to reach an energy transfer efficiency of 25% for $T = 600$K.

Thus, in the next subsection dedicated to the energy transfer modeling, the absence of $Yb^{3+} \rightarrow Nd^{3+}$ back-transfer will be assumed.

2.7.3 $Nd^{3+} \rightarrow Yb^{3+}$ Energy Transfer Modeling

In this subsection, the energy transfer parameter and efficiency will be discussed in more details. With the experimental data collected and presented in subsections 2.7.1 and 2.7.2, it is possible to develop two different approaches in order to compare the experimental results with the modeling. The first approach is based on the luminescence intensity analysis [98], and the second one is based on lifetime analysis [99].

In a similar way as in [97, 98] , it is possible to write the main rate equations for the Nd-Yb system as

$$\begin{cases} \frac{dN_{Nd1}}{dt} = -\frac{dN_{Nd2}}{dt} = -RN_{Nd1} + W_{Nd2}N_{Nd2} + K_{ET}N_{Nd2}N_{Yb1} \\ \frac{dN_{Yb1}}{dt} = -\frac{dN_{Yb2}}{dt} = W_{Yb2}N_{Yb2} - K_{ET}N_{Yb1}N_{Nd2} \end{cases} \tag{2.32}$$

where R is the pumping rate, N_i is the population density of the level i, $W_i = W_i^{rad} + W_i^{nr}$ is the total decay rate from the level i and K_{ET} is the energy transfer parameter (in cm^3s^{-1}). As portrayed in Figure 2.26 the energy levels are labeled as

- "Nd1" for the Nd $^4I_{9/2}$ level
- "Nd2" for the Nd $^4F_{3/2}$ level
- "Yb1" for the Yb $^2F_{7/2}$ level
- "Yb2" for the Yb $^2F_{5/2}$ level

The energy transfer efficiency ETE is defined as the number of Nd^{3+} ions de-excited via energy transfer towards Yb^{3+} divided by the total number of Nd^{3+} ions de-excited per time unit:

$$ETE = \frac{K_{ET}N_{Yb1}N_{Nd2}}{W_{Nd2}N_{Nd2} + K_{ET}N_{Yb1}N_{Nd2}} \tag{2.33}$$

ETE Determination Using Integrated Luminescence Intensity

The number of Nd^{3+} ions de-excited via Yb^{3+} emission can be evaluated from the Yb luminescence intensity when exciting Nd ions as

$$K_{ET} N_{\mathrm{Yb1}} N_{\mathrm{Nd2}} = \frac{k}{\eta_{\mathrm{Yb}}} \int_{850\ \mathrm{nm}}^{1100\ \mathrm{nm}} I_{lum}^{\mathrm{Yb}}(\lambda)\mathrm{d}\lambda \tag{2.34}$$

where $I_{lum}^{Yb}(\lambda)$ is the luminescence intensity emitted by Yb^{3+} ions, η_{Yb} is the quantum efficiency of the $^2F_{5/2}$ state of ytterbium, and k is a constant representing the absolute spectral response of the detection setup (as introduced in subsection 2.2.3) . This setup dependent coefficient k is not necessary to estimate, since all the spectra are recorded with the same experimental conditions and furthermore the calculations exposed here consider only intensity ratios.

In a similar way, it is possible to estimate the first term in the denominator of equation (2.33) as

$$W_{\mathrm{Nd2}} N_{\mathrm{Nd2}} = \frac{k}{\eta_{\mathrm{Nd}}} \int_{850\ \mathrm{nm}}^{2000\ \mathrm{nm}} I_{lum}^{\mathrm{Nd}}(\lambda)\mathrm{d}\lambda = 1.1 \times \frac{k}{\eta_{\mathrm{Nd}}} \int_{850\ \mathrm{nm}}^{1100\ \mathrm{nm}} I_{lum}^{\mathrm{Nd}}(\lambda)\mathrm{d}\lambda \tag{2.35}$$

where η_{Yb} is the quantum efficiency of the $^4F_{3/2}$ state of Nd^{3+} in absence of energy transfer. The last part of the equation considers the intensity integral only up to 1100 nm and thus a coefficient of 1.1 is needed in order to take into account the $^4F_{3/2} \rightarrow\ ^4I_{13/2}$ and $^4F_{3/2} \rightarrow\ ^4I_{15/2}$ emission bands located at 1.3 μm and 1.8 μm that have not been recorded experimentally. In fact, it is well known in the literature [98, 100] and confirmed by the Judd-Ofelt calculations exposed in subsection 2.4.2, that the branching ratios β_i corresponding to the four transitions from the $^4F_{3/2}$ meta-stable level have the following relation:

$$\begin{cases} \beta_{^4I_{9/2}} + \beta_{^4I_{11/2}} \approx 9\beta_{^4I_{13/2}} \\ \beta_{^4I_{15/2}} \approx 0 \end{cases} \tag{2.36}$$

Since the $^4F_{3/2} \rightarrow\ ^4I_{13/2}$ represents 10% of the total $^4F_{3/2}$ radiative rate, it explains the 1.1 coefficient in equation (2.35). The energy gap between the $^4F_{3/2}$ level and its lower lying level $^4I_{13/2}$ (and also between the Yb $^2F_{5/2}$ and $^2F_{7/2}$ levels) is large enough compared to the maximum CaF_2 phonon energy so that multiphonon relaxation can be neglected. Thus the Nd and Yb quantum efficiency η_{Yb} and η_{Nd} in absence of energy transfer can be considered equal to one.

Finally, the energy transfer efficiency can be written as:

$$ETE = \frac{\int I_{lum}^{\mathrm{Yb}}(\lambda)\mathrm{d}\lambda}{1.1 \int I_{lum}^{\mathrm{Nd}}(\lambda)\mathrm{d}\lambda + \int I_{lum}^{\mathrm{Yb}}(\lambda)\mathrm{d}\lambda} \tag{2.37}$$

where all the intensity integrals are measured between 850 nm and 1100 nm.

For the calculations of the intensity integrals it is necessary to isolate the Nd and Yb contributions which otherwise overlap in the 1 μm range. To separate the two contributions when exciting at 791 nm, we used, the emission spectrum of $CaF_2 : 0.5\%Nd, 5\%Gd$ exciting again at 791 nm, to subtract the Nd emission spectrum from the luminescence spectra of $CaF_2 : Nd, Yb, Gd$, as displayed in Figure 2.33. The result of this subtraction represents the Yb emission contribution. To perform this subtraction, the spectra are normalized on the 863 nm peak of neodymium, where no luminescence of ytterbium occurs.

To further support the pertinence of such a subtraction one has to keep in mind that Nd ions can be part of two types of clusters:

- $Nd - Gd$ clusters, that are the dominant cluster type for low Yb concentration
- $Nd - Yb$ clusters, that are responsible for the $Nd \rightarrow Yb$ energy transfer and which concentration increases when increasing the Yb concentration.

As mentioned earlier, the emission spectra from Nd ions within $Nd - Yb$ clusters cannot be observed since it is quenched by energy transfer towards Yb ions. This explains why the sole contribution of Nd emission from $Nd - Gd$ clusters is sufficient for the subtraction. Following the subtraction of the Nd-Gd spectrum, we were able to separate the Yb and Nd emission contributions and thus to derive the ETE according to equation 2.33. The results are given in Table 2.8.

$CaF_2 : 0.5\%Nd, ..$	ETE
$0.2\%Yb, 4.8\%Gd$	0.16
$0.4\%Yb, 4.6\%Gd$	0.3
$0.7\%Yb, 4.3\%Gd$	0.44
$1\%Yb, 4\%Gd$	0.57
$2\%Yb, 3\%Gd$	0.65
$3\%Yb, 2\%Gd$	0.7

TABLE 2.8: ETE for different Yb and Gd concentrations, estimated using the integrated luminescence intensity.

It is worthy to notice that besides $Nd - Yb$ clusters Yb ions can be part of two other types of clusters: $Yb - Yb$ and $Yb - Gd$ clusters, which become dominant for large Yb concentration. So, when exciting Yb ions at 978 nm one can observe contributions from the three types of Yb containing clusters ($Nd - Yb$, $Yb - Gd$ and $Yb - Yb$).

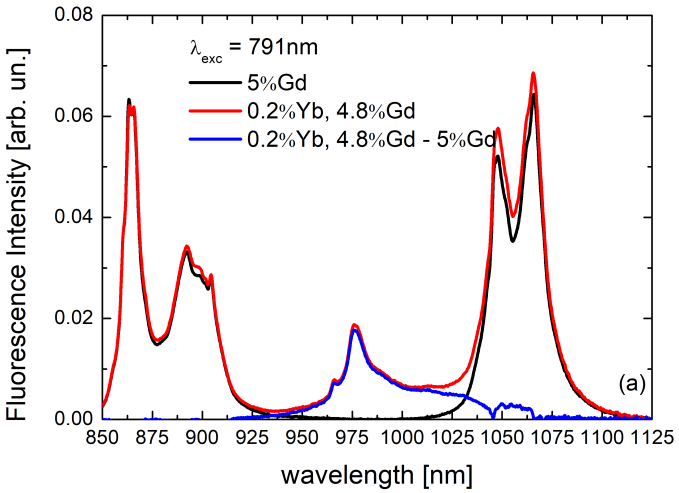
λexc = 791nm
5%Gd
0.2%Yb, 4.8%Gd
0.2%Yb, 4.8%Gd - 5%Gd
(a)
Fluorescence Intensity [arb. un.]
wavelength [nm]
0.00
0.02
0.04
0.06
0.08
850 875 900 925 950 975 1000 1025 1050 1075 1100 1125

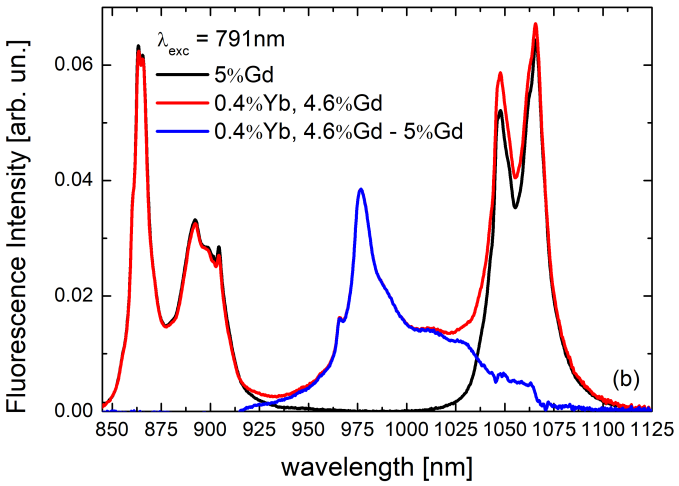
λexc = 791nm
5%Gd
0.4%Yb, 4.6%Gd
0.4%Yb, 4.6%Gd - 5%Gd
(b)
Fluorescence Intensity [arb. un.]
wavelength [nm]
0.00
0.02
0.04
0.06
850 875 900 925 950 975 1000 1025 1050 1075 1100 1125

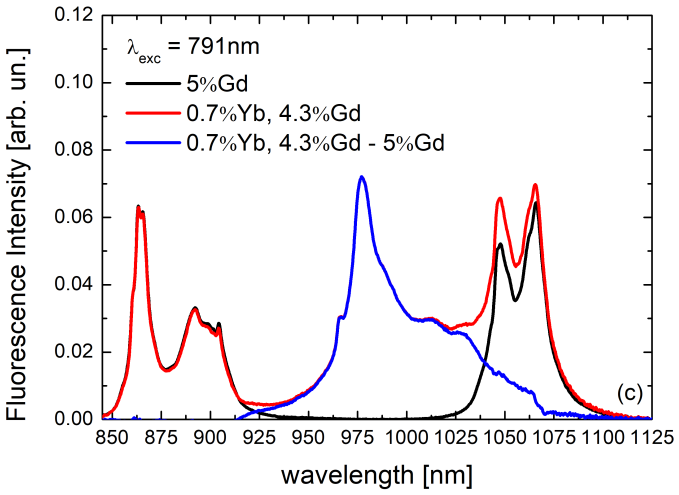
λexc = 791nm
5%Gd
0.7%Yb, 4.3%Gd
0.7%Yb, 4.3%Gd - 5%Gd
(c)
Fluorescence Intensity [arb. un.]
wavelength [nm]
0.00
0.02
0.04
0.06
0.08
0.10
0.12
850 875 900 925 950 975 1000 1025 1050 1075 1100 1125

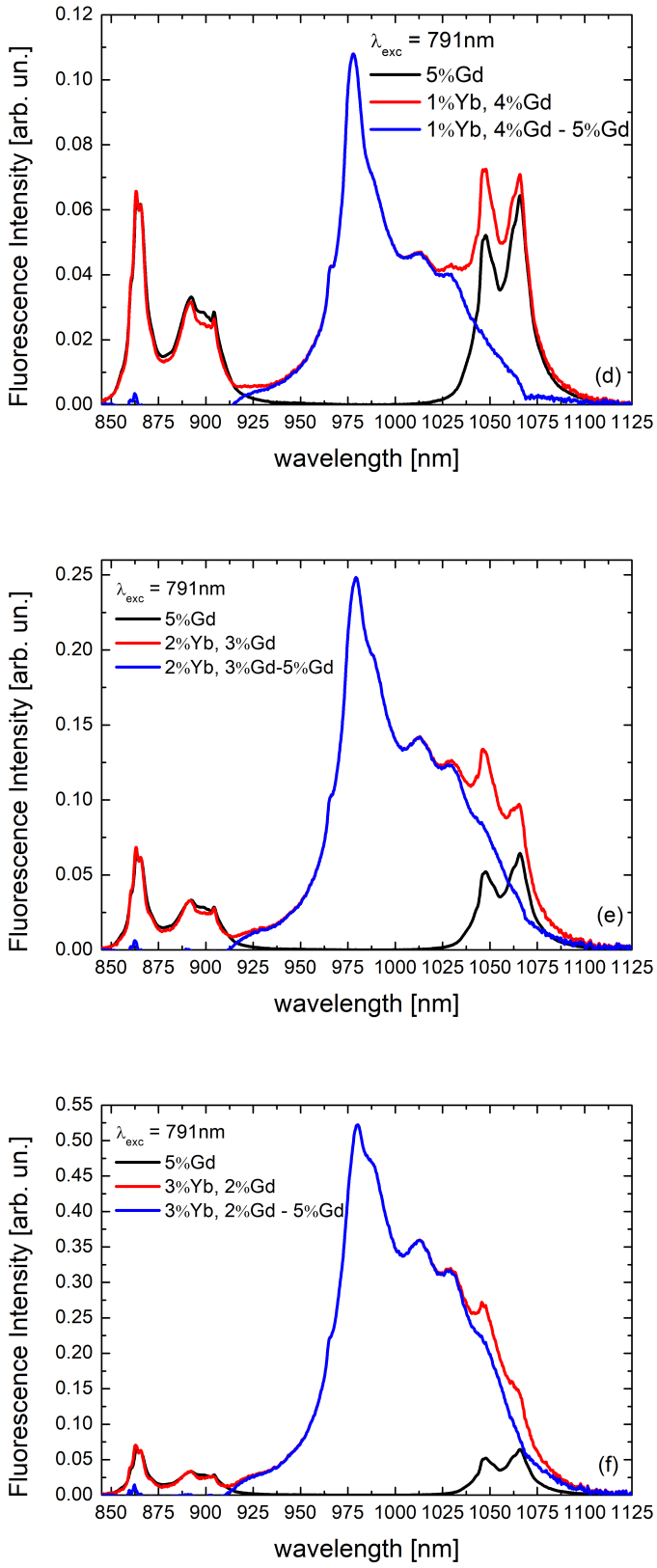

FIGURE 2.33: Luminescence of $CaF_2 : 0.5\%Nd, 5\%Gd$, $CaF_2 : Nd, Yb, Gd$ and calculated difference in blue for every ytterbium concentration. Normalization is performed on the 863 nm peak of neodymium, where no luminescence of ytterbium is involved.

Figure 2.36 shows a comparison between the Yb emission spectra exciting Yb at 978 nm and exciting Nd at 791 nm. One can observe a significant difference between the two Yb spectra which is more substantial at high Yb concentration (3at.%). The 791 nm excited spectrum is the signature of the $Nd-Yb$ clusters while the 978 nm excited spectrum contains contributions from all three Yb containing clusters. The $Nd-Yb$ cluster spectrum appears broader than the all Yb encompassing spectrum. This indicates a larger inhomogeneous broadening for $Nd-Yb$ clusters than for the two other types of Yb clusters ($Yb-Yb$ and $Yb-Gd$). Among these last two clusters it is clear that the $Yb-Yb$ clusters become more dominant than $Yb-Gd$ when the Yb concentration increases and the Gd decreases. This statement is further supported by Figure 2.34 which shows a comparison between the luminescence of $CaF_2 : 5\%Yb$ and $CaF_2 : 0.5\%Nd, 3\%Yb, 2\%Gd$. As expected, the two spectra are very similar indicating that the Yb-Yb clusters are dominant in $CaF_2 : 0.5\%Nd, 3\%Yb, 2\%Gd$.

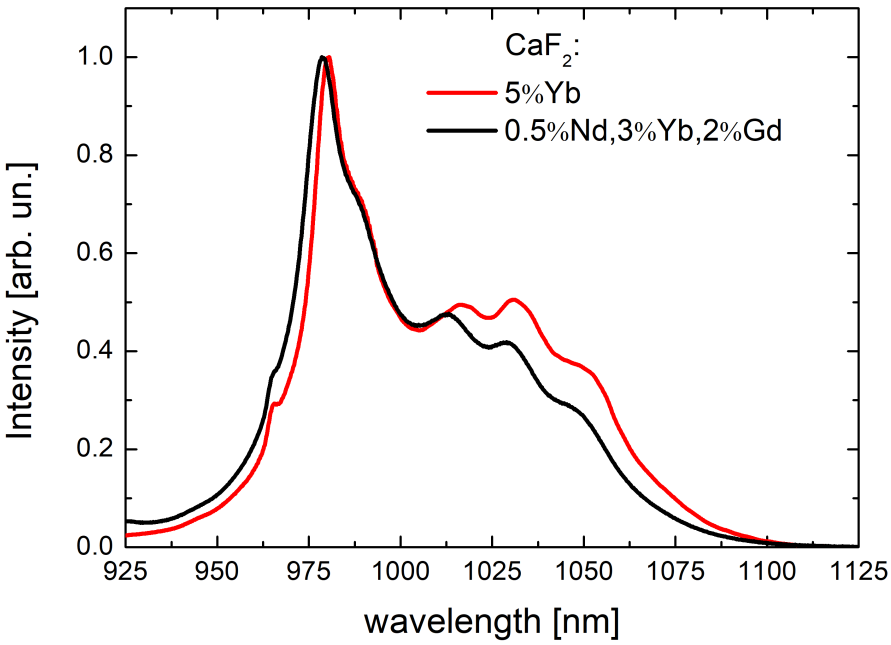

FIGURE 2.34: Luminescence spectrum of $CaF_2 : 5\%Yb$ compared with $CaF_2 : 0.5\%Nd, 3\%Yb, 2\%Gd$.

ETE Determination using Nd decays

The Nd to Yb energy transfer rate is simply connected to the fluorescence lifetime as

$$\tau^{-1}_{Nd,Yb,Gd} = \alpha_{ET} + \tau^{-1}_{Nd,Gd} \tag{2.38}$$

where $\tau_{Nd,Yb,Gd}$ is the $^4F_{3/2}$ lifetime in $CaF_2 : 0.5\%Nd, Yb, Gd$ which can be easily measured by exciting at 791 nm and detecting at 863 nm, α_{ET} is the energy transfer rate, and $\tau_{Nd,Gd}$ is the $^4F_{3/2}$ lifetime without energy transfer as measured in $CaF_2 : 0.5\%Nd, 5\%Gd$ (section 2.4). The energy transfer rate is related to the energy transfer parameter K_{ET} introduced before as

$$\alpha_{ET} = K_{ET} N_{Yb} \tag{2.39}$$

It is possible to estimate α_{ET} from eq. (2.38) and derive K_{ET} by a linear adjustment of α_{ET} as a function of the acceptor concentration (Yb) with eq. (2.39), as reported in Figure 2.35

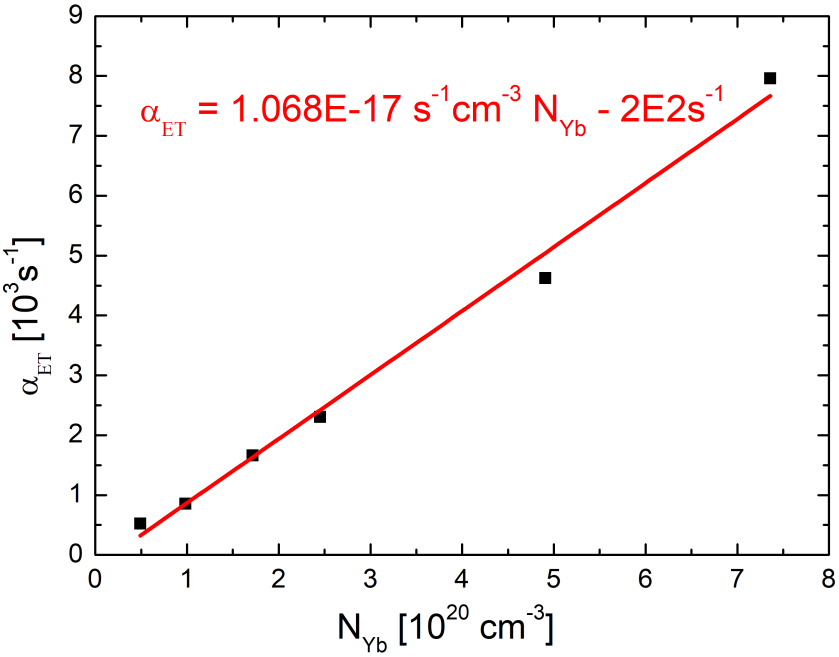

FIGURE 2.35: Energy transfer rate α_{ET} in function of the acceptor concentration N_{Yb}, deriving the energy transfer parameter K_{ET} from a linear fit.

The energy transfer rate exhibits a true linear dependence with the Yb concentration confirming equation 2.35.
One can notice the presence of a non-zero intercept in contradiction with eq. (2.39). This intercept represents the value of α_{ET} for $N_{Yb} = 0$, and is most likely due to an error in the value of $\tau_{Nd,Gd}$, estimated as $\tau_{Nd,Gd} = 490\ \mu s$. In order to have a zero intercept, one should use $\tau_{Nd,Gd} = 545\ \mu s$. This discrepancy corresponds roughly to a 10% error in $\tau_{Nd,Gd}$ which is a standard uncertainty when estimating lifetimes.

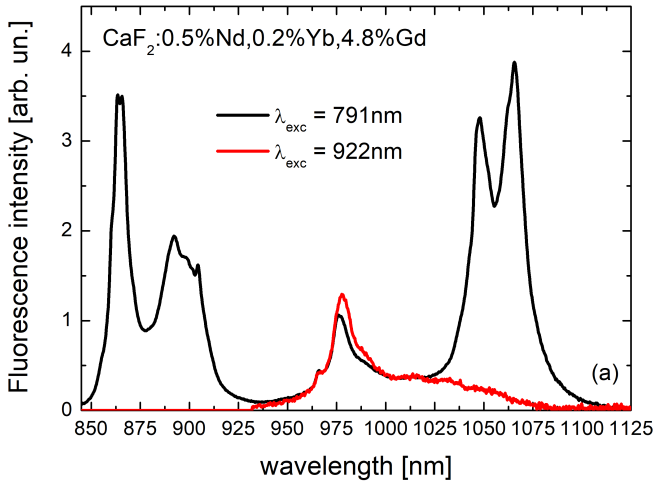
CaF2:0.5%Nd,0.2%Yb,4.8%Gd
λexc = 791nm
λexc = 922nm
(a)
Fluorescence intensity [arb. un.]
wavelength [nm]
0
1
2
3
4
850 875 900 925 950 975 1000 1025 1050 1075 1100 1125

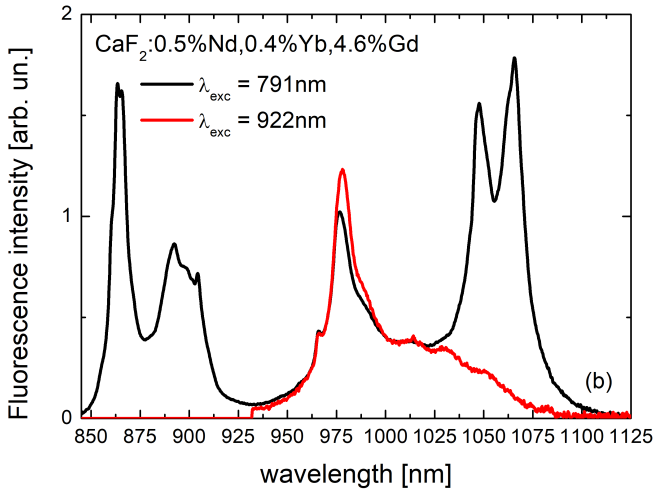
CaF2:0.5%Nd,0.4%Yb,4.6%Gd
λexc = 791nm
λexc = 922nm
(b)
Fluorescence intensity [arb. un.]
wavelength [nm]
0
1
2
850 875 900 925 950 975 1000 1025 1050 1075 1100 1125

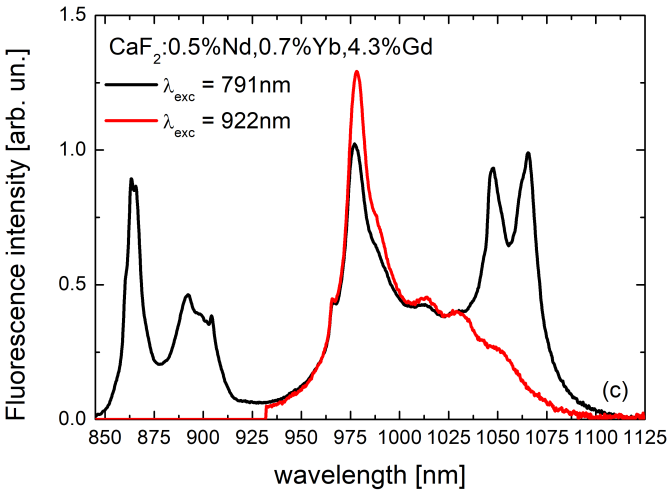
CaF2:0.5%Nd,0.7%Yb,4.3%Gd
λexc = 791nm
λexc = 922nm
(c)
Fluorescence intensity [arb. un.]
wavelength [nm]
0.0
0.5
1.0
1.5
850 875 900 925 950 975 1000 1025 1050 1075 1100 1125

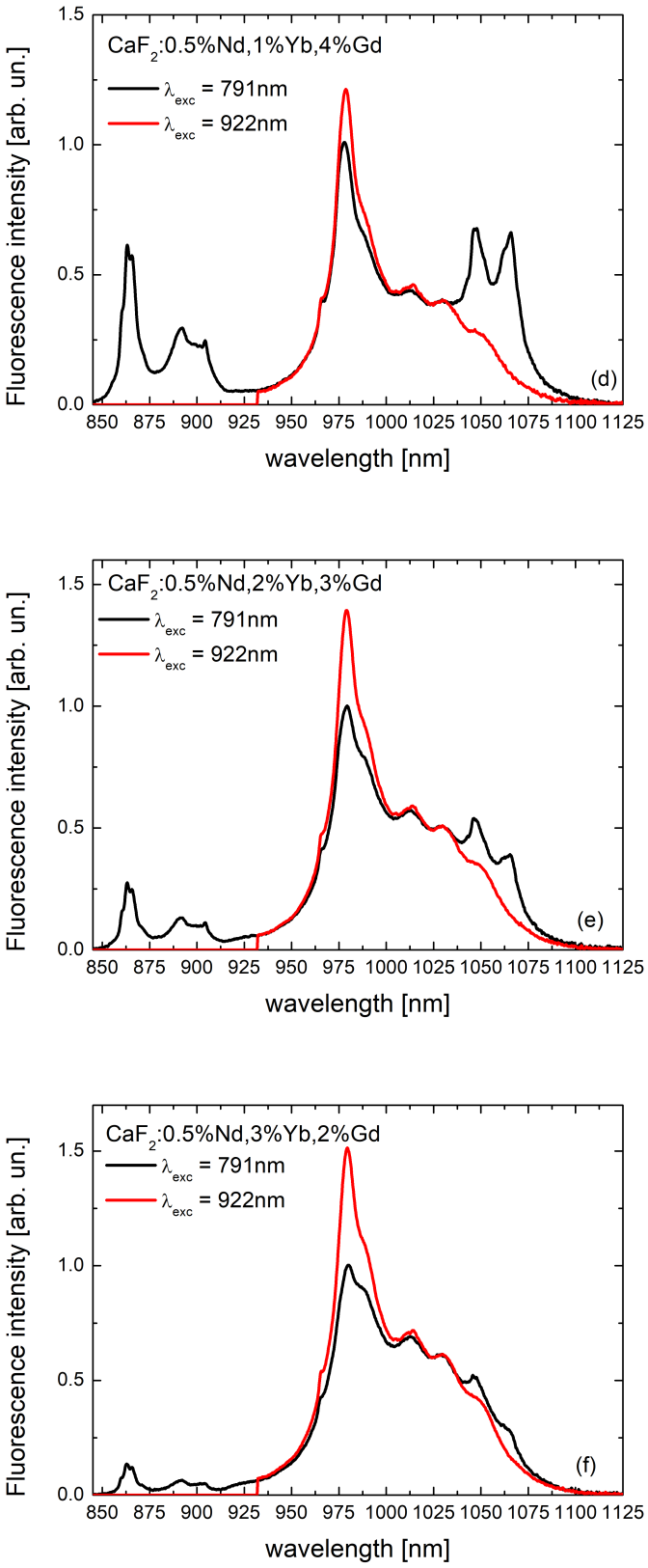

FIGURE 2.36: Luminescence of $CaF_2 : Nd, Yb, Gd$ excited at 791 nm and 922 nm for every gadolinium concentration. Normalization is performed on the 863 nm peak of neodymium, where no luminescence of ytterbium is involved.

The energy transfer efficiency can be defined as:

$$ETE = \frac{\tau^{-1}_{Nd,Yb,Gd} - \tau^{-1}_{Nd,Gd}}{\tau^{-1}_{Nd,Yb,Gd}} = 1 - \frac{\tau_{Nd,Yb,Gd}}{\tau_{Nd,Gd}} \tag{2.40}$$

and can be thus calculated and compared with the ETE values calculated using the luminescence integrals.

Both results are reported in Figure 2.37, from which it is possible to see that both approaches give consistent results, within a 10% error. In particular, the Nd to Yb energy transfer for the $CaF_2 : 0.5\%Nd, 3\%Yb, 2\%Gd$ is very promising, with an ETE of $70 - 80\%$, which is among the highest ETE reported in the literature for Nd $\rightarrow$ Yb energy transfer. As a comparison, the highest ETE reported are 65% in $YAl_3(BO)_4$ crystal [97], 79% in $YAlO_3$ crystal [96], 75% in $Pb(PO_3)_2$ glass [93], and 80% in fluoroindogallate glass [92]. Lastly, it is worth noticing in Figure 2.37 that for low ytterbium concentration, the increase of ETE is spectacular with the increase of the Yb acceptor concentration. When the Yb concentration reaches 2at.% and 3at.%, the ETE starts to saturate as it approaches 100%. This very high ETE values show that $CaF_2 : 0.5\%Nd, x\%Yb, x\%Gd$ is a promising crystal for pumping Yb ions using Nd excitation.

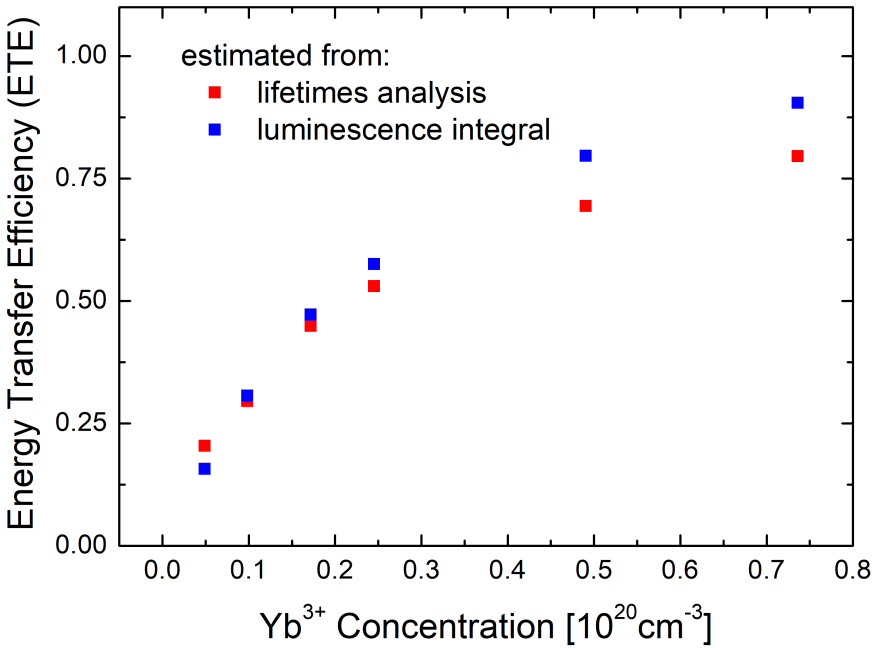

FIGURE 2.37: Energy transfer efficiency ETE in function of the acceptor concentration N_{Yb}, calculated from the luminescence integrals analysis and the lifetime analysis.

2.8 Conclusions

The results reported in this chapter give a detailed spectroscopic investigation of $CaF_2 : Nd, Bu$, where Bu is a buffer ion suppressing the occurrence of $Nd - Nd$ quenched clusters.

The co-doping with single buffer ion such as gadolinium, lanthanum, cerium, lutetium, yttrium and scandium clearly shows how the choice of the buffer ion can change the spectroscopic properties of $CaF_2 : Nd$, mainly dividing the buffers into two different groups. The buffer ions with larger size than Nd^{3+} ion, gadolinium, lanthanum and cerium, lead to a single dominant Nd emitting site, while the smaller ions, yttrium, lutetium and scandium, exhibit two different types of Nd sites. The two Nd sites have characteristic absorption and emission features and lifetimes, enabling not only their distinction in the spectral domain by choosing specific absorption and emission wavelengths, but also in lifetime, by choosing specific time windows using time-resolved spectroscopy to isolate the signature of each site. The first site, labeled N_1, and common to both groups of crystals, has a characteristic absorption peak around 791 nm and emission peak around 1049 nm, with a longer lifetime around $450 - 500$ μs, while the second site, labeled N_2, is characterized by an absorption peak around 797 nm, an emission peak around 1054 nm and a shorter lifetime, around $300 - 400$ μs. These two different centers are associated to quasi-rhombic centers for N_1 and quasi-tetragonal centers for N_2 [18].

Afterwards, an hybrid co-doping approach, employing one buffer from the large buffer group and one buffer from the smaller buffer group, growing $CaF_2 : Nd, Bu_1, Bu_2$ crystals has been investigated with interesting results. Depending on the concentration of the two buffers, it is possible to obtain intermediate spectroscopic behaviors, in between the two single co-doped crystals $CaF_2 : Nd, Bu_1$ and $CaF_2 : Nd, Bu_2$, enabling the tailoring of the spectroscopic properties by choosing carefully the buffer nature and concentration. The total buffer concentration was kept at 5at.% to ensure the absence of quenched $Nd - Nd$ clusters while not degrading further the thermo-mechanical properties. Moreover, the possibility to perform pre-growth simulations of the spectroscopic properties is successfully investigated, combining the spectra of the single co-doped $CaF_2 : Nd, Bu_1$ and $CaF_2 : Nd, Bu_2$ via linear combination, and obtaining exactly the experimental $CaF_2 : Nd, Bu_1, Bu_2$ spectrum. This enables a spectral engineering of $CaF_2 : Nd, Bu_1, Bu_2$, adjusting the nature and concentration of the buffers depending on the desired application. Moreover in the case of a monochromatic pumping of crystals with a small buffer ion such as Y, the pumping wavelength is critical to a sub-nanometer level in the $795 - 797$ nm to obtain the desired spectral shape, since within this spectral region the absorption coefficient of the N_2 sites rises spectacularly. We also investigated the possibility to further change the Nd spectroscopic properties by employing a third buffer ion while keeping the same total buffer concentration of 5at.%.

The linearity of this triple buffer approach has been corroborated, with the exception of scandium. In fact, while scandium alone breaks the $Nd - Nd$ clusters, we show that in a triple-co-doping structure scandium does not participate in the Nd cluster formation. The reason for this lies in its very small ionic radius (88 pm compared to 104 pm for yttrium for instance).

Few compositions have been identified leading to a rather flat emission profile around 1053 nm as wanted for the LMJ applications, such as $\mathbf{CaF_2 : 0.5\%Nd, 3\%Gd, 1.4\%Ce, 0.6\%Y}$ with a 5 nm flat emission band when excited at 797.0 nm, or $\mathbf{CaF_2 : 0.5\%Nd, 2.5\%Gd, 2.5\%Y}$ excited at 796.2 nm. The $\mathbf{CaF_2 : 0.5\%Nd, 4\%Gd, 1\%Y}$ crystal when excited at 797.0 nm also represents a valid alternative, with a rather flat profile of 5 nm, similar to the $3\%Gd, 1.4\%Ce, 0.6\%Y$ crystal. Finally, the $\mathbf{CaF_2 : 0.5\%Nd, 3.8\%Gd, 0.65\%Y, 0.55\%La}$ crystal also gives a flat emission profile over 4.4 nm which is slightly smaller than for the three other compositions.

Lastly, $CaF_2 : Nd, Yb, Gd$ crystals are studied with the particularity of using Yb ions both as active ions and buffer ions. This codoping is interesting because of its very large emission band when pumping neodymium ions, as well as the possibility to take advantage of the large absorption cross section of neodymium to populate the $^2F_{7/2}$ state of ytterbium by energy transfer from Nd. The Nd to Yb energy transfer efficiency (ETE) is estimated using two different approaches based on intensity measurements and lifetimes which give very similar results. A maximum ETE of 80% is achieved in $CaF_2 : 0.5\%Nd, 3\%Yb, 2\%Gd$ crystal.

In the next chapter, the laser gain characteristics are investigated, comparing a modeling approach with laser gain measurements using a dedicated pump-probe setup.

Chapter 3

Amplification Properties

3.1 Introduction

The results of Chapter 2, identified crystals with different co-doping combinations exhibiting interesting flat bands , namely CaF_2. : 0.5%Nd with 2.5%Gd, 2.5%Y or 4%Gd, 1%Y, or 3.8%Gd, 0.65%Y, 0.55%La and 3%Gd, 1.4%Ce, 0.6%Y. These materials are promising candidates as laser amplifiers for the LMJ applications. It is therefore interesting to study their amplification properties using both experimental and theoretical approaches. The front-end of the LMJ uses a 16 nm FWHM (full width at half maximum) probe beam centered at 1053.0nm which is amplified up to 1 J while preserving a large bandwidth of the amplified beam. The probe beam is subject to the well-known gain narrowing within the amplifier. Indeed, the center region of the probe spectrum experiences a higher gain than the spectral wings causing a spectral narrowing of the amplified beam. In order to assess the potentiality of our laser crystals to preserve a wide enough amplified beam, we designed in collaboration with the CEA-CESTA an amplification criterion.

This criterion consists in obtaining after amplification an amplified beam centered at 1053.0 nm with at least 3 nm of FWHM, with the input probe beam being a gaussian beam with a 16 nm FWHM centered at 1053.0 nm. The amplification factor (P_{out}/P_{in}) is set at 10^9 corresponding to a gain of 20.72. This criterion will be first discussed before investigating the crystals amplification properties . These properties are studied from a theoretical point of view by developing a calculation of the amplification factor P_{out}/P_{in} using the spectroscopy experimental data of Chapter 2. The results of this modeling are then compared to an actual measurement of the amplification factor using a dedicated pump-probe setup. This setup uses two tunable Ti-Saph lasers with both beams modulated at different frequencies, that will be described in details in section 3.6.

3.2 Amplification Criterion

The amplification, criterion presented earlier requires an amplified beam at the amplifier output with a FWHM at least of 3 nm around 1053 nm for a

FWHM = 16 nm input Gaussian beam. Thus, the input beam intensity can be expressed as a gaussian profile with a FWHM $\Delta\lambda_i$:

$$I_i(\lambda) = \exp\left(-4 \cdot \ln 2 \cdot \frac{\lambda^2}{\Delta\lambda_i^2}\right) \tag{3.1}$$

The amplifier based on CaF_2, Nd, Bu, will have a gain G. Thus the output intensity will be given by

$$I_{out}(\lambda) = \left[\exp -4 \cdot \ln 2 \cdot \frac{\lambda^2}{\Delta\lambda_i^2}\right] \cdot I_{fluo}(\lambda)^G \tag{3.2}$$

where $I_{fluo}(\lambda)$ is the fluorescence spectrum equivalent to the gain spectrum. For the LMJ applications, the wanted gain is $G = 20.72$, corresponding to an amplification factor of 10^9.

The calculation of the amplified spectrum has been performed for the four crystals mentioned earlier,using their respective fluorescence spectrum as gain spectrum. The different amplified spectra are compared in Figure 3.1, with the LGG70 phosphate glass currently employed in the LMJ. All tested crystals exhibit a wider FWHM spectrum, around $5-6$ nm than the 3 nm FWHM obtained with the LG770 glass. However, the centering of the amplified band at 1053 nm is not accurate. While all crystals have their maximum amplified signal at 1053 nm, the bandwidth falls sharply on the long wavelength part of the spectrum.

Figure 3.2 illustrates the impact of the amplification factor on the amplified spectrum for the $CaF_2 : 0.5\%Nd, 3\%Gd, 1.4\%Ce, 0.6\%Y$ crystal for gain factors of 10^3, 10^5, 10^7, 10^9. It is possible to see how the FWHM is sensibly reduced at higher gain values, as expected, while the wavelength for the maximum amplified intensity remains at 1053 nm.

3.3 Gain Modelling

We investigate in this section $CaF_2 : Nd, Bu$ gain and amplification properties . First we present a model of the laser amplification employing the spectroscopic properties presented in Chapter 2.

Figure 3.3 shows the labeling of the energy levels from level 1 for the ground state to level 4 for the $^4F_{5/2}$ level. A rate equation approach has been employed, with the common assumptions that the $^4F_{5/2} \rightarrow {}^4F_{3/2}$ and $^4I_{11/2} \rightarrow {}^4I_{9/2}$ transitions are extremely fast due to multiphonon relaxation. To provide a complete modeling of the amplification process, the spatial distribution of the pump and the probe beam are taken into account, considering them as Gaussian beams. As a reference for this model, the work of Fan [101, 102] has been first considered for the analytical approach, together with other similar studies [103–108]. The model developed here

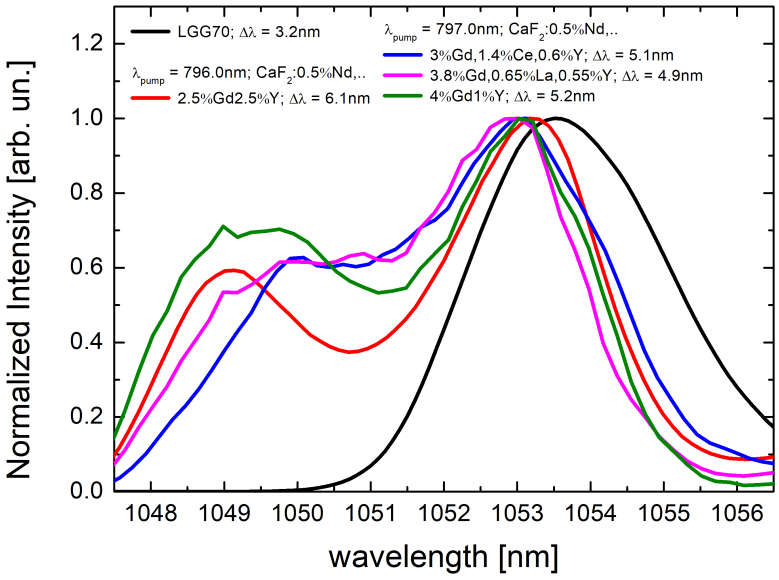

FIGURE 3.1: Amplified spectrum of a 16 nm FWHM probe beam centered at 1053 nm input beam with a gain $G = 20.72$ for different gain media, compared with the reference LGG70 glass currently used in the LMJ.

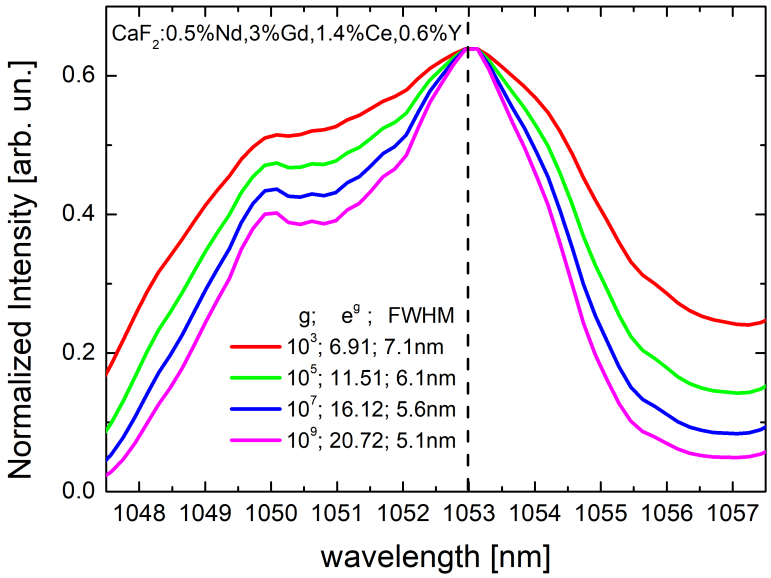

FIGURE 3.2: Amplified spectrum of a 16 nm input beam at 1053 nm employing the 3%Gd, 1.4%Ce, 0.6%Y as amplifying medium, for different values of gain.

includes the ground state depletion and gain saturation effects, that are usually not considered together when trying to develop a fully analytical analysis.

3.3.1 Rate Equations: Four-Level System

The $^4F_{5/2}$ level, labeled as number 4 (Figure 3.3) is pumped around $790 - 800$ nm, from which a nearly instantaneous non-radiative decay, occurs to populate the $^4F_{3/2}$ level, labeled in this scheme as number 3. The laser transition at 1 μm occurs between the $^4F_{3/2}$ and the $^4I_{11/2}$ (labeled as 2), from which ions relax by non-radiative relaxation to the ground state $^4I_{9/2}$, labeled as 1.

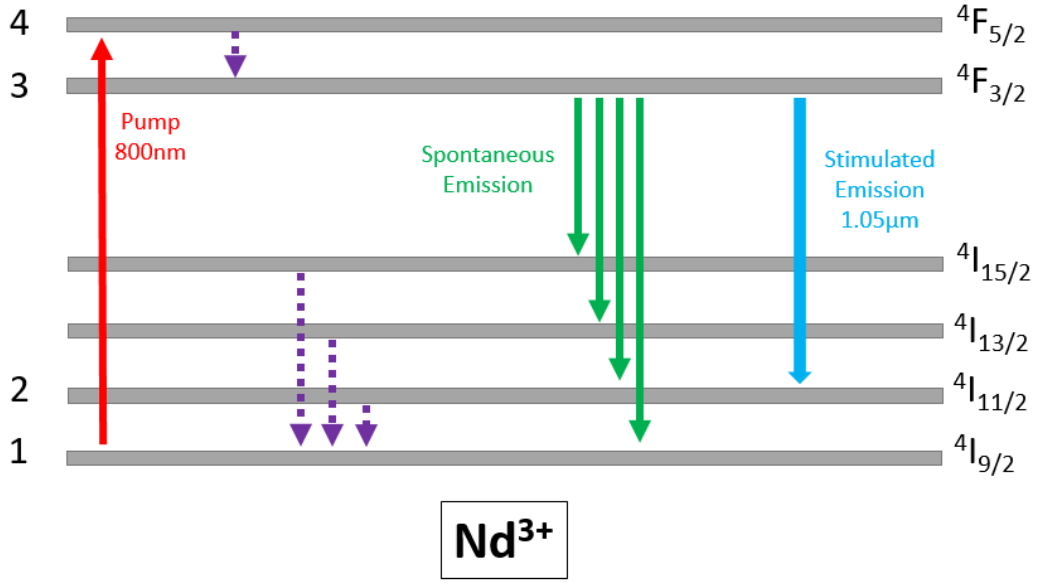

FIGURE 3.3: Four-level system diagram of Nd^{3+} for laser operation at 1.05 μm pumped at 800 nm

The rate equations of this system can be written as:

$$\frac{dN_1}{dt} = -RN_1 + W_{21}N_2 + W_{31}N_3 + B_{NR} \tag{3.3}$$

$$\frac{dN_2}{dt} = W_{32}N_3 + A_L(N_3 - N_2) - W_{21}N_2 \tag{3.4}$$

$$\frac{dN_3}{dt} = W_{43}N_4 - (W_{31} + W_{32})N_3 - A_L(N_3 - N_2) \tag{3.5}$$

$$\frac{dN_4}{dt} = RN_4 - W_{43}N_4 \tag{3.6}$$

where R is the pumping rate, $W_{ij} = \beta_{ij}W_i$ is the probability transition rate from level i to level j with β_{ij} the correspondent branching ratio and W_i

the total emission rate, A_L is the stimulated emission rate and the term B_{NR} takes into account the transition mediated by the intermediate levels $^4I_{15/2}$ and $^4I_{13/2}$.

The total relaxation rate $(W_{31} + W_{32})N_3$ term of the N_3 level in eq.(3.3) can be simply written as

$$W_3 N_3 = W_{31} N_3 + W_{32} N_3 \tag{3.7}$$

In steady state conditions, $\frac{dN_i}{dt} = 0$ for all levels i. This leads for the lower laser level N_2 to

$$W_2 N_2 = W_{32} N_3 + A_L (N_3 - N_2) \tag{3.8}$$

Since non-radiative transitions are considered to be nearly instantaneous, it is possible to set to zero the populations of the levels in which non-radiative relaxation take place, namely

$$N_2 = N_4 = 0 \tag{3.9}$$

This assumption, with eq.(3.7) and eq.(3.8), gives the following result for the ground state level population rewriting eq. (3.3):

$$\frac{dN_1}{dt} = -RN_1 + A_L N_3 + W_3 N_3 \tag{3.10}$$

In the same way, considering $\frac{dN_4}{dt} = 0$ and rewriting the upper laser level state population eq.(3.5)

$$\frac{dN_3}{dt} = RN_1 - W_3 N_3 - A_L N_3 \tag{3.11}$$

This shows clearly that $\frac{dN_1}{dt} = -\frac{dN_3}{dt}$, that is consistent with the total ion density N_T being constant. Thus,

$$N_T = N_1 + N_3 \tag{3.12}$$

In steady state conditions eq.(3.10) and eq.(3.11) become:

$$N_1 = \frac{A_L N_3 + W_3 N_3}{R} = \frac{A_L + W_3}{R}(N_T - N_1) \tag{3.13}$$

$$\Rightarrow N_1 = \frac{N_T}{1 + \frac{R_P}{W_3 + A_L}} = \frac{N_T}{1 + \frac{\tau_f R}{1 + \tau_f A_L}} \tag{3.14}$$

$$N_3 = N_T - N_1 = \frac{N_T}{1 + \frac{1 + \tau_f A_L}{\tau_f R}} \tag{3.15}$$

where $\tau_f = W_3^{-1}$ is the fluorescence lifetime of $^4F_{3/2}$ level.

The laser gain coefficient g, in cm^{-1} can then be derived as:

$$g = \sigma_{eL} N_3 - \sigma_{abs,L} N_2 = \frac{\sigma_{eL} N_T}{1 + \frac{1+\tau_f A_L}{\tau_f R}} \tag{3.16}$$

where σ_{eL} and $\sigma_{abs,L}$ are the emission and absorption cross sections at the laser wavelength and $N_2 = 0$.

3.3.2 Propagation in the Amplifying Medium

To accurately model the gain coefficient and the amplification properties of the gain medium, it is necessary to consider the spatial distribution of both the pump and probe beams.

Let's start considering an intensity $I_p(r,z)$ incident to the amplifying medium, where $z = 0$ corresponds to the input point of the beam into the crystal. The pump rate R, in s^{-1}, is defined as

$$R(r,z) = \sigma_{abs}(\lambda_p) \frac{I_p(r,z)}{h\nu_P} \tag{3.17}$$

where the intensity $I_p(r,z)$ is the pump beam intensity considered as Gaussian:

$$I_p(r,z) = I(0,z) \exp\Big(-\frac{2r^2}{\omega_p(z)^2}\Big) = \frac{2P_p}{\pi\omega_p^2(z)} \exp\Big(-\frac{2r^2}{\omega_p(z)^2}\Big) \tag{3.18}$$

where P_p is the pump power, and $\omega_p(z)$ is the waist of the beam, which for a Gaussian beam corresponds to

$$\omega_p(z) = \omega_{p,0} \sqrt{1 + \Big(M^2 \frac{z\lambda_p}{\pi\omega_{p,0}^2}\Big)^2} \tag{3.19}$$

with λ_p the wavelength of the pump photons, M^2 the beam quality factor and $\omega_{p,0}$ the waist at $z = 0$, while the pump beam intensity in the center of the beam $I_p(0,z)$ is simply

$$I(0,z) = \frac{2P_p}{\pi\omega_p^2(z)} \tag{3.20}$$

The pump beam intensity $I_p(r,z)$ can be simply calculated using the Lambert-Beer law,

$$\frac{dI_p(r,z)}{\mathrm{d}z} = -\alpha(r,z) I_p(r,z) \tag{3.21}$$

where $\alpha(r,z) = \sigma_{abs}(\lambda_p) * N_1(r,z)$ is the absorption coefficient and $\sigma_{abs}(\lambda_p)$ the absorption cross section.

In order to model numerically the propagation of the pump beam, the amplifying medium is divided in infinitesimal slices of a dz thickness along the propagation direction z and dr along the radial direction. Thus, from eq. (3.21), one can write :

$$I_p(r, z + \mathrm{d}z) = I_p(r, z)(1 - \alpha(r, z)\mathrm{d}z) \tag{3.22}$$

which enables a recursive approach of the pumping process that we modeled using a python code. Knowing the expressions of $N_1(r, z)$ (eq.(3.13)) and then $\alpha(r, z)$ (eq.(3.22)):

$$\begin{cases} N_1(r, z) = \frac{N_T}{1 + \frac{\tau_f R(r,z)}{1+\tau_f A_L(r,z)}} \\ \alpha(r, z) = \sigma_{abs}(\lambda_p) N_1(r, z) \end{cases} \tag{3.23}$$

one can derive the pump rate at $z + \mathrm{d}z$

$$R(r, z + \mathrm{d}z) = \frac{\sigma_{abs}(\lambda_p)}{h\nu_P} I_p(r, z)(1 - \alpha(r, z)\mathrm{d}z) \tag{3.24}$$

Eq. (3.23) shows that in order to perform the calculation of the $N_1(r, z)$ population, it is necessary to model the stimulated emission rate $A_L(r, z)$ which depends on the probe beam profile.

In a similar way as for the definition of the pump rate in eq.(3.17), the stimulated emission rate $A_L(r, z)$, in s^{-1} is defined as

$$A_L = \sigma_{eL}(\lambda_L) \frac{I_L(r, z)}{h\nu_L} \tag{3.25}$$

with $h\nu_L$ being the probe photon energy and $I_L(r, z)$ the intensity of the probe beam:

$$I_L(r, z) = I_L(0, 0) \exp\left(- \frac{2r^2}{\omega_L(z)^2} \right) \tag{3.26}$$

The intensity increase of the probe beam along the propagation direction because of the stimulated emission, can be calculated for every infinitesimal dz, in an analogue way as for the pumping process, as

$$I_L(r, z + \mathrm{d}z) = I_L(r, z)(1 + g(r, z)\mathrm{d}z) \tag{3.27}$$

with g(r,z) the gain coefficient introduced in eq.(3.16):

$$g(r, z) = \sigma_{eL} N_3(r, z) \tag{3.28}$$

from which one can derive

$$A_L(r, z + \mathrm{d}z) = \frac{\sigma_{eL}(\lambda_L)}{h\nu_L} I_L(r, z)(1 + g(r, z)\mathrm{d}z) \tag{3.29}$$

Thus, knowing the expressions of $N_3(r,z)$ (eq. 3.15) and then $g(r,z)$ (eq. 3.29)

$$\begin{cases} N_3(r,z) = N_T - N_1 = \frac{N_T}{1+\frac{1+\tau_f A_L(r,z)}{\tau_f R(r,z)}} \\ g(r,z) = \sigma_{eL} N_3(r,z) \end{cases} \tag{3.30}$$

one can derive the stimulated emission rate at $z + dz$ in a recursive approach:

$$A_L(r, z+dz) = \frac{\sigma_{eL}}{h\nu_L} I_L(r,z)(1 + g(r,z)dz) \tag{3.31}$$

The probe output power can then be calculated by integrating the probe intensity $I_L(r,z)$ over its radial dimension at the output of the laser crystal ($z = L_z$ with L_z the crystal length):

$$P_{L,out} = 2\pi \int_0^\infty I_L(r, L_z) r dr \tag{3.32}$$

from which the amplification factor can be calculated as the ratio between output power and input power,:

$$G_p = \frac{P_{L,out}}{P_{L,in}} \tag{3.33}$$

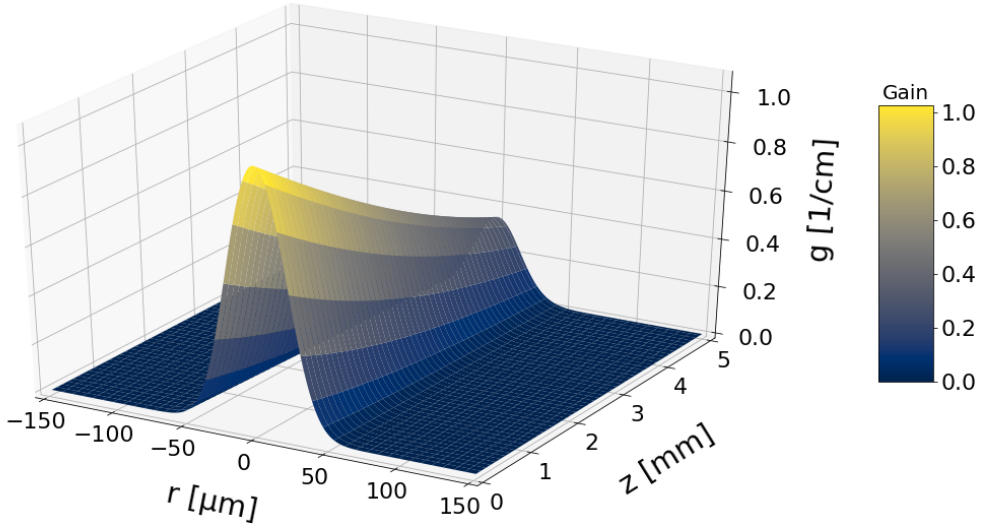

FIGURE 3.4: Gain coefficient per centimeter calculated in small signal conditions for a 5 mm thick $CaF_2 : 0.5\%Nd^{3+}, 5\%Lu^{3+}$ crystal: $P_{p,0} = 0.5$W, $P_{L,0} = 1$mW, $\omega_{p,0} = \omega_{L,0} = 50\mu$m, $\lambda_p = 797$nm, $\lambda_L = 1053$nm.

While this approach does not provide a fully analytical solution, it has the advantage of not neglecting the ground state depletion or the gain saturation and provide an accurate estimation of the amplification process. As an example, in Figure 3.4 it is displayed the gain coefficient g(r,z) in cm^{-1} of

a 5 mm thick $CaF_2 : 0.5\%Nd^{3+}, 5\%Lu^{3+}$ crystal for an incident pump power of 500 mW at 797 nm.

3.3.3 Ground State Depletion and Gain Saturation

From the final expression of the gain coefficient, eq.(3.16), it is possible to identify different saturation effects.

Ground State Depletion

First, when the incident pump power increases, more Nd^{3+} ions are pumped into the upper laser level N_3. This, in turn leads to a depletion of the ground state. This depletion affects the absorption coefficient which will decrease as the pump power increases, In other words the pump absorption starts to saturate. Eq.(3.16), shows that for a very large pumping rate ($R \to \infty$), the gain coefficient tends towards an upper limit value equal to $N_T \sigma_{eL}(\lambda_L)$:

$$g(r,z) = \sigma_{eL}(\lambda_L) \frac{N_T}{1 + \frac{1+\tau_f A_L(r,z)}{\tau_f R(r,z)}} \xrightarrow{R\to\infty} \sigma_{eL}(\lambda_L) N_T \tag{3.34}$$

This case corresponds to the situation where $N_3 = N_T$, i.e. the ground state is fully depleted in favor of the $^4F_{3/2}$ level.

It is worth noticing that in order to evaluate the impact of the ground state depletion (GSD) on the pump beam propagation, it is possible to calculate the ratio $\alpha(r,z)/\alpha_0$, where $\alpha_0 = \sigma_{abs} N_T$ is the absorption coefficient without GSD.

Gain Saturation

When a small probe signal is injected in a gain medium, the signal gets amplified in an exponential way as stated in eq. (3.27). However, for a strong enough input signal, the stimulated emission rate A_L becomes large enough to depopulate the $^4F_{3/2}$ emitting level. As a consequence the gain coefficient starts to decrease. Eq.(3.16) shows that for very high probe intensity ($A_L \to \infty$), the gain coefficient tends to zero :

$$g(r,z) = \sigma_{eL}(\lambda_L) \frac{N_T}{1 + \frac{1+\tau_f A_L(r,z)}{\tau_f R(r,z)}} \xrightarrow{A_L\to\infty} 0 \tag{3.35}$$

This well-known phenomenon is usually called gain saturation. It has to be noted that the condition $A_L \to \infty$ can be theoretically reached both for $P_{L,in} \to \infty$ or for $\omega_{L,0} \to 0$.

Figure 3.5 illustrates both the ground state depletion and the gain saturation, for different values of pump and probe power, using the numerical approach presented in the previous section, with $CaF_2 : 0.5\%Nd, 5\%Lu$ as amplifying medium, keeping the probe and pump waists constant as $\omega_p = \omega_L = 50\ \mu m$.

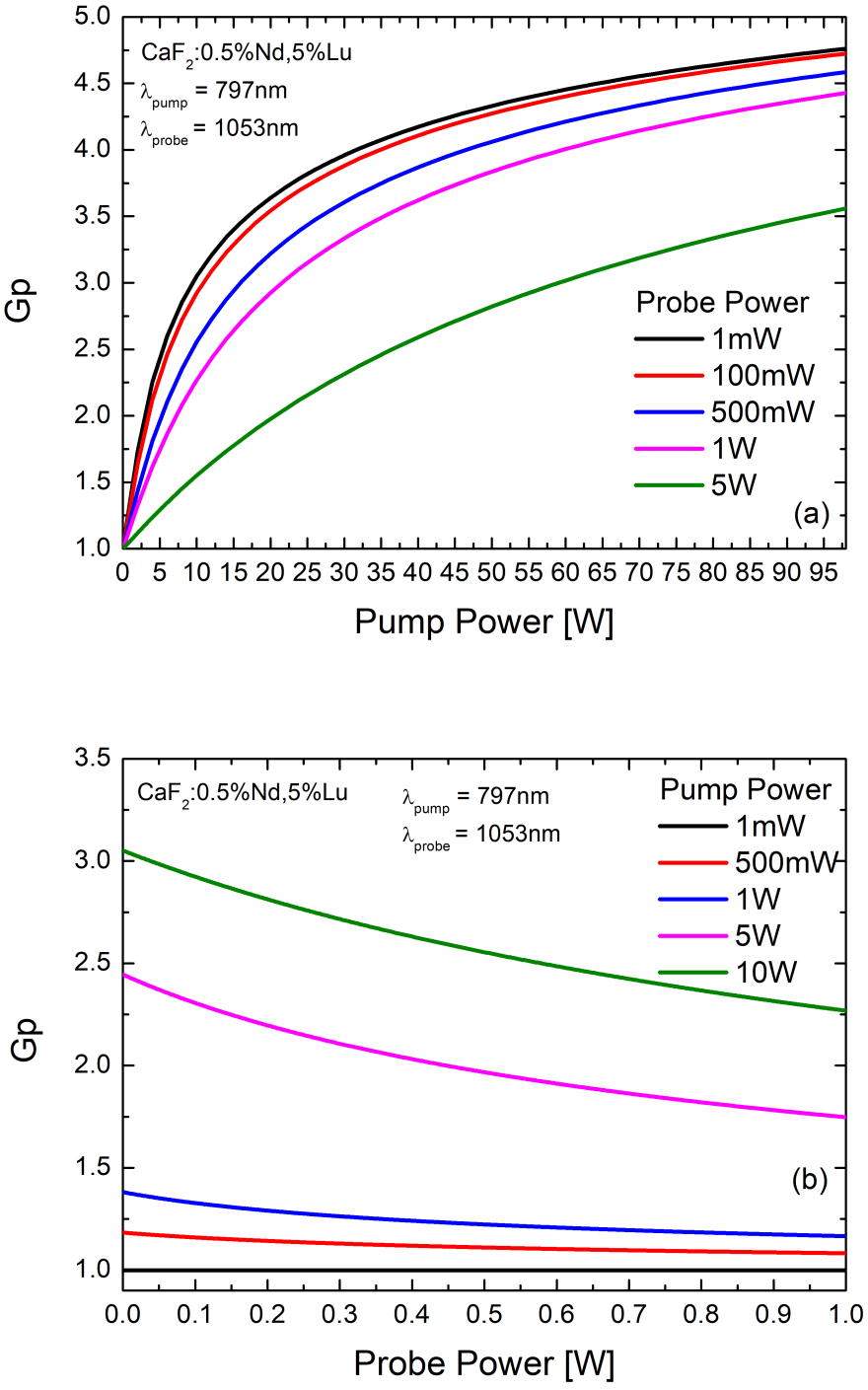

FIGURE 3.5: (a) Amplification factor as a function of the pump power, for different probe powers. (b) Amplification factor as a function of the probe power, for different pump power values. Waists values: $\omega_p = \omega_L = 50\ \mu$m.

To neglect the gain saturation effect in Figure 3.5,(a), one can look at the small probe power case (1 mW, black curve), which corresponds to the small signal gain (ssg) regime. While at small pump power, the amplification factor increases linearly, it starts to saturate at 10 W of pumping level. The same figure (3.5,(a)) shows the combination of ground state depletion and gain saturation when the probe power increases ($P_L = 5$ W, green curve). At small pump power, the slope of the linear gain increase is smaller (green curve) than when the probe power is small (black curve) illustrating the effect of gain saturation.

Figure (3.5,(b)) gives another example of gain saturation where one can see the decrease of the amplification factor with the probe power. This figure also shows the ground state depletion when comparing two curves at different pump powers. For instance, while the pump power is doubled from 5 to 10 W, the amplification factor goes from 2.4 to only 3.1 at low probe power.

The small signal gain coefficient g_{SS}, can be easily written by assuming that the probe power remains small. Eq. (3.16) becomes then:

$$g_{SS}(r,z) = \sigma_{eL}(\lambda_L)\frac{N_T\tau_f R(r,z)}{\tau_f R(r,z)+1} \tag{3.36}$$

which only takes into account the possible ground state depletion. Interestingly, the ratio between the gain $g(r,z)$ and the $g_{SS}(r,z)$ can be written:

$$\frac{g(r,z)}{g_{SS}} = \frac{\tau_f R(r,z)+1}{\tau_f R(r,z)+\tau_f A_L(r,z)+1} \tag{3.37}$$

3.4 Experimental Amplification Measurements

While the amplification can be calculated as presented in the previous section, we also implemented a dedicated pump-probe setup for the amplification measurements. Two tunable Coherent Ti:Sapphire, pumped by a Coherent Verdi V6 green laser have been combined acting as pump and probe beams respectively. The amplifying medium ($CaF_2 : Nd, Bu$ crystal), is pumped around 800 nm while the probe beam is tuned in the $1040 - 1060$ nm spectral range. A scheme of the experimental setup is presented in Figure 3.6.

Both pump and probe beams are modulated at very different frequencies, using two lock-in amplifiers as detection system. The two beams are overlapped using a dichroic mirror, and focused into the crystal with a 75 mm focal length lens. After the crystal the transmitted pump beam is filtered out using a long pass filter at 950 nm to allow the detection of the amplified signal around 1050 nm with a Thorlabs PDA100A-EC Si photodiode. The resulting experimental signal as depicted in Figure 3.7, is a square wave probe on/probe off signal, with a 50% intensity duty cycle. One can see in Figure 3.7 the low frequency modulation at 18 Hz of the probe beam being modulated by the higher frequency at 180 Hz of the pump beam. The intensity

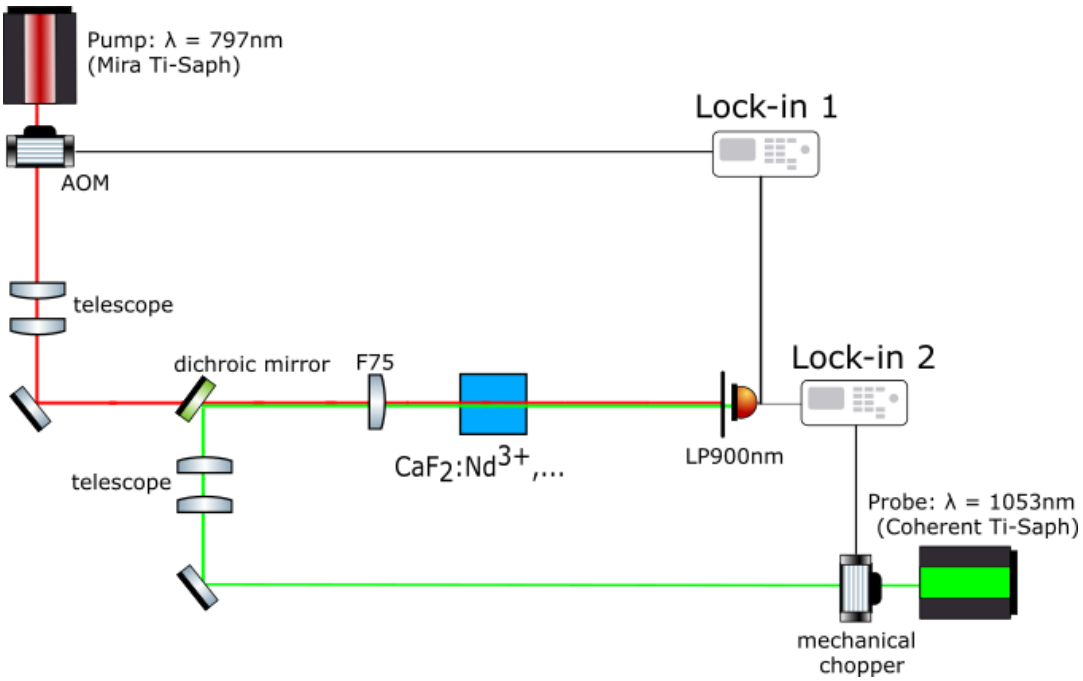

FIGURE 3.6: Experimental setup for the gain measurement.

variation ΔI between the pump on and off cases illustrates the magnitude of the laser probe amplification. In Figure 3.7 I_0 represents the incident probe beam intensity, and $I_0 + \Delta I$ the amplified probe beam intensity. This signal is then sent to the two lock-in amplifiers, one locked onto the pump frequency labelled "Lock-in 1" and the second one locked on the probe beam frequency, labelled "Lock-in 2". The output signal L1 from lock-in 1 at the pump frequency is proportional to $\Delta I/2$ since the pump beam is on the sample only half of the time. The output signal from L2 at the probe frequency is proportional to $I_0 + \Delta I/2$. From the definition of the amplification factor, one can derive:

$$G = \frac{I_{out}}{I_{in}} = 1 + \frac{\Delta I}{I_0} = \frac{L_1 + L_2}{L_2 - L_1} \tag{3.38}$$

The advantage of such a setup resides firstly in the tunability of both the pump and probe beams. Furthermore, this double modulation allows for a better management of possible thermal effects which would otherwise reduce the laser gain values or affect the measurement process.

3.5 Amplification Results

The experimental setup described in the previous section has been employed to characterize the amplification properties of $CaF_2 : Nd, Bu$. In order to be able to compare the amplification performance of each crystal, the same absorbed pump power of 400 mW for all crystals was used. To keep the same absorbed pump power, the incident pump power was adjusted taking into account the absorption coefficient of each crystal at the considered

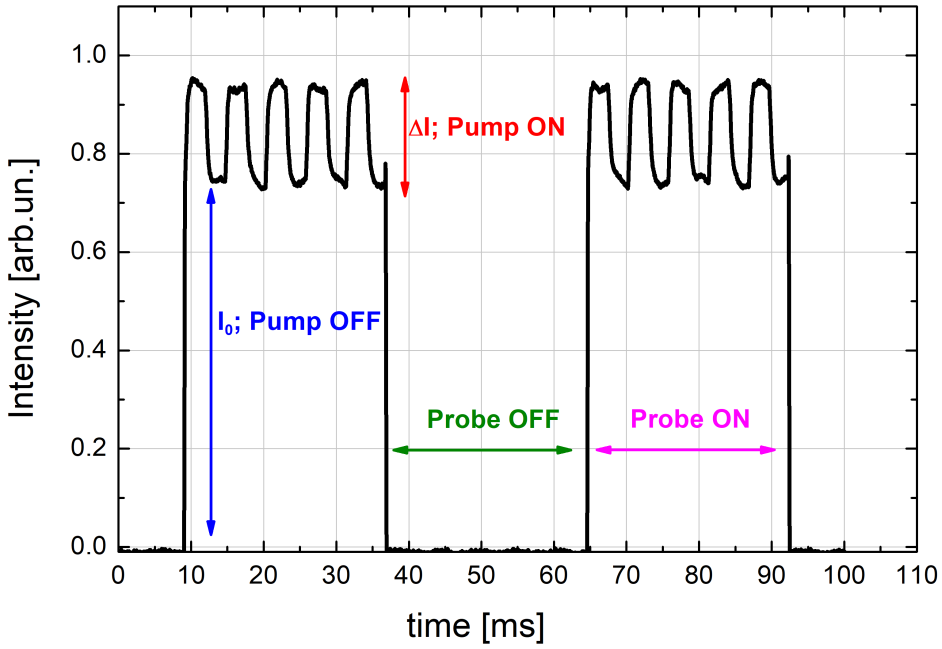

FIGURE 3.7: Typical experimental amplification signal with the double-modulation pump-probe setup.

pump wavelength either 797 nm or 791 nm.

The amplification strongly depends on the spatial overlap between the pump and probe beams. A specific attention was paid to maximizing this overlap by first having the same beam waists for both the pump and probe beams $\omega_p = \omega_L = 50$ μm. For a 50 μm beam waist, the Rayleigh distance $z_R = \pi\omega^2/\lambda$ is equal to 9.8 mm and 7.5 mm at 800 nm (pump) and 1053 nm (probe) respectively. The typical crystal thickness is 5 mm indicating that the divergence within the crystal for both the pump and probe beams is limited.

These amplification measurements are performed within small signal gain conditions, since the input probe power is about 1 mW and the pump and probe waists (radius) are both equal to 50 μm leading to a probe intensity equal to 0.013 kW/cm^2. The laser saturation intensity I_{sat} is defined as

$$I_{sat} = \frac{h\nu_L}{\sigma_{em}\tau_f} \tag{3.39}$$

with σ_{em} the emission cross-section, τ_f the emitting level lifetime and ν_L the laser photon frequency. Typically in CaF_2 crystals co-doped with buffer ions, I_{sat} is about 19 kW/cm^2 (at 1054 nm in $CaF_2 : Nd, Lu$, $\sigma_{em} = 3.17 \cdot 10^{-20}$cm^2 and $\tau_f = 300$ μs).

Using the model presented earlier, it is possible to evaluate the magnitude of the ground state depletion and gain saturation throughout the crystal within our experimental conditions. More specifically, the ratios α/α_0 and g/g_{SS}, introduced before can provide an estimation of the ground state depletion and gain saturation respectively, These ratios are reported in Figure 3.8 for $CaF_2 : 0.5\%Nd, 5\%Lu$ as a function of (r, z). The ratio g/g_{SS} is always close to one confirming that the probe intensity is far from creating any laser gain saturation.

However, Figure 3.8 shows that the contribution of the ground state depletion cannot be neglected, since the ratio α/α_0 reaches 0.727. From this modeling it is also possible to derive an effective absorption coefficient using the calculated value of the pump power at the output of the crystal ($z = L_z$ with L_z the crystal length):

$$P_{p,out} = 2\pi \int_0^{\infty} I_p(r, L_z) r \mathrm{d}r \tag{3.40}$$

and derive the absorption coefficient:

$$\alpha = \frac{1}{L_z} \ln \frac{P_{p,out}}{P_p} \tag{3.41}$$

Within our experimental conditions, the associated ratio $\alpha/\alpha_0 = 0.94$ (with $\alpha_0 = \sigma_{abs} N_T$). Thus, it is important to consider in this model the ground state depletion effect.

The experimental amplification values are compared with the model presented in section 3.3. The various spectroscopic parameters used for the modeling of the different crystals are reported in Table 3.1. As explained in Chapter 2, the radiative lifetimes are calculated from the Judd-Ofelt analyis, (see Table 3.1), the fluorescence lifetimes are taken from Table 2.1, the absorption cross sections are taken from the absorption measurements (see Figure 2.7) and the emission cross sections are calculated using the fluorescence spectra and the Füchtbauer-Ladenburg equation (introduced in eq.(2.3)):

$$\sigma_{em} = \frac{\beta \lambda^5}{8\pi c n^2 \tau_{rad}} \frac{I(\lambda)}{\int \lambda I(\lambda) \mathrm{d}\lambda} \tag{3.42}$$

with the branching ration $\beta = 0.5$ taken from Table 2.2.

A first experiment investigating the $CaF_2 : Nd, Bu$ ($Bu = Gd, La, Ce, Y, Lu, Sc$) crystals has been realized, measuring the amplification P_{out}/P_{in}, for both Nd^{3+} incorporation sites N_1 and N_2 which have been discussed in Chapter 2. As explained in chapter 2 the characteristic excitation /emission wavelength couple for N_1 and N_2 are $\lambda_p = 791$ nm and $\lambda_L = 1049$ nm for N_1, and $\lambda_p = 797$ nm and $\lambda_L = 1054$ nm for N_2. Figure 3.9, shows a comparison between the experimental amplification values and the calculated values from the model presented in section 3.3.

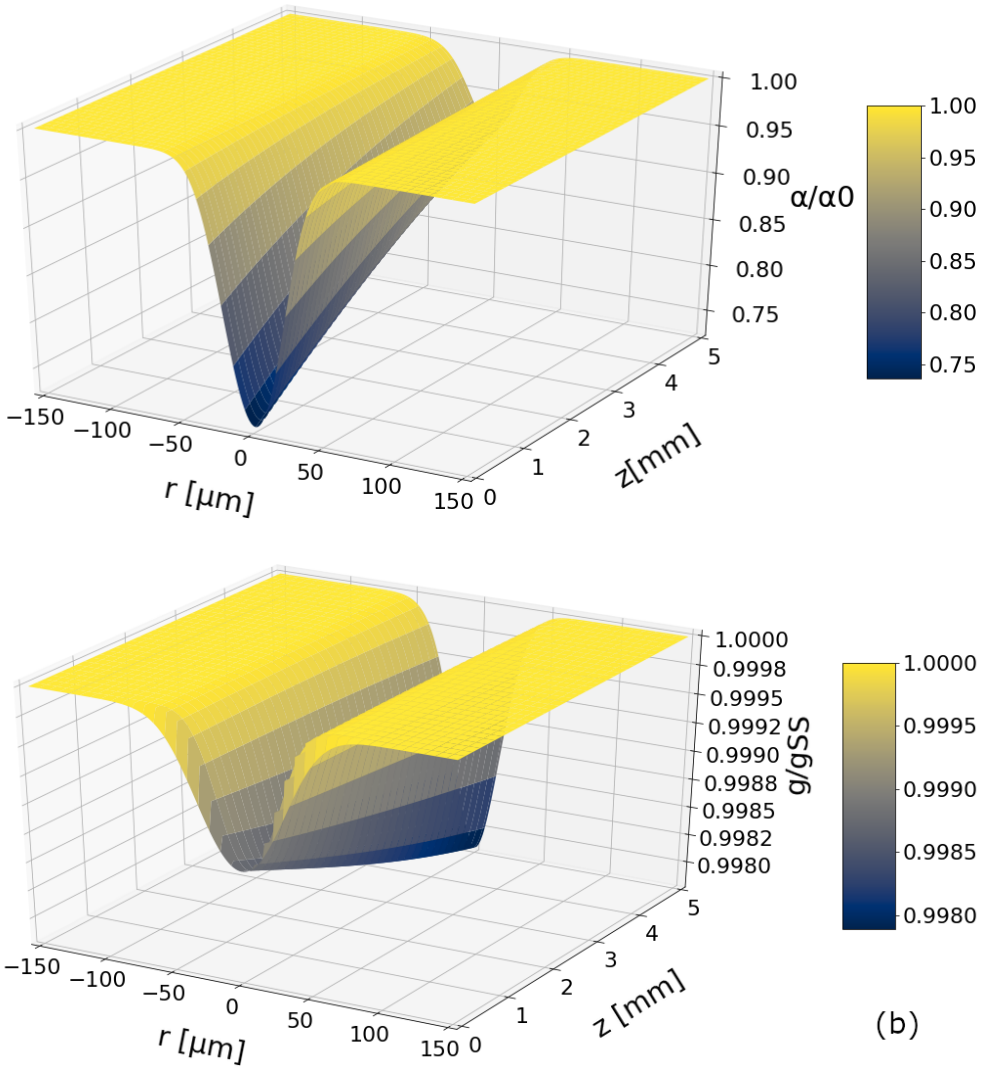

FIGURE 3.8: Ratio between the absorption coefficient and the unpumped absorption coefficient (a), and ratio between the gain coefficient and the small gain coefficient (b), propagated in a 5 mm thick $CaF_2 : 0.5\%Nd^{3+}, 5\%Lu^{3+}$ crystal: $P_{p,0} = 0.5$W, $P_{L,0} = 1$mW, $\omega_{p,0} = \omega_{L,0} = 50\mu$m, $\lambda_p = 797$nm, $\lambda_L = 1053$nm.

N1 center	$5\%Sc^{3+}$	$5\%Lu^{3+}$	$5\%Y^{3+}$	$5\%Gd^{3+}$	$5\%La^{3+}$	$5\%Ce^{3+}$
$\sigma_{abs}(791\text{ nm})$ $[10^{-24}\text{ m}^2]$	1.64	1.80	1.80	2.37	2.62	2.45
$\sigma_{em}(1049\text{ nm})$ $[10^{-24}\text{ m}^2]$	2.62	2.18	2.39	1.89	2.38	2.23
τ_{rad} $[\mu s]$	490	560	520	590	495	525
τ_f $[\mu s]$	470	450	440	490	450	410
P_p $[mW]$	698	680	680	564	548	558

N2 center	$5\%Sc^{3+}$	$5\%Lu^{3+}$	$5\%Y^{3+}$
$\sigma_{abs}(797\text{ nm})$ $[10^{-24}\text{ m}^2]$	1.43	2.65	1.86
$\sigma_{em}(1054\text{ nm})$ $[10^{-24}\text{ m}^2]$	2.44	3.17	2.97
τ_{rad} $[\mu s]$	490	560	520
τ_f $[\mu s]$	340	300	325
P_p $[mW]$	0.67	0.5	0.59

TABLE 3.1: Parameters used in the amplification model for each $CaF_2 : 0.5\%Nd, 5\%Bu$ for both N_1 and N_2 site. For all of them, $P_L = 1$ mW, $\omega_p = \omega_L = 50$ μm, $L_z = 5$ mm, $N_T = 1.225 \cdot 10^{26}$ m^{-3}, $\beta = 0.5$. The pump power is set in order that $P_{abs} = 400$ mW.

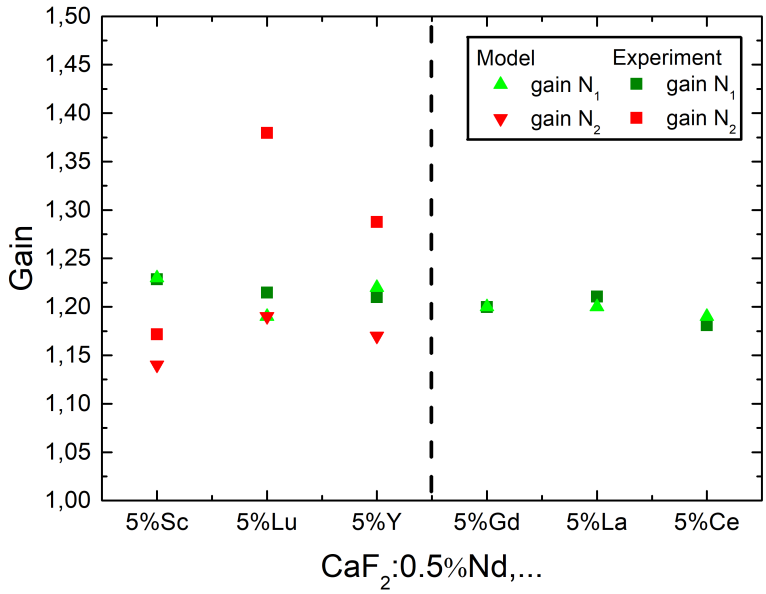

FIGURE 3.9: Amplification P_{out}/P_{in} for the N_1 and N_2 center for $CaF_2 : Nd, Bu$ (Bu = Gd, La, Ce, Y, Lu, Sc) crystal. For N_1 (blue), $\lambda_p = 791$ nm, $\lambda_L = 1049$ nm; for N_2 (red), $\lambda_{pump} = 797$ nm, $\lambda_{probe} = 1054$ nm. For all experiments and calculations, the absorbed pump power is kept at 400 mW, $P_{probe} = 1$ mW, $\omega(radius) = 50$ μm.

The first remark of Figure 3.9, is that the experimental amplification values (square boxes) are close to each other for the different crystals, meaning that the amplification performance is similar from crystal to another. The only exception is for the N_2 site in the Lu and Y codoped crystal for which the experimental amplification values are the highest reaching 1.38 for the Lu doped crystal while all the other amplification factors are around 1.2. This result is mainly due to the higher emission cross-section at 1054 nm when pumping at 797 nm (N_2 center) (see Table 3.1). When comparing the experimental values with the simulated amplification one can notice that the agreement is very good in the case of crystals containing large buffer ions, i.e. Gd, La, Ce co-doped crystals. As explained in Chapter 2, these crystals are characterized by one dominant N_1 center which explains the absence of N_2 amplification data for those crystals in Figure 3.9. The case of small buffer (Y, Lu, Sc) co-doped crystals, is more complicated as the agreement between the modeling and the experimental values is only satisfying for the N_1 center. A significant discrepancy appears for the N_2 site between modeling and experimental values. A more accurate model describing the contribution of both N_1 and N_2 centers would require the estimation of the concentration of each center in the crystal, which is particularly problematic, as already stated in Chapter 2. The difficulty to accurately model the amplification in crystals containing two active Nd^{3+} centers shows the strength of a direct measurement of the laser amplification as presented here.

The tunability feature of both pump and probe beams can be advantageously used to explore the amplification spectral dependence with both beams. The Nd laser emission around 1050 nm is a well-known four level laser scheme. As a consequence, the amplification spectral shape as a function of the pump wavelength is not affected by reabsorption losses at the laser probe wavelength as can be observed in quasi-three level laser scheme. Thus, one can compare the amplification spectral shape with the excitation spectrum presented in Chapter 2 provided that both are recorded at the same wavelength. Figure 3.10 shows examples of comparisons between the amplification of a laser probe at 1053 nm and the excitation spectrum recorded at 1053 nm with the same crystal. One can notice that the comparison is consistent for the two types of crystals identified in the optical spectroscopy investigation, i.e. double Nd_{3+} site crystals such as $CaF_2 : 0.5\%Nd, 5\%Lu$ and single Nd^{3+} site crystal such as $CaF_2 : 0.5\%Nd, 5\%Gd$. These successful comparisons show the consistency of the spectroscopic analysis and the laser amplification measurements.

The probe wavelength dependence of the amplification spectrum can be compared with the emission spectrum calibrated in cross section. In the case of small buffer ions, the emission spectrum depends on the pump wavelength (see Figure 2.9 for instance) which is not the case for large buffer ions with a dominant active Nd^{3+} center. So for small buffer ions, the amplification and emission spectra have to be recorded with the same pump wavelength. Figure 3.11 (b) shows a successful comparison in the case of $CaF_2 : 0.5\%Nd, 5\%Y$ when pumping in both cases at 797 nm. A

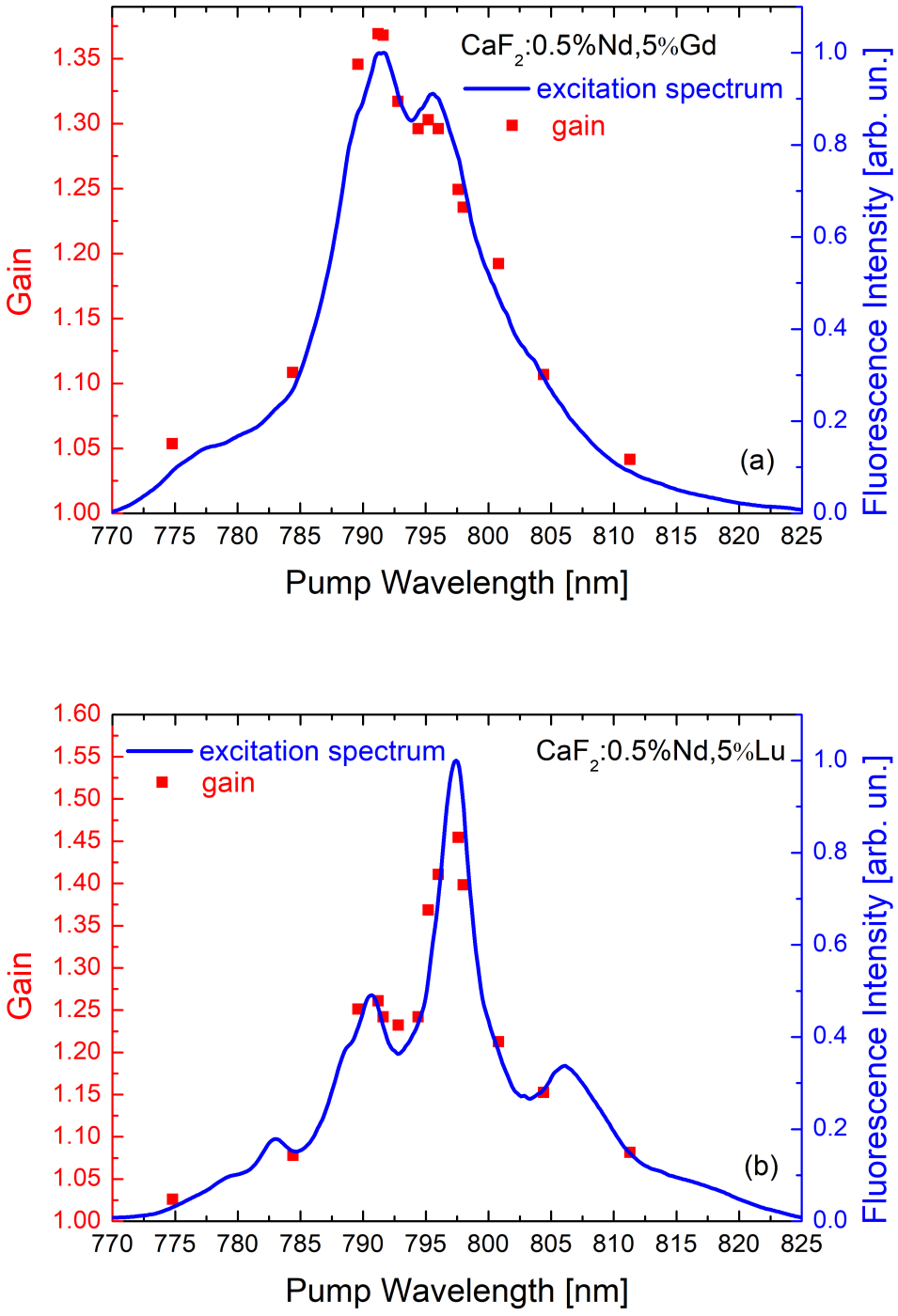

FIGURE 3.10: Excitation spectrum and amplification spectrum varying λ_{pump} for $CaF_2 : 0.5\%Nd, 5\%Gd$ (a) and $CaF_2 : 0.5\%Nd, 5\%Lu$ (b) with $P_{pump} = 920$ mW, $\lambda_{probe} = 1053$ nm, $P_{probe} = 1$ mW, $\omega(radius) = 50$ μm.

similar agreement is observed between the gain measurements and emission cross-sections for large buffer ions such as $CaF_2 : 0.5\%Nd, 5\%La$ in Figure 3.11 (a).

A general comparison of the laser amplification between six different crystals with a single buffer ion (Gd, La, Ce, Y, Lu, Sc) is presented in Figure 3.12 with a probe wavelength tuned between 1040 and 1060 nm, pumping at 797 nm with the same absorbed pump power of 400 mW. As in Figure 3.9, the highest gain value is observed for the 5%Lu co-doped crystal which presents a maximum gain value of 35% at 1054 nm. The 5%Y co-doped crystal which has similar spectroscopic properties as the 5%Lu (Figure 2.4), exhibits a very similar gain spectrum, but a smaller maximum gain value of 20% for the same absorbed pump power. As mentioned earlier, this difference can be explained by a higher emission cross section of the 5%Lu co-doped crystal. The other crystals present a maximum gain around 20% with a flatter profile around 1050 nm, which can be appealing for high-energy laser amplifiers.

As presented in Chapter 2, the most interesting crystals for a flat profile around 1050 nm are $2.5\%Gd, 2.5\%Y$, // $4\%Gd, 1\%Y$, // $3.8\%Gd, 0.65\%Y, 0.55\%La$ and $3\%Gd, 1.4\%Ce, 0.6\%Y$ co-doped $CaF_2 : 0.5\%Nd^{3+}$. The amplification properties of these crystals have been investigated while pumping at 797 nm using again the same absorbed pump power of 400 mW. The amplification as a function of the probe wavelength is presented in Figure 3.13, together with the 5%Lu as reference . It is possible to see that the amplification obtained is around 20%, which is very similar to all the other crystals co-doped with one single buffer ion (see Figure 3.12) . Moreover a flat profile in the $1048 - 1054$ nm spectral range is evidenced, validating the optical spectroscopy investigation of Chapter 2 and making those crystals promising for the LMJ applications.

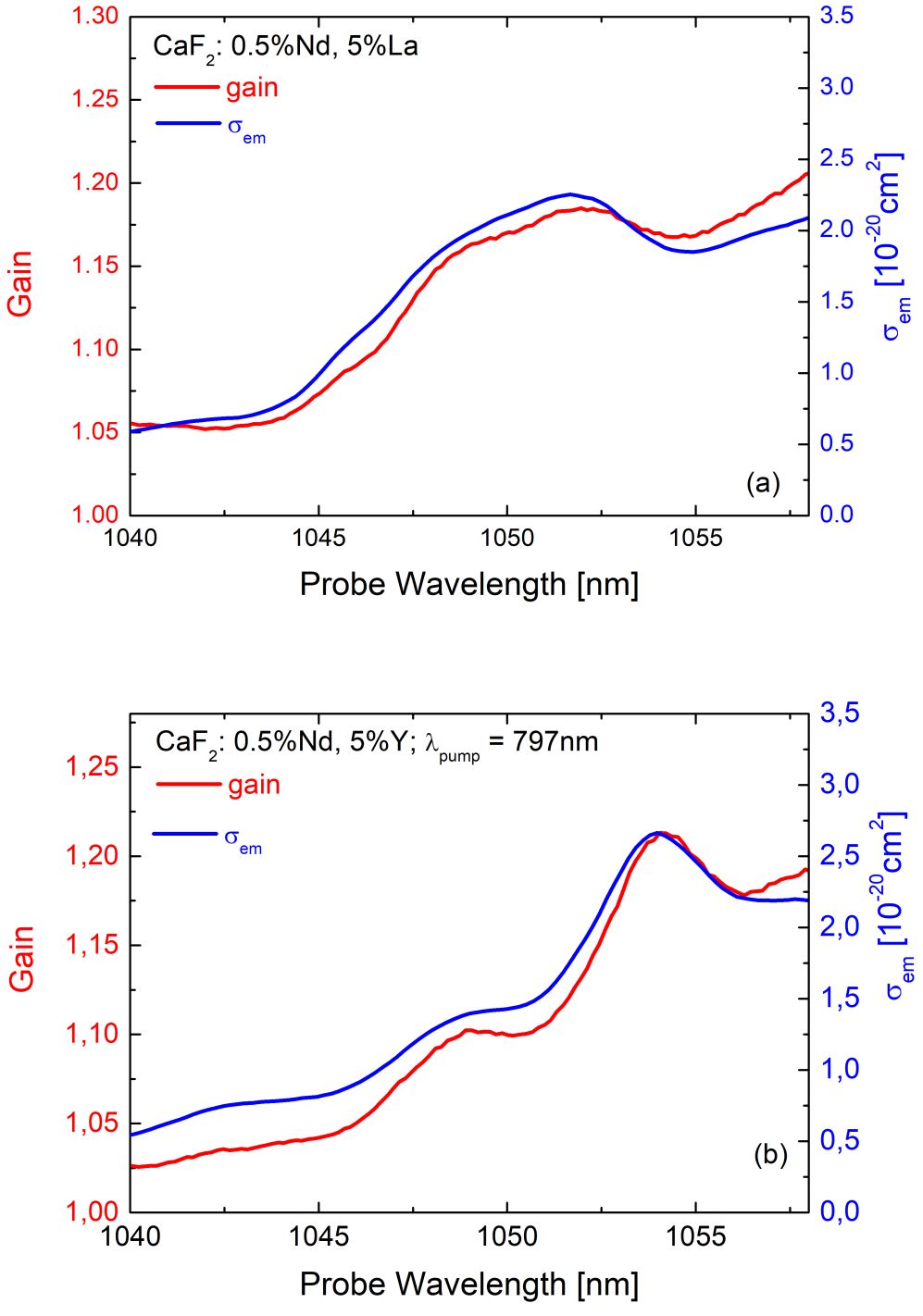

FIGURE 3.11: Emission cross section and amplification spectrum as a function of λ_{probe} for $CaF_2 : 0.5\%Nd, 5\%La$ (a) and $CaF_2 : 0.5\%Nd, 5\%Y$ (b) with $P_{abs} = 400$ mW, $\lambda_{pump} = 797$ nm, $P_{probe} = 1$ mW, $\omega(radius) = 50$ μm.

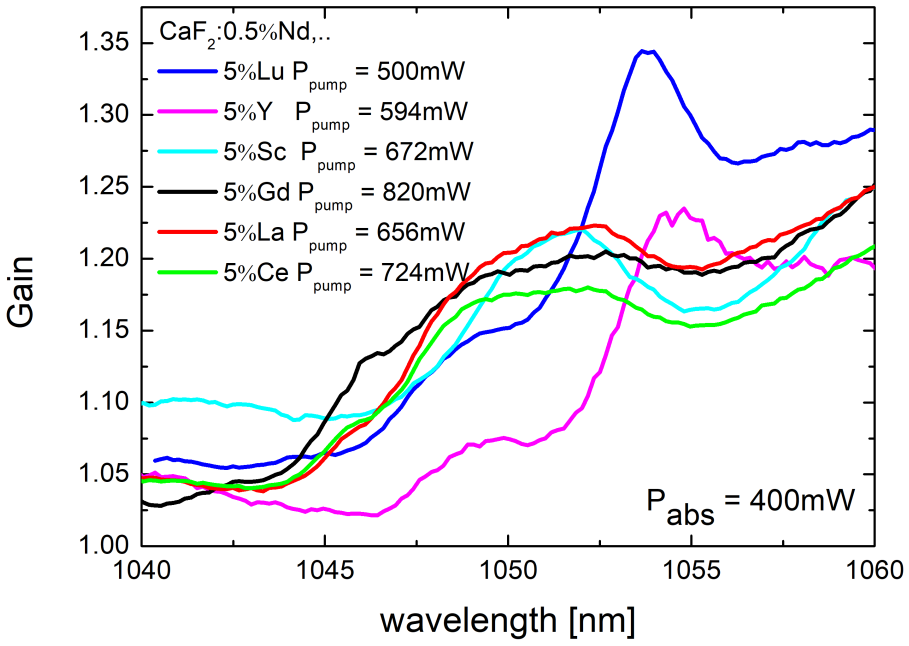

FIGURE 3.12: Amplification spectrum as a function of λ_{probe} for different buffers, with the same absorbed pump power $P_{abs} = 400$ mW. $\lambda_{pump} = 797$ nm, $P_{probe} = 1$ mW, $\omega(radius) = 50$ μm.

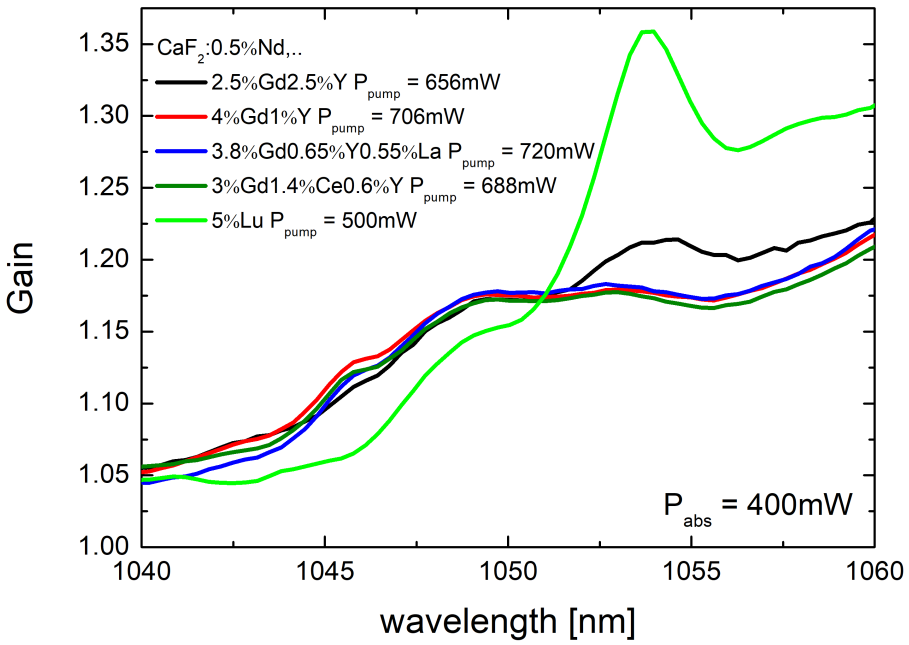

FIGURE 3.13: Amplification spectrum as a function of λ_{probe} for different samples, with the same absorbed pump power $P_{abs} = 400$ mW. $\lambda_{pump} = 797$ nm, $P_{probe} = 1$ mW, $\omega(radius) = 50$ μm.

3.6 Conclusions

The laser amplification properties of buffer ion co-doped $CaF_2 : Nd$ has been investigated in this chapter. Firstly, the collaboration with the CESTA helped define an amplification criterion which aims for a 3 nm FWHM amplified probe spectrum after a 10^9 amplification factor. This criterion has been tested with the most promising crystals identified in the spectroscopy study of Chapter 2, namely $CaF_2 : 0.5\%Nd$ codoped with $2.5\%Gd, 2.5\%Y$, // $4\%Gd, 1\%Y$, // $3.8\%Gd, 0.65\%Y, 0.55\%La$ and $3\%Gd, 1.4\%Ce, 0.6\%Y$ that gave the broadest fluorescence bands. The 3 nm FWHM of the amplified probe spectrum (typical of the Nd:LGG70 glass currently employed in the LMJ) is exceeded for all the studied crystals reaching around $5 - 6$ nm, while the centering at 1053.0 nm is more problematic. While all crystals have their maximum amplified signal at 1053 nm, the bandwidth falls sharply on the long wavelength part of the spectrum.

The laser amplification factor P_{out}/P_{in} with $CaF_2 : Nd$ codoped with buffer ions has been investigated using a dedicated double-modulation pump-probe setup. As a result a 35% amplification factor is measured in $CaF_2 : 0.5\%Nd, 5\%Lu$ at 1054 nm for 400 mW of absorbed pump power while the other buffer doped crystals lead to a laser gain of 20% for the same absorbed pump power. These results are compared to a dedicated model based on a rate equation approach which also comprises the probe and pump beam propagation within the amplifying medium. This model also takes into account saturation effects, such as the ground state depletion and the gain saturation. The comparison between the calculated and measured amplification shows a good agreement for crystals co-doped with large buffer ions (Gd, La, Ce) which exhibit one dominant Nd^{3+} active center. The case of small buffer ions is more complicated since an exact amplification calculation would require two sets of spectroscopic parameters for N_1 and N_2 as well as the determination of the concentration of each center in the crystal. This limitation further emphasizes the relevance of a direct experimental measurement of the laser gain as presented in this work.

The tunability feature of both pump and probe beams has been exploited to perform gain measurements at various pump and probe wavelengths. Amplification measurements realized on the most promising crystals for the LMJ applications, again namely the $2.5\%Gd, 2.5\%Y$, $4\%Gd, 1\%Y$, $3.8\%Gd, 0.65\%Y, 0.55\%La$ and $3\%Gd, 1.4\%Ce, 0.6\%Y$ co-doped $CaF_2 : Nd$, show a 20% amplification for 400 mW of absorbed pump power and 1 mW of probe power. More interestingly, the amplification spectrum as a function of the probe wavelength evidences a flat profile in the $1048 - 1055$ nm spectral range consistent with the Chapter 2 findings.

Chapter 4

Continuous-Wave Laser Operation

4.1 Introduction

Chapters 2 and 3 were dedicated to the spectroscopic properties and the laser gain coefficient study of various neodymium doped CaF_2 crystals. This fourth chapter is devoted to the investigation of the laser action of the most interesting of the studied laser materials.

Laser action with Neodymium doped CaF_2 has been investigated in the literature to some extent in plano-concave cavities, both under monochromatic and diode pumping. Stimulated emission from neodymium-based fluorides laser crystals was observed already at the end of the 1960's with few works from Kaminksii and Dmitruk with some hybrid CaF_2-LaF_3 and SrF_2-LaF_3 matrices [60, 109], investigating later a $CaF_2 : Nd, Gd$ crystal in the early 1980's [110]. However, as already explained in Chapter 2, the neodymium clustering and the subsequent quenching of the 1 μm transition [42, 44] at dopant concentration $\geq$ 1at.%, made researchers consider Nd-doped fluorides as hopeless for laser applications. However, the recent developments showed that the co-doping approach could efficiently isolate single Nd^{3+} ions by forming various types of clusters, and lead to interesting laser results. The work of Alimov et al. on SrF_2 [111] and of Su et al. on CaF_2 [57], achieved laser slope efficiencies of 23.7% and 10% respectively, but with the work of Doualan et al. [55] and Normani et al. [15, 40] on the optimization of the co-doping with yttrium and lutetium respectively, better laser performance were achieved with slope efficiencies reaching values around $40 - 50\%$ with absorbed powers at the threshold around $60 - 70$ mW. This result was replicated with lanthanum co-doping few years later, achieving 40% slope efficiency [63]. The approach of mixed fluorides has also been investigated, with the fabrication of an hybrid neodymium doped CaF_2-SrF_2 [112] crystal [63]. It is worth mentioning also the work of Jelinek et al. on $SrF_2 : Nd, Y$ [113], with the realization of a 1048 nm $-$ 1070 nm tunable cavity.

These laser results, together with the broad bands obtained in both the optical spectroscopy investigation of Chapter 2 and the laser gain investigation of Chapter 3, makes appealing the investigation of the laser properties of these laser crystals, with a focus on their tunability.

The setup chosen for the laser action study is depicted in Figure 4.1, which is a plano-concave cavity pumped with a Coherent titanium-sapphire laser. Different output couplers were used in the laser experiments with 8%, 4.5%, 1.7% and 0.8% transmission at 1065 nm and curvature radius of 100 mm. The pump beam is filtered at the output of the cavity with two Thorlabs longpass filters FEL950. In addition, to perform the tunability experiments, a Newlight BIR1020 Lyot filter at Brewster angle is implemented in the cavity. To reduce the thermal load on the crystal, the pump beam is modulated with a mechanical chopper with a frequency around 80 Hz.

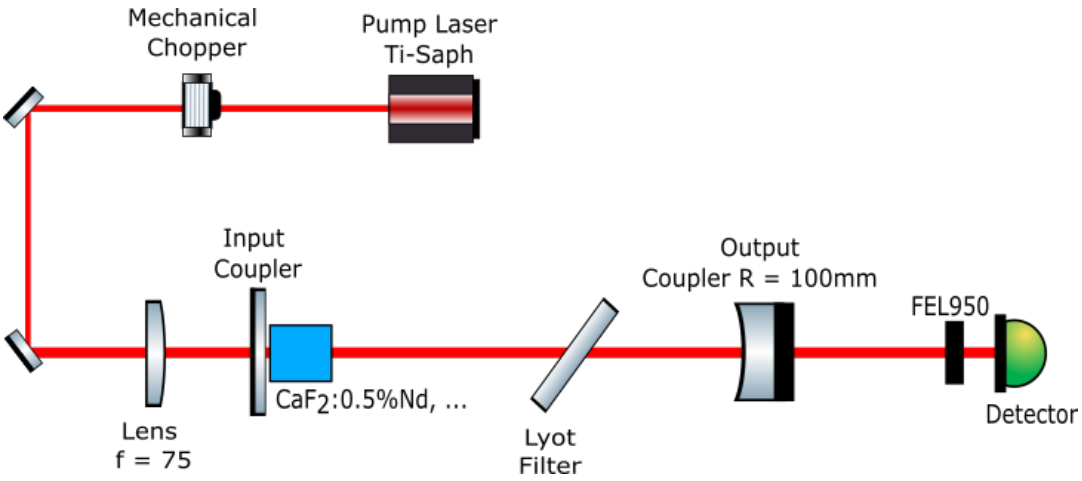

FIGURE 4.1: Plano-Concave Cavity Setup with the Lyot filter.

Finally, a preliminary study on molecular adherence with different calcium fluoride crystals is presented at the end of this chapter. The idea is to realize an hybrid $CaF_2||CaF_2 : Nd, Lu$ laser crystal, in which an undoped calcium fluoride laser crystal is bonded to a neodymium doped calcium fluoride (with buffer co-doping), in order to exploit the undoped CaF_2 crystal as a heat sink and improve the thermo-mechanical characteristics, without affecting the laser performance. The particularity of this approach is the absence of an intermediate interface like a bonding agent between the two crystals, to ensure the absence of scattering losses at the interface and thus an increase of the overall passive losses.

4.2 Laser Crystal Preparation

In order to obtain the best laser performance as possible, the crystalline quality and surface quality of the crystals has to be optimized. One of the first parameters to control is the growth velocity of the Bridgman-Stockbarger process, that after several years of experience at CIMAP, has been found to be ideal at 1.5 mm/h for CaF_2, to obtain a single crystal without impurities, polycrystalline phases and/or twinned crystals. The absence of residual stress in the obtained rod is verified qualitatively with a pair of crossed polarizers. An oriented seed can be used to ensure a crystal growth in the direction perpendicular to the $[1, 1, 1]$ crystallographic plane, which is the preferred

orientation to reduce thermally induced birefringence effects. Without seed, the growth will present a tilt angle with respect to the desired (111) direction.

In order to avoid scattering at the input and output faces of the laser crystal in the cavity, that would increase the passive losses, the surface quality is also a critical point. A precision cut of the crystal rod is performed to obtain a crystal disk. Then a surface roughness around $20-50$ nm, is obtained with a manual polishing machine for optical spectroscopy investigations, but for very high quality laser crystals the roughness has to be improved. Therefore, with the use of a Logitech precision polishing machine, and a three steps polishing process with three different diamond abrasives (15 μm, 9 μm and 3 μm, the latter being homemade) on three separate resin plates, a surface roughness of $5-10$ nm can be obtained. At the same time, the surface flatness is controlled with a MarOpto FI 1040Z Fizeau interferometer, operating at 632.8 nm, obtaining a flatness lower than $\lambda/4$ for a 7 mm diameter crystal. Lastly, the parallelism between the two crystal faces is ensured by superposing a beam reflected on the two faces.

4.2.1 Laser Crystal Orientation

After the growth of the rod, but prior to the cutting and polishing, the orientation of the laser crystal, perpendicular to the $[1,1,1]$ crystallographic plane has to be verified. As mentioned earlier, it is common to observe a tilt angle around $0-30^\circ$ to the desired orientation. This can be corrected by performing a diffraction analysis by recording a Laue diffraction pattern, and cutting accordingly the rod. The final crystal is then cored to a diameter $\phi = 7$ mm. The diffraction pattern is recorded with a ARL Equinox Laue diffractometer.

As an example, in Figure 4.2 is reported the diffractogram of a non-oriented $CaF_2 : 0.5\%Nd, 3.8\%Gd, 0.65\%Y, 0.55\%La$, with a 35° tilt, and a $[1,1,1]$ oriented crystal, where one can recognize the typical $[1,1,1]$ pattern. The two crystals were cut out of the same rod, sharing comparable surface and crystalline quality.

The advantage of orienting the crystal in the $[1,1,1]$ resides in the better laser performance, since the thermally induced birefringence, caused by the local mechanical stress induced by the heat deposition, is sensibly reduced [16, 17, 114–118]. The choice of the $[1,1,1]$ orientation rather than other directions, like $[1,0,0]$ or $[0,0,1]$, has been validated experimentally by showing that in cylindrical shaped crystals, the $[1,1,1]$ orientation minimizes the thermally induced local stress, and thus the consequent birefringence [119–122].

This effect is illustrated experimentally for the specific case of buffer ion co-doped $CaF_2 : Nd$, employing the two identical $CaF_2 : 0.5\%Nd, 3.8\%Gd, 0.65\%Y, 0.55\%La$ crystals presented in Figure 4.2, and the laser cavity described in Figure 4.1. Firstly, in Figure 4.4 is reported the laser output power obtained for 4 different output couplers.

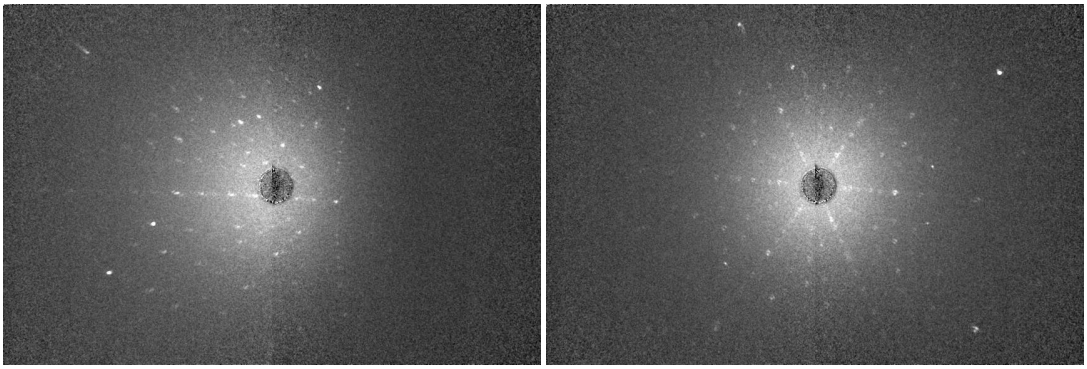

FIGURE 4.2: X-ray image with the Von Laue method of a non-oriented CaF_2 : 0.5%Nd, 3.8%Gd, 0.65%Y, 0.55%La (left) and the same crystal oriented $[1, 1, 1]$ (right).

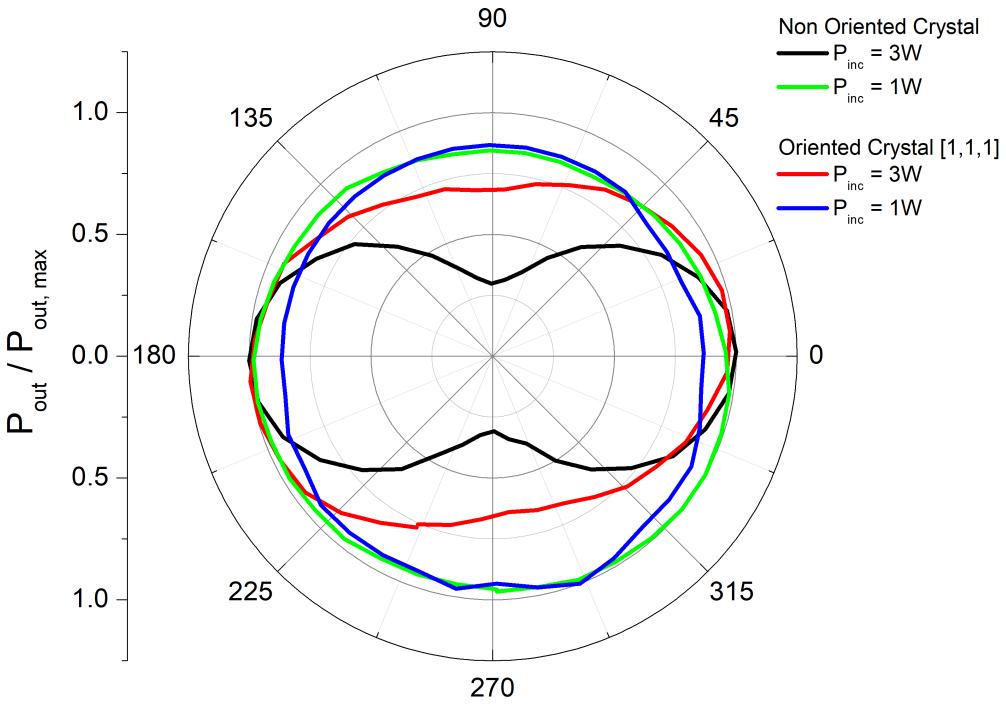

FIGURE 4.3: Depolarization effect in a non-oriented and $[1, 1, 1]$ oriented CaF_2 : 0.5%Nd, 3.8%Gd, 0.65%Y, 0.55%La crystal, with pump wavelength of $\lambda_{pump} = 797$ nm and output coupling $T = 0.8\%$. The graph is displayed in polar coordinates.

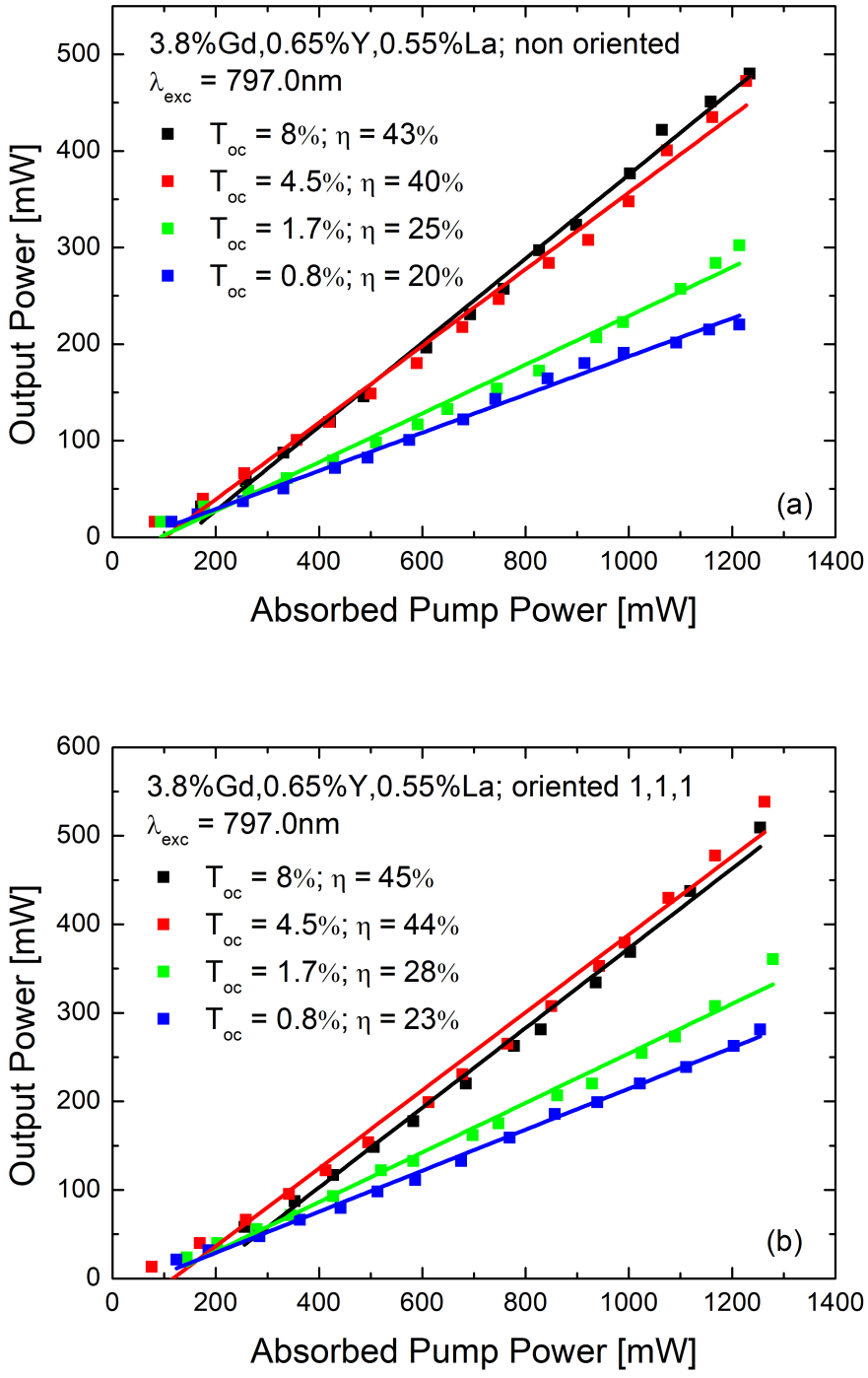

FIGURE 4.4: Slope efficiency of a non-oriented $CaF_2 : 0.5\%Nd, 3.8\%Gd, 0.65\%Y, 0.55\%La$ (a) and the same crystal oriented $[1,1,1]$ (b), with pump wavelength of $\lambda_{pump} = 797$ nm.

One can observe a slight improvement with the $[1,1,1]$ oriented crystal, of the order of few percents.

However, by introducing a polarizer outside the laser cavity, and studying the polarization of the laser beam with $P_{pump} = 1$ W and 3 W, one can observe a major polarization effect at high pump power due to thermally induced birefringence. This effect is illustrated in Figure 4.3, where the ratio between the output power and the maximum output power is shown in a polar coordinates plot as a function of the polarizer tilt angle. Here, in absence of polarizing elements within the laser cavity, the plot should be a circle since CaF_2 is an isotropic crystal leading to an unpolarized laser output beam. A major birefringence effect can be seen with a significantly polarized output beam under a 3 W pumping for the non-oriented crystal, while this effect is much less pronounced for the $[1,1,1]$ oriented crystal.

To further quantify this thermally induced birefringence, the total output power of the laser cavity can be divided into an unpolarized power term P_u and a polarized term P_p, and thus the measured power after the polarizer is written:

$$P_{out} = \frac{P_u}{2} + P_p \cos^2\theta \tag{4.1}$$

Eq. (4.1) can be used to fit the measured power after the polarizer as a function of the angle θ. Figure 4.5 shows a successful adjustment for the $P_{pump} = 3$ W with the non-oriented crystal (black curve in Figure 4.3).

It is possible to further quantify the induced birefringence effect by looking at the degree of polarization (DOP) which is defined as a function of the maximum and minimum measured output power:

$$DOP = \frac{P_{max} - P_{min}}{P_{max} + P_{min}} \tag{4.2}$$

These maximum and minimum output powers can be expressed as (eq. (4.1)):

$$\begin{cases} P_{max} = \frac{P_u}{2} + P_p \\ P_{min} = \frac{P_u}{2} \end{cases} \tag{4.3}$$

Thus, eq. (4.2) can be rewritten as

$$DOP = \frac{P_p}{P_p + P_u} \tag{4.4}$$

Under the same conditions and for a pump power of 3 W , the degree of polarization (DOP) is 0.55 in Figure 4.5 for the non-oriented crystal while it is only 0.04 for the $[1,1,1]$ oriented crystal, highlighting the importance of the $[1,1,1]$ orientation.

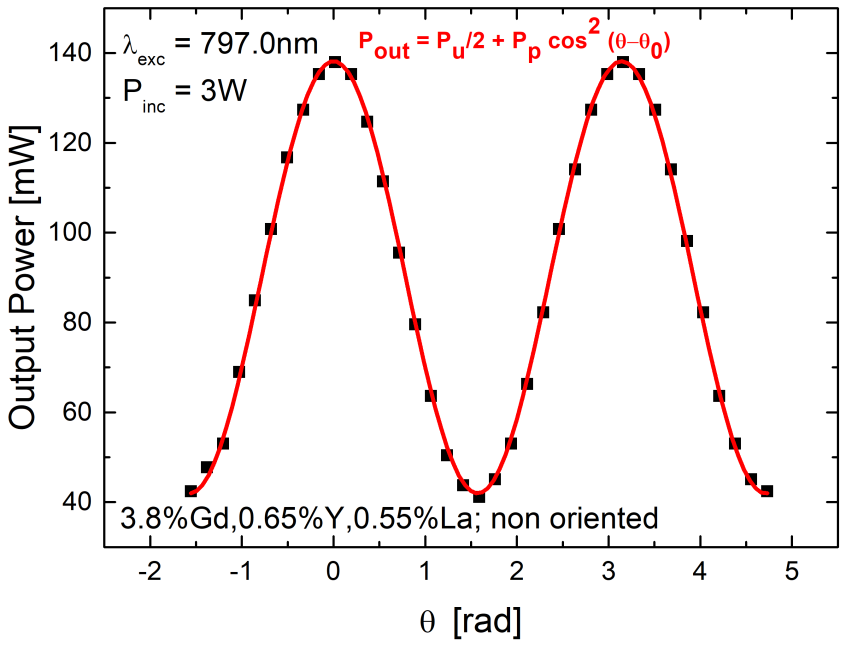

FIGURE 4.5: Birefringence effect in a non-oriented $CaF_2 : 0.5\%Nd, 3.8\%Gd, 0.65\%Y, 0.55\%La$ crystal, with pump wavelength of $\lambda_{pump} = 797$ nm and pump power $P_{pump} = 3$ W.

4.3 CW Laser Operation

Multiple laser crystals were investigated using the same plano-concave cavity. Table 4.1 shows the laser slope efficiency η_s and laser threshold powers obtained for the most interesting crystals. The slope efficiencies are for most crystals on the order of 40% while the laser threshold power remains significantly low around few tens of mW even for the highest output coupler transmission ($T = 8\%$). Such low laser thresholds illustrate both the good optical quality of the laser crystals and the very good quantum efficiency of the $^4F_{3/2}$ emitting laser level as already shown by the spectroscopic investigation of Chapter 2.

CaF_2 :	η_s	P_{th}
2.5%Gd, 2.5%Y	44%	60 mW
4%Gd, 1%Y	41%	74mW
3%Gd, 1.4%Ce, 0.6%Y	46%	60 mW
3.8%Gd, 0.55%La, 0.65%Y	45%	101 mW

TABLE 4.1: Laser slope efficiency and threshold power for the various laser crystals, with output coupler $T = 8\%$.

Among all the crystals we studied, a particular focus is devoted to the laser performance of selected crystals, starting with the

$CaF_2 : 0.5\%Nd, 2.5\%Gd, 2.5\%Y$ crystal, that gives interesting spectroscopic and amplification properties when pumped at 796 nm (see chapter 2, Figure 2.21). The other two selected crystals are $CaF_2 : 0.5\%Nd, 4\%Gd, 1\%Y$ and $CaF_2 : 0.5\%Nd, 3\%Gd, 1.4\%Ce, 0.6\%Y$ pumped at 797 nm. These crystals are selected since they exhibit broad and flat bands which meet the requirements of the LMJ applications. The output power as a function of the absorbed pump power for $CaF_2 : 0.5\%Nd, 2.5\%Gd, 2.5\%Y$ presented in Figure 4.6, and characterized by a laser efficiency of 44% for $T = 8\%$ with a laser wavelength at 1065 nm. The laser slope efficiency and threshold are similar to the laser results obtained with $CaF_2 : 0.5\%Nd, 5\%Lu$ [40], thus proving that an hybrid buffer co-doping, while complicating the crystal composition, does not affect the laser performance.

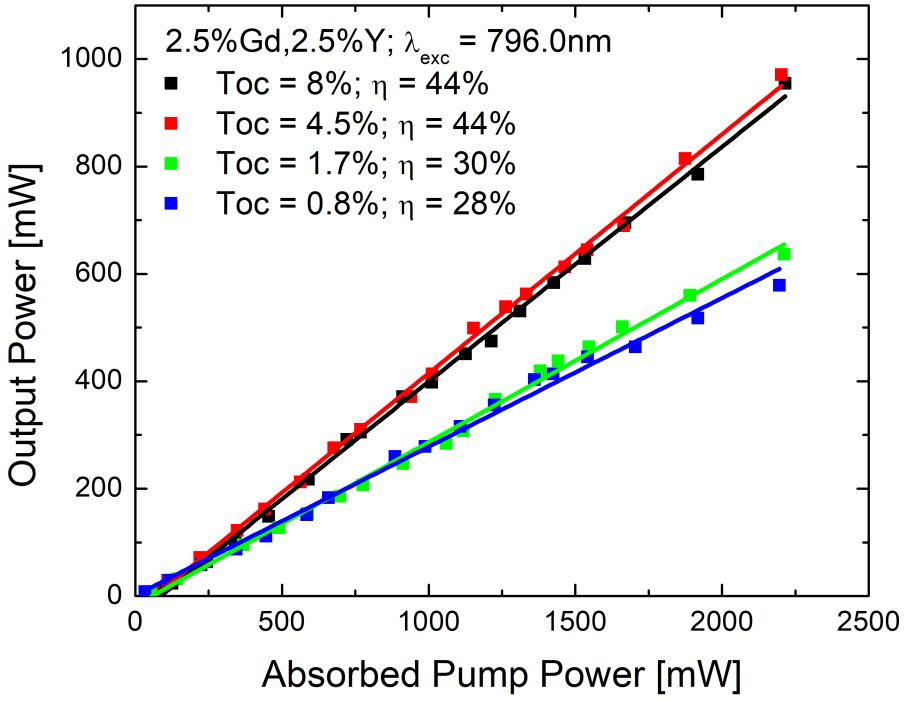

FIGURE 4.6: Laser output power versus absorbed pump power for the four output couplers $T = 0.8\%, 1.7\%, 4.5\%, 8\%$, of a $CaF_2 : 0.5\%Nd, 2.5\%Gd, 2.5\%Y$, with pump wavelength of $\lambda_{pump} = 796$ nm.

Similar laser performances are achieved with the other two crystals in terms of slope efficiency and threshold powers: $CaF_2 : 0.5\%Nd, 4\%Gd, 1\%Y$ (slope efficiency: 41%, threshold: 74 mW) and the $CaF_2 : 0.5\%Nd, 3\%Gd, 1.4\%Ce, 0.6\%Y$ (slope efficiency: 46%, threshold: 60 mW) pumping at 797 nm as presented in Figure 4.7.

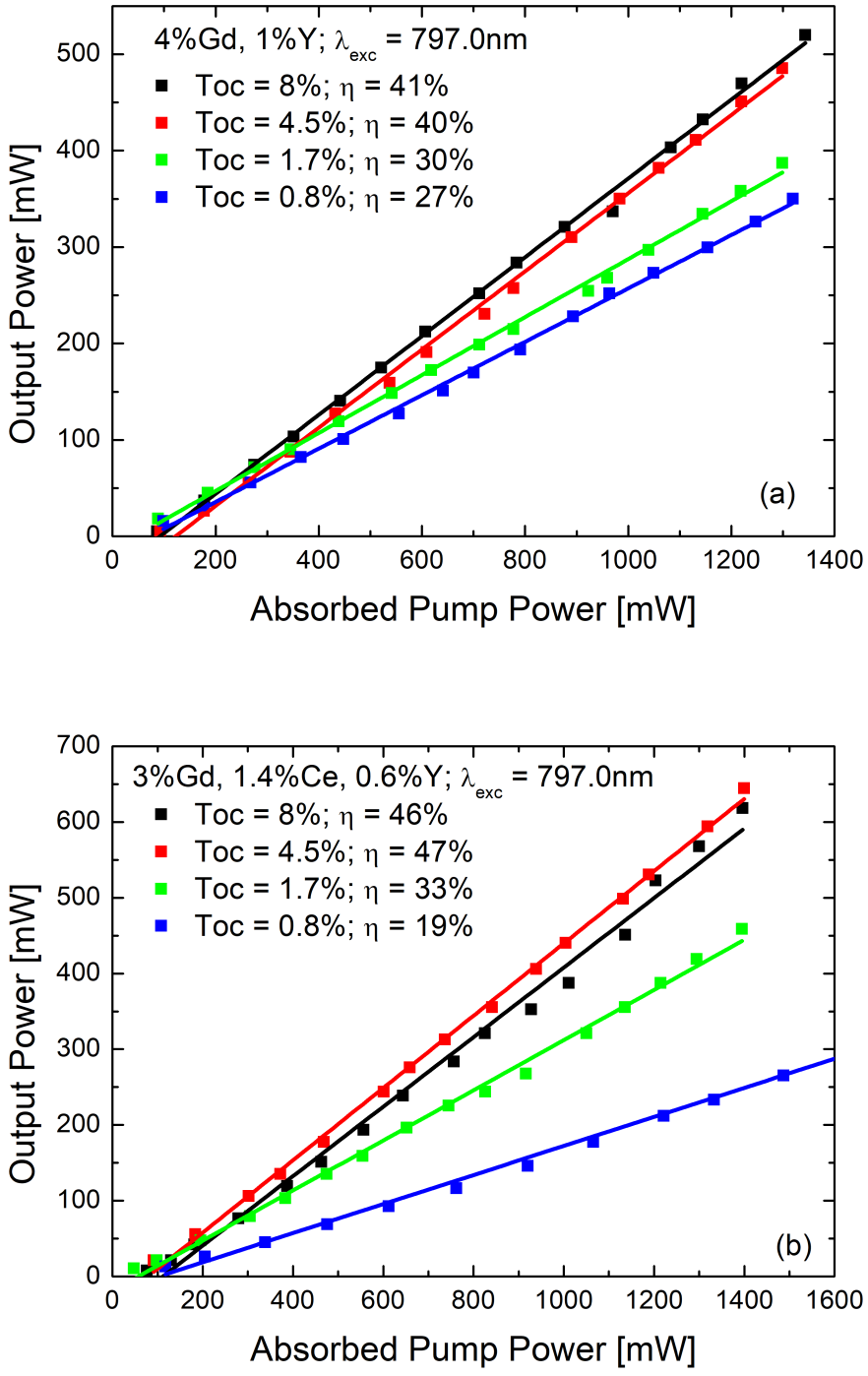

FIGURE 4.7: Laser output power versus absorbed pump power for the four output couplers $T = 0.8\%, 1.7\%, 4.5\%, 8\%$, of a $CaF_2 : 0.5\%Nd, 4\%Gd, 1\%Y$ (a) and $CaF_2 : 0.5\%Nd, 3\%Gd, 1.4\%Ce, 0.6\%Y$ (b), with pump wavelength of $\lambda_{pump} = 797$ nm.

The laser slope efficiency is traditionally written as:

$$\eta_s = \eta_p \frac{\lambda_p}{\lambda_L} \frac{T}{T+L} \tag{4.5}$$

where λ_p and λ_L are the pump and laser wavelength respectively and η_p the pump quantum efficiency (the number of excited ions in the $^4F_{3/2}$ emitting level for each absorbed pump photon), L the round trip losses and T the output coupler transmission.

Three main factors can degrade the laser performance and are not taken into account in eq. 4.5. The first one is represented by the thermal effects, in particular the thermal lensing that can affect the divergence and quality of the laser beam. The second factor is the spatial overlap between the pump and the laser beams which will directly affect the output power. The third one is represented by parasitic effects such as upconversion processes, which depopulate the emitting level. Accurate modelings taking into account upconversion processes have been proposed in the literature, but are beyond the scope of this work. The impact of these three limiting factors can be assessed by comparing the measured slope efficiencies with the theoretical limit of the slope efficiency η_0

$$\eta_0 = \frac{\lambda_p}{\lambda_L} \frac{T}{T+L} \tag{4.6}$$

and derive a value of the pump quantum efficiency η_p using eq. 4.5. Table 4.2 shows the comparison between η_0 and η_s for $CaF_2 : 0.5\%Nd, 3\%Gd, 1.4\%Ce, 0.6\%Y$ which gave the best laser performance. Round trip losses L introduced by the laser crystal will be presented in the next section and are estimated around 2%. For the calculation we used $\lambda_p = 797$ nm and $\lambda_p = 1065$ nm.

T [%]	η_s [%]	$\eta_0 = \frac{\lambda_p}{\lambda_L}\frac{T}{T+L}$ [%]	η_p [%]
0.8	19	21.3	89
1.7	33	34.4	96
4.5	47	51.9	90
8	46	60	77

TABLE 4.2: Measured slope efficiencies and theoretical slope efficiencies for each output coupler.

Table 4.2 shows measured slope efficiencies close to the theoretical slope efficiency η_0 leading to very high values of the pump quantum efficiency η_p. Therefore one can conclude that the three limiting factors mentioned earlier have a limited impact on the lasers developed in this study.

The laser beam parameters, such as the M^2, the waist ω_0 and the divergence have been measured with a beam profiler camera BladeCam-XHR

SNB5209, as displayed in Figure 4.8. The beam size has been measured at different positions z along the optical axis in the vicinity of the waist, as pictured in Figure 4.9.

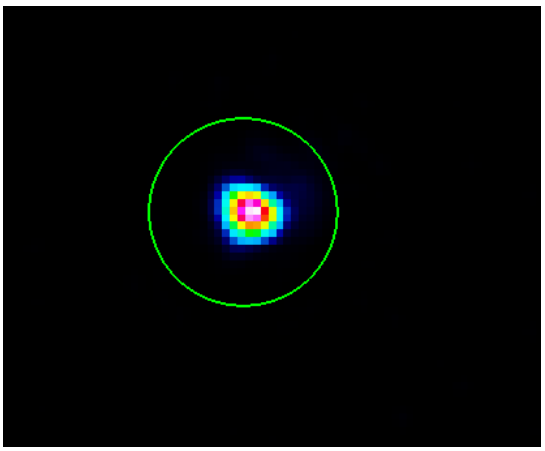

FIGURE 4.8: Image of the laser beam obtained with the $CaF_2 : 0.5\%Nd, 2.5\%Gd, 2.5\%Y$, with a lasing wavelength $\lambda_L = 1065$ nm.

The experimental values of the beam size as a function of z have been fitted with the well known equation [123–125]:

$$\omega(z) = \omega_0 \sqrt{1 + M^2 \left(\frac{z - z_0}{z_R} \right)^2} \tag{4.7}$$

with z_R the Rayleigh range defined as

$$z_R = \frac{\pi \omega_0^2}{\lambda} \tag{4.8}$$

From the fit of the beam profile in Figure 4.9 with eq. (4.7), one can derive the value of the waist $\omega_0 = 20$ μm along with the beam quality factor M^2 which is estimated to be 1.1.

The divergence θ can then be calculated as

$$\theta = \frac{M^2 \lambda}{\pi \omega_0} \tag{4.9}$$

The divergence of the beam θ in figure 4.8 is estimated at 20 mrad. Both divergence and M^2 values show the very good quality of the laser output beam. Along with the absence of output power saturation (Figure 4.6) due to thermal effects (thermal roll-over), the beam quality indicates that thermal effects have little impact on the laser output power within our absorbed power range (under 1.5 W). This is consistent with the laser slope efficiencies being close to the theoretical value (see Table 4.2).

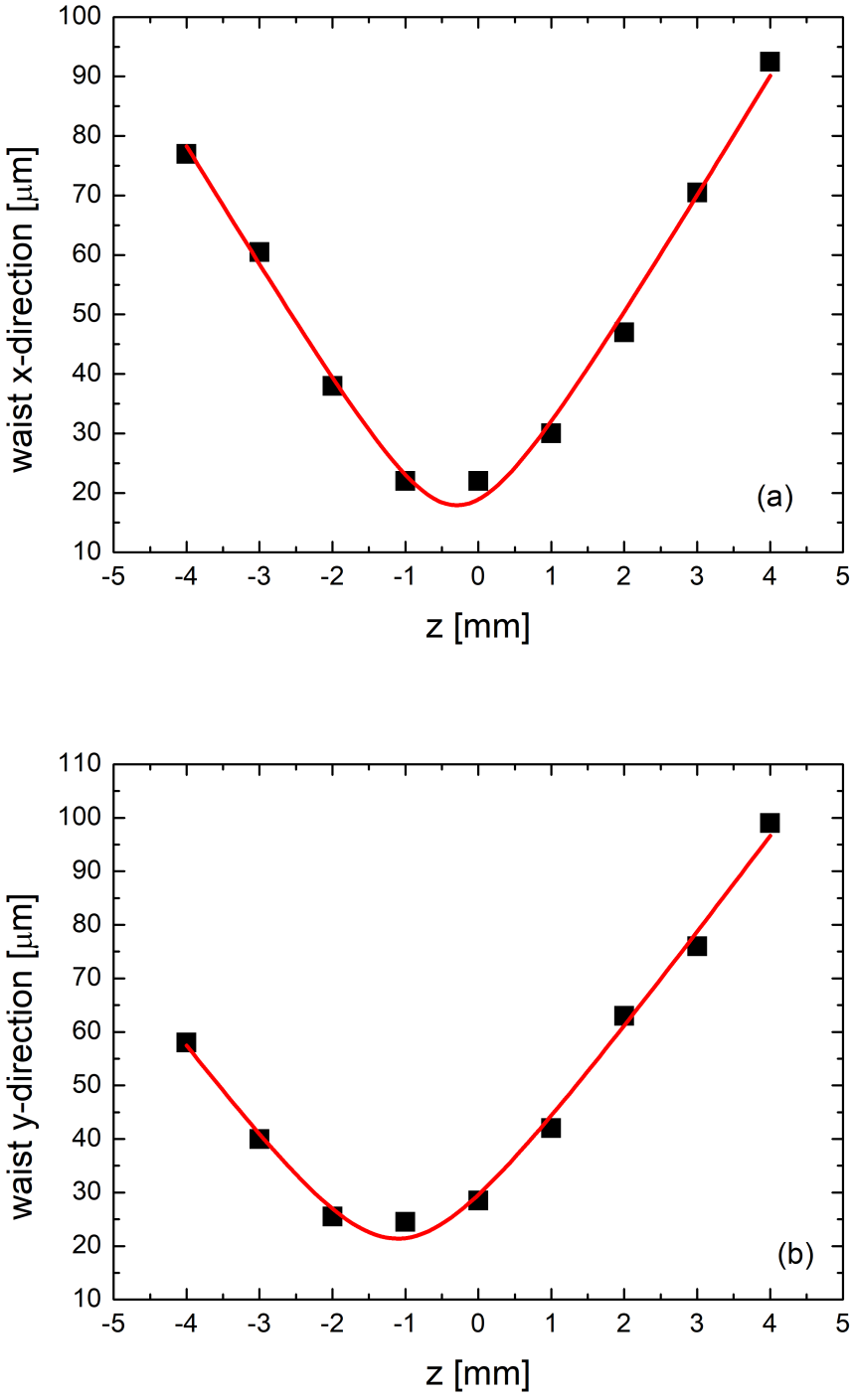

FIGURE 4.9: Fit of the laser beam divergence according to eq. (4.7) in order to derive the waist value and the M^2 for the laser beam generated by the $CaF_2 : 0.5\%Nd, 2.5\%Gd, 2.5\%Y$, with a lasing wavelength $\lambda_L = 1065$ nm for both the x direction (a) and the y direction (b).

As discussed in Chapter 2 the pump wavelength can be of importance for crystals containing small buffer ions since their spectroscopic signature can change with the pump wavelength. So the laser performance of $CaF_2 : 0.5\%Nd, 2.5\%Gd, 2.5\%Y$ was investigated by tuning the pump wavelength in the $794 - 797$nm range . Figure 4.10 shows that the slope efficiency and laser threshold for the $T = 8\%$ output coupler, hardly depend on the pump wavelength.

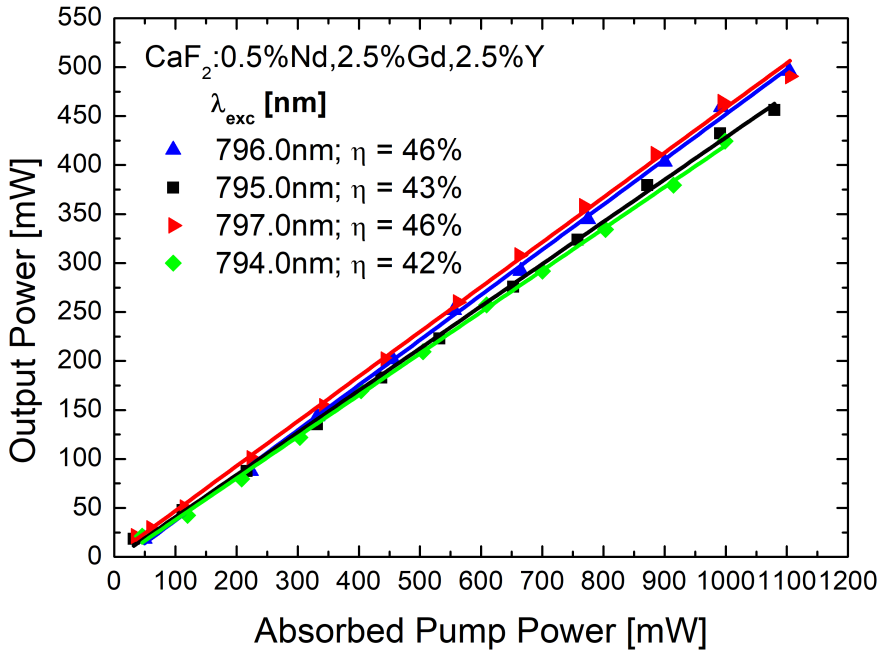

FIGURE 4.10: Laser output power versus absorbed pump power of a $CaF_2 : 0.5\%Nd, 2.5\%Gd, 2.5\%Y$, with output coupler $T = 8\%$, for different pump wavelengths.

4.3.1 Laser Tunability Investigation

One of the key features of these crystals resides in their large emission band, which can be illustrated by studying their laser tunability. For this purpose, a birefringent Lyot filter Newlight BIR1020 was inserted into the plano-concave cavity at Brewster angle (Figure 4.1) keeping an output coupler transmission of 8%.

The same four laser crystals have been tested with this tunable cavity: $CaF_2 : 0.5\%Nd$ co-doped with $2.5\%Gd, 2.5\%Y$ pumped at 796 nm, and $4\%Gd, 1\%Y$, // $3\%Gd, 1.4\%Ce, 0.6\%Y$, // $3.8\%Gd, 0.55\%La, 0.65\%Y$ all pumped at 797 nm, with the aim of achieving the broadest and flattest laser tunability around 1050 nm. The tunability of all 4 crystals was successfully investigated between 1048 nm and 1072 nm with the $T = 8\%$ output coupler,

as displayed in Figure 4.11. All of these laser crystals exhibit one main peak at 1065 nm and a flat region in the $1049 - 1055$ nm range, showing the potential of these crystals for tunable laser applications.

The laser tunability curve is intrinsically connected to the stimulated emission cross section. It is thus possible to simulate the tunability curve using the emission cross-section spectrum. First , we must recall that the output power of a laser cavity can be written as [126]

$$P_{out} = \frac{T}{T+L}\eta_p \frac{\lambda_p}{\lambda_L}(P_{abs} - P_{th}) \tag{4.10}$$

where T is the output coupler transmission, L the round trip losses , λ_p and λ_L the pump and laser photon wavelength respectively, η_p the pump quantum efficiency as explained in the previous section, P_{abs} the absorbed pump power and P_{th} the absorbed pump power at the laser threshold. A relation between the threshold absorbed power and the total Losses $(T+L)$ has been derived by Moulton et al. [103] as

$$P_{th} = \frac{\pi hc(\omega_p^2 + \omega_L^2)(L+T)}{4\sigma_L(\lambda_L)\lambda_p \eta_p \tau_f} \tag{4.11}$$

where ω_p and ω_L are the pump and laser beam waists, σ_L (λ_L) is the stimulated emission cross section and τ_f the fluorescence lifetime.

All parameters are wavelength independent except for the stimulated cross-section. The laser wavelength itself varies between 1048 nm and 1070 nm while the pumping wavelength is fixed. Thus the Stokes factor λ_p/λ_L will exhibit a 2% variation between 1048 and 1070 nm which can be neglected.

The wavelength dependence of the output power can be expressed by combining eq. 4.10 and eq. 4.11 and rewriting the output power as a function of the stimulated emission cross section:

$$P_{out} = A - \frac{B}{\sigma_L(\lambda_L)} \tag{4.12}$$

where A and B are given by:

$$\begin{cases} A = \frac{T}{T+L}\eta_p \frac{\lambda_p}{\lambda_L} P_{abs} \\ B = \frac{\pi hc(\omega_p^2+\omega_L^2)T}{4\tau_f \lambda_L} \end{cases} \tag{4.13}$$

We used the emission cross-section spectra of all four crystals and adjusted the A and B parameters so as to fit the tuning curve of each crystal. The agreement between the measured tuning curve and the calculated output power dependence is very satisfactory (Figure 4.11). The B/A ratio actually defines the shape of the tuning curve. Table 4.3 gives the B/A ratio for each studied crystal. Since these four crystals were selected for

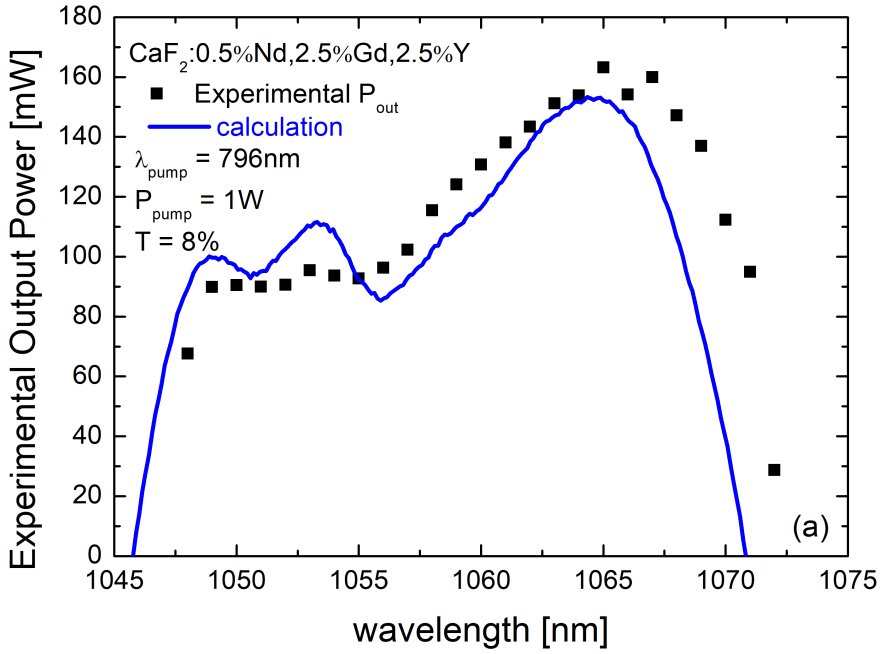
CaF2:0.5%Nd,2.5%Gd,2.5%Y
Experimental Pout
calculation
λpump = 796nm
Ppump = 1W
T = 8%
(a)
Experimental Output Power [mW]
wavelength [nm]
0
20
40
60
80
100
120
140
160
180
1045
1050
1055
1060
1065
1070
1075

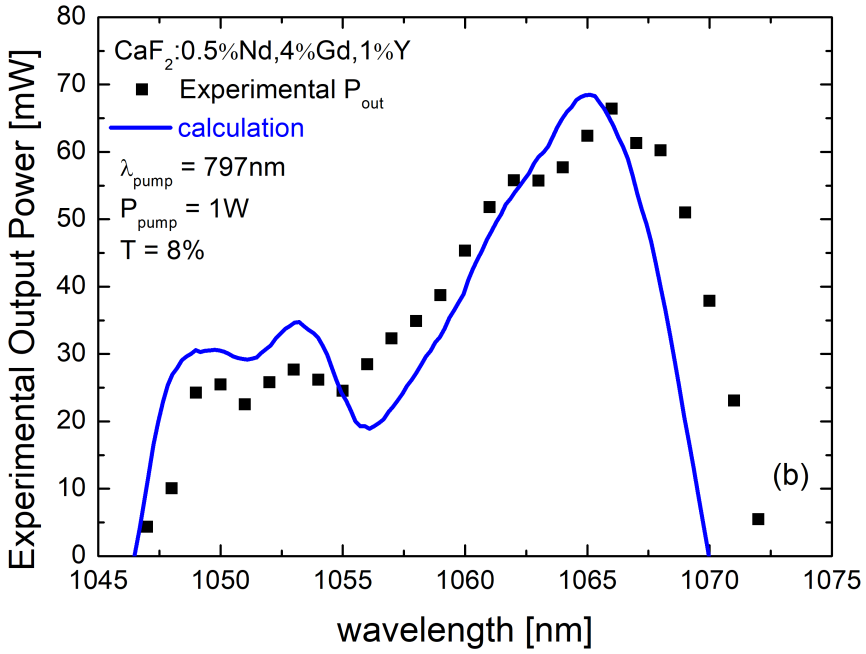
CaF2:0.5%Nd,4%Gd,1%Y
Experimental Pout
calculation
λpump = 797nm
Ppump = 1W
T = 8%
(b)
Experimental Output Power [mW]
wavelength [nm]
0
10
20
30
40
50
60
70
80
1045
1050
1055
1060
1065
1070
1075

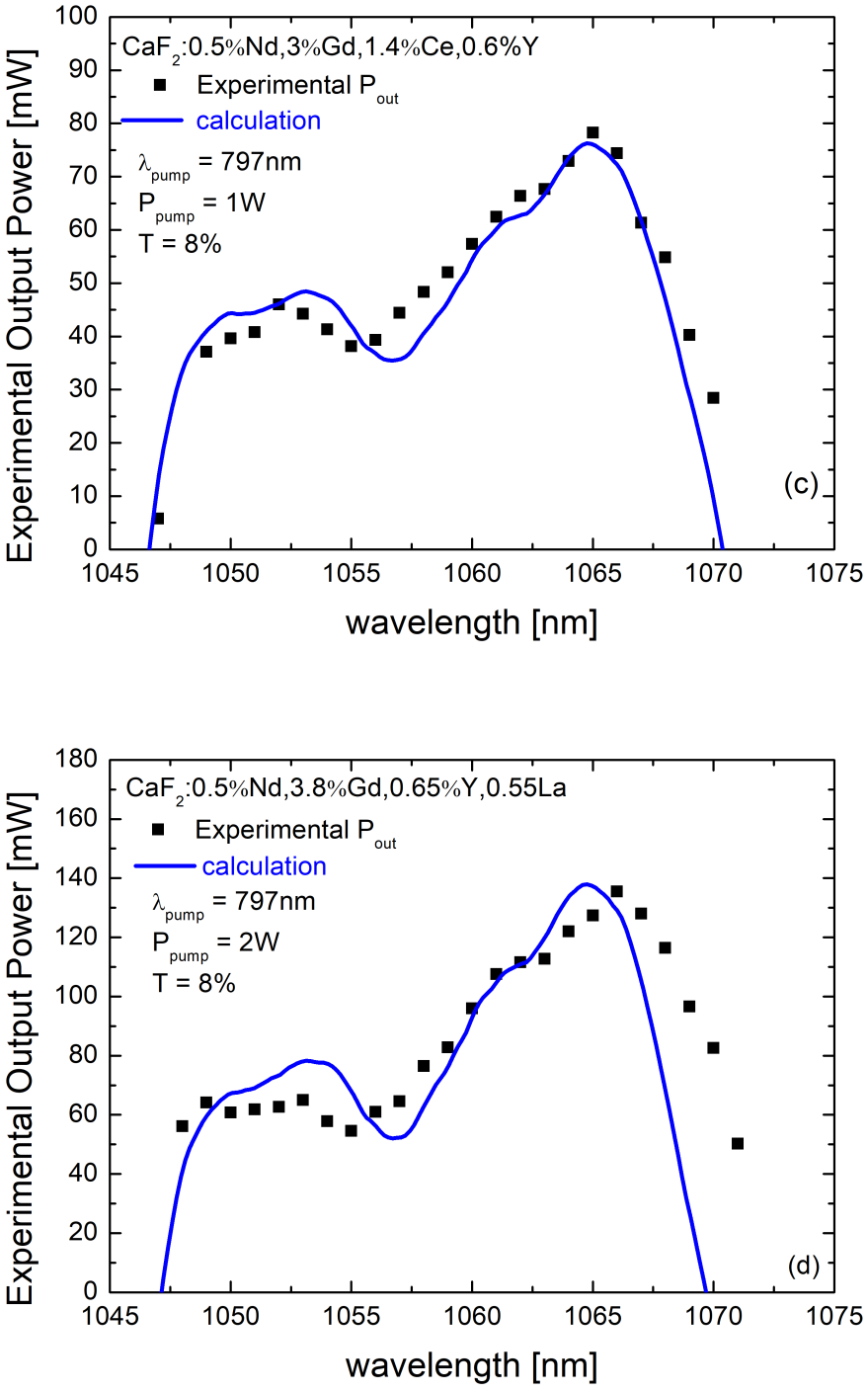

FIGURE 4.11: Tuning curves and reconstruction of a CaF_2 : 0.5%Nd co-doped with 2.5%Gd, 2.5%Y (a), 4%Gd, 1%Y (b), 3%Gd, 1.4%Ce, 0.6%Y (c) and 3.8%Gd, 0.55%La, 0.65%Y (d).

their spectral flatness around 1050 nm, it is not surprising that their tuning curves look alike and thus gives a similar B/A ratio. While the spectral shape description with eq. 4.12 is consistent with the experimental findings, the output power calculation is not straightforward as it can be affected by additional optical losses.

CaF_2 :	B/A
2.5%Gd, 2.5%Y	$1.43 \cdot 10^{-24}$ m^2
4%Gd, 1%Y	$1.42 \cdot 10^{-24}$ m^2
3%Gd, 1.4%Ce, 0.6%Y	$1.44 \cdot 10^{-24}$ m^2
3.8%Gd, 0.55%La, 0.65%Y	$1.64 \cdot 10^{-24}$ m^2

TABLE 4.3: Values of the ratio B/A for the fit in eq. (4.12) for the four studied crystals.

A critical unknown parameter is the optical losses introduced by the Lyot filter itself. As mentioned earlier, optical losses introduced by the crystal can be estimated around 2%. In order to determine optical losses introduced by the Lyot filter, we used the B/A ratio which can be expressed following eq. 4.14 as:

$$\frac{B/A}{\pi hc(\omega_p^2+\omega_L^2)(4\lambda_p\tau_f P_{abs})^{-1}} = \frac{T+L}{\eta_p} \tag{4.14}$$

From this equation, we can determine the ratio $(T+L)/\eta_p$ knowing the B/A ratio (Table 4.3) and the various parameters of eq. (4.12): $\omega_p = 25$ μm, $\omega_L = 20$ μm, $\tau_f = 370$ μs, $\lambda_p = 796$ nm. The $(T+L)/\eta_p$ values obtained for the studied crystals are between 0.6 and 0.7 suggesting high losses in the cavity, around 40% (besides $T = 8\%$ and the 2% crystal losses) knowing that η_p is typically around 0.8 for $T = 8\%$ (see Table 4.2) . This result of high losses is consistent with the low output power obtained in these tuning experiments (Figure 4.11) compared to the regular laser results (see Fig. 4.7).

One main contributing factor is related to the poor quality of the Lyot filter employed. This suggests that these laser results can be improved in the future by optimizing first the Lyot filter.

A tunability study with CaF_2 : 0.5%Nd, 2.5%Gd, 2.5%Y, for different pump wavelengths, keeping the absorbed pump power constant, is presented in Figure 4.12. As expected, the pump wavelength at 796 nm gives the flattest spectral profile around 1050 nm while the output power drastically increases around 1054 nm when pumping at 797 nm. This difference between the pumping at 796 nm and 797 nm is consistent with the findings of Chapter 2. As discussed in Figure 2.13 in Chapter 2, the absorption coefficient of the N_2 site presents a large increase at 797 nm and thus dominates the luminescence spectrum. This, in turns explains the increase of output power at 1054 nm which is characteristic of the N_2 site.

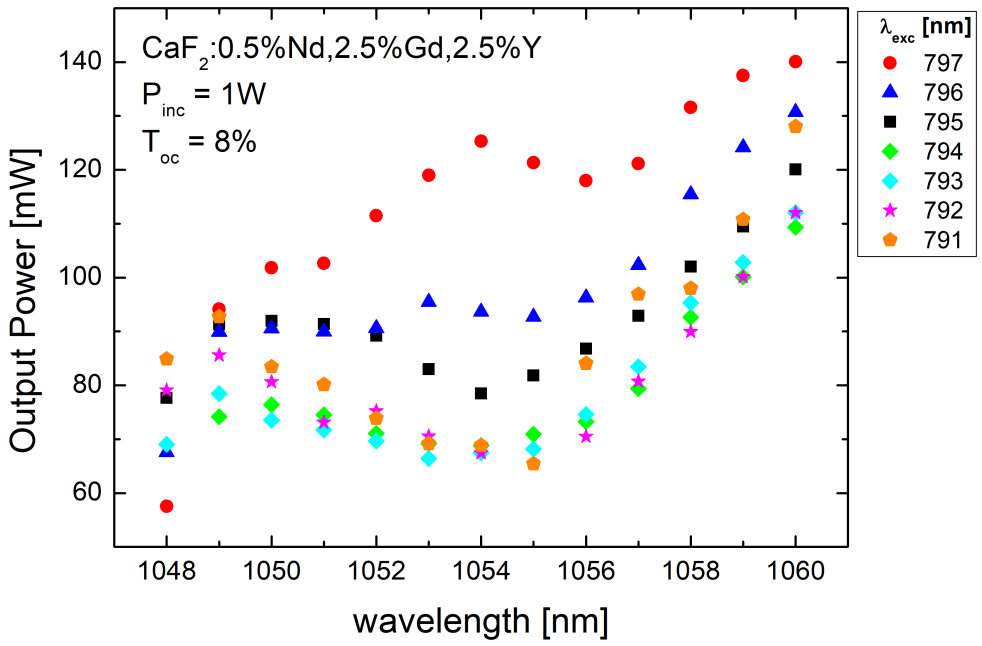

FIGURE 4.12: Tuning curve of a CaF_2 : 0.5%Nd, 2.5%Gd, 2.5%Y, with output coupler $T = 8\%$, for different pump wavelengths.

4.4 Round-Trip Losses Determination

This section is dedicated to the study and analysis of the passive losses (= round trip losses) in the laser cavity (without the Lyot filter) used in the previous section. Two different methods are presented and compared. The first one is the analysis based on the modeling work of Caird [127], that permits to derive the passive losses in the cavity from the output coupler transmission and the slope efficiency. The second method is the well known Findlay-Clay analysis [128], which is based on the laser threshold power as a function of the output coupler transmission.

4.4.1 Caird Analysis

Caird et al. [127, 129–135] developed a method for the calculation of the passive losses with a linear fit of the slope efficiency dependence with the output coupler transmission. As mentioned earlier, the laser slope efficiency as a function of the round trip losses L and the output coupler transmission T is traditionally written as:

$$\eta_s = \eta_p \cdot \frac{\lambda_p}{\lambda_L} \cdot \frac{T}{T+L} \tag{4.15}$$

The round-trip losses L can be written as $L = 2\delta l$, with l being the crystal length and δ the optical losses per length unit, and take into account scattering, background absorption and optical inhomogeneity within the

laser crystal. Additional optical losses factor due to excited state absorption for instance can be taken into account, but the corresponding development is beyond the scope of this work.

A simple inversion of eq. 4.15 leads to

$$\eta_s^{-1} = \eta_0^{-1}\left(1 + \frac{L}{T}\right) \tag{4.16}$$

where η_0 represents the maximum slope efficiency which can be achieved if $L = 0$, (no round trip losses):

$$\eta_0 = \eta_p \cdot \frac{\lambda_p}{\lambda_0} \tag{4.17}$$

Thus, using different output coupler transmissions T and measuring the corresponding slope efficiency, it is possible to estimate the round-trip losses L with a linear adjustment of η_s^{-1}, via eq.(4.16).

4.4.2 Findlay-Clay Analysis

Another model to assess the round-trip losses L is provided by the Findlay-Clay analysis, which relies on the dependence of the threshold power with the output coupler transmission [126, 128].

The laser oscillation condition in CW (continuous wave) operation is that the round- trip gain exactly equals the round trip losses, which can be written as:

$$R_1 R_2 \exp(g_0 - \delta)2l = 1 \tag{4.18}$$

with R_1 and R_2 are the reflectivity of the input and output couplers respectively, δ is the optical losses per length unit, l the crystal length and g_0 the laser gain coefficient at the threshold.

Eq. (4.18) can be conveniently rewritten as:

$$2g_0 l = -\ln R_1 R_2 + 2\delta \tag{4.19}$$

The reflectivity of the input coupler R_1 can be considered as equal to one and thus Eq. (4.19) can then be written as

$$-\ln R_2 = 2g_0 l - L \tag{4.20}$$

where $R_2 = 1 - T$ and $L = 2\delta l$, as described previously. It is possible to express $2g_0 l$ in terms of threshold power as

$$2g_0 l = P_{th}\frac{2\eta_p}{I_s A} \tag{4.21}$$

where η_p is the pump quantum efficiency, A is the pumped section of the laser crystal, and I_s is the saturation intensity given by

$$I_s = \frac{h\nu_L}{\sigma_{em}\tau_f} \tag{4.22}$$

Combining eq. 4.21 and eq. 4.22 enables to write the final Findlay-Clay analysis relation:

$$-\ln(1-T) = \frac{2\eta_p}{I_s A} P_{th} - L \tag{4.23}$$

It is worth to remark the convenient form of eq. (4.23), that enables a linear adjustment of $-\ln(1-T)$ as a function of the threshold power. One can then derive the round trip losses L simply as the intercept parameter.

4.4.3 Results and Comparison Between the Models

Both methods for the evaluation of the round trip losses L present advantages and shortcomings, related to the precision of the key parameters. For instance the estimation of the threshold power, a key parameter for the Findlay-Clay, can be difficult to estimate with a good accuracy for very low T when the threshold power is very low, on the order of few mW as in this study.

Figure 4.13 (a) presents a typical Findlay-Clay analysis with the dependence of $-\ln(1-T)$ with the threshold power and Figure 4.13 (b) a Caird analysis with the inverse slope efficiency η_s^{-1} versus the inverse output coupler transmission T^{-1} for the same $CaF_2 : 0.5\%Nd, 2.5\%Gd, 2.5\%Y$ crystal. The linear adjustment in the Findlay-Clay analysis gives an intercept value of 0.6% representing the round trip losses. A similar linear adjustment for the Caird analysis gives an intercept value η_0^{-1} of 2.08 which gives $\eta_0 = 48\%$ as maximum slope efficiency. Knowing η_0 and the adjustment slope in Figure 4.13 (b), one can derive $L = 0.58\%$ (Eq. 4.15). Thus, the two methods give the same results for the round trip losses L which at 0.6% can be considered as very low for each round trip in the cavity. This low L value illustrates the very good optical quality of the laser crystals used during this study. The low L value gives, as can be expected with eq. (4.15), a maximum slope efficiency ($\eta_0 = 48\%$) very close to the experimental slope efficiency found for a high output coupler transmission ($\eta = 44\%$ with $T = 8\%$, see Figure 4.6).

The same comparison between the Findlay-Clay and Caird methods has been performed on four other laser crystals, and the comparison is reported in Figure 4.14 while the fitting parameters for both models are given in Table 4.4. It is possible to observe that for all crystals except one the agreement between the two models is very good with round trip losses below 2% for all crystals. In the case of $CaF_2 : 0.5\%Nd, 4\%Gd, 1\%Y$ one can observe a significant discrepancy between the two methods. For this particular crystal, while the Caird analysis gives a trustable value with an acceptable linear adjustment, the Findlay-Clay analysis leads to unsatisfactory results

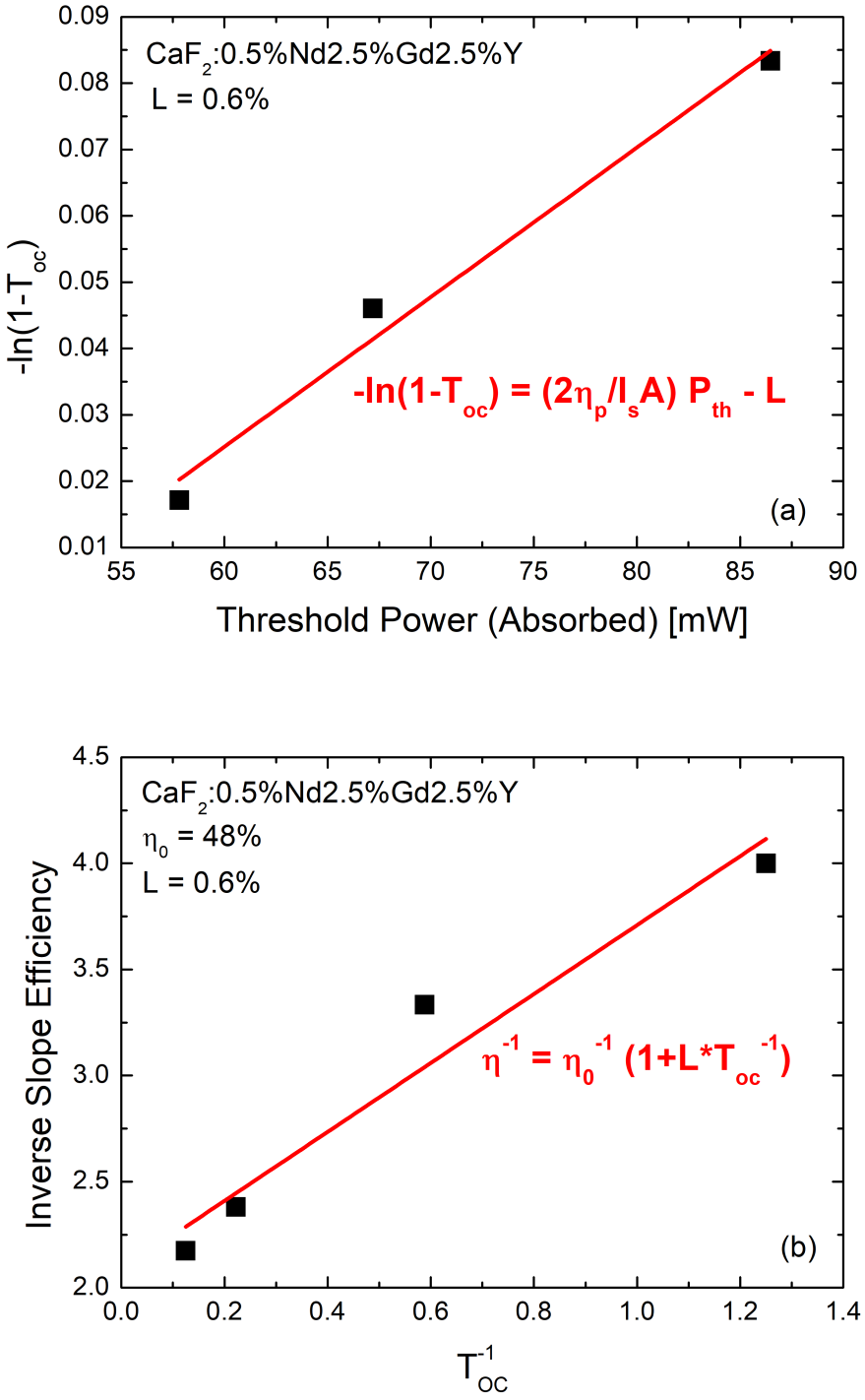

FIGURE 4.13: Passive losses calculation for the $CaF_2 : 0.5\%Nd, 2.5\%Gd, 2.5\%Y$, performed both with the Findlay-Clay analysis (a) and the Caird analysis (b).

with a poor linear adjustment due to uncertainties in the threshold power determination.

More generally, as mentioned earlier, the threshold power assessment is the main limiting factor in the Findlay-Clay analysis precision. As an illustration the threshold power for the output coupler $T = 0.8\%$ was for all crystals very low on the order of 1 mW and thus very unprecise. So these threshold power values with $T = 0.8\%$ were not taken into account in the Findlay Clay analysis.

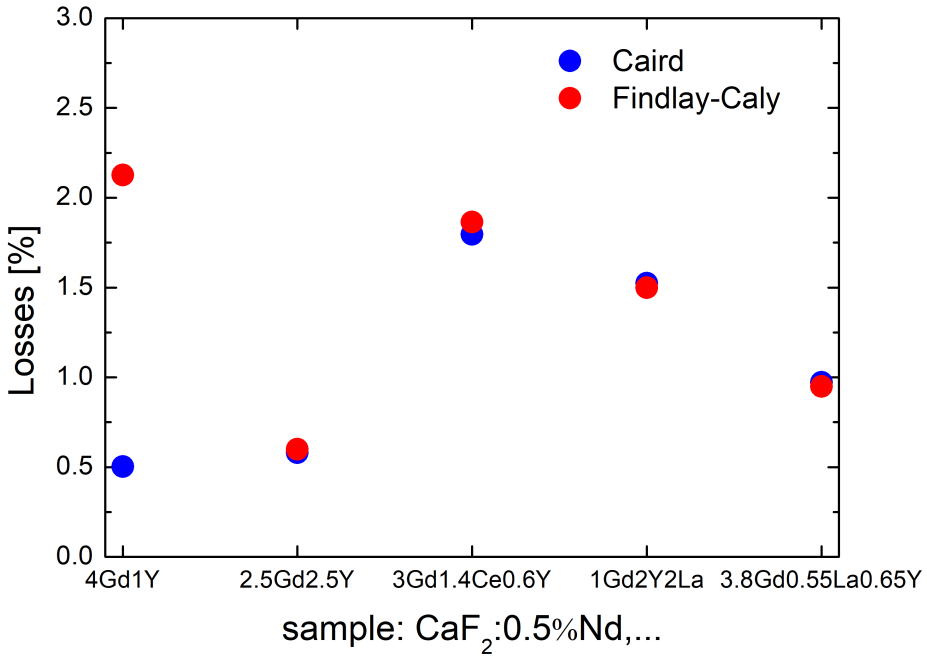

FIGURE 4.14: Passive losses calculated with the Findlay-Clay (red) and the Caird (blue) method for different laser crystals.

CaF_2 :	Slope Caird	Intercept Caird	Losses Caird	Losses F-C
2.5%Gd, 2.5%Y	0.012	2.06	0.006	0.006
4%Gd, 1%Y	0.012	2.45	0.005	0.02
3%Gd, 1.4%Ce, 0.6%Y	0.03	1.59	0.018	0.018
3.8%Gd, 0.55%La, 0.65%Y	0.02	2.02	0.01	0.0095
1%Gd, 2%La, 2%Y	0.036	2.36	0.015	0.015

TABLE 4.4: Fit parameters and losses for the Caird and Findlay-Clay (F-C) models.

4.5 Perspectives: Molecular Adherence

Heat deposited in a laser crystal during the pumping will have detrimental effects on the laser performance. It will lead to a lensing effect due to the inhomogeneous heating of the laser crystal. This in return will create wavefront distortions and depolarization effects. The origin of the thermal lensing can be a combination of thermo-optic effects due to transverse gradient of the refractive index with the temperature and photo-elastic effects caused by the thermally induced mechanical stress on the crystal. A future and promising perspective for a better heat management is the molecular adherence between different crystals which has never been done with Nd-doped fluorite crystals. A first idea is to bond an undoped CaF_2 with a Nd-Bu doped crystal, in order to take advantage of the very good thermal properties of pure CaF_2, exploiting it as a heat sink, reducing the thermal load on the laser crystal and thus limiting the detrimental thermo-optical and thermo-mechanical effects.

The main characteristic of this technique is the absence of a defined interface with a different refractive index, between the bonded crystals: the bond is of pure molecular nature without any bonding agent. The advantage resides in the lack of Fresnel reflection losses or scattering at the interface, that are critical for high-energy laser applications. Another interesting perspective is the realization of composite crystals, which would enable the investigation and combination of different spectroscopic and laser features from different materials [19].

The scientific interest for this particular technique has increased recently, but very few examples of successful molecular adherence composites have been documented in the literature, and none of them, to the best of our knowledge, refers to Nd-doped fluorites, making this research very interesting.

4.5.1 State of the Art

The molecular adherence technique refers to the contact between two surfaces, called optical contact, followed by a thermal treatment. Therefore, the first step to achieve molecular adherence is to reach the so-called optical contact, that is the formation of hydrogen bonds between the two surfaces that are very weak and unstable. An indication of achievement of this first step is the complete absence of interface fringes when the two bonded crystals are observed under direct light. According to the work of Meissner , the surfaces have to be prepared with a roughness around 0.5 nm in rms (root-mean-squared) and a flatness not worse than $\lambda/10$ in PV (peak-to-valley), and obviously cleaned to avoid the presence of impurities. The optical contact is finally achieved exercising a pressure on part of the sample starting from the outer part.

The second but not less important step is the thermal treatment, with the idea of diffusing the atoms on both sides of the interface providing a long range intermolecular bonding. Here the key parameters are the annealing duration, the temperature, which according to the literature should be between 40% and 90% of the fusion temperature, the pressure and characteristics of the annealing atmosphere, and the pressure exercised on the crystals.

Similar procedures can be found in the literature as diffusion bonding [19, 136–139] or direct bonding [140–142], together with the patented procedures of AFB®(Adhesive Free Bonding, Onyx Optics) [143] and CADB®(Chemical Activated Direct Bonding, Precision Photonics Corporation) [144]. The differences between these approaches do not reside in the final results, but in the technique itself used to achieve the bonding, such as the mechanical preparation of the surfaces, the thermal treatment and possible chemical cleaning and etching of the surfaces. The main difficulty for molecular adherence resides in the requirement of very high quality surfaces in terms of flatness, roughness and cleaning [140, 143]. Additionally these procedure may change substantially depending on the nature of the chosen crystals to bond.

Several critical issues can appear during a tentative bonding of two crystals. First a stress induced birefringence at the interface can appear depending on the different thermal properties of the two components [145].

Other issues can be encountered during the thermal treatment, especially when approaching the fusion temperature: for instance, the formation of a crystalline phase with a different refractive index has been observed with YLF, as well as the formation of latent scratches. Lastly, depending on the dopant concentration, the clustering of active ions has been observed with Nd : YAG forming inhomogeneous doping profiles [143].

In Table 4.5 are presented some remarkable examples of successful molecular adherence, to which we can add the work of Gaumé on Yb^{3+}-doped YAG, YCOB, SYS and BOYS [146].

4.5.2 A First Molecular Adherence Try: $CaF_2||CaF_2 : Nd, Lu$

As mentioned earlier, the high thermal conductivity of pure CaF_2 can be exploited to evacuate the thermal load accumulated by a doped $CaF_2 : 0.5\%Nd, 5\%Lu$ laser crystal, thus realizing a heat sink. A first experiment was performed in order to achieve molecular adherence between a 5 mm thick $CaF_2 : Nd, Lu$ and a 4 mm thick pure CaF_2. Both samples have been cored from a 18 mm diameter boule grown by the Bridgman method to a 14 mm diameter. From now on, this particular crystal composite will be referred to as $CaF_2||CaF_2 : 0.5\%Nd, 5\%Lu$.

Bonded Materials	Surface roughness, flatness	Thermal Treatment Temperature	Remarks	Ref
GSGG, GSGG	-, λ	950 °C, 16h	-	[147]
Ti : Al_2O_3, Ti : Al_2O_3	-, $\lambda/5$	1100 °C, 50 h	chemical treatment	[142]
YVO_4, Nd : YVO_4	-, $\lambda/8.5$	600 °C, 50h	contact pressure $P = 10^{-3}$ Pa	[148]
YAG, Yb : YAG; Yb : YAG, Yb : GGG	1 nm, $\lambda/4$	300 °C, 3 h 800°C, 2h 1200 °C, 20 h	contact pressure $P = 25$ Kg/cm^2 no contact pressure ambient pressure	[19]
YAG, Nd : YAG	-	-	fabricated with AFB®	[141]
Nd : YAG, Cr^{4+} : YAG	-	-	fabricated with AFB®	[137]
YAG, Yb : SYS	-	850 °C, 24 h	orientation (111) for YAG	[136]

TABLE 4.5: Some remarkable examples of successfully achieved molecular adherence, to which it is worth adding the work of R. Gaumè [146].

As already documented in the literature, one of the key factors is the surface quality, in terms of roughness and flatness. A "laser-quality" polishing preparation, as the one performed for the laser crystals used in section 4.3, is not sufficient. Thus, three extra steps of polishing have been added to the polishing process, using specific submicron-sized diamond abrasive grains. The surface roughness is then measured with a confocal interferometric microscope (Sensofar), while the flatness is measured with a MarOpto FI 1040Z Fizeau interferometer, using a working wavelength of 632.8 nm.

The polishing procedure allows to achieve a sub-nanometric roughness and a flatness not worse than $\lambda/12$ over a 14 mm diameter circular sample. A visual comparison between a laser-polished surface and a subnanometric polishing surface is shown in Figure 4.15, along with a graph showing the roughness profiles.

As described in section 4.2.1, the two crystals are oriented with the $[1,1,1]$ axis perpendicular to the polished surface,.

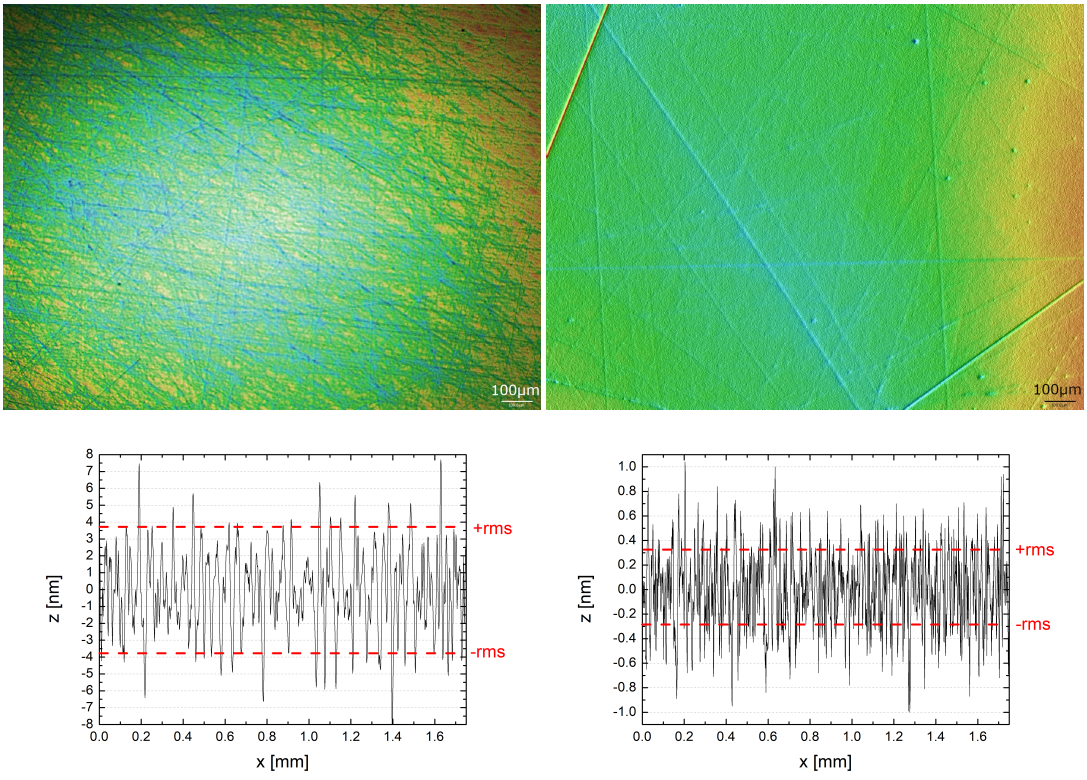

FIGURE 4.15: Comparison between laser polished surface and sub-nanometric polished surface, for $CaF_2 : 0.5\%Nd, 5\%Lu$

The pure CaF_2 and the $CaF_2 : 0.5\%Nd, 5\%Lu$ crystals have been prepared with one laser-quality polished surface, which will be used as the external surface of the final sample, and one subnanometric polished surface that will be used for the molecular adherence. The latter surfaces have been cleaned with acetone and placed in contact with each other, as can be seen in Figure

4.16. In this figure it is possible to observe the interference fringes of the interface.

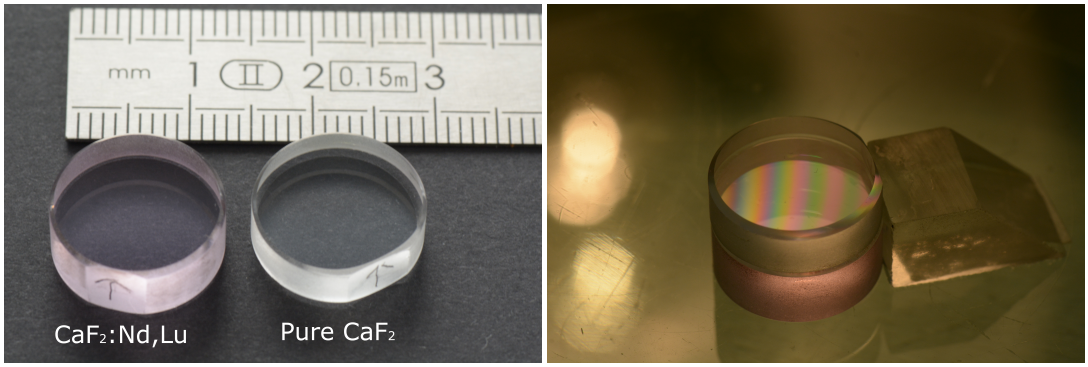

FIGURE 4.16: Left, the two crystals separately, with diameter $\phi = 14$ mm, and a 5 mm thickness for the doped sample and 4 mm for the pure CaF_2. Right the two crystals in contact.

After placing the two samples in contact, a small pressure, concentrated on a 1 mm^2, is exercised on the top surface, starting from the outer part of the crystal. A successful adherence can be observed on part of the sample as seen in Figure 4.17.

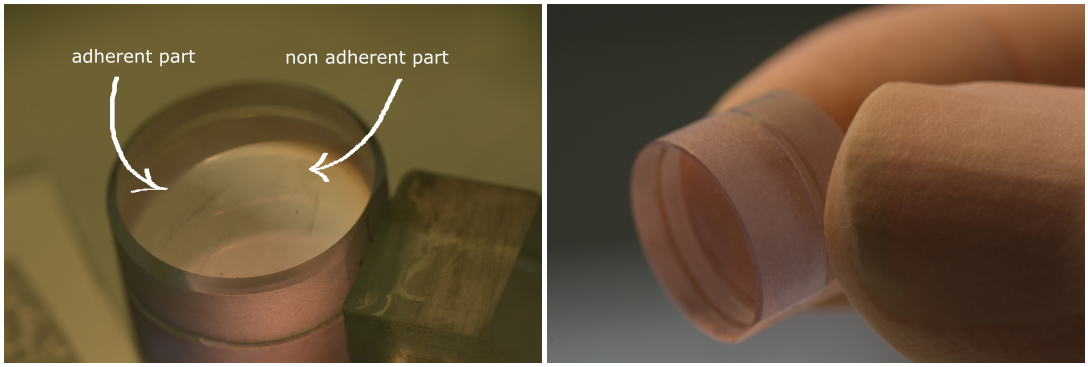

FIGURE 4.17: Left, a picture of the optical contact, showing the part of the crystal where the optical contact has been successfully achieved and the part where it is not. Right, a picture showing the stable bonding between the two crystals.

The sample is then examined using the Sensofar confocal microscope to record a bright field image, in which the contrast enables to distinguish the adherent part from the non-adherent part. A simple analysis of the images looking at the number of dark pixels compared to the total number of pixels, shows that the adherence is present on 30% of the sample, (Figure 4.18). Color variations in Figure 4.18 (left) give a qualitative view of the roughness distribution across the interface between the two crystals.

After having achieved molecular adherence on part of the sample, we performed a thermal treatment using a resistive oven. The vacuum level for this thermal annealing procedure is a key parameter. : traces of impurities,

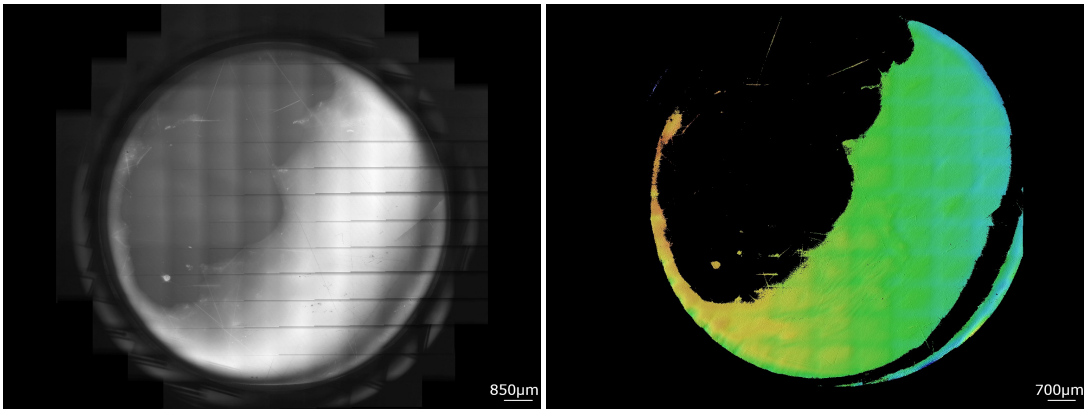

FIGURE 4.18: Sensofar picture before thermal treatment, bright field (left) and qualitative roughness. Molecular adherence is present on roughly 30% of the sample.

water and oxygen, have to be minimized, in order to avoid adhesion of water for instance which would impair the molecular adherence. For this reason, the oven is connected to a primary and turbo-molecular pump, in order to reach $8 \cdot 10^{-3}$ mbar. After pumping the oven chamber, the temperature is increased to be between $0.4 \cdot T_f$ (fusion temperature) and $0.6 \cdot T_f$. The last stage of the process is the cooling ramp. During this first annealing treatment, no pressure was applied on the sample.

The annealed sample was then characterized using the same types of images of the Sensofar microscope, showing that the adherent part has increased to 40%, as can be seen in Figure 4.19.

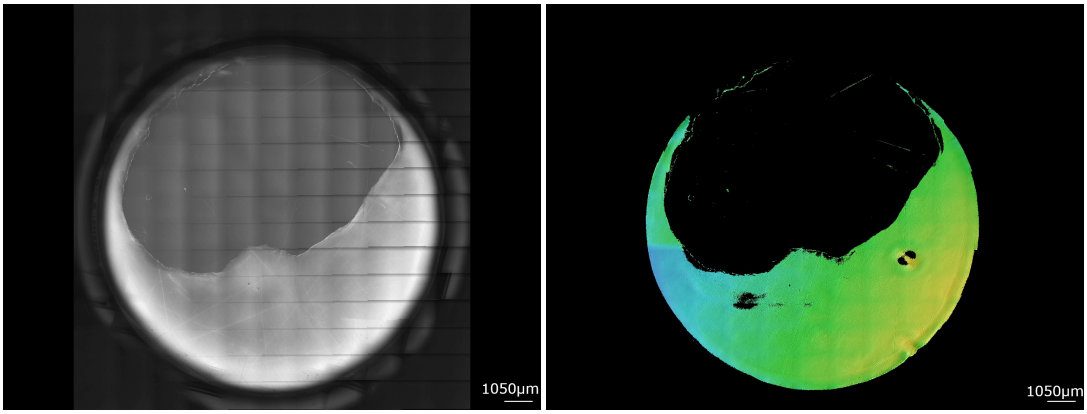

FIGURE 4.19: Sensofar picture after the first thermal treatment, bright field and roughness. Molecular adherence is present for roughly 40% of the sample. The roughness measurement is purely qualitative, due to the lack of resolution of the Sensofar microscope.

In order to extend the adherence to the entire sample surface, a second thermal treatment, analogous to the first one is performed reaching a temperature of 800 °C and more importantly adding a pressure of 1.2 kg/cm^2 by placing a weight on top of the sample. The result is depicted in Figure

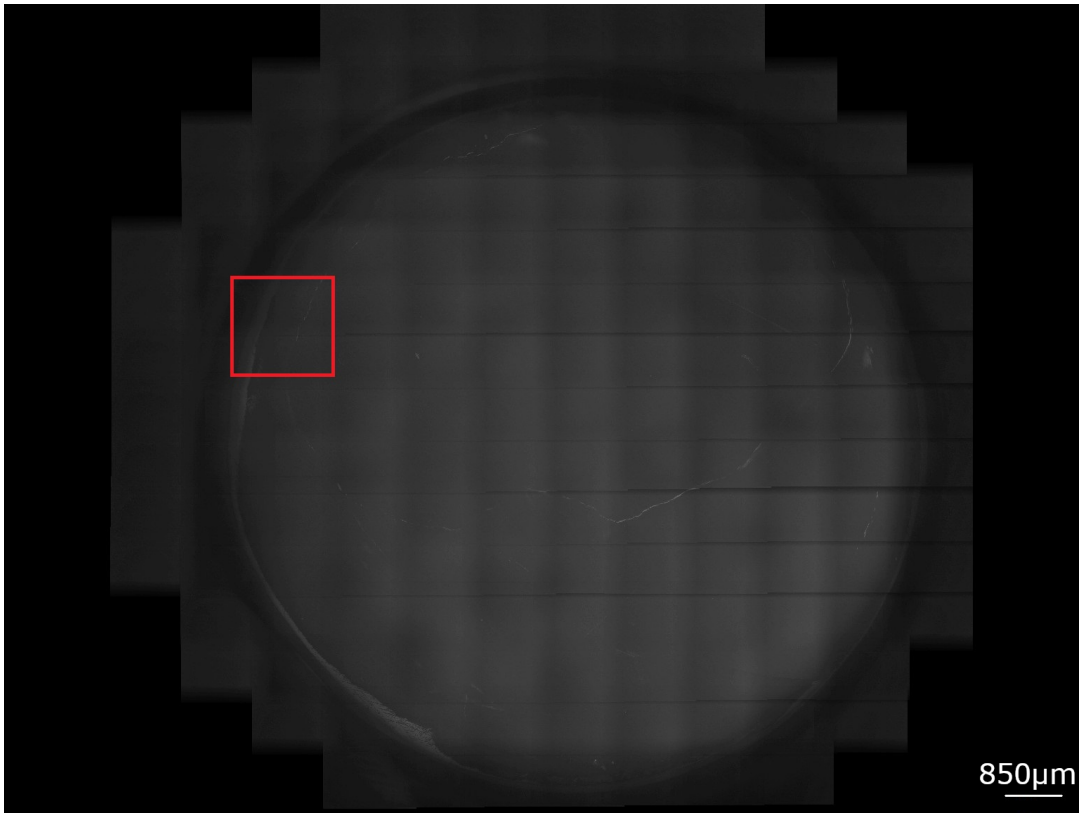

FIGURE 4.20: Bright field Sensofar picture after the second thermal treatment. The difference in contrast between the two parts of the interface is much lower. The red box identifies the reference for Figure 4.22.

4.20: the difference in contrast across the interface between the two crystals is no longer visible indicating a global adherence on the entire surface, but small defects can be observed illustrating an imperfect bonding. Because the adherence is taking place over the entire surface a confocal image illustrating the roughness distribution could not be recorded.

A third and last thermal treatment was performed, analogous to the second one but adding more pressure on the sample, with 2.8 kg/cm^2. The result is depicted in Figure 4.21, in which there is no observable contrast meaning that we cannot distinguish the interface between the two crystals. So one can assume that the molecular adherence is taking place over the entire surface with the exception of some imperfections at the border of the sample. The difference between the molecular adherence achieved after the second and third thermal treatment is illustrated in Figure 4.22, with a zoom on the red box of Figure 4.20 and 4.21 showing the improvement obtained after the pressure increase. At 1.2 kg/cm^2, the picture shows parts near the edge of the sample where the molecular adherence is incomplete. After the third thermal annealing, the molecular adherence is complete for the same area. As a conclusion, the third and last thermal treatment will be considered as a reference procedure for future bonded samples.

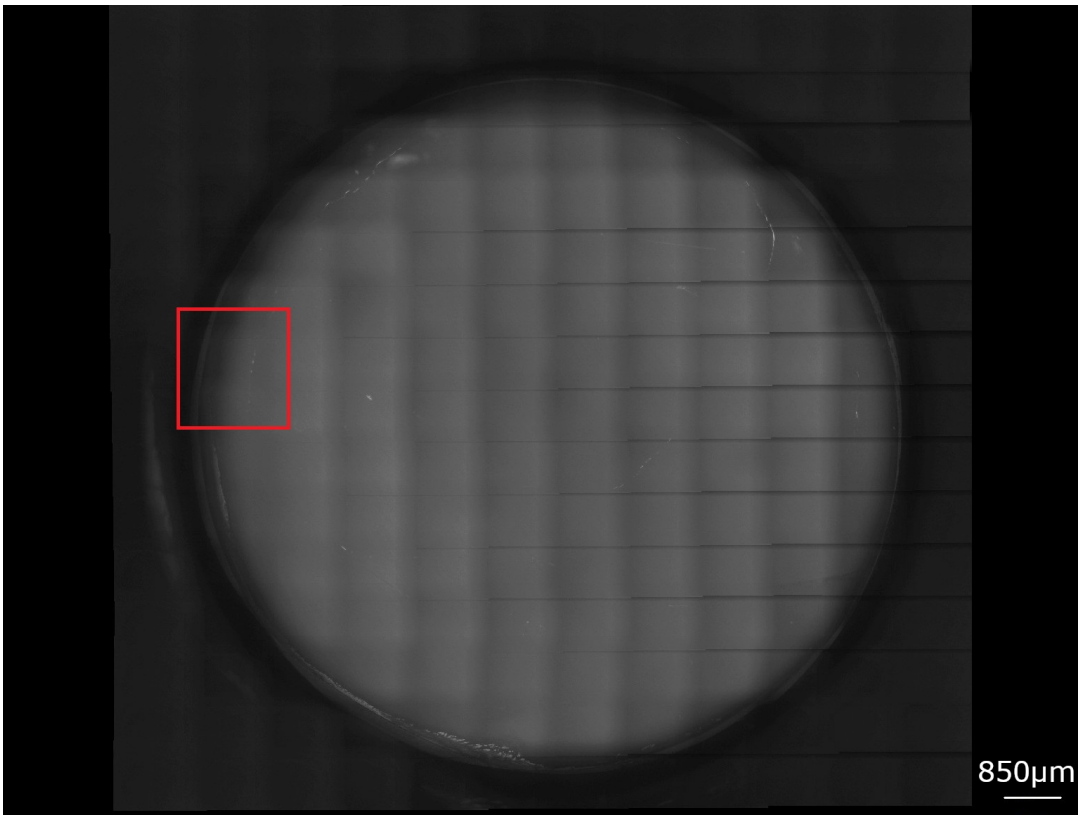

FIGURE 4.21: Sensofar picture after the third thermal treatment, bright field. There is no difference in contrast between the former adherent and non-adherent parts. The red box identifies the reference for Figure 4.22.

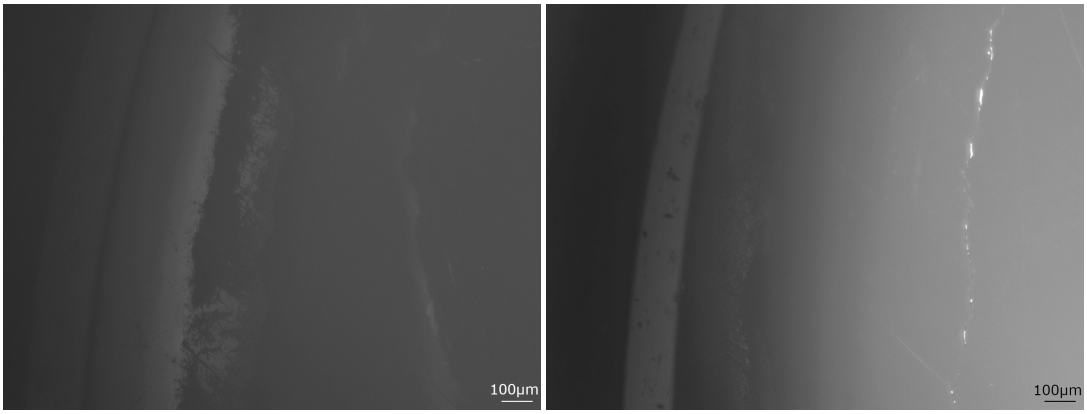

FIGURE 4.22: Comparison result after the second thermal treatment (left) and the third (right). The parts of the samples correspond at the zone of the sample identified with the red box in Figure 4.20 and 4.21 respectively.

To further investigate the quality of the $CaF_2||CaF_2 : 0.5\%Nd, 5\%Lu$ bonded structure, a 797 nm focused laser beam coming from a tunable Ti:Sapphire laser was sent through the sample. In Figure 4.23 one can clearly distinguish the undoped CaF_2 from the doped part of the sample. A green trace of the laser beam is observed which is characteristic of the upconversion mechanisms taking place among Nd ions within the Nd doped CaF_2. The laser power was 2 W with a spot size of 50 μm, which represents a laser intensity of 25 kW/cm^2 which had no effect on the bonding between the two crystals illustrating the quality of the molecular adherence.

Another interesting preliminary test is to observe the heat propagation throughout the bonded structure with a thermal camera. Figure 4.24 shows the heat flux propagation for a laser beam entering the structure from the left, passing first through the undoped CaF_2 before reaching the Nd doped part. One can first observe a strong heat deposition on the right part of the sample. This observation could be surprising as the laser beam is first absorbed by the left part of the doped crystal. However this is due to the abrupt change of medium at the solid/ air interface on the right part of the sample which induces a strong heat deposition. On the contrary, the heat propagates smoothly at the interface between the two crystals going from the doped part to the undoped part illustrating the desired heat sink behavior of the pure CaF_2.

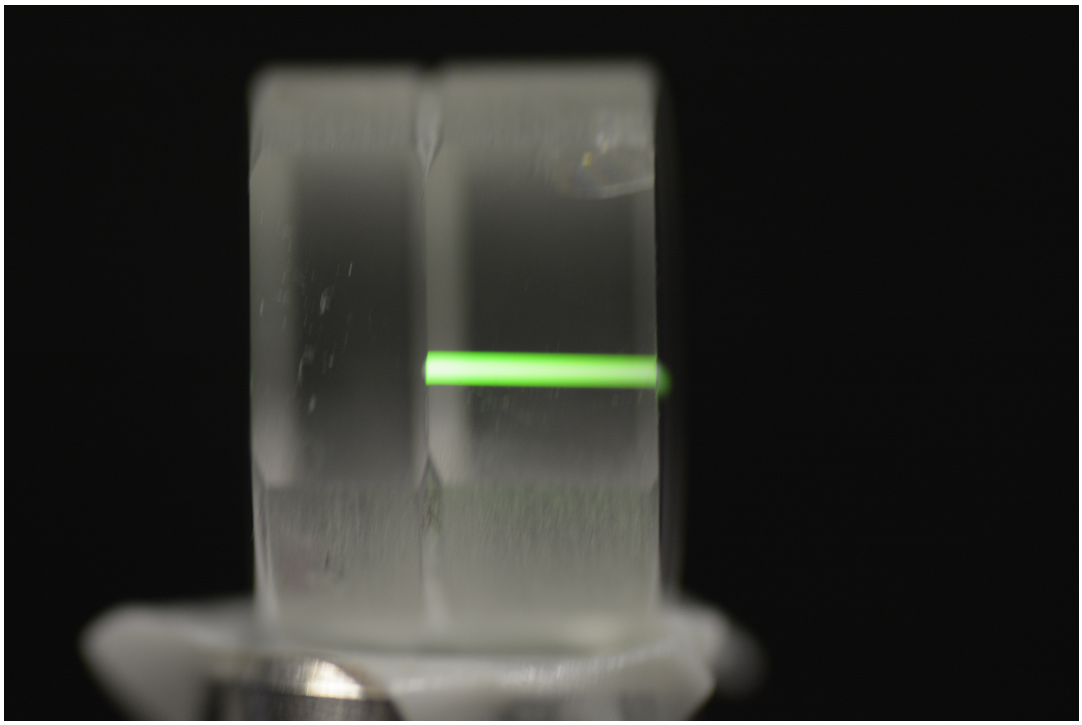

FIGURE 4.23: Titanium Sapphire laser beam at 797 nm, 2 W focalized that propagates through the sample. It is possible to see that only in the undoped part the Nd up-conversion is taking place.

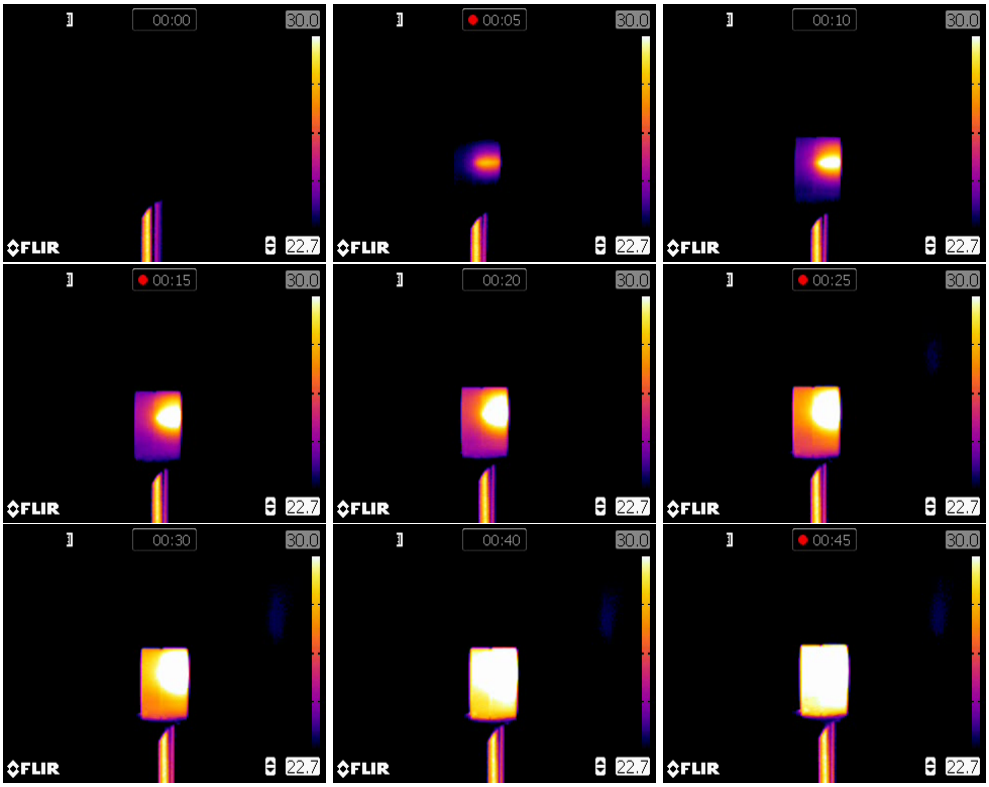

FIGURE 4.24: Temporal heat propagation due to laser excitation at 797 nm, 2 W focalized.

Finally, we performed a laser test, with the bonded sample using the same plano-concave cavity depicted in Figure 4.1 and the same Ti-Sa pump laser. Figure 4.25, shows the output power vs absorbed pump power for two output couplers with $T = 8\%$ and $T = 0.8\%$. The laser performance is compared with a 5 mm thick $CaF_2 : 0.5\%Nd, 5\%Lu$ crystal having the same diameter $\phi = 14$ mm as the $CaF_2||CaF_2 : 0.5\%Nd, 5\%Lu$ bonded structure.

With $T = 8\%$ no substantial difference between the two samples can be observed. However, when the intra-cavity power is increased, using $T = 0.8\%$a significant difference in the thermal roll-over appears with a less pronounced power saturation at high pumping power above 1.5 W power with the bonded sample (blue dots, Figure 4.25). This qualitative comparison is a first indication of a better heat management using the bonded sample. In this precise experiment the sample were placed in a copper holder without water cooling. Better laser performance at higher power can be achieved by optimizing not only the crystal cooling, but also the bonded crystal itself. Different bonded structure geometries can be considered to optimize the thermal management. For instance one could think of bonding an undoped CaF_2 on both sides of the laser crystal to further optimize the heat extraction.

Lastly, the sample was successfully cut from a cylindrical shape to a cubical one, without damaging the interface. A carbon coating was deposited on one of the cut pieces to record Scanning Electron Microscopy (SEM) images

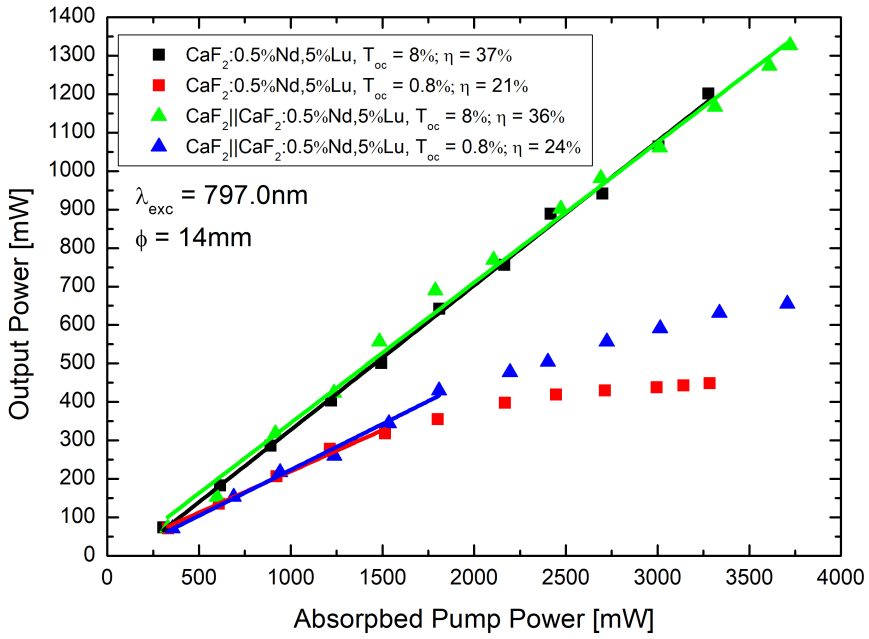

FIGURE 4.25: Laser test using a plano-concave cavity of $CaF_2||CaF_2 : 0.5\%Nd, 5\%Lu$ (△) compared with $CaF_2 : 0.5\%Nd, 5\%Lu$ (□) with the same diameter $\phi = 14$ mm and a of thickness 5 mm, for two output coupler transmission of 8% (green and black) and 0.8% (blue and red).

of the transverse section, as depicted in Figure 4.26, where it is possible to see the absence of defects at the interface between the doped sample and the undoped sample.

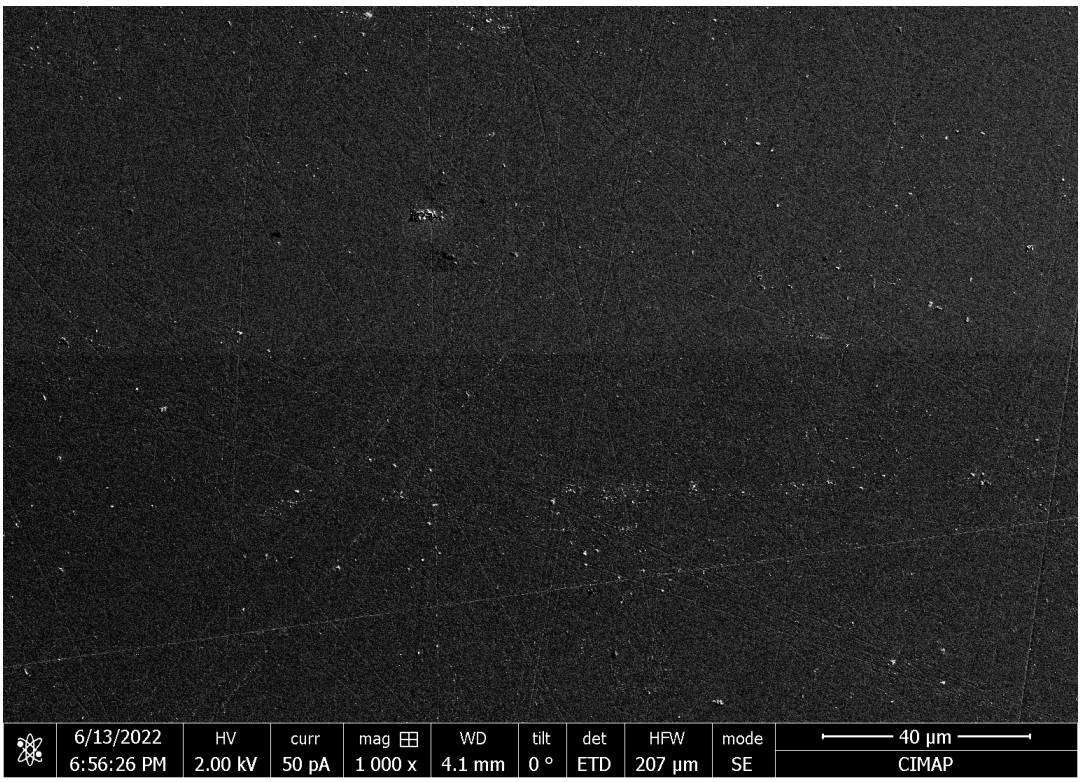

FIGURE 4.26: SEM image of the bonded sample. Upper the doped CaF_2, down the pure one. The bright points are simply residuals of the carbonation process.

4.6 Conclusions

In this chapter, the laser performance of neodymium-doped calcium fluoride with various buffer ions has been investigated.

First the role of the crystal preparation and orientation is discussed, focusing on the importance of orienting the crystal along the $(1, 1, 1)$ direction to avoid depolarization effects. Various laser crystals were investigated using the same plano-concave cavity. The laser slope efficiencies are for most crystals on the order of 40% as a function of the absorbed pump power while the laser threshold power remains significantly low around few tens of mW. A particular attention was dedicated to the $CaF_2 : 0.5\%Nd, 2.5\%Gd, 2.5\%Y$ crystal laser performance. Among the different results, one can point out that a slope efficiency of 44% as a function of the absorbed pump power was achieved when pumping at at 796 nm with a 8% output coupler transmission.The threshold pump power was 60 mW with a lasing wavelength of 1065.0 nm.

The low laser threshold powers recorded for all laser crystals demonstrate the good optical quality of the laser crystals and the very good quantum efficiency of the $^4F_{3/2}$ emitting laser. For the different output coupler transmissions, the recorded laser slope efficiencies are close to the

theoretical slope efficiency which indicates that parasitic effects such as an imperfect spatial overlap between the laser and pump beams do not take place in our experiments. Additionally, the laser beam characteristics are investigated leading to a $M^2 = 1.1$ and a divergence $\theta = 20$ mrad This very good quality of the output laser beam shows that thermal effects have a limited effect on the laser crystal performance within the absorbed pump range which is typically below 1.5 W.

The tunability of selected laser crystals was investigated using a birefringent filter inserted in the laser cavity and showed a strong coherence with the optical spectroscopy characteristics presented in Chapter 2. A tunabilty in the $1048 - 1070$ nm spectral range with a 6 nm flat region between 1049 and 1055 nm is achieved. A calculation of the tuning curve shape using the emission cross-section spectrum is presented showing a good agreement with the experimental tuning curve of several crystals such as $CaF_2 : 0.5\%Nd, 3\%Gd, 1.4\%Ce, 0.6\%Y$ and $CaF_2 : 0.5\%Nd, 4\%Gd, 1\%Y$.

The round trip losses due to the laser crystal are assessed using two different methods, namely the Findlay-Clay and Caird analysis. The two models gives similar values which are below 2% for all the studied crystals, illustrating once more the good optical quality of the laser crystals. Ironically, a drawback of this good quality is the corresponding low laser threshold. These low threshold values are accompanied by a rather large uncertainty when using a low transmission output coupler (in our study, $T = 0.8\%$) which limits the use of the Findlay-Clay analysis for low transmission output couplers.

Finally, a preliminary study on molecular adherence has been performed. A dedicated procedure has been identified to fabricate a bonded $CaF_2||CaF_2 : Nd, Lu$ crystal. The requirements for the surface quality and the thermal treatment procedure to achieve the desired result are presented. The recording of the heat propagation going from the doped part to the undoped part of the bonded sample illustrates the advantage of having a pure CaF_2 as a heat-sink. A $CaF_2 : Nd, Lu$, crystal with the same 14 mm diameter and 5 mm thickness showed poorer laser performance at high intra-cavity laser power while the undoped CaF_2 heat-sink enables better laser performance of the bonded sample due to a reduction of the thermal effects, opening the road for interesting perspectives. For instance new crystal bonding geometries can be envisioned with undoped crystal on both sides of the doped material or the concatenation of different crystals with different co-dopings, to obtain hybrid spectroscopic and laser behaviors, similarly to what was obtained by Mukhin et al. with $Yb : YAG||Yb : GGG$ [19].

Conclusions and Perspectives

The results presented in this work confirm the potential of $CaF_2 : Nd$ codoped with buffer ions as an efficient amplifier and laser material, in which the quenching of the Nd 1 μm transition is solved by the buffer ion co-doping. Within laser applications, the high thermal conductivity of CaF_2 (9.71 WmK^{-1}) makes it particularly appealing for high energy applications. A specific attention within this work was devoted to the role of the various buffer ions on the spectroscopic properties, amplification properties and CW laser performance. The interesting optical and amplification properties of the optimized compositions make these laser materials promising substitutes for the neodymium-doped phosphate glasses currently employed, which are limited by their thermal conductivity (roughly 10 times smaller than CaF_2). The results reported in this work and summarized in the following paragraphs represent interesting perspectives for the LMJ applications , but more generally for laser amplifier development around 1.05 μm because of the unusual broad bandwidth and flatness of the emission and absorption spectra of the laser crystals investigated.

The optical spectroscopy investigation revealed several interesting aspects. A first study of the co-doping with single-buffer ions, namely gadolinium, lanthanum, cerium, lutetium, yttrium and scandium clearly shows the impact of the buffer ion on the spectroscopic properties of $CaF_2 : Nd$, mainly dividing the buffers into two different groups. The buffer ions with larger size than Nd^{3+} ion, gadolinium, lanthanum and cerium, lead to a single dominant Nd emitting site labeled N1, while the smaller ions, yttrium, lutetium and scandium, exhibit two different types of Nd sites: a similar N1 site along with another Nd site labeled N_2. In fact, inserting trivalent lanthanide ions in CaF_2, gives rise to the formation of different optical centers, depending on the lattice position of the doping ion and the corresponding local symmetries created by the additional interstitial F^- ions. The small ionic radius of the dopant allows extensive relaxation of the dopant ion within its incorporation site and therefore the creation of different types of clusters depending on the relative position of the dopant and the associated interstitial F^- ions. On the opposite, large buffer ions will tend to occupy a specific position and will create only one type of cluster.

The two Nd sites N_1 and N_2 have characteristic absorption and emission features and lifetimes, enabling not only their distinction in the spectral domain by choosing specific absorption and emission wavelengths, but also in time, by choosing specific time windows using time-resolved spectroscopy to isolate the signature of each site. The N_1 site associated with

a quasi–rhombic symmetry is characterized by a couple of absorption and emission wavelengths, namely 791 nm - 1049 nm and a longer lifetime, of the order of $450 - 500\mu$s, while the N_2 site with a quasi–tetragonal symmetry is characterized by the excitation/emission couple of 797 nm-1054 nm and a shorter lifetime, of the order of $300 - 400\mu$s.

The co-doping with multiple buffer ions, mixing buffers from different sizes is investigated while keeping the same total buffer concentration of 5at.%, in order to ensure the absence of quenched Nd-Nd clusters while not degrading the crystal thermo-mechanical properties. Depending on the concentration of the different buffers, it is possible to obtain intermediate spectroscopic behaviors, in between the two single co-doped crystals $CaF_2 : Nd, Bu_1$ and $CaF_2 : Nd, Bu_2$, enabling the tailoring of the spectroscopic properties by choosing carefully the buffer nature and concentration. Moreover, the possibility to perform pre-growth simulations of the spectroscopic properties was successfully investigated, combining the spectra of the single co-doped $CaF_2 : Nd, Bu_1$ and $CaF_2 : Nd, Bu_2$ via linear combination, and obtaining exactly the experimental $CaF_2 : Nd, Bu_1, Bu_2$ spectrum. This enables a spectral engineering of $CaF_2 : Nd, Bu_1, Bu_2$, adjusting the nature and concentration of the buffers depending on the desired application. Moreover in the case of a monochromatic pumping of crystals with a small buffer ion such as Y, the pumping wavelength is critical to a sub-nanometer level in the $795 - 797$ nm to obtain the desired spectral shape, since within this spectral region the absorption coefficient of the N_2 sites rises spectacularly. The emission spectra using a third buffer ion were simulated in order to achieve the broadest and flattest emission profile around 1050 nm. These simulations were successfully compared to the experimental spectra.

From these studies, four different compositions were identified because of their broad and flat emission spectra, namely $CaF_2 : 0.5\%Nd$ with $2.5\%Gd, 2.5\%Y$, // $4\%Gd, 1\%Y$, // $3.8\%Gd, 0.65\%Y, 0.55\%La$ and $3\%Gd, 1.4\%Ce, 0.6\%Y$. Compared to the currently employed phosphate glasses, these compositions represent interesting crystalline substitutes because of their high thermal conductivity and also because of their flat fluorescence bands compared to the glass gaussian profile. This flatness is interesting as it can limit the FM-to-AM conversion within the front-end (as explained in Chapter 1). A limitation of these compounds resides in the fact that their fluorescence spectra fall on the long wavelength part of the 1053 nm mark.

The ytterbium co-doping of $CaF_2 : 0.5\%Nd$ has been also investigated, with the idea of using Yb ions both as active ions and buffer ions and taking advantage of the Nd high absorption cross section when pumping at 800 nm. The study of the energy transfer between the neodymium ion and the ytterbium ion revealed an Nd to Yb energy transfer efficiency around 80% in $CaF_2 : 0.5\%Nd, 3\%Yb, 2\%Gd$ crystal, while exhibiting very broad luminescence bands. These preliminary results show that these crystals although not necessarily interesting for the LMJ applications, are actually

interesting for broadband lasers or amplifiers around 1 μm.

To assess the potential of the four promising crystals, namely the 2.5%Gd, 2.5%Y, // 4%Gd, 1%Y, // 3.8%Gd, 0.65%Y, 0.55%La and 3%Gd, 1.4%Ce, 0.6%Y co-doped CaF_2 : 0.5%Nd, a criterion on the amplification properties has been designed. This consists in having after amplification a laser beam centered at 1053.0 nm with at least 3 nm of FWHM, with the input probe beam being a gaussian beam with a FWHM of 16 nm centered at 1053.0 nm, for an amplification factor (P_{out}/P_{in}) at 10^9. The amplification using these crystals, compared with the LGG70 (Nddoped phosphate glass), revealed a significant improvement from the 3 nm FWHM, reaching values around $5-6$ nm . However, the centering at 1053 nm after the amplification still show a drop of the spectrum on the long wavelength part although the results obtained represent a significant improvement to the previous study on CaF_2 : Nd, Lu.

A pump-probe setup was implemented in order to study the amplification properties of the different crystals. As a result a 35% amplification factor is measured in CaF_2 : 0.5%Nd, 5%Lu at 1054 nm for 400 mW of absorbed pump power while the other buffer doped crystals lead to a laser gain of 20% for the same absorbed pump power. These results are compared to a dedicated model based on a rate equation approach which also comprises the probe and pump beam propagation within the amplifying medium. This model also takes into account saturation effects, such as the ground state depletion and the gain saturation. The comparison between the calculated and measured amplification shows a good agreement for crystals co-doped with large buffer ions (Gd,La, Ce) which exhibit one dominant Nd^{3+} active center. The case of small buffer ions is more complicated since an exact amplification calculation would require two sets of spectroscopic parameters for N_1 and N_2 as well as the determination of the concentration of each center in the crystal. This limitation further emphasizes the relevance of a direct experimental measurement of the laser gain as presented in this work.

The tunability feature of both pump and probe beams was exploited to perform gain measurements at various pump and probe wavelengths. Amplification measurements using the 4 most promising crystals show a 20% amplification for 400 mW of absorbed pump power within small signal conditions. More interestingly, the amplification spectrum as a function of the probe wavelength evidences a flat profile in the $1048-1055$ nm spectral range consistent with the Chapter 2 findings.

Finally, the laser properties of these crystals within a plano-concave cavity are investigated .First the importance of the crystal preparation is discussed, explaining the polishing procedure to minimize the scattering losses on the surface, and the role of the crystal orientation along the $(1,1,1)$ direction to avoid depolarization effects. The same crystals investigated in the amplification properties part reveal a laser slope efficiency on the order

of 40% as a function of the absorbed pump power, while the laser threshold power remains significantly low around few tens of mW. The low laser thresholds demonstrate the high quality of the fabricated crystals and the very good quantum efficiency of the $^4F_{3/2}$ emitting laser. For the different output coupler transmissions, the recorded laser slope efficiencies are close to the theoretical slope efficiency which indicates that parasitic effects such as an imperfect spatial overlap between the laser and pump beams do not take place in our experiments. A characterization of the laser beam parameters lead to a measured $M^2 = 1.1$ and a divergence $\theta = 20$ mrad.

With the insertion of a Lyot filter in the cavity, it was possible to obtain tunable cavities in the 1048-1070 nm spectral range, with a 6 nm flat region between 1049 and 1055 nm. The tuning curve was successfully compared with a calculation based on the emission cross section spectrum.

The determination of the passive losses, using both Findlay-Clay and the Caird methods, showed a good agreement betwen both analysis with round-trip losses below 2% , thus confirming the good optical quality of the crystals.

A preliminary study on molecular adherence was carried out, with the aim of fabricating a bonded $CaF_2||CaF_2 : Nd, Lu$ crystal, with the idea of developing a Nd based CaF_2 crystal with improved laser performance, exploiting a pure CaF_2 as heat sink. This particular domain is fairly new and the literature is not particularly extensive. The surface quality of the bonded faces has to be sub-nanometric while the thermal treatment was made at 800°C. The recording of the heat propagation going from the doped part to the undoped part of the bonded sample illustrates the successful molecular adherence and the advantage of having a pure calcium fluorite as a heat-sink. A SEM image of the sample showed the absence of interface with a different refractive index between the two bonded crystals. A $CaF_2 : Nd, Lu$, crystal with the same 14 mm diameter and 5 mm thickness showed poorer laser performance at high intra-cavity laser power than the bonded sample due to a reduction of the thermal effects, opening the road for interesting perspectives. For instance, new crystal bonding geometries can be envisioned with undoped crystal on both sides of the doped material or the concatenation of different crystals with different co-doping, to obtain hybrid spectroscopic and laser behaviors, similarly to what was obtained by Mukhin et al. with $Yb : YAG||Yb : GGG$ [19].

This work shows how the use of various buffer (Bu) ions in $CaF_2 : Nd, Bu$ can lead to a spectral engineering of the emission band using the same matrix host. This unique feature can be interesting for future amplifier and laser developments. In particular in the case of Inertial Confinement Fusion, a possible new ICF architecture called Stardriver [149–152] consists in using roughly 10000 beamlets on the target with a variety of wavelengths, thus expanding the concept of the four-color scheme already implemented at the

NIF. As introduced already in section 1.2.3, multiple beams with slightly different wavelengths reduce the CBET effect, minimizing the plasma instabilities and improving the laser-plasma coupling, thus maximizing the overall efficiency of the ICF. $CaF_2 : Nd, Bu$ could be a good candidate for this next ICF generation as it would be possible to use the same material, with slightly different co-dopings to achieve multiple beamlets with wavelength shifts of the order of few nanometers from the usual 1053 nm.

References

1. Tassart, J. Overview of inertial fusion and high-intensity laser plasma research in Europe. *Nuclear fusion* **44,** S134 (2004).
2. Miquel, J.-L. & Prene, E. LMJ & PETAL status and program overview. *Nuclear Fusion* **59,** 032005 (2018).
3. Tajima, T. & Mourou, G. Zettawatt-exawatt lasers and their applications in ultrastrong-field physics. *Physical Review Special Topics-Accelerators and Beams* **5,** 031301 (2002).
4. Tikhonchuk, V. Progress and opportunities for inertial fusion energy in Europe. *Philosophical Transactions of the Royal Society A* **378,** 20200013 (2020).
5. Casner, A, Caillaud, T, Darbon, S., Duval, A, Thfouin, I, Jadaud, J., Le-Breton, J., Reverdin, C, Rosse, B, Rosch, R, *et al.* LMJ/PETAL laser facility: Overview and opportunities for laboratory astrophysics. *High Energy Density Physics* **17,** 2–11 (2015).
6. Hammel, B. *et al.* The NIF Ignition Program: progress and planning. *Plasma physics and controlled fusion* **48,** B497 (2006).
7. Spaeth, M. L., Manes, K., Kalantar, D., Miller, P., Heebner, J., Bliss, E., Spec, D., Parham, T., Whitman, P., Wegner, P., *et al.* Description of the NIF laser. *Fusion Science and Technology* **69,** 25–145 (2016).
8. MIQUEL, J.-L., BATANI, D. & BLANCHOT, N. Overview of the laser mega joule (LMJ) facility and PETAL project in France. *The Review of Laser Engineering* **42,** 131 (2020).
9. Craxton, R., Anderson, K., Boehly, T., Goncharov, V., Harding, D., Knauer, J., McCrory, R., McKenty, P., Meyerhofer, D., Myatt, J., *et al.* Direct-drive inertial confinement fusion: A review. *Physics of Plasmas* **22,** 110501 (2015).
10. Nakai, S & Takabe, H. Principles of inertial confinement fusion-physics of implosion and the concept of inertial fusion energy. *Reports on progress in physics* **59,** 1071 (1996).
11. Strickland, D. & Mourou, G. Compression of amplified chirped optical pulses. *Optics communications* **55,** 447–449 (1985).
12. Batani, D, Koenig, M, Miquel, J., Ducret, J., d'Humieres, E, Hulin, S, Caron, J, Feugeas, J., Nicolai, P., Tikhonchuk, V, *et al.* Development of the PETawatt Aquitaine Laser system and new perspectives in physics. *Physica Scripta* **2014,** 014016 (2014).

13. Campbell, J. H., McLean, M., Hawley-Fedder, R. A., Suratwala, T. I., Ficini-Dorn, G & Trombert, J.-H. *Development of continuous glass melting for production of Nd-doped phosphate glasses for the NIF and LMJ laser systems* in *Third International Conference on Solid State Lasers for Application to Inertial Confinement Fusion* **3492** (1999), 778–786.

14. Caird, J. A., Ramponi, A. & Staver, P. Quantum efficiency and excited-state relaxation dynamics in neodymium-doped phosphate laser glasses. *JOSA B* **8,** 1391–1403 (1991).

15. Normani, S. $Nd, Lu : CaF_2$ *for high-energy lasers* Theses (Normandie Université, 2017).

16. Stoffel, D. *Caractérisation du matériau Nd : Lu : CaF2 pour l'amplification laser à 1053 nm* Thèse de doctorat dirigée par Balcou, Philippe et Montant, Sébastien Lasers, Matière et Nanosciences Bordeaux 2019. PhD thesis (2019).

17. Stoffel, D., Montant, S., Goossens, J.-P., Normani, S., Braud, A., Doualan, J.-L. & Camy, P. *Laser material* $Nd : Lu : CaF_2$ *characterization for amplification application at 1053 nm (Conference Presentation)* in *Solid State Lasers XXVII: Technology and Devices* **10511** (2018), 105111T.

18. Basiev, T., Karasik, A. Y. & Shubochkin, R. Selective laser excitation and inhomogeneous band broadening of Nd^{3+} ions in disordered $CaF_2 - YF_3$ crystals. *Journal of luminescence* **64,** 259–265 (1995).

19. Mukhin, I., Perevezentsev, E. & Palashov, O. Fabrication of composite laser elements by a new thermal diffusion bonding method. *Opt. Mater. Express* **4,** 266–271 (2014).

20. Drake, R. P. in *High-Energy-Density Physics* 1–20 (Springer, 2018).

21. Betti, R & Hurricane, O. Inertial-confinement fusion with lasers. *Nature Physics* **12,** 435–448 (2016).

22. Rothenberg, J. E., Browning, D. F. & Wilcox, R. B. *Issue of FM to AM conversion on the National Ignition Facility* in *Third International Conference on Solid State Lasers for Application to Inertial Confinement Fusion* **3492** (1999), 51–61.

23. Hocquet, S., Penninckx, D., Bordenave, E., Gouédard, C. & Jaouën, Y. FM-to-AM conversion in high-power lasers. *Applied optics* **47,** 3338–3349 (2008).

24. Duluc, M, Penninckx, D, Loiseau, P, Riazuelo, G & D'humières, E. Optical smoothing with reduced FM-to-AM conversion in high-power lasers using spectral distribution. *Physical Review Applied* **12,** 054055 (2019).

25. Hocquet, S, Bordenave, E, Goossens, J., Gouedard, C, Videau, L & Penninckx, D. *Amplitude modulation filtering of FM-to-AM conversion due to the focusing grating of LMJ* in *Journal of Physics: Conference Series* **112** (2008), 032016.

26. Lindl, J. D., Amendt, P., Berger, R. L., Glendinning, S. G., Glenzer, S. H., Haan, S. W., Kauffman, R. L., Landen, O. L. & Suter, L. J. The physics basis for ignition using indirect-drive targets on the National Ignition Facility. *Physics of plasmas* **11,** 339–491 (2004).
27. Lehmberg, R. & Obenschain, S. Use of induced spatial incoherence for uniform illumination of laser fusion targets. *Optics Communications* **46,** 27–31 (1983).
28. Garnier, J. C., Gouedard, C., Videau, L. & Migus, A. *Which optical smoothing for LMJ and NIF?* in *Solid State Lasers for Application to Inertial Confinement Fusion: Second Annual International Conference* **3047** (1997), 260–271.
29. Kato, Y., Mima, K., Miyanaga, N., Arinaga, S., Kitagawa, Y., Nakatsuka, M. & Yamanaka, C. Random phasing of high-power lasers for uniform target acceleration and plasma-instability suppression. *Physical Review Letters* **53,** 1057 (1984).
30. Skupsky, S, Short, R., Kessler, T, Craxton, R., Letzring, S & Soures, J. Improved laser-beam uniformity using the angular dispersion of frequency-modulated light. *Journal of Applied Physics* **66,** 3456–3462 (1989).
31. Veron, D, Ayral, H, Gouedard, C, Husson, D, Lauriou, J, Martin, O, Meyer, B, Rostaing, M & Sauteret, C. Optical spatial smoothing of Nd-glass laser beam. *Optics communications* **65,** 42–46 (1988).
32. Rothenberg, J. E. *Two-Dimensional beam smoothing by spectral dispersion for direct drive inertial confinement fusion* in *Solid State Lasers for Application to Inertial Confinement Fusion (ICF)* **2633** (1995), 634–644.
33. Hüller, S., Raj, G., Luo, M., Rozmus, W. & Pesme, D. Crossed beam energy transfer between optically smoothed laser beams in inhomogeneous plasmas. *Philosophical Transactions of the Royal Society A* **378,** 20200038 (2020).
34. Penninckx, D., Coïc, H., Leblanc, A., Chatagnier, A., Bourgeade, A., d'Humières, E. & Loiseau, P. *Impact of FM-AM conversion on smoothing by spectral dispersion* in *High Power Lasers for Fusion Research III* **9345** (2015), 184–191.
35. Eliseev, V., Rozmus, W, Tikhonchuk, V. & Capjack, C. Interaction of crossed laser beams with plasmas. *Physics of Plasmas* **3,** 2215–2217 (1996).
36. Kruer, W. L., Wilks, S. C., Afeyan, B. B. & Kirkwood, R. K. Energy transfer between crossing laser beams. *Physics of Plasmas* **3,** 382–385 (1996).
37. Kirkwood, R., Afeyan, B., Kruer, W., MacGowan, B., Moody, J., Montgomery, D., Pennington, D., Weiland, T. & Wilks, S. Observation of energy transfer between frequency-mismatched laser beams in a large-scale plasma. *Physical review letters* **76,** 2065 (1996).

38. Igumenshchev, I., Seka, W, Edgell, D., Michel, D., Froula, D., Goncharov, V., Craxton, R., Divol, L, Epstein, R, Follett, R, *et al.* Crossed-beam energy transfer in direct-drive implosions. *Physics of Plasmas* **19,** 056314 (2012).

39. Bates, J., Follett, R., Shaw, J., Obenschain, S., Lehmberg, R., Myatt, J., Weaver, J., Kehne, D., Wolford, M., Myers, M., *et al.* Suppressing cross-beam energy transfer with broadband lasers. *High Energy Density Physics* **36,** 100772 (2020).

40. Normani, S, Braud, A, Soulard, R, Doualan, J., Benayad, A, Menard, V, Brasse, G, Moncorgé, R, Goossens, J. & Camy, P. Site selective analysis of $Nd^{3+} - Lu^{3+}$ codoped CaF_2 laser crystals. *CrystEngComm* **18,** 9016–9025 (2016).

41. Stark, J. Beobachtungen über den Effekt des elektrischen Feldes auf Spektrallinien. I. Quereffekt. *Annalen der Physik* **348,** 965–982 (1914).

42. Payne, S. A., Caird, J. A., Chase, L. L., Smith, L. K., Nielsen, N. D. & Krupke, W. F. Spectroscopy and gain measurements of Nd^{3+} in SrF_2 and other fluorite-structure hosts. *J. Opt. Soc. Am. B* **8,** 726–740 (1991).

43. Danielmeyer, H. G., Blätte, M. & Balmer, P. Fluorescence quenching in Nd:YAG. *Applied physics* **1,** 269–274. ISSN: 1432-0630 (1973).

44. Catlow, C., Chadwick, A., Greaves, G. & Moroney, L. Direct observations of the dopant environment in fluorites using EXAFS. *Nature* **312,** 601–604 (1984).

45. Voron'ko, Y. K. & Osiko, V. Nature of Concentration Quenching of the Luminescence of Nd^{+++} Ions in Crystals. *ZhETF Pisma Redaktsiiu* **5,** 357 (1967).

46. Orlovskii, Y. V., Basiev, T. T., Osiko, V. V., Gross, H. & Heber, J. Fluorescence line narrowing (FLN) and site-selective fluorescence decay of Nd^{3+} centers in CaF_2. *Journal of luminescence* **82,** 251–258 (1999).

47. Corish, J., Catlow, C. R. A., Jacobs, P. W. M. & Ong, S. H. Defect aggregation in anion-excess fluorites. Dopant monomers and dimers. *Phys. Rev. B* **25,** 6425–6438 (10 1982).

48. Orlovskii, Y. V., Basiev, T., Vorob'Ev, I., Osiko, V., Papashvili, A. & Prokhorov, A. Site-selective measurements of $^4G_{5/2}$; $^2G_{7/2}$ nonradiative relaxation rate in $Nd : SrF_2$, $Nd : La : SrF_2$, and $Nd : Sr : LaF_3$ laser crystals. *Laser Physics* **6,** 448–455 (1996).

49. Han, T. P. J., Jones, G. D. & Syme, R. W. G. Site-selective spectroscopy of Nd^{3+} centers in CaF_2:Nd^{3+} and SrF_2:Nd^{3+}. *Phys. Rev. B* **47,** 14706–14723 (22 1993).

50. Wang, Q., Su, L., Li, H., Zheng, L., Guo, X., Jiang, D., Zhao, H., Xu, J., Ryba-Romanowski, W., Solarz, P. & Lisiecki, R. Optical spectra and excited state relaxation dynamics of Nd^{3+} in CaF_2 single crystal. *Journal of Alloys and Compounds* **509,** 8880–8884. ISSN: 0925-8388 (2011).

51. Voron'ko, Y. K., Mikaelyan, R. & Osiko, V. Investigation of the Nd 3+ Optical Centers in CaF_2-Nd^{3+}-TR^{3+} Crystals (Type 1). *Soviet Journal of Experimental and Theoretical Physics* **26,** 318 (1968).

52. Bagdasarov, K. S., Voronko, Y. K., Kaminskii, A. A., Krotova, L. V. & Osiko, V. V. Modification of the Optical Properties of CaF_2 TR^{3+} Crystals by Yttrium Impurities. *Physica Status Solidi (b)* **12,** 905–912 (1965).

53. Ma, F., Zhang, Q, Jiang, D., Su, L., Shao, Y., Wang, J., Tang, F, Xu, J, Solarz, P, Ryba-Romanowski, W, *et al.* Spectroscopic, dielectric properties and local structure observation by EXAFS for Nd, Y : CaF_2 crystal. *Laser Physics* **24,** 105703 (2014).

54. Kaminskii, A., Osico, V., Prochorov, A. & Voronko, Y. K. Spectral investigation of the stimulated radiation of Nd^{3+} in $CaF_2 - YF_3$. *Physics Letters* **22,** 419–421 (1966).

55. Doualan, J., Su, L, Brasse, G, Benayad, A, Ménard, V, Wang, Q, Braud, A, Camy, P, Xu, J & Moncorgé, R. *Spectroscopic and infrared laser properties of* Nd : CaF_2 *crystals obtained via codoping with* Y^{3+} *and* Lu^{3+} *buffer ions* in *Advanced Solid State Lasers* (2013), AW1A–10.

56. Fernandez, J, Oleaga, A, Azkargorta, J, Iparraguirre, I, Balda, R, Voda, M & Kaminskii, A. Nd^{3+} laser spectral dynamics in $CaF_2 - YF_3 - -NdF_3$ crystals. *Optical Materials* **13,** 9–16 (1999).

57. Su, L., Wang, Q., Li, H., Brasse, G, Camy, P, Doualan, J., Braud, A, Moncorgé, R, Zhan, Y., Zheng, L., *et al.* Spectroscopic properties and CW laser operation of Nd, Y-codoped CaF_2 single crystals. *Laser Physics Letters* **10,** 035804 (2013).

58. Jiang, D., Zhan, Y., Zhang, Q., Ma, F., Su, L., Tang, F., Qian, X. & Xu, J. Nd, Y : CaF_2 laser crystals: novel spectral properties and laser performance from a controlled local structure. *CrystEngComm* **17,** 7398–7405 (2015).

59. Li, X., Hao, Q., Jiang, D., Wu, Q., Zhang, Z., Zhang, Z., Liu, J. & Su, L. Smooth and flat photoluminescence spectra of Nd 3+ active ions in tri-doped CaF_2 single crystals. *Optical Materials Express* **10,** 704–714 (2020).

60. Dmitruk, M., Kaminskii, A., Osiko, V. & Tevosyan, T. Induced emission of hexagonal $LaF_3 - SrF_2 - Nd^{3+}$ crystals at Room-Temperature. *physica status solidi (b)* **25,** K75–K78 (1968).

61. Wang, S., Jiang, D., Wu, Q., Cao, Z., Pang, S., Wang, J., Qian, X., Liu, J, Mei, B. & Su, L. Effect of La^{3+} proportion on spectroscopic and continuous wave laser properties of Nd, La : CaF_2 single crystals. *Laser Physics* **29,** 015801 (2018).

62. Li, C., Zhang, F., Liu, J., Su, L., Jiang, D., Liu, J., Liu, J. & Xu, J. Continuous-wave and mode-locked operation of a diode-pumped Nd, La : CaF_2 laser. *Optical Materials Express* **5,** 1972–1978 (2015).

63. Wang, S., Jiang, D., Wu, Q., Pang, S., Wang, J., Qian, X., Liu, J., Mei, B. & Su, L. Spectral properties and highly efficient continuous-wave laser operation in $Nd, Gd : CaF_2$ crystals. *Journal of Alloys and Compounds* **781,** 629–632 (2019).

64. Zhang, F., Wu, Y., Liu, J., Pang, S., Ma, F., Jiang, D., Wu, Q. & Su, L. Mode locked Nd^{3+} and Gd^{3+} co-doped calcium fluoride crystal laser at dual gain lines. *Optics Laser Technology* **100,** 294–297 (2018).

65. Kaminskii, A., Zhmurova, Z., Lomonov, V. & Sarkisov, S. Two stimulated emission $^4F_{3/2} \rightarrow {}^4I_{11/2,13/2}$ channels of Nd^{3+} ions in crystals of the $CaF_2 - ScF_3$ system. *Physica Status Solidi. A, Applied Research* **84,** K81–K84 (1984).

66. Petit, V, Doualan, J., Camy, P, Ménard, V & Moncorgé, R. CW and tunable laser operation of Yb^{3+} doped CaF_2. *Applied Physics B* **78,** 681–684 (2004).

67. Bridgman, P. W. Certain Physical Properties of Single Crystals of Tungsten, Antimony, Bismuth, Tellurium, Cadmium, Zinc, and Tin. *Proceedings of the American Academy of Arts and Sciences* **60,** 305–383. ISSN: 01999818. (2022) (1925).

68. Stockbarger, D. C. The Production of Large Single Crystals of Lithium Fluoride. *Review of Scientific Instruments* **7,** 133–136 (1936).

69. Goodman, C. *Crystal Growth* (Springer, 1974).

70. Lambert, J. H. *Photometria sive de mensura et gradibus luminis, colorum et umbrae* (sumptibus vidvae E. Klett, typis CP Detleffsen, 1760).

71. Beer, A. & Beer, P. Determination of the absorption of red light in colored liquids. *Annalen der Physik und Chemie* **86,** 78–88 (1852).

72. Dieke, G. H. & Crosswhite, H. The spectra of the doubly and triply ionized rare earths. *Applied optics* **2,** 675–686 (1963).

73. Aull, B. & Jenssen, H. Vibronic interactions in Nd:YAG resulting in nonreciprocity of absorption and stimulated emission cross sections. *IEEE Journal of Quantum Electronics* **18,** 925–930 (1982).

74. Krupke, W. Induced-emission cross sections in neodymium laser glasses. *IEEE Journal of Quantum Electronics* **10,** 450–457 (1974).

75. Fowler, W. B. & Dexter, D. L. Relation between Absorption and Emission Probabilities in Luminescent Centers in Ionic Solids. *Phys. Rev.* **128,** 2154–2165 (5 1962).

76. Inokuti, M. & Hirayama, F. Influence of Energy Transfer by the Exchange Mechanism on Donor Luminescence. *The Journal of Chemical Physics* **43,** 1978–1989 (1965).

77. *Erbium-Doped Fiber Amplifiers: Principles and Applications* (ed Desurvire, E.) (John Wiley & Sons, 1994).

78. Judd, B. R. Optical absorption intensities of rare-earth ions. *Physical review* **127,** 750 (1962).

79. Ofelt, G. Intensities of crystal spectra of rare-earth ions. *The journal of chemical physics* **37,** 511–520 (1962).
80. Laporte, O. & Meggers, W. F. Some rules of spectral structure. *JOSA* **11,** 459–463 (1925).
81. Vleck, J. V. The Puzzle of Rare-earth Spectra in Solids. *Journal of physical chemistry* **41,** 67–80 (1937).
82. Walsh, B. M. in *Advances in spectroscopy for lasers and sensing* 403–433 (Springer, 2006).
83. Gschneidner, K. A. & Eyring, L. *Handbook on the physics and chemistry of rare earths* (Elsevier, 1998).
84. Carnall, W. T., Fields, P. R. & Wybourne, B. G. Spectral Intensities of the Trivalent Lanthanides and Actinides in Solution. I. Pr^{3+}, Nd^{3+}, Er^{3+}, Tm^{3+}, and Yb^{3+}. *The Journal of Chemical Physics* **42,** 3797–3806 (1965).
85. Carnall, W., Fields, P. & Rajnak, K. Electronic energy levels in the trivalent lanthanide aquo ions. I. Pr^{3+}, Nd^{3+}, Pm^{3+}, Sm^{3+}, Dy^{3+}, Ho^{3+}, Er^{3+}, and Tm^{3+}. *The Journal of chemical physics* **49,** 4424–4442 (1968).
86. Kaminskii, A. A. *Laser crystals: Their physics and properties* (Springer-Verlag, 1990).
87. Sardar, D., Velarde-Montecinos, R. & Vizcarra, S. Spectroscopic properties of Nd^{3+} in CaF_2. *physica status solidi (a)* **136,** 555–560 (1993).
88. Krupke, W. Radiative transition probabilities within the 4 f 3 ground configuration of Nd: YAG. *IEEE Journal of Quantum Electronics* **7,** 153–159 (1971).
89. Shannon, R. D. Revised effective ionic radii and systematic studies of interatomic distances in halides and chalcogenides. *Acta Crystallographica Section A* **32,** 751–767 (1976).
90. Defect aggregation in anion-excess fluorites II. Clusters containing more than two impurity atoms. *Journal of Solid State Chemistry* **51,** 159–169. ISSN: 0022-4596 (1984).
91. Siebold, M, Bock, S, Schramm, U, Xu, B, Doualan, J.-L., Camy, P. & Moncorgé, R. Yb : CaF_2 - a new old laser crystal. *Applied Physics B* **97,** 327–338 (2009).
92. De Sousa, D., Batalioto, F, Bell, M., Oliveira, S. & Nunes, L. Spectroscopy of Nd^{3+} and Yb^{3+} codoped fluoroindogallate glasses. *Journal of Applied Physics* **90,** 3308–3313 (2001).
93. Liégard, F, Doualan, J., Moncorgé, R & Bettinelli, M. $Nd^{3+} \rightarrow Yb^{3+}$ energy transfer in a codoped metaphosphate glass as a model for Yb^{3+} laser operation around 980 nm. *Applied Physics B* **80,** 985–991 (2005).
94. Rivera-López, F, Babu, P, Basavapoornima, C., Jayasankar, C. & Lavín, V. Efficient $Nd^{3+} \rightarrow Yb^{3+}$ energy transfer processes in high phonon energy phosphate glasses for 1.0 μ m Yb^{3+} laser. *Journal of Applied Physics* **109,** 123514 (2011).

95. Petit, V, Camy, P, Doualan, J.-L. & Moncorgé, R. CW and tunable laser operation of Yb^{3+} in Nd : Yb : CaF_2. *Applied physics letters* **88,** 051111 (2006).

96. Weber, M. J. Optical Properties of Yb^{3+} and $Nd^{3+} - Yb^{3+}$ Energy Transfer in $YAlO_3$. *Physical Review B* **4,** 3153 (1971).

97. Jaque, D, Ramirez, M., Bausá, L., Solé, J. G., Cavalli, E, Speghini, A & Bettinelli, M. $Nd^{3+} \rightarrow Yb^{3+}$ energy transfer in the $YAl_3(BO_3)_4$ nonlinear laser crystal. *Physical Review B* **68,** 035118 (2003).

98. Jaque, D., de La O Ramirez, M., Bausá, L., Speghini, A., Bettinelli, M. & Cavalli, E. Influence of Nd^{3+} and Yb^{3+} concentration on the $Nd^{3+} \rightarrow Yb^{3+}$ energy-transfer efficiency in the $YAl_3(BO_3)_4$ nonlinear crystal: determination of optimum concentrations for laser applications. *JOSA B* **21,** 1203–1209 (2004).

99. Serrano, D, Braud, A, Doualan, J., Bolaños, W, Moncorgé, R & Camy, P. Two-step quantum cutting efficiency in $Pr^{3+} - Yb^{3+}$ codoped KY_3F_{10}. *Physical Review B* **88,** 205144 (2013).

100. Jaque, D, Capmany, J, Luo, Z. & Solé, J. G. Optical bands and energy levels of ion in the nonlinear laser crystal. *Journal of Physics: Condensed Matter* **9,** 9715 (1997).

101. Fan, T. & Byer, R. Modeling and CW operation of a quasi-three-level 946 nm Nd: YAG laser. *IEEE Journal of Quantum Electronics* **23,** 605–612 (1987).

102. Fan, T. Y. & Byer, R. L. Diode laser-pumped solid-state lasers. *IEEE journal of Quantum Electronics* **24,** 895–912 (1988).

103. Moulton, P. An investigation of the Co : MgF_2laser system. *IEEE journal of quantum electronics* **21,** 1582–1595 (1985).

104. Risk, W. Modeling of longitudinally pumped solid-state lasers exhibiting reabsorption losses. *JOSA B* **5,** 1412–1423 (1988).

105. Taira, T., Tulloch, W. M. & Byer, R. L. Modeling of quasi-three-level lasers and operation of cw Yb: YAG lasers. *Applied optics* **36,** 1867–1874 (1997).

106. Digonnet, M. J. & Gaeta, C. Theoretical analysis of optical fiber laser amplifiers and oscillators. *Applied Optics* **24,** 333–342 (1985).

107. Migus, A., Shank, C, Ippen, E & Fork, R. Amplification of subpicosecond optical pulses: theory and experiment. *IEEE Journal of Quantum Electronics* **18,** 101–109 (1982).

108. Rustad, G. & Stenersen, K. Modeling of laser-pumped Tm and Ho lasers accounting for upconversion and ground-state depletion. *IEEE Journal of Quantum Electronics* **32,** 1645–1656 (1996).

109. Kaminskii, A., Osiko, V. & Udovenchik, V. Room-temperature induced emission of neodymium-doped $SrF_2 - LaF_3$ crystals. *Journal of Applied Spectroscopy* **6,** 23–25 (1967).

110. Kaminskii, A., Agamalyan, N., Deniseneo, G., Sarkisov, S. & Fedorov, P. Spectroscopy and laser emission of disordered $GdF_3 - CaF_2 : Nd^{3+}$ trigonal crystals. *physica status solidi (a)* **70,** 397–406 (1982).

111. Alimov, O., Basiev, T., Doroshenko, M., Fedorov, P., Konyushkin, V., Nakladov, A. & Osiko, V. Investigation of Nd^{3+} ions spectroscopic and laser properties in SrF_2 fluoride single crystal. *Optical Materials* **34,** 799–802 (2012).

112. Liu, J, Fan, M., Su, L., Jiang, D., Ma, F., Zhang, Q & Xu, J. Laser performance of diode-pumped Nd, Y-codoped $CaF_2 - -SrF_2$ mixed crystal. *Laser Physics* **24,** 035802 (2014).

113. Jelínek, M., Kubeček, V., Su, L., Jiang, D., Ma, F., Zhang, Q., Cao, Y. & Xu, J. Pulsed and continuous-wave laser operation of TGT-grown Nd, Y-codoped: SrF_2 single crystal. *Laser Physics Letters* **11,** 055001 (2014).

114. Foster, J. & Osterink, L. Thermal effects in a Nd: YAG laser. *Journal of Applied Physics* **41,** 3656–3663 (1970).

115. Massey, G. Criterion for selection of cw laser host materials to increase available power in the fundamental mode. *Applied Physics Letters* **17,** 213–215 (1970).

116. Koechner, W. Absorbed pump power, thermal profile and stresses in a cw pumped Nd: YAG crystal. *Applied Optics* **9,** 1429–1434 (1970).

117. Koechner, W. & Rice, D. Effect of birefringence on the performance of linearly polarized YAG: Nd lasers. *IEEE Journal of Quantum Electronics* **6,** 557–566 (1970).

118. Karr, M. Nd: YAIG laser cavity loss due to an internal Brewster polarizer. *Applied Optics* **10,** 893–895 (1971).

119. Joiner, R., Marburger, J & Steier, W. Elimination of stress-induced birefringence effects in single-crystal high-power laser windows. *Applied Physics Letters* **30,** 485–486 (1977).

120. Vyatkin, A. G., Snetkov, I. L., Palashov, O. V. & Khazanov, E. A. *Specificity of Thermally Induced Depolarization in* CaF_2 in *CLEO: Science and Innovations* (2013), CTu1O–5.

121. Snetkov, I., Vyatkin, A., Palashov, O. & Khazanov, E. Drastic reduction of thermally induced depolarization in CaF_2 crystals with [111] orientation. *Optics Express* **20,** 13357–13367 (2012).

122. Koechner, W. & Rice, D. K. Birefringence of YAG: Nd laser rods as a function of growth direction. *JOSA* **61,** 758–766 (1971).

123. Siegman, A. E. *New developments in laser resonators* in *Optical resonators* **1224** (1990), 2–14.

124. Siegman, A. E. Defining, measuring, and optimizing laser beam quality. *Laser Resonators and Coherent Optics: Modeling, Technology, and Applications* **1868,** 2–12 (1993).

125. Siegman, A. E. *How to (maybe) measure laser beam quality* in *Diode Pumped Solid State Lasers: Applications and Issues* (1998), MQ1.

126. Koechner, W. & Bass, M. *Solid-State Lasers* (Springer New York, 2003).

127. Caird, J. A., Payne, S. A., Staver, P. R., Ramponi, A. & Chase, L. Quantum electronic properties of the Na3Ga2Li3F12: Cr3+ laser. *IEEE Journal of Quantum Electronics* **24,** 1077–1099 (1988).

128. Findlay, D & Clay, R. The measurement of internal losses in 4-level lasers. *Physics Letters* **20,** 277–278 (1966).

129. Lai, S. T. & Shand, M. L. High efficiency cw laser-pumped tunable alexandrite laser. *Journal of applied physics* **54,** 5642–5644 (1983).

130. Shand, M & Lai, S. CW laser pumped emerald laser. *IEEE journal of quantum electronics* **20,** 105–108 (1984).

131. Struve, B, Huber, G, Laptev, V., Shcherbakov, I. & Zharikov, E. Tunable room-temperature cw laser action in Cr^{3+} : GdScGa − garnet. *Applied Physics B* **30,** 117–120 (1983).

132. Huber, G. & Petermann, K. in *Tunable solid state lasers* 11–19 (Springer, 1985).

133. Drube, J, Struve, B & Huber, G. Tunable room-temperature cw laser action in Cr3+: GdScAl-garnet. *Optics communications* **50,** 45–48 (1984).

134. Moulton, P. F. Spectroscopic and laser characteristics of Ti: Al 2 O 3. *JOSA B* **3,** 125–133 (1986).

135. Danielmeyer, H. G. Progress in Nd: YAG lasers. *In: Lasers. Volume 4.(A76-39776 19-36) New York* **4,** 1–71 (1976).

136. Druon, F., Chénais, S., Balembois, F., Georges, P., Gaumé, R. & Viana, B. Diode-pumped continuous-wave and femtosecond laser operations of a heterocomposite crystal $Yb^{3+} : SrY_4(SiO_4)_3O||Y_2Al_5O_{12}$. *Opt. Lett.* **30,** 857–859 (2005).

137. Kalisky, Y. Y., Kravchik, L. & Kokta, M. R. *Performance of diode-end-pumped* Cr^{4+}, Nd^{3+} : YAG *self-Q-switched and* Nd : YAG/Cr^{4+} : YAG *diffusion-bonded lasers* in *Laser Crystals, Glasses, and Nonlinear Materials Growth and Characterization* (ed Kalisky, Y. Y.) **4970** (SPIE, 2003), 35 –44.

138. Li, T, Zhuo, Z & Zhao, S. Diode-pumped passively Q-switched mode-locked YVO_4/Nd : YVO_4 composite crystal laser with LT-GaAs saturable absorber mirror. *Laser Physics Letters* **5,** 267–270 (2008).

139. Zhuo, Z., Li, T., Li, X. & Yang, H. Investigation of Nd : YVO_4/YVO_4 composite crystal and its laser performance pumped by a fiber coupled diode laser. *Optics Communications* **274,** 176–181. ISSN: 0030-4018 (2007).

140. Haisma, J., Spierings, B. A. C. M., Biermann, U. K. P. & van Gorkum, A. A. Diversity and feasibility of direct bonding: a survey of a dedicated optical technology. *Appl. Opt.* **33,** 1154–1169 (1994).

141. Mackenzie, J. I. & Shepherd, D. P. End-pumped, passively Q-switched Yb:YAG double-clad waveguide laser. *Opt. Lett.* **27,** 2161–2163 (2002).

142. Sugiyama, A., Fukuyama, H., Sasuga, T., Arisawa, T. & Takuma, H. Direct bonding of Ti:sapphire laser crystals. *Appl. Opt.* **37,** 2407–2410 (1998).

143. Meissner, H. E. *US Patent* 5846638 (1998).

144. Traggis Nick, M. & J., C. *US Patent* US20090294050A1 (2009).

145. Lee, H.-C. & Meissner, H. E. *US Patent* US7803451B2 (2010).

146. Gaume, R. *A crystal chemistry approach for high-power ytterbium doped solid-state lasers. Diffusion-bonded crystals and new crystalline hosts.* Theses (Chimie ParisTech, 2002).

147. Meissner, H. E. *US Patent* US7803451B2 (1992).

148. Sugiyama, A. & Nara, Y. Improved direct bonding method of Nd : YVO_4 and YVO_4 laser crystals. *Ceramics International* **31,** 1085–1090. ISSN: 0272-8842 (2005).

149. Eimerl, D., Campbell, E. M., Krupke, W. F., Zweiback, J., Kruer, W., Marozas, J., Zuegel, J, Myatt, J, Kelly, J, Froula, D, *et al.* StarDriver: a flexible laser driver for inertial confinement fusion and high energy density physics. *Journal of Fusion Energy* **33,** 476–488 (2014).

150. Eimerl, D., Skupsky, S., Myatt, J. & Michael Campbell, E. A StarDriver-class laser achieving 1% beam uniformity in 1 ns. *Journal of Fusion Energy* **35,** 459–469 (2016).

151. Eimerl, D. & Schmitt, A. J. StarDriver: an estimate of the bandwidth required to suppress the $2\omega_{pe}$ instability. *Plasma Physics and Controlled Fusion* **58,** 115006 (2016).

152. Eimerl, D, Skupsky, S & Campbell, E. *StarDriver: Recent results on beam smoothing and LPI mitigation* in *Journal of Physics: Conference Series* **717** (2016), 012015.